UNIONE EUROPEA
Fondo Sociale Europeo

PON RICERCA E INNOVAZIONE

UNIVERSITÀ DEGLI STUDI FIRENZE
Da un secolo, oltre.

DOTTORATO DI RICERCA IN
Fisica e Astronomia

CICLO XXXVII - PON ex DM1061

Development of Perovskite-based Solar Cells for Indoor Photovoltaics

Settore Scientifico Disciplinare
PHYS/03A

Dottorando

Usman Ali Shah

Supervisore

Prof. Francesco Biccari

Coordinatore
Prof. Giovanni Modugno

ځان ژوندي په ځمکه بنخکه لکه تخم که لوي غواړي ده خاورو په مقام شه

Rehman Baba *"Pashto Poet"*

"Never give up, no matter how hard life gets no matter how much pain you feel. Pain will eventually subside, nothing remains forever, so keep going and don't give up".

Imran Khan (Former Prime Minister of Pakistan)

Dedication

To my beloved wife, whose unwavering support and love carried me through this journey. Thank you for your patience, strength, and for caring for our precious daughter, who was born back in Pakistan during my first year of this PhD. I am grateful to you both for enduring the distance and separation, which made this accomplishment possible.

To my daughter, whose smile and spirit have been my greatest motivation, even from afar.

And to my parents, brothers, and sisters, whose constant encouragement and belief in me have been my pillars of strength.

This work is as much yours as it is mine.

Acknowledgments

As I begin writing the acknowledgment section of my thesis, I feel it is time to reveal something I have kept private for years, even from my beloved family members and close friends. During the course of my first PhD, when I was stranded in Pakistan for an extended period due to the COVID-19 pandemic, I experienced profound mental struggles. At one point, I sought the help of a psychiatrist and, for four consecutive months, discreetly took prescribed medication to cope with the overwhelming circumstances. Today, as I write these lines, I am profoundly grateful to Almighty Allah, the Most Beneficent and Most Merciful, who not only guided me through those challenging times but also blessed me with another opportunity to pursue my goals in good health. Alhamdulillah.

The PhD journey is undoubtedly a challenging experience that tests an individual's patience, resilience, and ability to navigate various situations. It also reveals the true nature of those around us. I am deeply grateful to everyone who has supported me and contributed to my journey, and I wish to personally acknowledge their invaluable contributions.

During my PhD, I spent time in three different cities—Florence and Rome in Italy, as well as Tampere, Finland—so the list of people to thank is long. However, I cannot overlook the opportunity to express my sincere appreciation to each of them.

I would like to take this opportunity to express my deepest gratitude to my supervisor, Prof. Francesco Biccari, for his patient, honest, and friendly guidance since the beginning of my PhD program in January 2022 at the University of Florence, Italy. I must admit that you are the kind of mentor every PhD candidate aspires to have. As my PhD journey approaches its conclusion and the path ahead remains uncertain, I know one thing for sure: if I leave here, I will always miss the warmth with which you welcomed me into your office. Over the past three years, every time I gently knocked on your door, you would immediately recognize it was me and respond with a cheerful "Avanti" in Italian. Upon entering, the warmth and kindness with which you greeted me each time made me feel valued and accepted.

I would also like to extend my heartfelt thanks to Dr. Emanuele Calabrò, who mentored me at the Centre for Hybrid and Organic Solar Energy (CHOSE) at the University of Rome Tor Vergata, Rome, Italy, during my industrial internship with the company “Halocell Europe”. His unmatched patience, understanding, and guidance was invaluable. He taught me the fabrication of perovskite solar cells from scratch to completion, providing me with a strong foundation and practical

expertise in this field. His mentorship not only enhanced my technical skills but also inspired me to pursue excellence in my research endeavours.

I cannot forget Professor Paola Vivo from the University of Tampere, Finland, who turned out to be a true blessing in disguise. From our very first Zoom meeting to the six months I spent at the University of Tampere under her kind guidance, I always felt valued and accepted. Her unwavering support and generosity have left me profoundly grateful, and I struggle to find the words to fully express my appreciation. To her, I want to say from the bottom of my heart: I am thankful to you beyond what words can convey.

I would also like to express my heartfelt gratitude to someone in the PhD office of my university (whose name I intentionally leave unmentioned, as it is forever etched in my heart and will forever be cherished). At a critical moment, their generous and unexpected support turned what seemed impossible into a reality for me. This experience reaffirmed my belief that kind people exist everywhere, and their acts of kindness leave an everlasting impression, turning us into their admirers for life.

I am deeply thankful to my flatmates for their support, companionship, and the countless memories we created together. First and foremost, I extend my gratitude to Dr. Ghulam Murtaza, who was the first person I contacted in Florence, Italy, from Pakistan. He offered invaluable guidance, support, and facilitated my stay in their apartment, which made my initial transition much smoother. I am also incredibly grateful to Dr. Muhammad Atif, Dr. Muhammad Ali Umair, and Saqib Hayat. Without their friendship and company, this journey would have been far more challenging. Their presence made my PhD experience not only bearable but truly enjoyable.

A special thanks to Dr. Ramin Emadi from Iran, my close friend at the Department of Physics and Astronomy, who always simplified the complex bureaucratic hurdles in Italy for me. I am equally thankful to Dr. Ashish Yadav, Dr. Shamaila Manzoor, and Dr. Huaqing Luo for being wonderful friends and delightful coffee break companions. Your friendship added warmth and joy to my time at the department.

I am incredibly thankful to my flatmates in Rome, Italy, for making my life easier and more colourful during my industrial internship stay with them. First and foremost, my warmest thanks go to Naseer Khan Marwat for his unwavering support and warm welcome, which made my transition to Rome smooth and comfortable. I am also deeply grateful to Abrar Khan, Muhammad Kamran, Nauman Wahab, Shakir Ullah Khan, Salman Khan, and Sohaib Khan. Without their

companionship and friendship, my time in Rome would not have been as memorable and enjoyable as it turned out to be. Thank you all for the wonderful moments we shared!

I would also like to express my heartfelt gratitude to my colleagues at CHOSE for their invaluable assistance during my experiments. I am truly grateful to Dr. Jie Xu, Zeynab Skafi, and Gyanendra Shankar for their exceptional cooperation and support. Your guidance and willingness to help made a significant difference in my work. Without your assistance, completing the project would not have been as smooth or achievable. Thank you for being such an integral part of my journey!

I would also like to extend my heartfelt thanks to my colleagues at Tampere University for their support and assistance during my fellowship period in Finland. I am especially grateful to Dr. G.K. Murthy Grandhi (My project supervisor), Dr. Debjit Manna, Dr. Ceylan Doyranli, Dr. Yi Han, Dr. Basheer AL-Anesi, and Dr Krishnaiah Mokurala. Your incredible support and companionship provided immense comfort and made my time at Tampere University both productive and enjoyable. Thank you for being such wonderful colleagues and friends!

I cannot forget to mention my dear friends, who remain close to my heart despite being far away during this time. They extended their support whenever I needed it, without hesitation. Special thanks go to Irfan Khan, Tauheed Shah (My Shah Ji Gul), and Dr. Muhammad Ishaq. I am truly proud and grateful to have you in my life.

I would also like to extend my heartfelt gratitude to Dr. Laila Naureen for her unwavering motivation and encouragement throughout my PhD, especially during the times when I was struggling. I am also deeply thankful to Pier Paolo Bonaccini for his tireless efforts in refining my manuscript and conducting the photoluminescence measurements. Furthermore, I must acknowledge Nicoleta Enea, my only foreign PhD colleague from the same batch. We collaborated in organizing courses and scheduling exams with our professors, and without her support, the process would have been far more challenging for me.

Last but certainly not least, I am at a loss for words to express my gratitude to Dr. Umar Farooq, who has been a constant source of comfort and support throughout my research journey over the years. Without him, many of my achievements would have remained dreams. I genuinely wish everyone could have a friend like you in their life. What makes our bond even more extraordinary is that, despite being in regular contact, we haven't had the chance to meet in person for years. It's been far too long, and I truly and deeply miss you!

I thought the list was complete, but I must extend it further to include Dr Naseer Kammalamuriyil Ahammed Basheer, who proved to be an angel sent by the Almighty. His generous help at the last moments enabled me to meet the thesis submission deadline, and for that, I will be forever grateful to him. Thank you very much, and may God bless you.

Abstract

Indoor photovoltaics (IPVs) are emerging as a vital technology for powering low-power electronic devices, particularly in the rapidly expanding Internet of Things (IoT) ecosystem. Perovskite solar cells (PSCs) stand at the forefront of IPV research, demonstrating remarkable potential under low-light conditions due to their exceptional optoelectronic properties and high indoor power conversion efficiencies (iPCEs). This thesis explores two key studies aimed at advancing the performance and stability of PSCs for both indoor and outdoor applications.

The first study focuses on enhancing PSC performance and stability using three iodide-based passivation layers including Phenethyl Ammonium Iodide (PEAI), Octyl Ammonium Iodide (OAI), and Guanidinium Iodide (GUI) along with the Lewis base molecule 1,3-bis(diphenylphosphino)propane (DPPP), which, to the best of current knowledge, has not been reported before and is introduced for the first time in n-i-p structured PSCs in this thesis. Scanning electron microscopy (SEM) and X-Ray diffraction (XRD) results revealed that among all samples, the DPPP-passivated sample demonstrated superior morphological and structural stability after aging in ambient environment for a year compared to the other counterparts. Moreover, under 1000 lux light-emitting diode (LED) light illumination, the device incorporating DPPP achieved highest iPCE of 33.14%, close to the highest iPCE of 34.47% obtained by a device incorporating PEAI. Additionally, the device incorporating DPPP exhibited the highest stability under thermal stress (85°C) and 1000 lux indoor light illumination with T80 (time taken for the cell performance to drop to 80% of its initial value) of 753 hrs.

The second study delved into the role of dopants in 2,2',7,7'-Tetrakis[N,N-di(4-methoxyphenyl)amino]-9,9'-spirobifluorene (Spiro-OMeTAD) hole transport layer (HTL) for PSCs under indoor lighting. Low-temperature planar n-i-p structure devices based on a SnO_2 electron transport layer (ETL) were fabricated, demonstrating adaptability to flexible substrates. While doped Spiro-OMeTAD devices delivered exceptionally higher efficiencies under standard 1-sun illumination compared to their undoped counterparts, a different trend emerged under indoor lighting. Under 1000 lux of white light-emitting diode (WLED) illumination, devices with undoped Spiro-OMeTAD achieved comparable efficiencies (with highest iPCE of 28.37%) with reduced hysteresis compared to doped devices (highest iPCE of 29.36%). Furthermore, under extremely low-light conditions (50 lux), the undoped devices outperformed their doped counterparts, achieving a highest iPCE of 13.65%, compared to the doped devices maximum iPCE of approximately 4%.

Additionally, despite the growing emphasis on environmentally friendly fabrication processes for PSCs, triple-cation perovskite (PVK) absorbers synthesized with the eco-friendly solvent anisole as antisolvent, remain unexplored in IPVs. This thesis also bridges this gap, representing a significant step toward greener PVK-based IPV technologies.

Overall, the thesis results underscore the potential of innovative passivation strategies to optimize PSCs performance and stability under low-light conditions and highlights the significance of ETL materials and the potential of undoped HTLs for achieving efficient and stable PSCs under challenging indoor lighting environments.

List of Publications

1. **Shah, U.A**., Chen, S., Khalaf, G.M.G., Jin, Z. and Song, H., 2021. Wide bandgap Sb_2S_3 solar cells. *Advanced Functional Materials*, *31*(27), p.2100265.
2. **Shah, U.A**., Wang, A., Irfan Ullah, M., Ishaq, M., Shah, I.A., Zeng, Y., Abbasi, M.S., Umair, M.A., Farooq, U., Liang, G.X. and Sun, K., 2024. A Deep Dive into Cu_2ZnSnS_4 (CZTS) Solar Cells: A Review of Exploring Roadblocks, Breakthroughs, and Shaping the Future. *Small*, p.2310584.
3. Farooq, U., **Shah, U.A**., Ishaq, M., Hu, J.G., Ahmed, S., Chen, S., Zheng, Z.H., Su, Z.H., Fan, P. and Liang, G.X., 2023. Defects passivation by solution-processed titanium doping strategy towards high efficiency kesterite solar cells. *Chemical Engineering Journal*, *451*, p.139109.
4. Farooq, U., Han, B., **Shah, U.A**., Yang, F., Li, S., Song, Y., Hassan, A., Li, Z. and Wang, J., Solvent Engineering-Enabled Surface Defect Passivation in $Cu_2ZnSn(S, Se)_4$ Solar Cells with Low Open-Circuit Voltage Losses and Improved Carrier Lifetime. *ChemSusChem*, p.e202402391.
5. Farooq, U., Ishaq, M., **Shah, U.A**., Chen, S., Zheng, Z.H., Azam, M., Su, Z.H., Tang, R., Fan, P., Bai, Y. and Liang, G.X., 2022. Bandgap engineering of lead-free ternary halide perovskites for photovoltaics and beyond: Recent progress and future prospects. *Nano Energy*, *92*, p.106710.
6. Tufail, M., Shah, W.H., **Shah, U.A**, Khan, W.M., Syed, W.A. and Safeen, A., 2019. Effects of Sn doping on the seebeck coefficient and electrical conductivity of $TL_9Sb_{1-x}Sn_xTe_6$ nanoparticles. *Chalcogenide Letters*, *16*(4), pp.175-184.
7. Luo, Y., Ma, H., Ahmad, N., **Shah, U.A**., Zheng, Z., Chen, S., Su, Z., Zhao, J., Zhang, X. and Liang, G., 2025. Rapid Thermal-Driven Crystal Growth and Defect Suppression in Antimony Selenide Thin Film for Efficient Solar Cells. *Small*, *21*(1), p.2403051.
8. Chen, S., Ishaq, M., Xiong, W., **Shah, U.A**, Farooq, U., Luo, J., Zheng, Z., Su, Z., Fan, P., Zhang, X. and Liang, G., 2021. Improved Open-Circuit Voltage of Sb_2Se_3 Thin-Film Solar Cells Via Interfacial Sulfur Diffusion-Induced Gradient Bandgap Engineering. *Solar Rrl*, *5*(10), p.2100419.
9. Zeng, Y., Huang, J., Li, J., Sun, K., **Shah, U.A**., Deng, H., Zhang, X., Sha, C., Qian, C., Song, H. and Hao, X., 2022. Comparative study of TiO_2 and CdS as the electron transport layer for Sb_2S_3 solar cells. *Solar RRL*, *6*(10), p.2200435.
10. Abbasi, M.S., Sultana, R., Ahmed, I., Adnan, M., **Shah, U.A**., Irshad, M.S., Vu, H.N., Do, L.T., Vu, H.H.T., Pham, T.D. and Nang, H.X., 2024. Contemporary advances in organic

11. thermoelectric materials: Fundamentals, properties, optimization strategies, and applications. *Renewable and Sustainable Energy Reviews*, *200*, p.114579.
12. Ishaq, M., Deng, H., Farooq, U., Zhang, H., Yang, X., **Shah, U.A**. and Song, H., 2019. Efficient copper-doped antimony sulfide thin-film solar cells via coevaporation method. *Solar RRL*, *3*(12), p.1900305.
13. Li, M., Chen, S., Zhao, X., Xiong, K., Wang, B., **Shah, U.A**., Gao, L., Lan, X., Zhang, J., Hsu, H.Y. and Tang, J., 2022. Matching charge extraction contact for infrared PbS colloidal quantum dot solar cells. Small, 18(1), p.2105495.
14. Li, M., Chen, S., Zhao, X., Xiong, K., Wang, B., **Shah, U.A**., Gao, L., Lan, X., Zhang, J., Hsu, H.Y. and Tang, J., 2022. Matching Charge Extraction Contact for Infrared PbS Colloidal Quantum Dot Solar Cells (Small 1/2022). *Small*, *18*(1), p.2270005.
15. Ishaq, M., Li, X., Mehmood, S., Zhong, Y.M., Mansoor, A., **Shah, U.A**., Chen, S., Chen, Y., Zheng, Z. and Liang, G., 2024. Heterojunction interface engineering enabling high transmittance and record efficiency in Sb_2S_3 semitransparent solar cell. *Chemical Engineering Journal*, *501*, p.157646.
16. Zhang, H., Yuan, S., Deng, H., Ishaq, M., Yang, X., Hou, T., **Shah, U.A**., Song, H. and Tang, J., 2020. Controllable orientations for Sb_2S_3 solar cells by vertical VTD method. *Progress in Photovoltaics: Research and Applications*, *28*(8), pp.823-832.
17. Mateen, M., Shi, H., Huang, H., Li, Z., Ahmad, W., Rafiq, M., **Shah, U.A**., Sajid, S., Ren, Y., Park, J. and Chi, D., 2023. Graded 2D/3D Perovskite Hetero-Structured Films with Suppressed Interfacial Recombination for Efficient and Stable Solar Cells via DABr Treatment. *Molecules*, *28*(4), p.1592.
18. Xu, Z., Gao, Q., Cui, C., Yuan, S., Kou, D., Zhou, Z., Zhou, W., Meng, Y., Qi, Y., Ishaq, M. and **Shah, U.A**., 2023. Gradient Conduction Band Energy Engineering Driven High-Efficiency Solution-Processed $Cu_2ZnSn(S, Se)_4/Zn_xCd_{1-x}S$ Solar Cells. *Advanced Functional Materials*, *33*(3), p.2209187.

List of Abbreviations

Au – Gold
Br – Bromine
CBM – Conduction Band Minimum
Cs – Cesium
DMF – Dimethylformamide
DMSO – Dimethylsulfoxide
DPPP – 1,3-bis(diphenylphosphino)propane
DSSCs – Dye-Sensitized Solar Cells
EQE – External Quantum Efficiency
ETL – Electron Transport Layer
FA – Formamidinium
FF – Fill Factor
GUI – Guanidinium Iodide
HTL – Hole Transport Layer
I – Iodine
IPCE – Incident Photon to Current Efficiency
iPCE – Indoor Power Conversion Efficiency
iPCEs – Indoor Power Conversion Efficiencies
IPV – Indoor Photovoltaic
IPVs – Indoor Photovoltaics
IOT – Internet of Things
ITO – Indium Tin Oxide (In_2O_3)

J_{sc} – Short-circuit Current Density
LED – Light Emitting Diode
MA – Methylammonium
MPP – Maximum Power Point
OAI – Octylammonium Iodide
OPVs – Outdoor Photovoltaics
Pb – Lead
PbI_2 – Lead Iodide
PEAI – Phenethylammonium Iodide
PL – Photoluminescence
PSCs – Perovskite Solar Cells
PV – Photovoltaic
PVK – Perovskite
QDSs – Quantum Dot Solar Cells
R_{sh} – Shunt Resistance
R_s – Series Resistance
SEM – Scanning Electron Microscope
SPO – Stabilized Power Output
Si – Silicon
SnO_2 – Tin Dioxide
Spiro-OMeTAD – 2,2',7,7'-Tetrakis[N,N-di(4-methoxyphenyl)amino]-9,9'-spirobifluorene
t – Goldschmidt Tolerance Factor
TiO_2 – Titanium Dioxide
TR-PL – Time Resolved Photoluminescence
V – Voltage
VBM – Valence Band Maximum
V_{oc} – Open Circuit Voltage
WLED – White Light Emitting Diode
XRD – X-ray Diffraction
μ – Octahedral Factor

Table of Contents

Table of Contents xxv
Introduction 1
Thesis Motivation 3
Research Aims/Objectives 3
Achieved Milestones 3
Structure of the Thesis 4
References 5
Chapter 1 9
Indoor Photovoltaics 9
1.1 Light Intensity and PVs 9
1.2 History of IPVs 10
1.3 Importance of IPV Technology 10
1.4 Sources of Indoor Lighting 11
1.5 IPV Performance Parameters 13
1.6 Challenges of IPV Technology 18
References 22
Chapter 2 27
Perovskite Solar Cells 27
2.1 What are PVKs? 27
2.2 Metal Halide PVKs 27
2.3 Crystal Structure of Lead Metal Halide PVKs 28
2.4 Typical PVK Materials for PVs 29
2.4.1 Methylammonium Lead Iodide ($MAPbI_3$) 29
2.4.2 Formamidinium Lead Iodide ($FAPbI_3$) 30
2.4.3 Cesium Lead Iodide ($CsPbI_3$) 30
2.4.4 Cesium Lead Bromide ($CsPbBr_3$) 30
2.5 Mixed Ion PVK Materials 30
2.6 Synthesis of PVKs for PVs 32
2.7 Formation of Defects in Solution Processed PVKs 34
2.8 Device Structures of PSCs 36
2.9 Working Principle of n-i-p Structure PSCs 37
2.9.1 Transparent Conductive Oxides (TCOs) 37
2.9.2 ETL 38

2.9.3 HTL 39
2.9.4 Top Counter Electrode 40
2.10 A Literature Reviewe of n-i-p Structure Pb-based Triple Cation PVKs for IPVs 41
2.11 Issues to be addressed 46
2.11.1 Hysteresis 46
2.11.2 Stability 47
2.11.3 Toxicity 50
2.12 Summary 52
References 54
Chapter 3 69
Materials and Methods 69
3.1 A Brief Overview of Synthesis and Characterization Approaches 69
3.2 Study 1st : Passivation Layers Incorporation in Device Structure 69
3.2.1 Materials 69
3.2.2 Perovskite Solution 70
3.2.3 Passivation Solutions 70
3.2.4 Spiro-OMeTAD Solution 70
3.2.5 Devices Fabrication 70
3.3 Study 2nd : Fabrication of Devices with Doped- and Undoped-Spiro-OMeTAD 73
3.3.1 Materials 73
3.3.2 Absorber Triple Cation PVK Solution 73
3.3.3 Preparation of Dopants Solutions for Spiro-OMeTAD 74
3.3.4 Doped and Undoped Spiro-OMeTAD Solutions Preparation 74
3.3.5 Device Fabrication 74
3.4 Structural Investigation 76
3.4.1 X-ray Diffraction (XRD) 76
3.4.2 Scanning Electron Microscopy (SEM) 76
3.5 Optical measurements 77
3.5.1 Optical properties 77
3.5.2 Photoluminescence (PL) Spectroscopy 77
3.6 Electrical measurements 78
3.6.1 Current-voltage characteristics 78
3.6.2 EQE Measurements 80
Reference/s 81
Chapter 4 83
Comparative Study of Different Passivation Layers for n-i-p Perovskite Solar Cell for Indoor Applications 83

4.1 Motivation 83
4.2 Introduction 84
4.3 Results and Discussions 86
4.3.1 Surface Morphology of the PVK Films 87
4.3.2 XRD Analysis 88
4.3.3 PL Measurements 89
4.3.4 PV performances of the PSCs under indoor light illumination 93
4.3.5 PV performances of the PSCs under STC 96
4.3.6 Aging and stability 100
4.3.7 Fabrication and Characterization of DPPP-BS devices and Samples 102
4.3.8 Thermal Stability Testing 104
4.4 Conclusion 106
References 107
Chapter 5 113
To Dope or Not to Dope: Investigating the Necessity of Spiro-OMeTAD Doping in Perovskite Solar Cells for IPVs 113
5.1 Motivation 113
5.2 Introduction 114
5.3 Results and Discussions 115
5.3.1 Measurements Under Standard 1-Sun Illumination 117
5.3.2 Measurements Under Indoor Illumination 119
5.3.3 Measurements at Varying Light WLED Illumination 122
5.4 Conclusion 131
5.5 Future Work 132
Chapter 6 137
Conclusions and Future Work 137
6.1 Conclusions 137
6.2 Outlook and Future Prospects 138

Introduction

The global population is rapidly increasing, and industrialization and modernization have reached unprecedented levels in developed countries. However, the world continues to rely heavily on traditional non-renewable and unsustainable energy resources like fossil fuels [1], which not only harm the environment but also accelerate the depletion of these limited resources [2,3]. Moreover, on the one hand, a recently published report highlights that in many developing and poor nations, a substantial portion of their residents still lacks access to electricity, reaching 685 million globally [4]. On the other hand, in stark contrast, the developed world is rapidly transitioning into a fully digital age, driven by the rise of smart devices and advanced technologies such as the Internet of Things (IoT). This digital revolution has led to an increasing reliance on batteries for power [5]. However, the frequent need to replace batteries presents significant challenges, including environmental impact, resource depletion, safety concerns, and escalating costs [6,7]. Therefore, addressing these challenges requires the urgent development of affordable, accessible, reliable, and sustainable energy solutions.

The sun, central star in solar system, provides Earth with vast amounts of energy [8], delivering 1.75×10^{17} watts in less than an hour, enough to meet global annual energy demands [9]. Solar energy holds immense potential to reduce fossil fuel dependence [10], but harvesting it efficiently remains a challenge. Photovoltaic (PV) technology directly converts light into electricity via PV cell made from semiconductor materials [11]. A single PV cell generates a small amount of power output under sunlight, but solar panels, made of interconnected PV cells, increase the power output to practical levels [12–14]. Therefore, being serving as the fundamental building blocks of solar panels, these PV cells, also known as solar cells, are key to advancing renewable energy and reducing reliance on fossil fuels.

Beyond sunlight, PV cells can harness energy from artificial indoor light sources, a process known as indoor PV (IPV) technology. While IPVs produce significantly lower power than conventional outdoor PV (OPV) systems, their output is well-suited for low-power electronic devices operating in the micro-watt (μW) to watt (W) range [15]. Therefore, IPVs is currently gaining significant attention due to the growing need for sustainable energy solutions to power the rapidly growing market of IoT devices, wearable electronics, and self-sustaining smart sensors [5]. However, on the one hand, indoor light sources exhibit spectral distributions and intensities that differ significantly from the standard AM1.5G solar spectrum [16]. While, on the other hand, PV research has traditionally focused on harvesting outdoor sunlight. Therefore, there is an emerging need for

targeted research and development to design and optimize solar cell materials, device architectures, and bandgap engineering specifically tailored for the unique characteristics of indoor light.

Since Becquerel discovered the PV effect in 1839 , PVs have evolved through three generations, both in terms of their development timeline and the semiconductor materials used [17]. The first generation, mono- or polycrystalline silicon-based PV technologies, and the second generation, thin-film PV technologies, have been commercialized [18]. However, first-generation cells face issues such as high fabrication costs, weight, and inflexibility [19]. Thin-film PV technologies, developed to address the drawbacks of first-generation cells, offer cost-effective fabrication and flexibility. However, mature thin-film technologies such as $CuInGaSe_2$ (CIGS) contain rare elements like indium (In) and gallium (Ga), while CdTe contains the toxic element cadmium (Cd), both of which restrict their commercial competitiveness [20,21].

In response, third-generation PV technologies, including Organic Photovoltaics (Organic PVs) [22], Dye-Sensitized Solar Cells (DSSCs) [23], Quantum Dot Solar Cells (QDSs) [24], and Perovskite Solar Cells (PSCs) [25], offer low-cost, solution-processable materials with potential for flexible, lightweight, and affordable solar panels. These technologies are also suitable for both outdoor and indoor PV applications. However, despite their potential, third-generation PV technologies are still at the lab scale and face significant challenges in efficiency, stability, toxicity and scalability before they can be commercialized.

Among emerging third-generation PV technologies, PSCs have garnered unparalleled attention due to their exceptional optoelectronic properties, becoming a central focus in recent PV research. Unlike materials such as silicon (Si) or CdTe, the term “perovskite (PVK)” refers to a family of compounds with the general formula ABX_3, where “A and B” are metal cations, and “X” is an anion. Historically, back in 2012, Kim et al. [26] reported the first solid-state device based on PVK absorber. Since then, much has been learned, investigated, optimized and applied, and remarkable advancements has been achieved in the field at the lab scale under standard testing conditions. As a result, unlike Si, CdTe, and CIGS technologies, which took decades to mature, PSCs have skyrocketed in efficiency race, reaching certified 26.39% [27], and surpassed mature thin-film technologies as well as all the other third generation PV technologies, while significantly narrowed the gap with Si-based solar cells [28].

Beyond outdoor PVs, PSCs have also excelled in lab-scale research for IPVs, driven by their exceptional optoelectronic properties and the flexibility in tuning their bandgaps ranging from 1.15

eV [29] to over 3 eV [30], covering the entire visible spectrum of light [31]. In 2015, Kawata et al. [32] firstly reported the potential of PSCs under indoor illumination. Since then, in less than a decade, PVK-based IPV devices have surpassed the 40% efficiency milestone under indoor lighting, outperforming both traditional and emerging IPV technologies [33–36]. Nevertheless, despite significant breakthroughs in PSCs for both indoor and outdoor applications, challenges such as stability, toxicity, and performance reproducibility persist, hindering their market entry [37–39]. Addressing these issues is crucial for the successful commercialization of PSCs.

Thesis Motivation

As explained, despite notable progress, the commercialization of PSCs remains distant due to issues related to stability, toxicity, reproducibility, and performance. While numerous strategies have been applied to address these challenges in PSCs for outdoor applications. However, IPVs is an emerging field that requires renewed attention. Therefore, this thesis aims to explore how optimization strategies can influence the performance and stability of PSCs under different operating conditions.

Research Aims/Objectives

The key aims and objectives of this thesis are:

- To investigate the impact of various passivation layers, including Phenethylammonium Iodide (PEAI), Octylammonium Iodide (OAI), Guanidinium Iodide (GUI) and 1,3-bis(diphenylphosphino)propane (DPPP) on the stability of triple-cation PVK films, as well as their effect on the performance and stability of triple-cation PVK-based solar cells under both indoor and outdoor lighting conditions.
- To investigate whether traditional dopants in the 2,2',7,7'-Tetrakis[N,N-di(4-methoxyphenyl)amino]-9,9'-spirobifluorene (Spiro-OMeTAD) hole transport layer (HTL) for SnO_2-based n-i-p structure PSCs are equally critical for achieving high performance under both outdoor and indoor conditions, or if their importance varies between these operating environments.

Achieved Milestones

- Improved the stability of triple-cation PVK films through passivation layers deposition.

- Improved the performance and stability of triple-cation PVK-based solar cells under both indoor and outdoor lighting conditions by incorporating passivation layers in the device architecture.
- Pioneered the integration of DPPP as a passivation layer in n-i-p structure perovskite solar cells.
- Demonstrated comparable performance under indoor illumination using doped and undoped Spiro-OMeTAD hole transport layers.
- Developed eco-friendly triple-cation PVK-based solar cells for IPVs by replacing chlorobenzene with green anisole as an antisolvent.
- Achieved the highest indoor power conversion efficiency (iPCE) to date for undoped Spiro-OMeTAD-based PSCs under 1000 lux white light emitting diode (WLED) illumination a record iPCE under extremely low 50 lux WLED illumination

Structure of the Thesis

1. **Chapter 1** provides an overview of IPV technology, covering differences between indoor lighting and sunlight, the history and need for IPVs, materials selection, PV performance parameters, and the impact of light intensity. It concludes with challenges faced by current IPV technologies.
2. **Chapter 2** discusses perovskite materials, focusing on Pb-based mixed cation PVKs, their crystal structure, optoelectronic properties, synthesis methods, and defects. It also reviews the different functional layer of n-i-p structure PSCs and concludes with advancements and challenges in Pb-based triple-cation PVKs for IPV applications.
3. **Chapter 3** provides details about the materials used for the device layers, including their purity and sources. It also outlines the solution preparation methods, device fabrication protocols, and characterization techniques applied to both samples and devices.
4. **Chapter 4** examines the impact of passivation layers (OAI, GUI, PEAI, and DPPP) on the properties and stability of triple cation PVK films, comparing passivated and non-passivated films over time. It also evaluates the influence of these passivation layers on the performance and stability of devices under different lighting and environmental conditions.
5. **Chapter 5** explores whether Spiro-OMeTAD dopants are essential for device performance under low light conditions.
6. **Chapter 6** concludes the thesis, summarizing the findings and suggesting future research directions.

References

1. https://www.energyinst.org/statistical-review.

2. Yang, X., Pang, J., Teng, F., Gong, R. & Springer, C. The environmental co-benefit and economic impact of China's low-carbon pathways: Evidence from linking bottom-up and top-down models. *Renewable and Sustainable Energy Reviews* **136**, 110438 (2021).

3. Curtin, J. *et al.* Quantifying stranding risk for fossil fuel assets and implications for renewable energy investment: A review of the literature. *Renewable and Sustainable Energy Reviews* **116**, 109402 (2019).

4. https://sdg.iisd.org/news/un-report-records-first-drop-in-energy-access-in-decade/.

5. Chatterjee, A. *et al.* Powering internet-of-things from ambient energy: a review. *Journal of Physics: Energy* **5**, 022001 (2023).

6. Hwang, S. & Yasuda, T. Indoor photovoltaic energy harvesting based on semiconducting π-conjugated polymers and oligomeric materials toward future IoT applications. *Polym J* **55**, 297–316 (2023).

7. White, B. E. Beyond the battery. *Nat Nanotechnol* **3**, 71–72 (2008).

8. Hossain, E. *The Sun, Energy, and Climate Change*. (Springer Nature Switzerland, Cham, 2023). doi:10.1007/978-3-031-22196-5.

9. Kumavat, P. P., Sonar, P. & Dalal, D. S. An overview on basics of organic and dye sensitized solar cells, their mechanism and recent improvements. *Renewable and Sustainable Energy Reviews* **78**, 1262–1287 (2017).

10. Kabir, E., Kumar, P., Kumar, S., Adelodun, A. A. & Kim, K.-H. Solar energy: Potential and future prospects. *Renewable and Sustainable Energy Reviews* **82**, 894–900 (2018).

11. Zhang, C., Zhang, J., Ma, X. & Feng, Q. *Semiconductor Photovoltaic Cells*. (Springer Singapore, Singapore, 2021). doi:10.1007/978-981-15-9480-9.

12. https://www.brsolarsystem.com/news/what-is-the-difference-between-a-solar-cell-an-78604947.html#:~:text=Solar%20Cell%3A%20The%20basic%20unit,that%20make%20up%20solar%20panels.

13. https://www.cnet.com/home/energy-and-utilities/solar-cell-module-panel-and-array-whats-the-difference/#google_vignette.

14. https://www.energy.gov/eere/solar/solar-photovoltaic-technology-basics.

15. Pecunia, V., Occhipinti, L. G. & Hoye, R. L. Z. Emerging Indoor Photovoltaic Technologies for Sustainable Internet of Things. *Adv Energy Mater* **11**, (2021).

16. Kim, S., Jahandar, M., Jeong, J. H. & Lim, D. C. Recent Progress in Solar Cell Technology for Low-Light Indoor Applications. *Current Alternative Energy* **3**, 3–17 (2019).

17. Solak, E. K. & Irmak, E. Advances in organic photovoltaic cells: a comprehensive review of materials, technologies, and performance. *RSC Adv* **13**, 12244–12269 (2023).

18. Singh, B. P., Goyal, S. K. & Kumar, P. Solar PV cell materials and technologies: Analyzing the recent developments. *Mater Today Proc* **43**, 2843–2849 (2021).

19. Buitrago, E., Novello, A. M. & Meyer, T. Third-Generation Solar Cells: Toxicity and Risk of Exposure. *Helv Chim Acta* **103**, (2020).

20. Liu, F. *et al.* Emerging inorganic compound thin film photovoltaic materials: Progress, challenges and strategies. *Materials Today* **41**, 120–142 (2020).

21. Efaz, E. T. *et al.* A review of primary technologies of thin-film solar cells. *Engineering Research Express* **3**, 032001 (2021).

22. Jain, A. *et al.* Advances in organic solar cells: Materials, progress, challenges and amelioration for sustainable future. *Sustainable Energy Technologies and Assessments* **63**, 103632 (2024).

23. Arkan, F., Pakravesh, F., Barati Darband, F., Sabagh, S. & Izadyar, M. Recent progress toward high-performance dye-sensitized solar cells: a review. *Journal of the Iranian Chemical Society* **21**, 577–638 (2024).

24. Sahai, S., Jangra, A., Thomas, L. M. & Satsangi, V. R. Quantum Dots as Efficient Solar Energy Absorber: Review on Photovoltaics and Photoelectrochemical Systems. *Journal of The Institution of Engineers (India): Series D* **105**, 553–566 (2024).

25. Elangovan, N. K. *et al.* Recent developments in perovskite materials, fabrication techniques, band gap engineering, and the stability of perovskite solar cells. *Energy Reports* **11**, 1171–1190 (2024).

26. Kim, H.-S. *et al.* Lead Iodide Perovskite Sensitized All-Solid-State Submicron Thin Film Mesoscopic Solar Cell with Efficiency Exceeding 9%. *Sci Rep* **2**, 591 (2012).

27. Qu, G. *et al.* Self-assembled materials with an ordered hydrophilic bilayer for high performance inverted Perovskite solar cells. *Nat Commun* **16**, 86 (2025).

28. https://www.nrel.gov/pv/cell-efficiency.html.

29. Zhao, B. *et al.* High Open-Circuit Voltages in Tin-Rich Low-Bandgap Perovskite-Based Planar Heterojunction Photovoltaics. *Advanced Materials* **29**, (2017).

30. Liu, D., Yang, C. & Lunt, R. R. Halide Perovskites for Selective Ultraviolet-Harvesting Transparent Photovoltaics. *Joule* **2**, 1827–1837 (2018).

31. Lei, Y., Chen, Y. & Xu, S. Single-crystal halide perovskites: Opportunities and challenges. *Matter* **4**, 2266–2308 (2021).

32. Kawata, K., Tamaki, K. & Kawaraya, M. Dye-sensitised and Perovskite Solar Cells as Indoor Energy Harvestors. *Journal of Photopolymer Science and Technology* **28**, 415–417 (2015).

33. Muhammad, B. T., Kar, S., Stephen, M. & Leong, W. L. Halide perovskite-based indoor photovoltaics: recent development and challenges. *Mater Today Energy* **23**, 100907 (2022).

34. Guo, Z., Jena, A. K. & Miyasaka, T. Halide Perovskites for Indoor Photovoltaics: The Next Possibility. *ACS Energy Lett* **8**, 90–95 (2023).

35. Wang, K.-L., Zhou, Y.-H., Lou, Y.-H. & Wang, Z.-K. Perovskite indoor photovoltaics: opportunity and challenges. *Chem Sci* **12**, 11936–11954 (2021).

36. Burwell, G. *et al.* Wide-Gap Perovskites for Indoor Photovoltaics. *Solar RRL* **8**, (2024).

37. Yang, C. *et al.* Achievements, challenges, and future prospects for industrialization of perovskite solar cells. *Light Sci Appl* **13**, 227 (2024).

38. Goetz, K. P. & Vaynzof, Y. The Challenge of Making the Same Device Twice in Perovskite Photovoltaics. *ACS Energy Lett* **7**, 1750–1757 (2022).

39. Correa-Baena, J.-P. *et al.* Promises and challenges of perovskite solar cells. *Science (1979)* **358**, 739–744 (2017).

Chapter 1

Indoor Photovoltaics

1.1 Light Intensity and PVs

As mentioned in introduction, an IPV device generates electricity from low-intensity, artificial light sources such as light emitting diode (LED), fluorescent, or incandescent lighting, etc. Before discussing IPVs, let's first understand the nature of light we encounter daily. As illustrated in **Figure 1.1**, light intensity varies in both outdoor and indoor environments, measured in lux. Lux represents the amount of light (luminous flux) per unit area perceived by the human eye. It is the photometric equivalent of power per unit area (W/m²), weighted by the sensitivity of eye to different wavelengths, and is commonly used to describe indoor lighting levels.

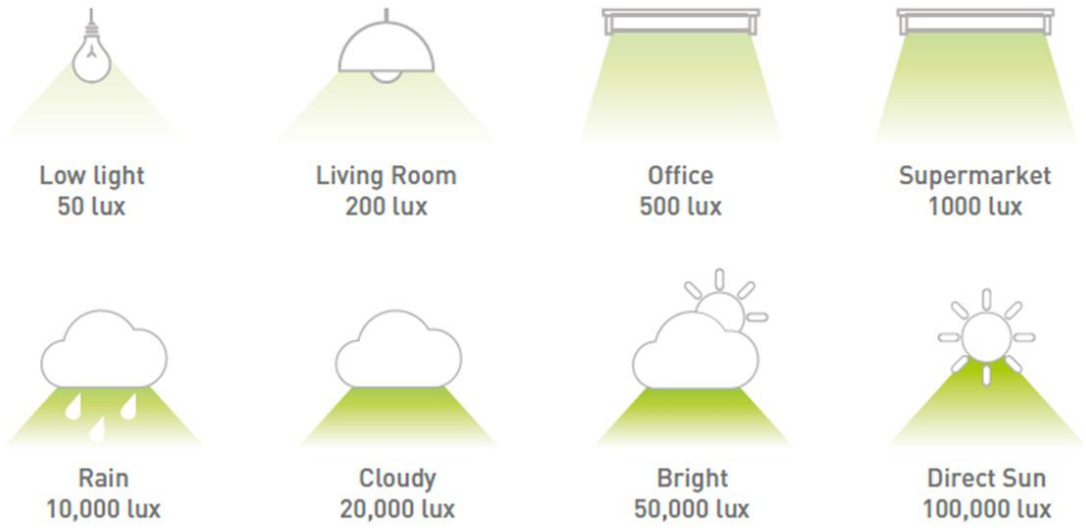

Figure 1.1. Conditions of light at different levels [1].

Direct sunlight provides a maximum intensity of 100,000 lux, while low ambient light or night lighting gives around 50 lux. Overcast or shady days provide 50,000 lux, and indoor lighting typically reaches 200 lux. This highlights the significant variation in light intensity from indoor to outdoor environments, which is crucial for PV applications. Traditional PV testing is conducted under AM 1.5 filtered light at 1000 W/m² (≈100,000 lux) to match outdoor conditions [2,3]. However, no standardized light intensity exists for IPV devices, which are tested at intensities ranging from 50 to 1000 lux, allowing them to capture and convert a wide range of indoor lighting. Thus, the main difference between IPVs and OPVs technologies is the light intensity they encounter. While

both technologies operate on the same PV principle, IPV devices and modules are designed for capturing lower light intensities, distinguishing them from OPVs counterparts [4].

1.2 History of IPVs

My generation, along with those older than me, grew up using calculators with small solar strips. I was also fortunate to receive a Casio digital wristwatch with a tiny solar panel, a gift from my uncle working in Saudi Arabia. I proudly told others it didn't need a battery, as it powered itself from light. From a historical standpoint, the development of solar calculators and watches after 1970, when Si-based PV technology surged, is viewed as the birth of IPV technology. In 1976, Citizen launched the Quartz Crystron Solar Cell watch, the first powered by any light source [5], and Sharp released the EL-8026, the first solar-powered calculator. Sharp later developed an ultraviolet PV cell calculator in 1979 operating under fluorescent light [6]. Subsequent advances in thin-film a-Si solar cells led to broader use of these products globally. Therefore, in literature, solar-powered watches and calculators are often linked to birth of IPV technology [7,8]. However, IPV technology was developed several years before these products. Remarkably, long before solar calculators and watches, IPV technology had made a groundbreaking leap in 1957 with the "Acopian Solar Radio" developed by Acopian and Workman. This radio used a Se-based solar cell and required no batteries or electricity, operating on sunlight or indoor light. The instruction sheet of it even suggested using light sources like a flashlight or candle could activate it in emergencies [9].

1.3 Importance of IPV Technology

The IoT has revolutionized how we interact with the world, connecting devices like smart appliances, wearables, and sensors to enhance efficiency and automation [10,11]. However, many IoT devices rely on batteries, limiting their lifespan and increasing maintenance costs [12]. This dependence also raises environmental concerns, as improper battery disposal can contaminate soil and water, and battery production depletes finite resources like lithium, cobalt, and nickel [13]. As demand for IoT devices grows, so does the need for materials, leading to resource depletion, environmental harm, and potential geopolitical conflicts. The disposal of batteries used in these devices is a major concern, with 78 million batteries expected to be discarded daily by 2025 in European Union (EU) unless measures are taken to extend their lifespans [14]. This highlights the urgent need for alternatives to disposable batteries. Given that many IoT devices consume very low power ranging from µW to W, as illustrated in **Figure 1.2**, energy harvesting solutions, such as IPVs, are gaining renewed attention. IPVs harness indoor lighting to power these devices or charge their batteries, extending their life and reducing battery waste. Therefore, with growing

demand for eco-friendly power sources, IPV offers a sustainable energy solution for low-power IoT devices. To unlock the potential of IPVs, more research is needed to discover new materials optimized for low-light conditions, as traditional PV materials like Si are less effective indoors. Therefore, investigating the potential of novel semiconductors for IPVs is the need of hour to further advance the technology. With ongoing advancements, IPV technologies will play a critical role in the future of low-power electronics and the IoT ecosystem.

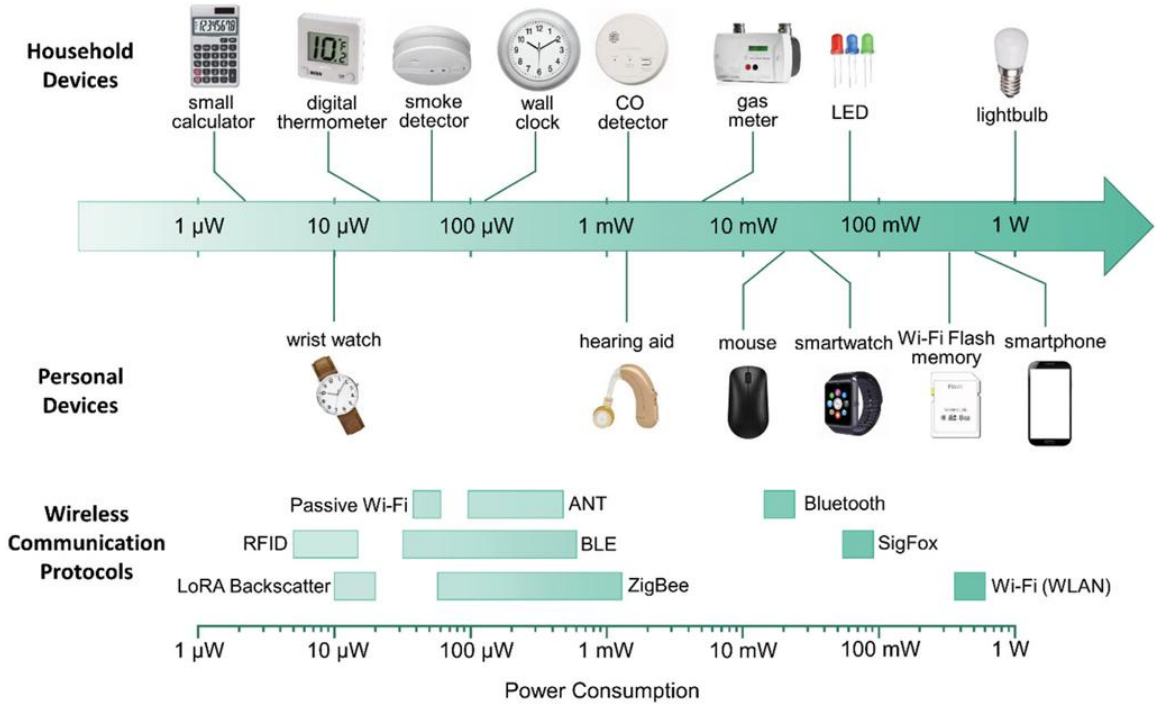

Figure 1.2. Energy usage of common household devices and personal gadgets alongside popular wireless communication protocols [15].

1.4 Sources of Indoor Lighting

As mentioned before, currently, no standard model exists for evaluating PV devices under artificial indoor lighting. Researchers are using various artificial light sources like LEDs, incandescent bulbs, CFLs, and fluorescent tubes to test devices [16–19]. LEDs, in particular, are gaining popularity due to their energy efficiency. However, regardless of differences in design, lifespan, or brightness, IPV performance is highly dependent on the type of light source used [17,20]. In addition to artificial light sources, indirect sunlight, or light diffused through windows, also provides lower intensity (200–1000 lux) compared to direct sunlight (~100,000 lux) [21]. The amount of sunlight entering a room depends on factors such as window size, orientation, cloud cover [22], along with geographic location, season, and time of day. Therefore, while artificial light is the only source at night, daytime indoor lighting can vary with a mix of diffused sunlight and artificial lighting [8].The performance of solar cell devices depends not only on light intensity but also on the spectrum of

light they receive [20]. Indoor artificial light sources mainly cover the visible range (400–700 nm), whereas the standard solar spectrum extends into ultraviolet and infrared regions [8,21]. **Figure 1.3(a-g)** compares spectral characteristics of various light sources with the sensitivity of human eye and PV materials absorption. Xenon lamps mimic sunlight but lack intensity in green and red, while incandescent and halogen bulbs peak in red and infrared. For IPV applications, aligning the spectral response of absorber materials with indoor light sources is essential for optimizing PV efficiency. Fluorescent and white LEDs, with their light range (350–750 nm) aligning well with human eye sensitivity, are particularly favourable for IPV efficiency [23,24]. Additionally, **Figure 1.3(h)** compares the solar spectrum (AM 1.5G) with the spectral response of various PV technologies. c-Si cells align well with the full spectrum, while next-generation PVs like Organic PVs, PSCs, and DSSCs respond mainly in the visible range. This demonstrates that achieving high efficiency across the broader AM 1.5G solar spectrum requires lower bandgap absorber materials, such as c-Si (1.12 eV). In contrast, the narrower wavelength range of indoor light (400–700 nm) is best suited to wide bandgap absorbers for optimal efficiency. Theoretical calculations support these observations. For instance, as can be seen in **Figure 1.4(a)**, achieving high efficiency in OPVs is theoretically possible with an absorber material having a bandgap of approximately 1.34 eV, based on the AM 1.5G spectrum [25]. In contrast, the optimal bandgap for an ideal absorber material to achieve maximum efficiency under indoor lighting conditions (400–700 nm) is approximately 1.9 eV [26,27].

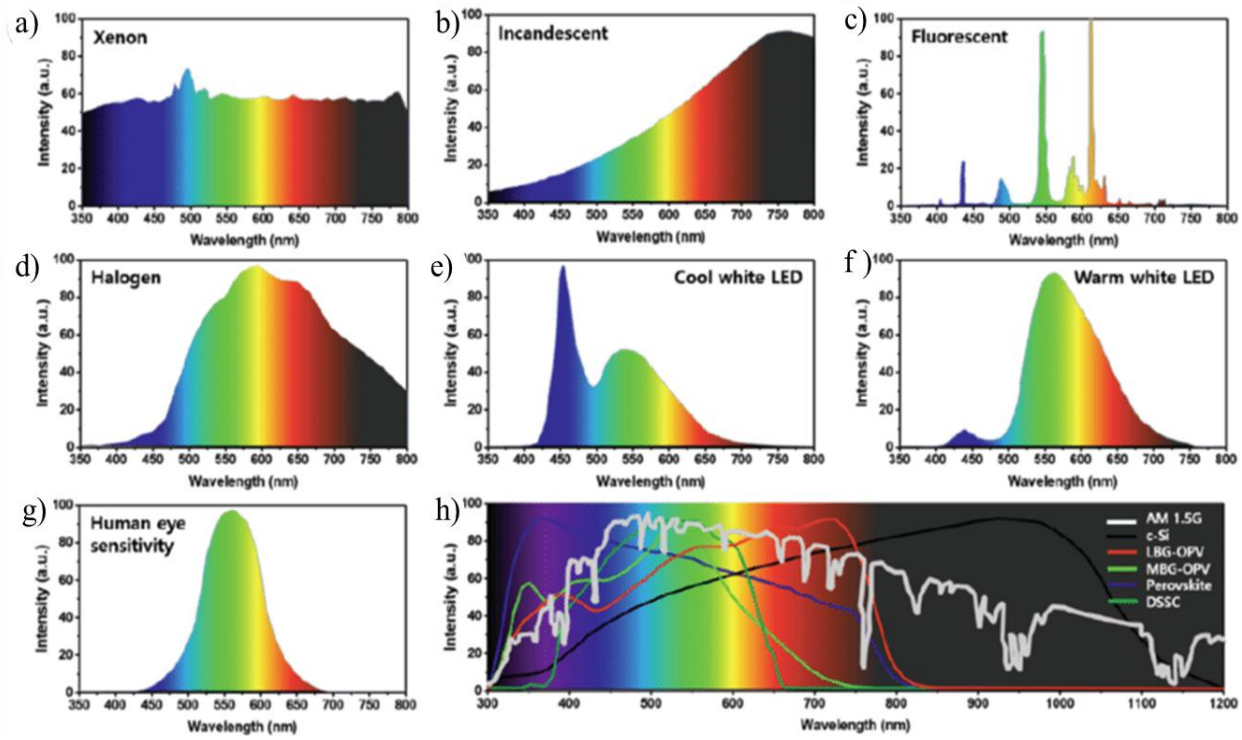

Figure 1.3. Spectra of the different indoor light sources. a) Xenon lamp, b) incandescent lamp, c) fluorescent lamp, d) halogen lamp, e) cool white LED, f) warm white LED, g) human eye sensitivity spectrum, and h) AM 1.5G spectrum overlaid with spectral response of various photovoltaic devices [23].

1.5 IPV Performance Parameters

A single-junction solar cell, as can be seen in **Figure 1.4(b)**, converts light into electricity through the PV effect. When light strikes the semiconductor absorber, photons excite electrons, creating electron-hole pairs [28]. The electric field at the p-n junction separates these pairs, directing electrons to the n-side contact and holes to the p-side contact. This separation creates a flow of electrons, producing direct current (DC) when connected to an external circuit, enabling electricity generation.

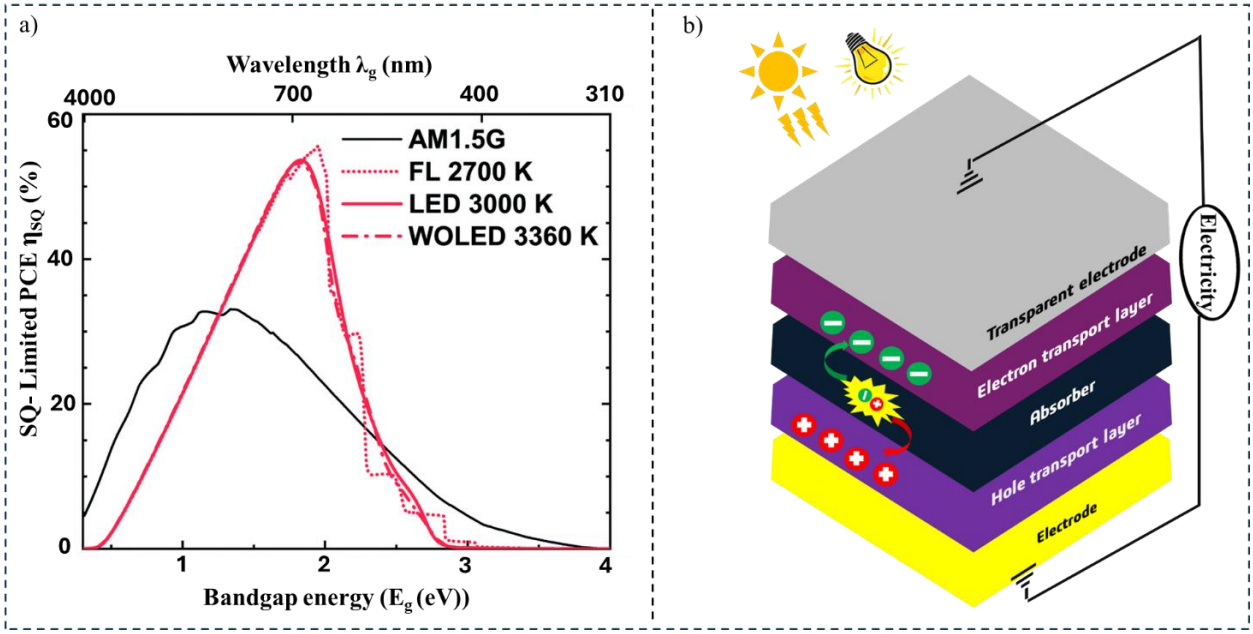

Figure 2.4. a) Shockley–Queisser (S-Q)-limited power conversion efficiency (PCE) vs. bandgap energy (E_g) relationships depending on incident light sources (L = 300 lx for all artificial indoor light sources, except for AM 1.5 G) [29], b) a schematic illustration of single-junction solar cell.

To evaluate the performance of a solar cell device, whether under outdoor or indoor conditions, J-V curves are typically used, with an example curve shown in **Figure 1.5**. From the J-V curve, key performance metrics such as V_{oc} (the open circuit of voltage), J_{sc} (current density in the condition of short circuit), FF (fill factor), and PCE (power conversion efficiency) can be determined.

- The V_{oc} represents the voltage at the terminal of the cell when no current is flowing. It occurs at the point where the curve intersects the x-axis, as visually indicated by rightmost green point in the **Figure 1.5**.
- The J_{sc} represents the current density when the voltage between the terminals is zero. It occurs where the curve intersects the y-axis and visually indicated by uppermost green point in the **Figure 1.5**.

- The FF describes the "squareness" of the J-V curve and indicates the quality of the solar cell. Mathematically, it's the ratio of the maximum power obtainable from the cell (P_{max} = $J_{max} \times V_{max}$) to the product of J_{sc} and V_{oc}.
- J_{max} (the red dot on the vertical axis, slightly below J_{sc} in the **Figure 1.5**) and V_{max} (the red dot on the horizontal axis, slightly left of V_{oc} in the **Figure 1.5**) represent the current density and voltage at the maximum power point (MPP) indicated by the red point marked as P_{max}, in the **Figure 1.5**.
- P_{max}, which is the product of J_{max} and V_{max}, is visually represented by shaded rectangular area in **Figure 1.5**.
- PCE describes the overall efficiency of the solar cell, and mathematically it is written as;

$$\text{PCE (\%)} = \frac{P_{\text{max}}}{P_{\text{in}}} \times 100 = \frac{J_{sc} \cdot V_{oc} \cdot FF}{P_{in}} \times 100$$

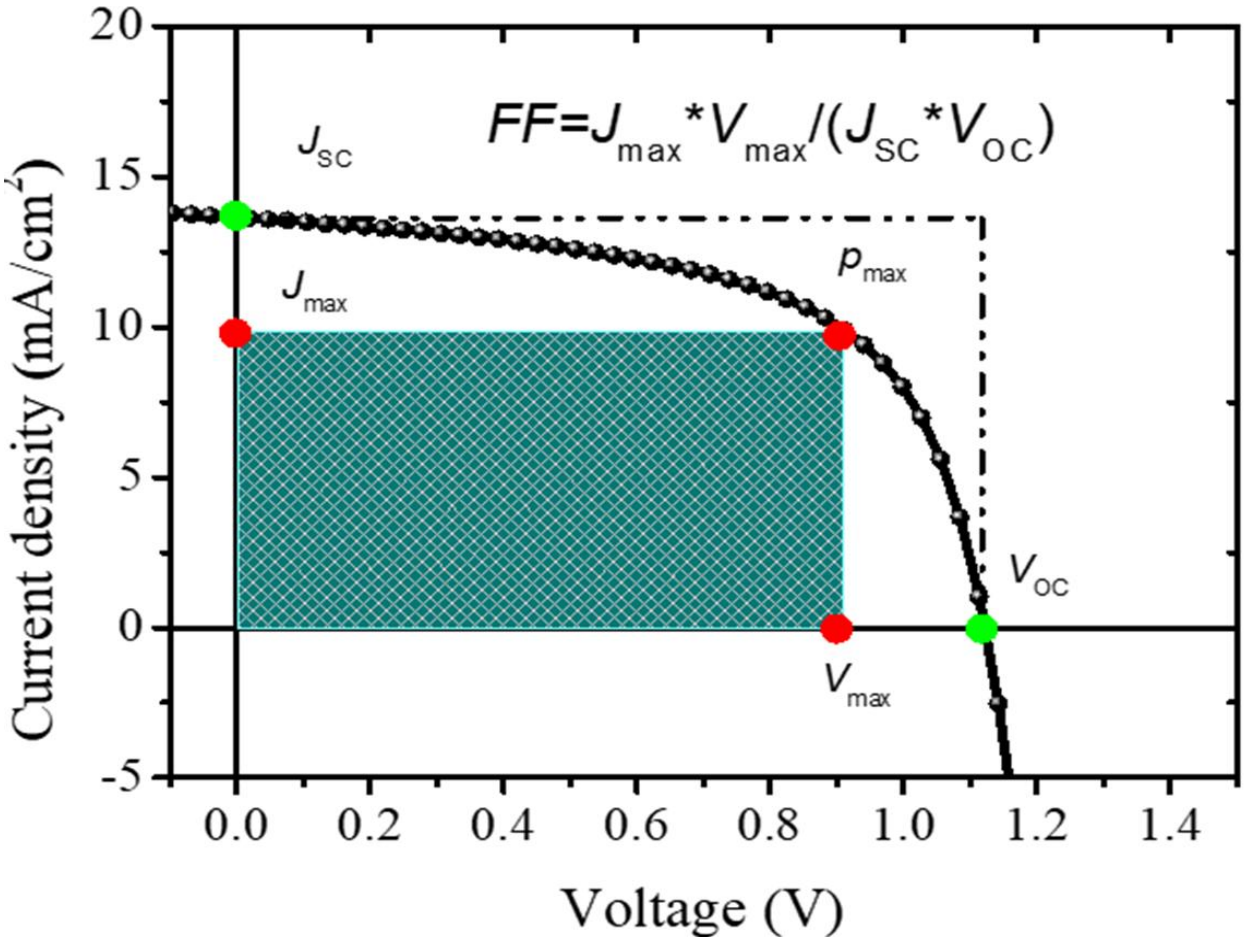

Figure 1.5. Typical J-V curve and corresponding parameters of a solar cell (Picture taken from Xie Thesis with permission, University of Nottingham, Ningbo, China [30].

The key performance metrics are consistent across both indoor and outdoor conditions. However, P_{in}, the light intensity in the PCE formula, differs between the two. While a standard P_{in} value is known for outdoor conditions, it varies for IPVs. Therefore, it is essential to understand how light intensity influences PV performance metrics.

To understand how light intensity affects solar cell performance, we discuss an electrical circuit model that represents the behaviour of a solar cell [31]. The equivalent circuits for a solar cell in the dark and under illumination are shown in **Figure 1.6(a) and 1.6(b)**, respectively. In the dark, the circuit consists only of a diode, as no light to generate photocurrent. In contrast, the illuminated model includes a current source, diode, and resistive elements: series resistance (R_s) and shunt resistance (R_{sh}), reflecting real-world inefficiencies such as resistive losses and leakage paths.

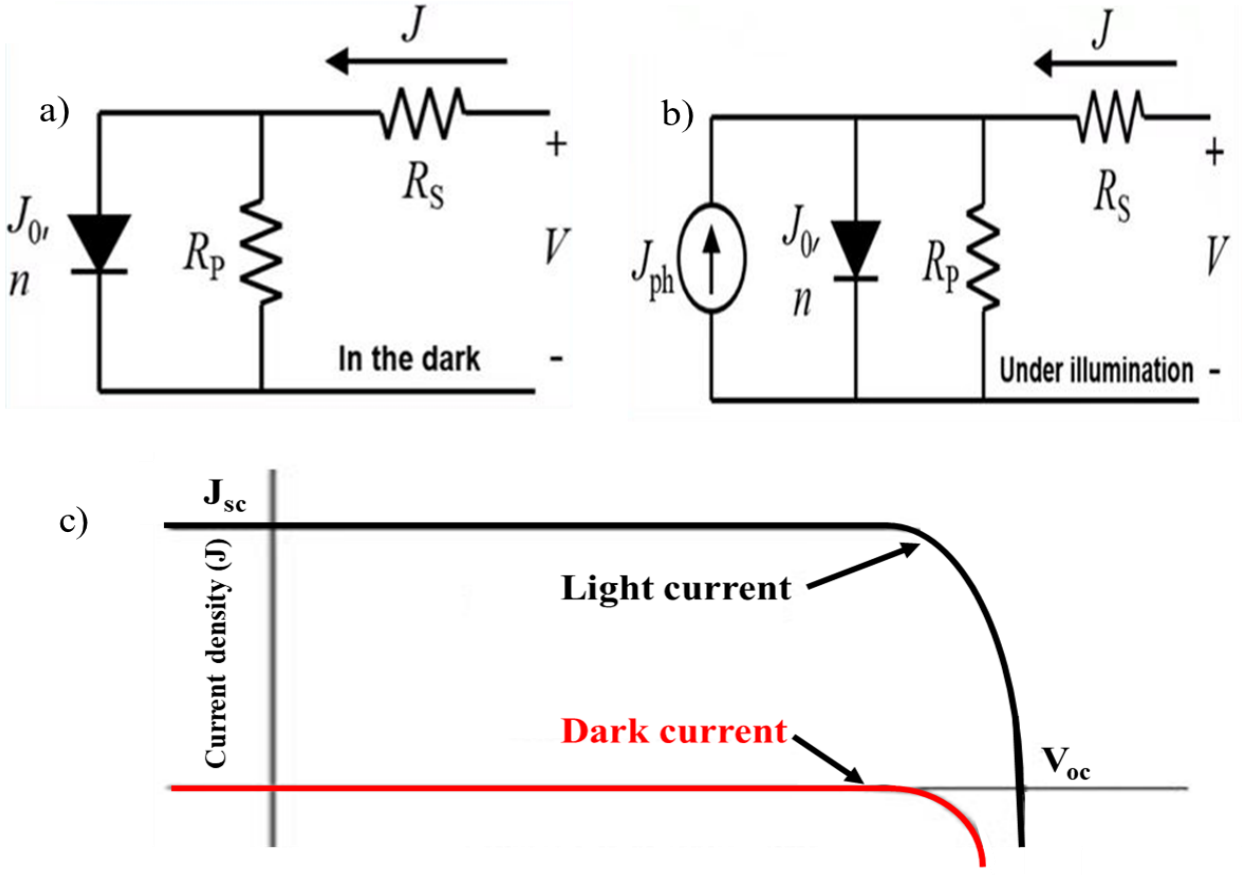

Figure 2.6. Equivalent-circuit models in the a) dark and b) under illumination [32], and c) current—voltage characteristic of ideal diode in the light and the dark [33].

As can be seen in **Figure 1.6c**, the current-voltage relationship for most solar cells can be written by assuming the superposition approximation, which states that the current is equal to J-V curve in the dark plus the J_{sc}. For an ideal diode, the dark current can be expressed as [33]:

$$J_{\text{dark}}(V) = J_0\left(e^{\frac{qV}{k_BT}} - 1\right) \tag{2.1}$$

Using Kirchhoff's current law, the output current (J) of an ideal solar cell can be stated as follows:

$$J = J_{sc} - J_{\text{dark}} \tag{2.2}$$

therefore, the current of an ideal solar cell can be written as:

$$J = J_{sc} - J_0\left(e^{\frac{qV}{k_BT}} - 1\right) \tag{2.3}$$

This expression does not consider parasitic resistances. Here, J_0 is a constant, k_B is Boltzmann's constant, V is the voltage across the diode, and T is the temperature.

When considering that a real solar cell behaves as a non-ideal diode (with an ideality factor) and includes internal resistances, which can be divided into R_S and R_{sh}, the solar cell J-V curve becomes [34]:

$$J = J_{sc} - J_0\left(e^{\frac{q(V+JAR_s)}{mk_BT}} - 1\right) - \frac{V + JAR_s}{R_{sh}} \tag{2.4}$$

Where A is the area of PV cell.

The ideality factor (m) is a parameter indicates how closely a solar cell follows the ideal diode equation (for ideal diodes, m = 1). It is a real and an important parameter related to the quality of the solar cell material and the recombination processes, with typical values ranging between 1 and 2. A value close to 1 indicates a lower photogenerated recombination, and value close to 2 indicates higher photogenerated recombination [35]. R_S represents the total resistance within the cell, consisting of interfacial and active layer resistances, electrode resistances, and various contact and interconnect resistances [36]. R_{sh} is the parallel resistance across the p-n junction of the cell; a higher R_{sh} reduces the amount of photogenerated current flowing through alternate paths. A decrease in R_{sh} leads to a loss of photogenerated carriers, reducing overall power output [37].

Since the light intensity in outdoor and indoor conditions are different, the influence of abovementioned factors on the performance parameters of devices should be considered in a context of light intensity. For instance, according to the power law behaviour, the J_{sc} of a device is directly dependent on the incident light intensity [7] and can be expressed as:

$$J_{sc} \propto I^{\alpha} \tag{2.5}$$

Here, I represent the intensity of incident light, and α is the recombination factor, typically less than or equal to 1 ($\alpha \leq 1$). For ideal solar cells, a value of $\alpha = 1.0$ is standard. A slope deviating from unity suggests the presence of bimolecular recombination [38].

By deriving an expression for V_{oc}, the voltage that develops between the terminals of an illuminated ideal diode with no current flow (J=0), Equation 2.3 can be reformulated as follows:

$$V_{oc} = \frac{mk_BT}{q} \ln\left(\frac{J_{sc}}{J_0} + 1\right) \tag{2.6}$$

From above equation, it can be inferred that unlike J_{sc} which correlates linearly with the light intensity, V_{oc} increases logarithmically with light intensity [33].

In 1961, Shockley and Queisser introduced the concept of detailed balance limits for the maximum possible efficiency of solar cells under standard light illumination. Their approach, which doesn't rely on operational equations to adjust for changes in efficiency with light intensity, was later expanded by Martin Green in 1981 and is expressed in well-known empirical equations [39,40].

According to Green's equations, the FF is indirectly dependent on light intensity while being closely related to the R_{sh} and R_s of the cells. There are two key scenarios in which FF can be significantly influenced by the R_{sh} and R_s of the cell. For example, when both R_s and R_{sh} of a cell are considered in the FF calculation, the equation for determining FF is as follows:

$$FF_{s+sh} = FF_s\left[1 - \frac{(v_{oc} + 0.7)FF_s}{v_{oc}\, r_{sh}}\right] \tag{2.7}$$

While in the scenario where R_{sh} is so large that it can be considered negligible while R_s is significant, the optimal equation is as follows:

$$FF_s = FF_0(1 - r_s) \tag{2.8}$$

In the above equations, FF_{s+sh} represents the FF that accounts for both series and shunt resistance, FFs is the FF that considers only the *Rs*, and FF_0 is the ideal FF that does not consider either *Rs* and *Rsh*. v_{oc} is the normalized open-circuit voltage given by:

$$v_{oc} = V_{oc}/V_T \tag{2.9}$$

where V_T is the thermal voltage,

$$V_T = \frac{k_B T}{q} \tag{2.10}$$

where r_s and r_{sh} are the normalized series and shunt resistance, respectively, and given by:

$$r_s = R_s/R_{CH} \tag{2.11}$$

And

$$r_{SH} = R_{SH}/R_{CH} \tag{2.12}$$

where R_{CH} is the characteristic resistance, expressed as:

$$R_{CH} = V_{OC}/(J_{SC} \times A) \tag{2.13}$$

where *A* is the area of the PV device.

In conclusion, as outlined, J_{sc} is directly dependent on light intensity, V_{oc} is logarithmically dependent on light, while the FF is indirectly affected. However, the influence of R_s and R_{sh} is significant for FF, and both parameters are impacted by light intensity. For instance, it has been reported that solar cell performance increases with light intensity until R_s begins to affect device performance [41]. In contrast, at low light intensities, the effect of R_s on cell performance diminishes [41]. Furthermore, under low light conditions, fewer charge carriers are generated, and R_{sh} decreases; thus, low R_{sh} is often associated with poor performance of a device in low light [40]. Consequently, high R_{sh} is crucial, while R_s becomes less critical in dim lighting, potentially providing greater opportunities for developing IPV technology [42]. Lastly, since all the aforementioned parameters contribute to PCE, a comprehensive understanding of how light intensity influences these factors, both theoretically and experimentally, is essential for achieving significant breakthroughs in IPV technology in the future.

1.6 Challenges of IPV Technology

As mentioned before, IPV technology has been recognized for decades, but its development gained momentum in the last 20 years due to advancements in information technology. Especially, Kevin Ashton's introduction of the IoT paradigm in 1998 [43] sparked renewed interest in IPV as a power source for IoT devices [44]. So far, Various IPV technologies have been developed for harvesting

indoor light based on different absorber materials. Recent comprehensive reviews summarize their progress [15,44–52]. Therefore, rather than summarizing progress, this section will briefly highlight the challenges faced by these technologies. **Table 1.1** provides a concise summary of the potential, benefits, advancements, and challenges associated with each of these IPV technologies.

c-Si dominates the OPV field but has a narrow bandgap of 1.12 eV, making it ineffective for low-light harvesting due to spectral mismatch with indoor lighting. In contrast, thin-film a-Si and hydrogenated a-Si (a-Si:H) with a bandgap of ~1.7 eV are more suitable for IPVs [53]. These devices perform well under indoor light but face challenges like low photovoltage generation in low-light conditions [23]. Additionally, a-Si is typically made using costlier chemical vapor deposition (CVD) and sputtering techniques, increasing manufacturing expenses [54]. CdTe and CIGS are mature thin-film PV materials with direct bandgaps higher than c-Si. CdTe has a bandgap of 1.44 eV, while CIGS ranges from 1.0 eV to 1.6 eV [55], making CIGS more suitable for indoor light harvesting. However, CIGS devices show low R_{sh} and reduced efficiency under low light [56], and their performance degrades under continuous fluorescent exposure [18]. CdTe, in contrast, shows greater stability under low-light conditions, improving its commercial viability, though its maximum iPCE under indoor LED is only 18% [57]. Moreover, CdTe and CIGS involve toxic materials (Cd, Se) and rare elements (Te, In, Ga), which raise environmental concerns and production challenges. Group III-V semiconductors, such as GaAs, InP, InGaP, and AlGaAs, are ideal for indoor light harvesting due to their tunable band gaps (1.4 to 1.9 eV), which match LED and fluorescent light spectra. This results in efficient light harvesting, higher output voltages, and reduced thermalization and below-bandgap losses [44]. However, their significantly higher cost compared to Si-based cells limits their widespread adoption [58]. DSSCs use a dye to absorb light, freeing electrons that create a current, which is carried to the electrodes by a liquid electrolyte. They are a leading choice for indoor power generation due to their simple design, cost-effectiveness, and ability to maintain high photovoltages in artificial light [59,60]. However, challenges remain with the use of platinum and ruthenium as electrodes, and liquid electrolytes face issues like temperature instability, volatility, and sealing concerns, limiting scalability, flexibility, and safety [61,62]. Organic PVs are promising for IPVs due to their tunable bandgaps, high absorption, semitransparency, solution processing, and affordability. These features make them suitable for powering indoor devices with minimal energy use. However, challenges like low carrier mobility, structural disorder, and high bulk resistance hinder the improvement of their PCE [48,50]. PVKs are excellent PV materials for both indoor and outdoor use due to their tunable bandgaps, high external quantum efficiencies (EQEs), flexibility, simple manufacturing, and cost-effectiveness [48]. While their PCE in outdoor conditions is approaching that of c-Si solar cells, PVKs significantly outperform other PV technologies in

indoor conditions. Despite this, challenges such as low iPCE compared to the theoretical limit, performance reproducibility, stability, and toxicity issues must be addressed for commercialization [47].

Table 1.1: A brief summary of the potential, benefits, advancements, and challenges of various indoor photovoltaic (IPV) technologies.

Material	Bandgap (eV)	Record iPCE (%)	Stability	Cost	Challenges
c-Si	1.12	15.5 [57]	Good	High, due to fabrication cost.	Unsuitable for IPVs.
a-Si:H	~1.7	36.0 [63]	Good	High, due to fabrication cost.	Low photovoltage under low light, high manufacturing cost.
CdTe	1.44	18% [57]	Good	High, due to reliance on rare element (Te)	Toxicity of Cd, scarcity of Te, low efficiency under indoor light.
CIGS	1.0–1.6	12.5% [57]	Low under indoor lightings.	High due to rare materials (In, Ga)	Low stability and low R_{sh} under indoor light; scarcity of constituent elements.
Group III-V	~1.4–1.9	39.9% [57] (GaInP)	Excellent	High costs of materials and fabrication	Extremely high cost.
DSSCs	Tunable	35.6% [64]	Poor	Low	Sealing, leakage, temperature instability, rare counter electrode materials.
Organic	Tunable	36.4% [65]	Poor	Low	Low carrier mobility, high bulk resistance, structural disorder.
PVKs	Tunable (1.15–3.0)	45.51% [66]	Poor	Low	Stability, toxicity, hysteresis, efficiency below theoretical limit

In short, IPVs represent an exciting and rapidly developing field, essential for reducing reliance on battery power in low-power electronic and smart devices. Although the field itself is not entirely new, it has recently garnered significant attention. Historically, limited efforts were dedicated to its advancement, as the PV community primarily focused on harnessing standard sunlight.

However, the current modernization and widespread adoption of IoT devices have reignited interest in IPVs. There is still much to explore, evaluate, and examine to fully unlock the potential of this promising technology. Both experimental and theoretical investigations are urgently needed, as traditional PV technologies are not well-suited for IPV applications. Hence, it is vital to invest efforts and resources into developing emerging PV technologies tailored for IPVs. Among these, PVK-based IPV technology currently leads the field. However, the challenges associated with PVK-based PV technologies need to be addressed as a matter of priority. In line with the primary focus of this thesis, the next chapter explores PVKs and PVK-based solar cells in detail, examining their potential, the challenges faced by this emerging technology, possible solutions, and a comprehensive review of the relevant literature.

.

References

1. https://gcell.com/dye-sensitized-solar-cells/advantages-of-dscc/indoor-dye-sensitize-solar-cells.

2. Du, T. *et al.* Light-intensity and thickness dependent efficiency of planar perovskite solar cells: charge recombination *versus* extraction. *J Mater Chem C Mater* **8**, 12648–12655 (2020).

3. Zhu, S. & Li, Y. Performances of perovskite solar cells at low-intensity light irradiation. *Solid State Electron* **173**, 107903 (2020).

4. https://www.ossila.com/pages/indoor-photovoltaics-indoor-solar-panels.

5. https://teddybaldassarre.com/blogs/watches/citizen-watch-review.

6. https://www.computinghistory.org.uk/det/30369/Sharp-EL-835-Elsimate-Calculator/.

7. Jagadamma, L. K. & Wang, S. Wide-Bandgap Halide Perovskites for Indoor Photovoltaics. *Front Chem* **9**, (2021).

8. Mishra, S. *et al.* Solution-processed next generation thin film solar cells for indoor light applications. *Energy Advances* **1**, 761–792 (2022).

9. https://www.acopian.com/radiohome.html.

10. Laghari, A. A., Wu, K., Laghari, R. A., Ali, M. & Khan, A. A. RETRACTED ARTICLE: A Review and State of Art of Internet of Things (IoT). *Archives of Computational Methods in Engineering* **29**, 1395–1413 (2022).

11. Kizza, J. M. Internet of Things (IoT): Growth, Challenges, and Security. in 557–573 (2024). doi:10.1007/978-3-031-47549-8_25.

12. https://sally-r.com/2023/10/the-future-of-iot-sustainable-sensors-powered-by-indoor-solar-cells/.

13. Dehghani-Sanij, A. R., Tharumalingam, E., Dusseault, M. B. & Fraser, R. Study of energy storage systems and environmental challenges of batteries. *Renewable and Sustainable Energy Reviews* **104**, 192–208 (2019).

14. https://cordis.europa.eu/article/id/430457-up-to-78-million-batteries-will-be-discarded-daily-by-2025-researchers-warn.

15. Pecunia, V., Occhipinti, L. G. & Hoye, R. L. Z. Emerging Indoor Photovoltaic Technologies for Sustainable Internet of Things. *Adv Energy Mater* **11**, (2021).

16. Lojpur, V. & Validzic, I. L. J. Influence of Different Light Sources, Light Intensities, and Water Flow Lens (WFL) System on Dye-Sensitized Solar Cell Performances. *IEEE J Photovolt* **9**, 492–498 (2019).

17. Mengounou Mengata, G., Ngoffe Perabi, S., Ndi, F. E. & Wiysahnyuy, Y. S. Characterization of solar photovoltaic modules powered by artificial light for use as a source for smart sensors. *Energy Reports* **8**, 12105–12116 (2022).

18. Sacco, A., Rolle, L., Scaltrito, L., Tresso, E. & Pirri, C. F. Characterization of photovoltaic modules for low-power indoor application. *Appl Energy* **102**, 1295–1302 (2013).

19. Apostolou, G., Reinders, A. & Verwaal, M. Comparison of the indoor performance of 12 commercial <scp>PV</scp> products by a simple model. *Energy Sci Eng* **4**, 69–85 (2016).

20. Agbo, S. N., Merdzhanova, T., Rau, U. & Astakhov, O. Illumination intensity and spectrum-dependent performance of thin-film silicon single and multijunction solar cells. *Solar Energy Materials and Solar Cells* **159**, 427–434 (2017).

21. Venkateswararao, A., Ho, J. K. W., So, S. K., Liu, S.-W. & Wong, K.-T. Device characteristics and material developments of indoor photovoltaic devices. *Materials Science and Engineering: R: Reports* **139**, 100517 (2020).

22. Randall, J. F. *Designing Indoor Solar Products*. (Wiley, 2005). doi:10.1002/0470017155.

23. Kim, S., Jahandar, M., Jeong, J. H. & Lim, D. C. Recent Progress in Solar Cell Technology for Low-Light Indoor Applications. *Current Alternative Energy* **3**, 3–17 (2019).

24. Jahandar, M., Kim, S. & Lim, D. C. Indoor Organic Photovoltaics for Self-Sustaining IoT Devices: Progress, Challenges and Practicalization. *ChemSusChem* **14**, 3449–3474 (2021).

25. Shockley, W. & Queisser, H. J. Detailed Balance Limit of Efficiency of *p-n* Junction Solar Cells. *J Appl Phys* **32**, 510–519 (1961).

26. Freunek, M., Freunek, M. & Reindl, L. M. Maximum efficiencies of indoor photovoltaic devices. *IEEE J Photovolt* **3**, 59–64 (2013).

27. *Solar Cell Nanotechnology*. (Wiley, 2013). doi:10.1002/9781118845721.

28. Akinoglu, B. G., Tuncel, B. & Badescu, V. Beyond 3rd generation solar cells and the full spectrum project. Recent advances and new emerging solar cells. *Sustainable Energy Technologies and Assessments* **46**, 101287 (2021).

29. Ho, J. K. W., Yin, H. & So, S. K. From 33% to 57% – an elevated potential of efficiency limit for indoor photovoltaics. *J Mater Chem A Mater* **8**, 1717–1723 (2020).

30. Lin Xie. High-Efficiency Organic Photovoltaics for Indoor and Outdoor Applications. (University of Nottingham, Ningbo, China, Ningbo, 2023).

31. Bader, S., Ma, X. & Oelmann, B. One-diode photovoltaic model parameters at indoor illumination levels – A comparison. *Solar Energy* **180**, 707–716 (2019).

32. Goo, J. S., Shin, S.-C., You, Y.-J. & Shim, J. W. Polymer surface modification to optimize inverted organic photovoltaic devices under indoor light conditions. *Solar Energy Materials and Solar Cells* **184**, 31–37 (2018).

33. Nelson, J. *The Physics of Solar Cells*. (PUBLISHED BY IMPERIAL COLLEGE PRESS AND DISTRIBUTED BY WORLD SCIENTIFIC PUBLISHING CO., 2003). doi:10.1142/p276.

34. Teh, C. J. Q., Drieberg, M., Hasan, K. N. M., Shah, A. L. & Ahmad, R. Indoor PV Modeling Based on the One-Diode Model. *Applied Sciences* **14**, 427 (2024).

35. Muhammadsharif, F. F. & Hashim, S. A Simple and Efficient Determination of the Ideality Factor of Solar Cells and Modules from the Knee Point of the Shunt Resistance Curve. *Arab J Sci Eng* **48**, 8217–8225 (2023).

36. Servaites, J. D., Yeganeh, S., Marks, T. J. & Ratner, M. A. Efficiency Enhancement in Organic Photovoltaic Cells: Consequences of Optimizing Series Resistance. *Adv Funct Mater* **20**, 97–104 (2010).

37. Al Mahdi, H., Leahy, P. G. & Morrison, A. P. Experimentally derived models to detect onset of shunt resistance degradation in photovoltaic modules. *Energy Reports* **10**, 604–612 (2023).

38. Bi, D. *et al.* Efficient and stable CH3NH3PbI3-sensitized ZnO nanorod array solid-state solar cells. *Nanoscale* **5**, 11686 (2013).

39. Green, M. A. Solar cell fill factors: General graph and empirical expressions. *Solid State Electron* **24**, 788–789 (1981).

40. Reich, N. H. *et al.* Crystalline silicon cell performance at low light intensities. *Solar Energy Materials and Solar Cells* **93**, 1471–1481 (2009).

41. Ruhle, K., Juhl, M. K., Abbott, M. D. & Kasemann, M. Evaluating Crystalline Silicon Solar Cells at Low Light Intensities Using Intensity-Dependent Analysis of *I–V* Parameters. *IEEE J Photovolt* **5**, 926–931 (2015).

42. Park, S. Y. *et al.* Alkoxybenzothiadiazole-Based Fullerene and Nonfullerene Polymer Solar Cells with High Shunt Resistance for Indoor Photovoltaic Applications. *ACS Appl Mater Interfaces* **10**, 3885–3894 (2018).

43. Khan, W. Z. *et al.* Industrial internet of things: Recent advances, enabling technologies and open challenges. *Computers & Electrical Engineering* **81**, 106522 (2020).

44. Chakraborty, A. *et al.* Photovoltaics for indoor energy harvesting. *Nano Energy* **128**, 109932 (2024).

45. Yan, N., Zhao, C., You, S., Zhang, Y. & Li, W. Recent progress of thin-film photovoltaics for indoor application. *Chinese Chemical Letters* **31**, 643–653 (2020).

46. Li, M., Igbari, F., Wang, Z. & Liao, L. Indoor Thin-Film Photovoltaics: Progress and Challenges. *Adv Energy Mater* **10**, (2020).

47. Wang, K.-L., Zhou, Y.-H., Lou, Y.-H. & Wang, Z.-K. Perovskite indoor photovoltaics: opportunity and challenges. *Chem Sci* **12**, 11936–11954 (2021).

48. Dou, D., Sun, H., Li, C., Gan, S. & Li, L. Perovskite-Based Indoor Photovoltaics and their Competitors. *Adv Funct Mater* **34**, (2024).

49. Chen, X. *et al.* Indoor photovoltaic materials and devices for self-powered internet of things applications. *Mater Today Energy* **44**, 101621 (2024).

50. Abubaker, S. A. & Pakhuruddin, M. Z. Progress and development of organic photovoltaic cells for indoor applications. *Renewable and Sustainable Energy Reviews* **203**, 114738 (2024).

51. Barichello, J. *et al.* Bifacial dye-sensitized solar cells for indoor and outdoor renewable energy-based application. *J Mater Chem C Mater* **12**, 2317–2349 (2024).

52. Farooq, U., Wang, J., Pan, Z. & Li, Z. Empowering Indoor Photovoltaics: Stable Lead-Free Perovskites and Beyond. *Solar RRL* **8**, (2024).

53. Kao, M.-H. *et al.* Low-Temperature Growth of Hydrogenated Amorphous Silicon Carbide Solar Cell by Inductively Coupled Plasma Deposition Toward High Conversion Efficiency in Indoor Lighting. *Sci Rep* **7**, 12706 (2017).

54. Sreejith, S., Ajayan, J., Kollem, S. & Sivasankari, B. A Comprehensive Review on Thin Film Amorphous Silicon Solar Cells. *Silicon* **14**, 8277–8293 (2022).

55. Lee, T. D. & Ebong, A. U. A review of thin film solar cell technologies and challenges. *Renewable and Sustainable Energy Reviews* **70**, 1286–1297 (2017).

56. Kasemann, M., Rühle, K., Gad, K. M. & Glunz, S. W. Photovoltaic energy harvesting for smart sensor systems. in (eds. Schmid, U., Sánchez de Rojas Aldavero, J. L. & Leester-Schaedel, M.) 87631T (2013). doi:10.1117/12.2018052.

57. Müller, D. *et al.* Indoor Photovoltaics for the Internet-of-Things – A Comparison of State-of-the-Art Devices from Different Photovoltaic Technologies. *ACS Appl Energy Mater* **6**, 10404–10414 (2023).

58. Raj, V., Haggren, T., Wong, W. W., Tan, H. H. & Jagadish, C. Topical review: pathways toward cost-effective single-junction III–V solar cells. *J Phys D Appl Phys* **55**, 143002 (2022).

59. Haridas, R. *et al.* Indoor light-harvesting dye-sensitized solar cells surpassing 30% efficiency without co-sensitizers. *Mater Adv* **2**, 7773–7787 (2021).

60. Devadiga, D., Selvakumar, M., Shetty, P. & Santosh, M. S. Dye-Sensitized Solar Cell for Indoor Applications: A Mini-Review. *J Electron Mater* **50**, 3187–3206 (2021).

61. Xie, L. *et al.* Recent progress of organic photovoltaics for indoor energy harvesting. *Nano Energy* **82**, 105770 (2021).

62. Mozaffari, S., Nateghi, M. R. & Zarandi, M. B. An overview of the Challenges in the commercialization of dye sensitized solar cells. *Renewable and Sustainable Energy Reviews* **71**, 675–686 (2017).

63. Kim, G., Lim, J. W., Kim, J., Yun, S. J. & Park, M. A. Transparent Thin-Film Silicon Solar Cells for Indoor Light Harvesting with Conversion Efficiencies of 36% without Photodegradation. *ACS Appl Mater Interfaces* **12**, 27122–27130 (2020).

64. Meethal, S. M. *et al.* Asymmetric dual species copper(<scp>ii</scp> / <scp>i</scp>) electrolyte dye-sensitized solar cells with 35.6% efficiency under indoor light. *J Mater Chem A Mater* **12**, 1081–1093 (2024).

65. Kim, T. H. *et al.* Record indoor performance of organic photovoltaics with long-term stability enabled by self-assembled monolayer-based interface management. *Nano Energy* **112**, 108429 (2023).

66. Wang, Y. *et al.* Defect Passivation Refinement in Perovskite Photovoltaics: Achieving Efficiency over 45% under Low-Light and Low-Temperature Dual Extreme Conditions. *Advanced Materials* **36**, (2024).

Chapter 2

Perovskite Solar Cells

2.1 What are PVKs?

In 1839, Gustav Rose, a mineralogist from the University of Berlin, discovered a previously unidentified mineral in the Ural Mountains of Russia. This mineral, containing $CaTiO_3$, was named "Perovskite" in honour of Count Lev A. Perovski, president of the Russian Geological Society [1]. While $CaTiO_3$ is the "founding father" of the PVK family, its wide bandgap (~3.5 eV) limits its use in PVs. The term "PVK" now refers to a broad class of compounds having crystallographic structure similar to that of $CaTiO_3$ and general formula ABX_3, where "A and B" are cations and "X" is an anion. This structure accommodates various elements, enabling numerous combinations and properties [2].

Over 40 naturally occurring PVK minerals, including oxides, halides, and arsenides, have been identified [3]. Depending on their compositions and optoelectronic properties, these PVKs find applications in PVs and other optoelectronic technologies [4,5]. Due to their versatility, PVK semiconductors are currently a hot topic of research in materials science. Since this thesis primarily focuses on PVs, the discussion will concentrate on PVKs specifically used in PV applications.

2.2 Metal Halide PVKs

Over the past two decades, metal halide PVKs have revolutionized next-generation PV research due to their exceptional optoelectronic properties. Their tunable bandgaps, enabled by compositional engineering, make them suitable for both outdoor and indoor single-junction device architectures. Beyond PVs, these materials show potential in LEDs, photodetectors, and energy storage devices [6].

In PVs, as can be seen in **Figure 2.1**, metal halide PVKs can be categorized into two groups: organic-inorganic hybrid PVKs, and all-inorganic PVKs [5]. Following the general ABX_3 formula, "A" is a monovalent cation (e.g., Cs^+, Rb^+, MA^+, FA^+), "B" is a divalent cation (e.g., Pb^{2+}, Sn^{2+}, Ge^{2+}), and "X" is a halide anion (e.g., I^-, Br^-, Cl^-). Organic-inorganic lead halide PVKs feature MA or FA at the A site, while all-inorganic lead halide PVKs use Cs or Rb. Pb-free perovskites replace Pb with elements like Sn or Ge, offering organic-inorganic or all-inorganic variations. Among these, organic-inorganic and all-inorganic lead (Pb) halide PVKs are the most efficient for

PVs. Efforts to develop Pb-free alternatives are underway to address toxicity concerns, but they remain in the developmental phase and are not yet as competitive as Pb-based PVKs.

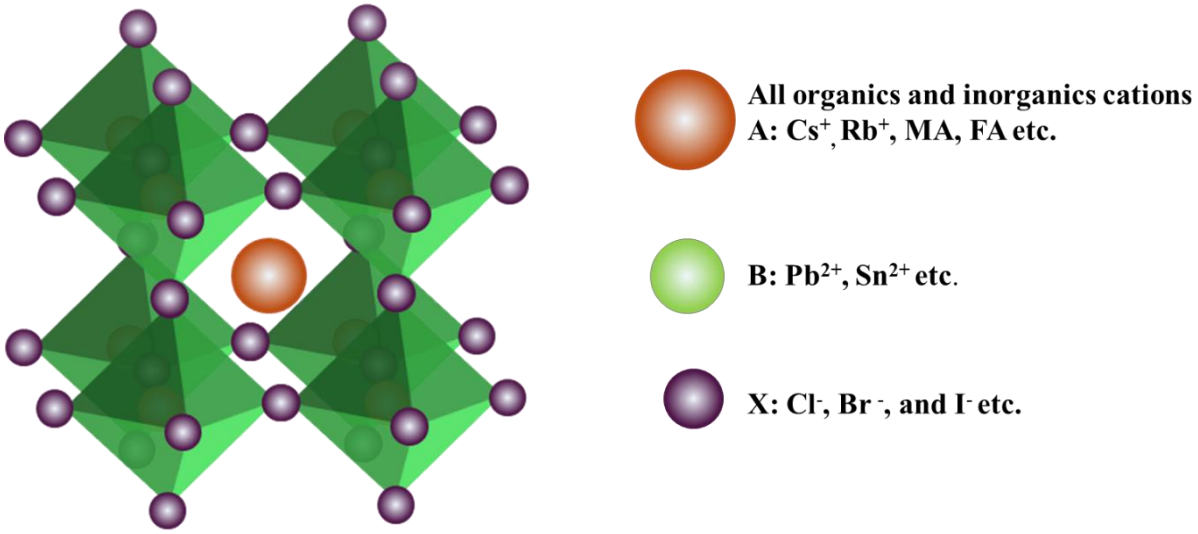

Figure 2.1. Schematic diagram of ABX_3 metal halide PVK crystal structure.

2.3 Crystal Structure of Lead Metal Halide PVKs

The crystal structure of PVK semiconductors significantly influences their thermal and phase stability [7], which are crucial for the performance of PVK thin films in solar cells. In the ideal 3-Dimensional (3D) cubic ABX_3 structure, the X anions are octahedrally coordinated to the B cations, while the A cations are coordinated to the X anions in a 12-fold cuboctahedral arrangement. The A cation is typically larger than the B cation, allowing the $[BX_6]^{4-}$ octahedra to share corners and form a 3D framework. The A-site cations occupy the cavities within this framework [8].

Ionic sizes play a key role in the stability and structural distortions of PVKs, impacting their properties [9]. The Goldschmidt tolerance factor (t) is used to assess the degree of distortion and stability [10], defined as:

$$t = \frac{R_B + R_X}{\sqrt{2}(R_A + R_X)}$$

where R_A, R_B and R_X represents effective ionic radii for A, B, and X atoms in ABX_3 PVK, respectively. To maintain a stable 3D structure, t should ideally fall between 0.8 and 1.0 [11]. A t close to 1 suggests a cubic phase, between 0.9 and 1.0 indicates a tetragonal phase, and values

between 0.8 and 0.9 point to a tilted orthorhombic phase [12]. If t exceeds 1 or falls below 0.8, non-PVK structures are formed [13].

For instance, $CsPbI_3$, with a bandgap of 1.7 eV, is widely used in PV devices and is highly stable due to its all-inorganic composition. However, with a t of 0.81, $CsPbI_3$ lies near the stability threshold, leading to phase transitions upon cooling. The α phase is stable only at high temperatures, transforming into the β and γ phases at lower temperatures. Eventually, the structure collapses into the non-optoelectronic δ phase, unsuitable for solar cells [14,15]. To maintain the black phase and prevent this transition, stabilization protocols are commonly applied to $CsPbI_3$ in solar cell devices, rather than using the pure material [16,17].

For evaluating the metal halide PVK structural stability, another key dimensionless geometric factor is the octahedral factor (μ), which is defined as the ratio of the B-cation radius to the X-anion radius, and expressed as:

$$\mu = \frac{r_B}{r_X}$$

where r_B represents B cation radius and r_X represents X-anion radius. This factor predicts the formation of the BX_6 octahedron and the stability of the PVK structure. A stable structure requires μ to fall within the range $0.414 < \mu < 0.732$ [18]. Structures with $\mu > 0.41$ are considered stable [19].

2.4 Typical PVK Materials for PVs

Most typical PVK materials for PVs consist of a single cation (organic or inorganic) paired with lead (Pb) and halide anions. These materials are renowned for their tunable optical and electronic properties, which contribute to their high efficiency in solar cells. Common single-cation Pb PVKs used in PV include:

2.4.1 Methylammonium Lead Iodide ($MAPbI_3$)

Methylammonium lead iodide ($MAPbI_3$) was one of the first PVK materials used in solar cells [20]. Determined by its stoichiometry, $MAPbI_3$ exhibits a bandgap of 1.55–1.64 eV [21–23], a high absorption coefficient (10^4–10^5 cm^{-1}), and excellent charge carrier properties, including mobilities of 2–66 $cm^2V^{-1}s^{-1}$ and diffusion lengths of ~1 μm [24]. These properties enable $MAPbI_3$-based devices to achieve PCEs exceeding 20% under 1-sun illumination [25,26] and over 35% under warm-white LED light (301.6 μW cm^{-2}) [27]. However, $MAPbI_3$ suffers from thermal instability,

decomposing at temperatures above 85 °C due to the loss of organic MA^+ cation, which limits its long-term stability and operational durability in solar cells [28].

2.4.2 Formamidinium Lead Iodide ($FAPbI_3$)

$FAPbI_3$ is a widely studied PVK material for PV applications. Compared to $MAPbI_3$, it offers superior thermal stability due to the greater chemical stability of the FA cation. Its bandgap (1.45–1.51 eV) is closer to the optimal 1.34 eV for outdoor PVs [23,29,30], and it features a low exciton binding energy (~10 meV) and long carrier diffusion lengths (~6.6 μm in single crystals) [31]. These properties enable $FAPbI_3$-based devices to achieve PCE exceeding 23% under 1-sun illumination [32] . However, $FAPbI_3$ faces structural stability issues. With a t >1, it tends to form the non-photoactive δ-phase at room temperature [33], while the photoactive α-phase is stable only above 150 °C [34]. Overcoming this phase instability is a key challenge in advancing $FAPbI_3$-based PSCs.

2.4.3 Cesium Lead Iodide ($CsPbI_3$)

$CsPbI_3$ is a highly stable PVK material for PV applications due to its inorganic A-site cation. The α-phase of $CsPbI_3$ has a bandgap of 1.73 eV [35], suitable for IPVs but higher than optimal limit for OPVs. It exhibits a charge carrier mobility of 25 $cm^2V^{-1}s^{-1}$ [36] and depending on the fabrication approach, exhibits long carrier lifetimes exceeding 10 μs (vapor-deposited) or 0.2 μs (spin-coated). Moreover, its charge carrier diffusion length reaches ~1 μm [37], contributing further to its superior PV performance. Devices using $CsPbI_3$ have demonstrated >21% PCE under 1-sun illumination [38] and indoor power conversion efficiency (iPCE) of 38.93% under indoor lighting [39]. Despite these advantages, as mentioned before, $CsPbI_3$ faces challenges with phase stability due to its low t (~0.81). Addressing this limitation is essential for its practical application.

2.4.4 Cesium Lead Bromide ($CsPbBr_3$)

The all-inorganic $CsPbBr_3$ is highly promising for its exceptional environmental and phase stability, attributed to its fully inorganic composition and higher t of 0.92 [40]. Single crystals of $CsPbBr_3$ show impressive electron mobility (1000 $cm^2\ V^{-1}\ s^{-1}$) and electron lifetime (2.5 μs), surpassing other Cs-based PVKs [41–44]. Its diffusion lengths are reported 1 μm for electrons and 12 μm for holes [41]. The bandgap of 1.92–2.3 eV [45,46] suits IPVs but is too high for OPVs, limiting its efficiency to over 11% under 1-sun illumination [47]. However, mixed-halide $CsPbI_2Br$ devices have achieved 32.6% iPCE [48], suggesting potential for further research into $CsPbBr_3$ and related compositions for both indoor and outdoor applications.

2.5 Mixed Ion PVK Materials

Compositional engineering through cation and anion substitution is a useful strategy to realize desirable bandgap tuning for indoor and outdoor PV applications while enhancing the environmental and structural stability of PVKs. Unlike pure PVKs such as $MAPbI_3$, $FAPbI_3$, or $CsPbBr_3$, mixed PVKs incorporate multiple ionic species at the A-site, B-site, or X-site of the ABX_3 structure, resulting in superior properties like improved crystallinity, stability, and optimized optoelectronic performance. In 2013, Noh et al. [49] demonstrated the successful substitution of I^- ions with Br^- in in $MAPbI_3$ PVK material to tune their optical properties. By adjusting the I^- and Br^- ratios in $MAPb(I_{1-x}Br_x)_3$, they observed a shift in the absorption wavelength onset from 786 nm (1.58 eV) for $MAPbI_3$ to 544 nm (2.28 eV) for $MAPbBr_3$, as shown in **Figure 2.2(a)**. The devices also exhibited colour changes from dark brown (x = 0) to yellow (x = 1) with increasing Br^- content (**Figure 2.2b**). The bandgap variation with Br^- content, estimated from the absorption onset, is presented in **Figure 3.2(c)**. This method has since become a widely adopted strategy for tuning the bandgap and optoelectronic properties of PVK materials [50].

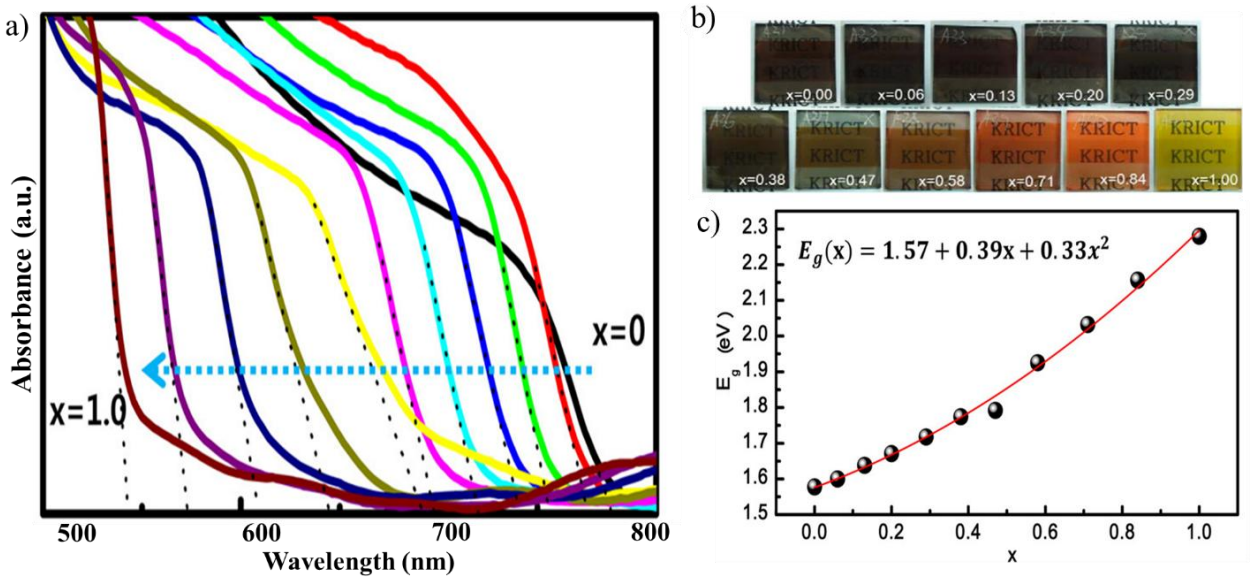

Figure 2.2. (a) UV–vis absorption spectra of FTO/bl-TiO_2/mp-TiO_2/ $MAPb(I_{1-x}Br_x)_3$/Au cells measured using an integral sphere. (b) Photographs of 3D TiO_2/$MAPb(I_{1-x}Br_x)_3$ bilayer nanocomposites on FTO glass substrates. (c) A quadratic relationship of the bandgaps of $MAPb(I_{1-x}Br_x)_3$ as a function of Br composition (x) [49].

Unlike halogen mixing at the X-site for bandgap tuning, mixing cations at the A-site significantly influences the structural and optoelectronic properties of PVKs. Adjusting the A-site cation size alters the BX_6 octahedral network, affecting the B–X bond length and the bandgap of the material [51]. In 2014, Pellet et al. [52] achieved a breakthrough by using $(MA)_x(FA)_{1-x}PbI_3$ (x = 0–1) as light-harvesting pigments in mesoscopic solar cells. They found that adding 20% MA to FA prevented

δ-phase formation while preserved the red-shifted bandgap of $FAPbI_3$. This breakthrough spurred advancements in PSCs and enabled the development of highly efficient and stable absorber materials. **Figure 2.3(a)** highlights the evolution of complex organic–inorganic PVK A-site compositions [53], while **Figure 2.3(b)** showcases record PCE values achieved with different A-cation compositions up to June 2022.

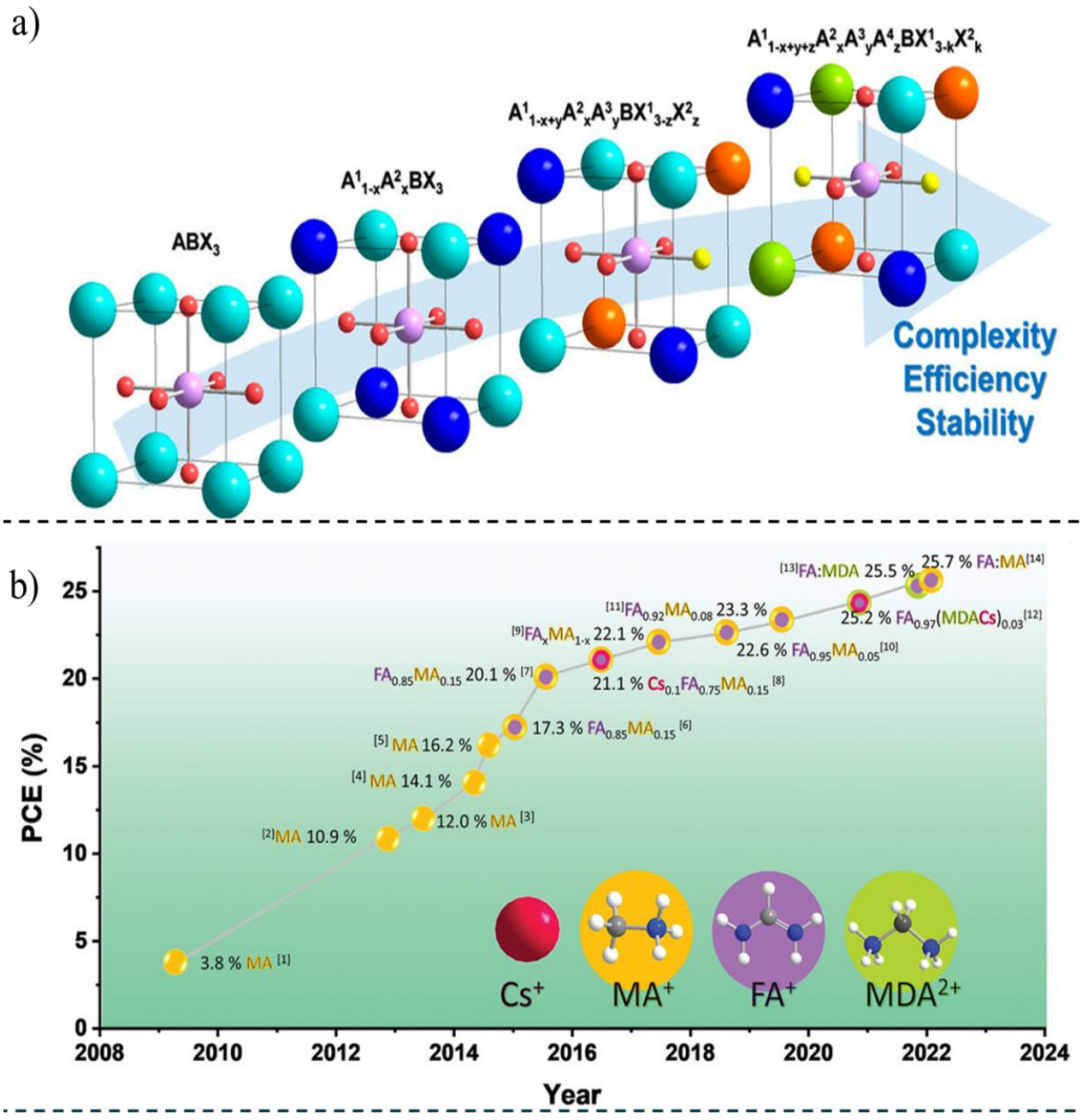

Figure 2.3. a) A-site cation engineering in ABX_3 PVKs leading to more complex, stable, and highly efficient PSCs while structural composition and chemical composition are not well understood yet. A-site cations (turquoise, blue, green, and orange) representing monovalent cations are located at the corners of the B-centered unit cells, where B (violet) is Pb and X (red, yellow) is I (or Br) [53] , b) Some of the record PCE values reported for PSCs made of different A-cation compositions reported over the years (some of the data points obtained from NERL) The data point number is given in brackets at each composition [54].

2.6 Synthesis of PVKs for PVs

The synthesis of high-quality PVK films is critical for PSC performance, ensuring better light absorption, reduced charge recombination, and longer carrier diffusion lengths [55]. Synthesis methods are mainly categorized into solution-based and vapor deposition methods. Solution-based methods are preferred for their simplicity, cost-effectiveness, and scalability, while vapor deposition methods are less common due to their complexity and higher cost but offer highly uniform and pure films [56–59].

The one-step spin-coating method, as illustrated in **Figure 2.4(a),** is the most commonly used solution-based approach, where a precursor solution containing both organic and inorganic precursors is spin-coated onto a substrate and annealed to form the PVK film [60]. The two-step spin-coating method, as illustrated in **Figure 2.4(c)**, involves depositing an inorganic precursor (e.g., PbI_2) first, followed by an organic precursor, and then annealing to form the PVK film [61,62]. Alternatively, as illustrated in **Figure 2.4(c),** a dipping method can be used for the organic precursor, followed by rinsing and annealing [63,64].

The Vapor-Assisted Solution Process (VASP) combines solution-based deposition with vapor-phase processing, as illustrated in Figure **Figure 2.4(e),** to produce high-quality PVK films. This hybrid approach helps control crystallization and film morphology, addressing issues like incomplete conversion and poor uniformity seen in pure solution-based methods. In VASP, a thin metal halide precursor layer (e.g., PbI_2) is deposited onto the substrate, usually by spin-coating or dip-coating. The film is then dried, exposed to organic halide vapor (e.g., MAI or FAI), and annealed to complete the reaction, promote crystallization, and improve film quality [65,66].

Among entirely vacuum-based methods, the co-evaporation method, as illustrated in **Figure 2.4(b)**, is commonly used for high-quality PVK thin films, offering precise control over composition, thickness, and stoichiometry. Organic halide and metal halide precursors are evaporated simultaneously using thermal heating in separate crucibles. Their deposition rates are independently controlled to achieve the desired stoichiometry, with the reaction between precursors initiates during the evaporation process and completing on the substrate [67–69]. In contrast, sequential evaporation, as illustrated in the **Figure 2.4(d)**, deposits the precursors in two steps, with the metal halide layer first and the organic halide layer second, followed by a reaction during deposition or annealing [70–72].

2.7 Formation of Defects in Solution Processed PVKs

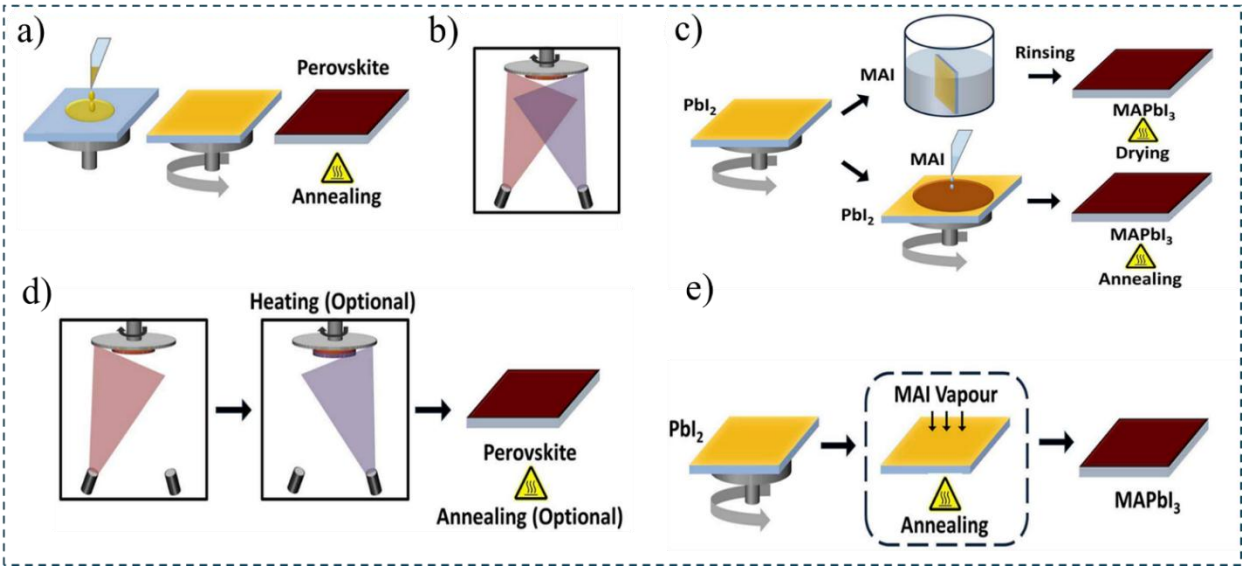

Figure 2.4. Illustration of different PVK deposition methods a) solution-based one step method b) co-evaporation c) solution-based two-step method d) sequential evaporation e) vapor-assisted solution process (VASP) [58].

Typically, during a solar cell operation, photoexcited charge carriers quickly dissociate into electron-hole pairs within ~2 picoseconds [73]. These carriers then migrate to the interfaces, where they are extracted by the charge transport layers. However, recombination can occur before they reach the electrodes, either radiatively (releasing energy as a photon) or non-radiatively (releasing energy as a phonon) [74–76]. This recombination reduces the charge carriers available for current generation, leading to a loss of photocurrent. The issue becomes more severe in the presence of structural defects, such as dislocations in the absorber material or charge-selective layers, which act as recombination centres and accelerate the process [77,78].

Solution-processed PVKs have emerged as outstanding materials for PVs and optoelectronics due to their unique properties, ease of fabrication, and cost-effectiveness. However, they face challenges that hinder their performance. Particularly, the formation of defects in solution-processed PVKs is a critical issue that affects their structural, optical, and electronic properties, ultimately influencing the performance and stability of corresponding PSCs[79,80]. These defects, which are more prevalent in polycrystalline films compared to single crystals [81], mainly occur at grain boundaries, within grains, and on the surface. While the low formation energy of PVKs enables solution processing at low temperatures, it also compromises the crystallinity, leading to high defect densities. These defects can disrupt energy band alignment between the PVK and charge transport layers, ultimately compromise device performance and stability [82].

Defects in PVKs are classified by their origin and structure [83]. In the ABX_3 PVK system, common defects include vacancies, interstitials, anti-site substitutions, substitutional and interstitial impurities, line defects, grain boundaries, and unsaturated surface bonds. These defects are illustrated in **Figure 2.5**, where the green, black, and blue dots represent A-, B-, and X-site ions, respectively, while red and grey dots indicate impurities [78].

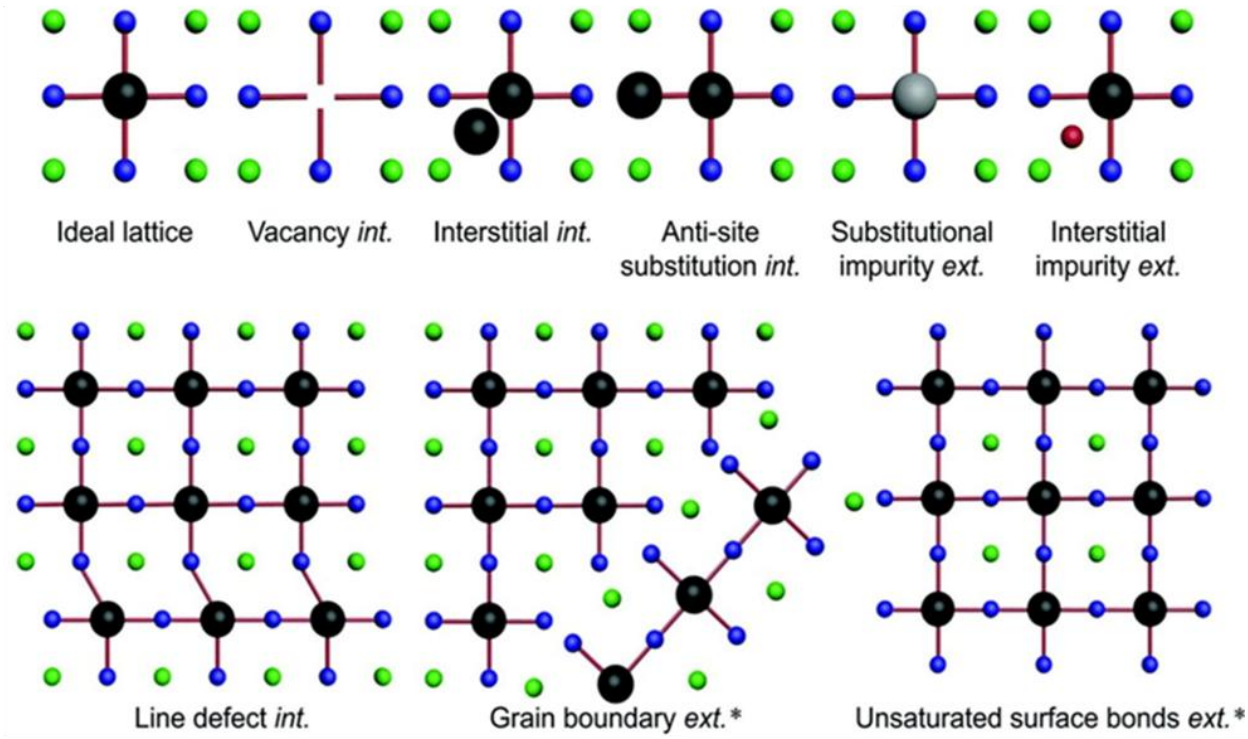

Figure 2.5. Schematic representation of an ideal PVK lattice with AMX_3 formula and the possible defects in it (Green, black and blue dots represent the A-, M- and X-site ions respectively; Red and grey dots represent the impurities) [78].

The performance of PSCs is significantly impacted by the presence of point defects in PVKs [84]. Point defects are referred to those defects that form around a single lattice point and encompass various types, such as vacancy, interstitial, antisite, substitution, Frenkel, Schottky, and substitutional impurities. Vacancy defects occur when atoms leave their positions due to thermal fluctuations, leading to charge accumulation, reduced mobility, and deep-level trap zones that cause recombination. Interstitial defects arise when an atom displaced during a vacancy moves to an interstitial site. Antisite substitution occurs when atoms of different species exchange positions in the lattice. Frenkel defects happen when an ion leaves its lattice position and occupies an interstitial site. Schottky defects form when cations and anions leave the lattice in a stoichiometric ratio, creating vacant sites. Substitutional impurities replace original atoms in the lattice with impurities from the PVK precursor [85]. In addition to point defects, surface defects, such as

undercoordinated ions and dangling bonds, are particularly detrimental to PSCs performance [86]. These defects hinder charge extraction and collection at the electrode interfaces [83,87]. When charge carriers encounter dangling bonds, they often recombine instead of contributing to photocurrent generation. Dangling bonds are responsible for creating point defects and defect arrays at surfaces and grain boundaries [88]. Irregular grain boundaries exacerbate these issues, suppressing both device performance and stability [89,90]. Grain boundaries often lack stoichiometric compositions due to the sublimation of organic molecules during thermal annealing. Consequently, most defects in solution-processed PVK films are located at grain boundaries or on surfaces [91,92]. These surface defects can induce charge recombination through non-radiative channels, impairing device performance and accelerating PVK degradation [86]. In summary, defect formation in solution-processed PVKs is unavoidable and presents significant challenges to the performance and stability of PSCs. As a result, defect engineering has become a critical area of focus in PSCs research [84,85,88].

2.8 Device Structures of PSCs

A solar cell operates in three stages. Firstly, light absorption by the absorber material generates electron-hole pairs. Subsequently, the electrons and holes are extracted by ETL and HTL, respectively. Finally, the extracted carriers are at their respective electrodes to produce electrical current [93].

Single-junction solar cells utilize various device architectures across PV technologies. As can be seen in **Figure 2.6(b)** and **Figure 2.6(c)**, PSCs are commonly designed in two architectures: regular n-i-p and inverted p-i-n [94]. In these terms, "n" represents the ETL, "i" the PVK absorber, and "p" the HTL. The primary distinction lies in the layer first exposed to incoming light. In the n-i-p architecture, light strikes the absorber PVK through the ETL side, whereas in the p-i-n structure, light strikes the absorber PVK through the HTL side.

Moreover, n-i-p structure PSCs can be further classified into mesoscopic and planar structures. As can be seen in **Figure 2.6(a)**, mesoscopic structures include a layer of mesoporous PVK. In contrast, as can be seen in **Figure 2.6(b)**, planar structures consist only of planar layers [95]. Compared to planar PVK devices, mesoporous devices require high-temperature sintering of the TiO_2 layer, which can increase processing time and overall manufacturing costs [96].

In addition to the conventional configurations described above, PSCs can also be designed in ETL-free [97,98] and HTL-free [99] configurations. In these structures, one of the charge transport layers,

either the ETL or HTL, is omitted, and the configuration is named based on the missing layer with the suffix "free." Despite the critical role of both transport layers in typical PSCs, their exclusion offers several advantages, including reduced fabrication costs, lower processing temperatures, and decreased toxicity and degradation risks of the final devices.

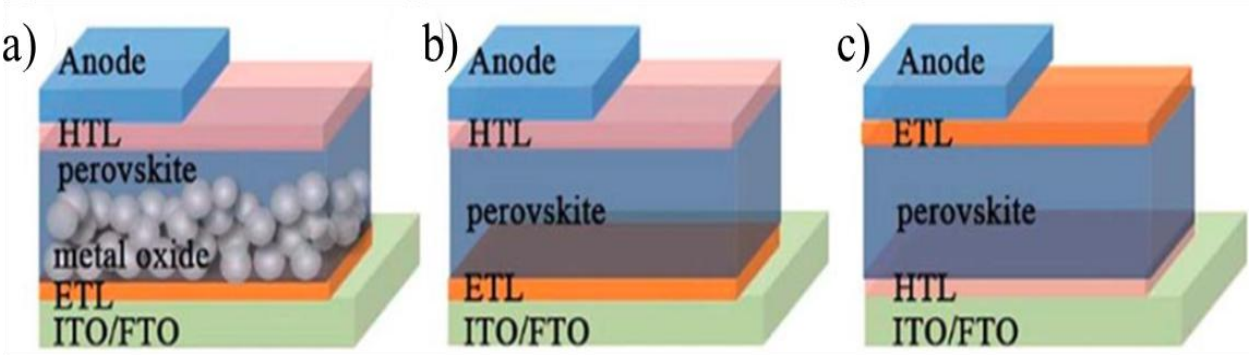

Figure 2.6. Device architectures of a) mesoporous, b) regular (n–i–p) and c) inverted (p–i–n) PSCs [94].

Since this thesis focuses on the fabrication of n-i-p structure PVK devices based on rigid substrates, the primary focus from this point onward will be on explaining n-i-p structure devices on rigid substrates.

2.9 Working Principle of n-i-p Structure PSCs

In the n-i-p structure of PSCs, the PVK layer absorbs light, generating charge carriers (electrons and holes). The exciton binding energy of PVK materials (2 to 50 meV) allows excitons to dissociate into free carriers at room temperature [100]. These carriers are efficiently extracted through the charge transport layers. For $MAPbI_3$, electron transfer through the ETL (PCBM) and hole transfer through the HTL (spiro-OMeTAD) occur in approximately 0.37 ± 0.02 ns and 0.64 ± 0.03 ns, respectively [101]. The extracted electrons and holes are collected at the cathode and anode, generating electrical power when connected to an external circuit [102]. A typical band diagram and working principle of the n-i-p device is shown in **Figure 2.7**. While in subsequent section, a brief overview of different functional layer of n-i-p structure PSCs is provided.

2.9.1 Transparent Conductive Oxides (TCOs)

In n-i-p structure PSCs, TCOs are essential for collecting electrons from the ETL layer while allowing light to pass through for efficient operation. Key attributes for TCOs include high optical transparency, electrical conductivity, chemical stability, and compatibility with ETLs. Sn-doped In_2O_3 (ITO) is commonly used due to its high transmission (>80%), conductivity ($10^4\ \Omega^{-1}\ cm^{-1}$),

and stability [103]. However, its electrical conductivity decreases with high-temperature treatments, limiting its use in high-temperature processed ETLs [104]. For such devices, FTO is preferred due to its superior thermal stability, wide bandgap (~3.6 eV), and low cost [105]. Aluminum- doped zinc oxide (AZO) is another alternative, offering low cost and comparable electrical properties to ITO, and have been used in n-i-p structure PSCs [106,107]. Commonly used TCOs in n-i-p structure devices and their respective band alignments with commonly used ETLs are illustrated in **Figure 2.8**.

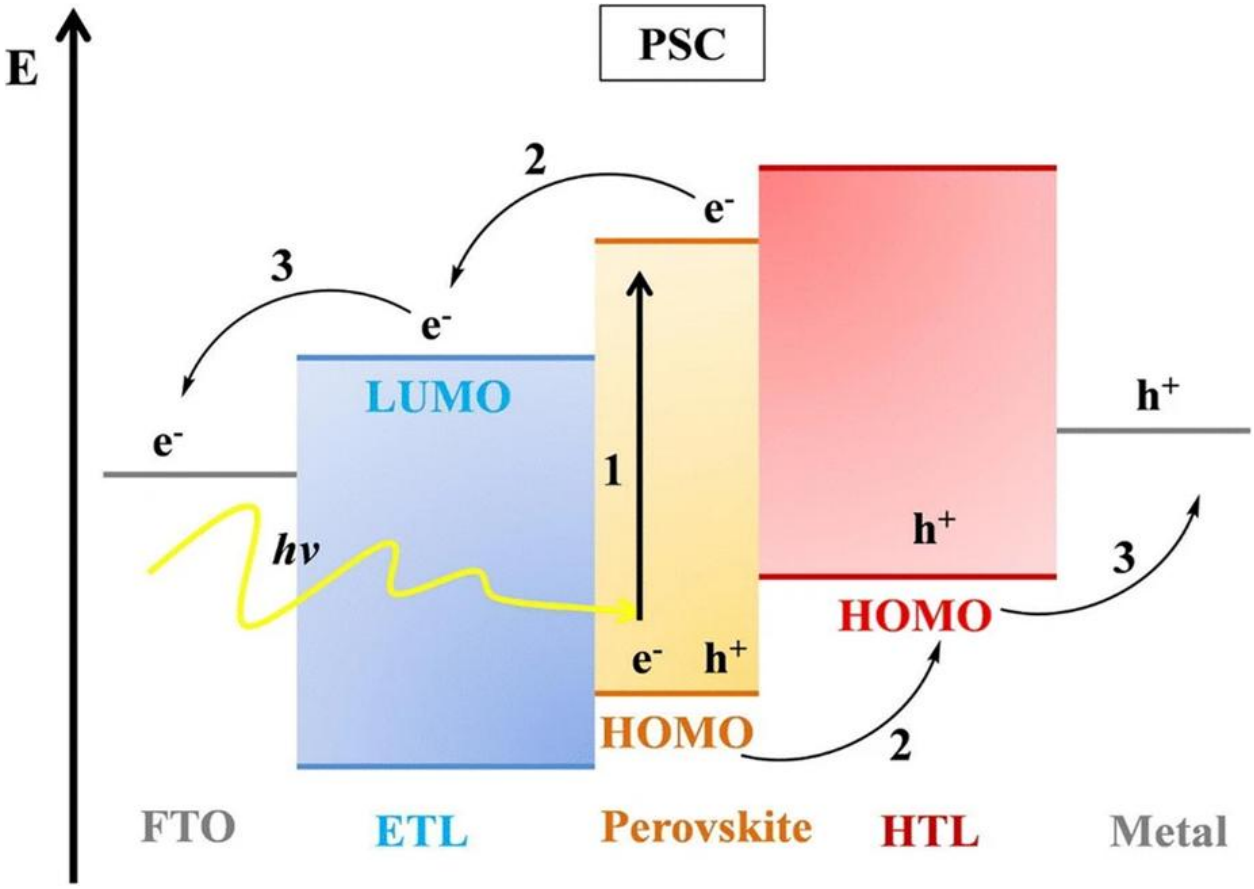

Figure 2.8. Band diagram and operation principle of PSC [108].

2.9.2 ETL

In n-i-p structure PSCs, the ETL is a crucial n-type layer that collects electrons and prevents holes from reaching the anode. It plays a key role in the device by forming a p-n junction with the PVK absorber. Key considerations when selecting ETL materials for n-i-p structure PSCs include:

1. Wide bandgap for maximum light transmission to the absorber PVK.
2. High optical transparency for efficient light transmission.
3. Well-aligned conduction band minimum (CBM) for effective electron transport.
4. High electron mobility for fast electron transit and reduced recombination.

5. Deep valence band maximum (VBM) to block holes from the absorber.
6. Low temperature processability for commercial and flexible substrate compatibility.
7. Minimal lattice mismatch with the PVK absorber.
8. Use of abundant, non-toxic elements.
9. Uniform, pinhole-free synthesis for complete coverage.
10. Thin layer for fast electron transport and low resistive losses.
11. Focus on novel ETL materials for advancements.

Common ETLs in n-i-p structure PSCs include metal oxides like titanium dioxide (TiO_2) and tin dioxide (SnO_2). TiO_2 is widely used for its good charge extraction, stability, and high transmittance, while SnO_2 is a promising alternative with higher electron mobility, deeper conduction band, low temperature processability and better stability under UV exposure [109,110]. For interested readers, a comprehensive and up-to-date review of ETLs used in n-i-p structure PSCs is available in the referenced study [111]. In addition, some widely used ETLs, along with their corresponding band alignments with common adjacent PVK absorbers and TCOs, are illustrated in the **Figure 2.8**.

2.9.3 HTL

In n-i-p structure PSCs, HTL is crucial for extracting and transporting holes from the absorber to the cathode while blocking electrons. Key considerations for selecting an HTL in n-i-p structure PSCs include:

1. High hole mobility for efficient charge transport and reduced resistive losses.
2. Proper valence band maximum (VBM) alignment with the VBM of perovskite for efficient hole transfer.
3. A sufficiently higher CBM to prevent electron backflow and reduce recombination losses.
4. High thermal and chemical stability for long-term device reliability.
5. Thin, uniform, and pinhole-free deposition for effective hole extraction.
6. Low temperature processability.
7. Excellent adhesion to both the absorber PVK and electrode layers for stability.
8. Use of non-toxic, inorganic, and abundantly available materials.
9. Ongoing research into novel HTL materials for enhanced performance, stability, and cost-effectiveness.

A range of organic and inorganic HTLs have been used in n-i-p structure PSCs. Among these, some widely used HTLs, along with their corresponding band alignments with common adjacent PVK absorbers and counter electrodes, are illustrated in the **Figure 2.8**. Organic HTMs offer higher performance but lower stability, while inorganic HTMs provide better stability but typically lower performance [112–114]. The instability of common organic HTMs, like spiro-OMeTAD and Poly[bis(4-phenyl)(2,4,6-trimethylphenyl)amine] (PTAA), is partly due to the common dopants that added to improve their properties like hole mobility and energy band alignment. However, these dopants compromise the stability of corresponding devices [115–117]. Therefore, ongoing research is exploring alternative dopants to improve stability [115], but whether these dopants are equally significant in both OPVs and IPVs remains unclear, an issue this thesis will investigate.

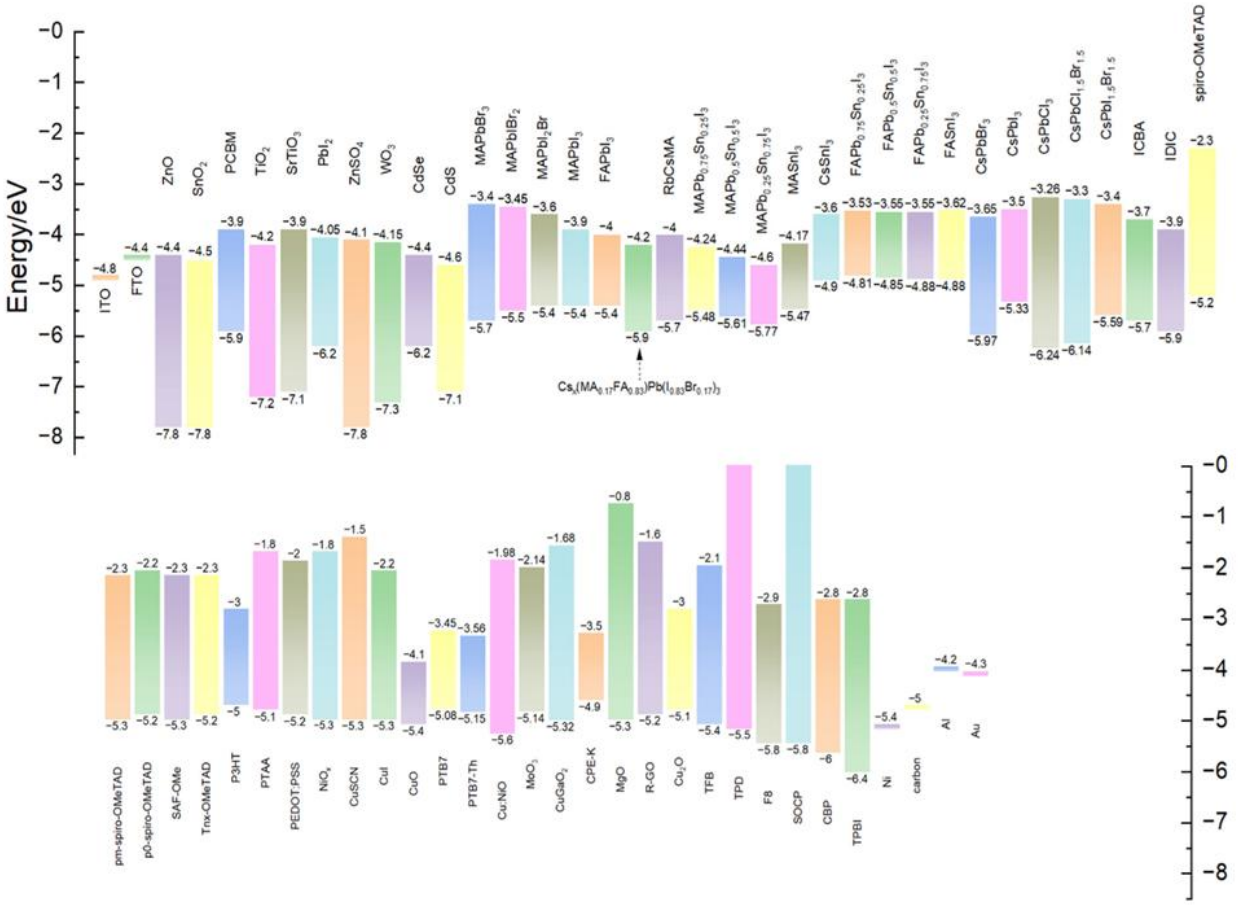

Figure 2.8. Commonly used anodes, cathodes, ETLs, HTLs, perovskites, and their respective band alignments [118].

2.9.4 Top Counter Electrode

In n-i-p structure PSCs, the "top" counter electrode refers to the electrode that is positioned on the surface opposite to the substrate. This electrode plays a crucial role in collecting holes and completing the circuit. Precious metals like gold (Au) and silver (Ag) are commonly used due to

their excellent conductivity and matched work functions with conventional HTMs [119]. However, Au is expensive, and Ag is unstable. To overcome these limitations, efforts have been made to replace them with low-cost carbon-based electrodes in HTM-free devices, where the carbon electrode serves as both the HTM and the counter electrode [120,121]. Despite these advancements, HTM-free devices still show lower efficiency due to inefficient charge extraction compared to HTM-based devices. Other materials, such as platinum (Pt), nickel (Ni), copper (Cu), chromium (Cr), tungsten (W), molybdenum (Mo) [119], and the conductive polymer PEDOT :PSS [122], have also been investigated as top counter electrodes in n-i-p structure PSCs. However, despite progress in developing alternative top electrodes, Au remains the preferred choice due to its superior performance. Therefore, most high-performing n-i-p structure PSCs still use Au as top electrodes. Widely used top counter electrodes, along with their corresponding band alignments with common adjacent common HTLs are illustrated in the **Figure 2.8**.

2.10 A Literature Reviewe of n-i-p Structure Pb-based Triple Cation PVKs for IPVs

As previously mentioned, PVKs are exceptional materials for PV applications, owing to their outstanding optoelectronic properties and the remarkable compositional flexibility enabled by the partial or complete substitution of constituent ions at all three sites (A, B, and X) in their ABX_3 crystal structure [123]. As illustrated in **Figure 2.9**, such elemental modifications enable precise tuning of the bandgap of halide perovskites, ranging from 1.15 eV for $MAPb_{0.5}Sn_{0.5}I_3$ [124] to over 3 eV for $MAPbCl_3$ [125], covering the entire visible spectrum [126]. This tunability is particularly advantageous for optimizing light absorption under indoor conditions, which is critical for enhancing the performance of devices under investigation.

Pb-based triple cation PVKs have attracted considerable attention for IPVs due to their structural and environmental stability, excellent optoelectronic properties, bandgap tunability, and reduced hysteresis under indoor illumination. In 2019 Juang et al. [127] were the first to evaluate the indoor performance of triple cation PVK-based n-i-p structured devices. Their work was based on the standard recipe for triple cation PVKs previously reported by Saliba et al. [128] Under 200 lux fluorescent tube light illumination, they achieved iPCE of 23.4% for triple cation PVK-based device compared to 16.0% under the same light conditions for cobalt-based DSSCs.

Since then, advancements in efficiency and stability have been made through strategies like bandgap, interface, and film engineering to optimize absorber properties, reduce defects, improve stability, and enhance charge transfer under low-light conditions. Since solar cells require different optimal bandgaps for outdoor and indoor light due to spectral differences. Bandgap engineering is

thus key to optimizing device performance under indoor illumination. Rafiku et al. [129] first explored bandgap tuning in triple-cation PVKs for IPVs. Comparing Br-rich and Br-poor PVKs-based devices, they found Br-rich devices outperformed Br-poor counterparts under fluorescent lighting (200 lx, 65 μW cm^{-2}).

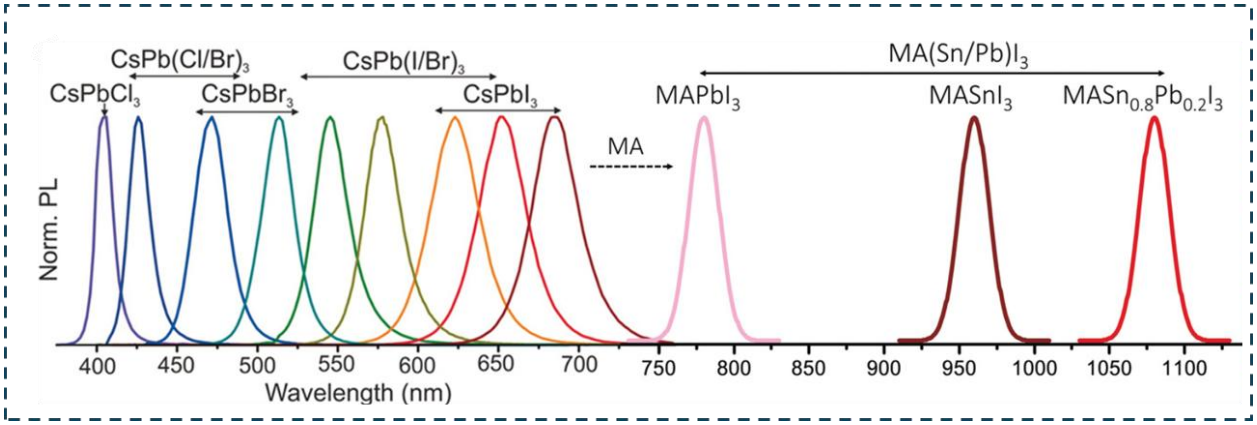

Figure 2.9. Representative PL spectra of different compositions from the bluest CsPbCl3 to the most redshifted $CH_3NH_3(Sn_{0.8}/Pb_{0.2})I_3$ perovskite [130] .

Later, Xu et al. [131] systematically investigated the impact of bandgap engineering on triple-cation PVK-based devices under indoor illumination by varying Br concentrations ($0 \leq x \leq 100\%$). The corresponding films photographs, UV-Vis absorption spectra, and bandgaps are shown in **Figure 2.10(a-c)**. Interestingly, they found that PVKs with higher Br concentrations and bandgaps closer to the theoretical limit of 1.9 eV for IPVs did not achieve the best performance. Instead, a device with a Br content of x = 0.17 (Eg = 1.61) and improved film quality delivered the highest iPCE values of 22.0% at 200 lx and 27.1% at 1000 lx under LED illumination. These findings emphasize that optimizing absorber PVK quality is more critical than targeting the ideal bandgap for achieving superior indoor performance. In a subsequent attempt [132], they developed flexible n-i-p devices using a triple-cation PVK absorber on a low-cost polyethylene terephthalate (PET) substrate. By increasing the Br content from 0% (Eg = 1.531 eV) to 16% (Eg = 1.637 eV), they achieved a 42% improvement in iPCE. Further enhancement was realized by introducing tetrabutylammonium bromide (TBAB) at the PVK/HTM interface. The TBA^+ cations intercalated into the PVK structure, substituted FA cations, improved absorber quality, and formed a lower-dimensional structure on the 3D matrix. This modification increased iPCE by 26%, from 27.6% without TBAB to 32.5% with TBAB under 1000 lx LED illumination, while also improved device stability. However, unlike solely optimizing the bandgap by varying anion composition, Srathongsian et al. [133] went beyond, and comprehensively studied the influence of both cation and anion compositions in $Cs_x(FA_{0.88}MA_{0.12})_{1-x}Pb(I_{1-\gamma}Br_\gamma)_3$ for indoor light harvesting. To examine

their impact on morphology, defects, stability, and performance, they explored Cs content (5–40%) and Br content (17% or 30%). The optimal composition, 10% Cs and 30% Br stroked the right balance and enabled low-cost, carbon-based devices with the highest iPCE of 31.94% and good stability under low light cycles. Further modifications in the device stack and size yielded functional devices with reduced hysteresis and iPCE of 30.09% on a 1 cm² active area. Connecting two such cells in series enabled a module capable of powering humidity and temperature sensors under 1000 lux illumination, as illustrated in **Figure 2.10(d)**.

In addition to bandgap engineering, strategies have been implemented to improve absorber quality and minimize detrimental surface defects. For instance, Mica et al. [134] synthesized $Cs_{0.06}MA_{0.15}FA_{0.79}PbI_{0.85}Br_{0.153}$ PVK films with varying thicknesses and integrated them into n-i-p structured devices. Under illumination from a standard white LED with an incident power of 0.9 mW/cm², the device incorporating a 640 nm thick triple-cation PVK layer with enhanced surface morphology achieved the highest iPCE of 21.4%. To establish a new balance between the generation and transmission of excitons and increase the power output of the tripe cation PVK-based device, yang et al. [135] incorporated *N*,*N*′-bis(dimethylaminopropyl-*N*‴-oxide)-perylene-3,4,9,10 tetracarboxidiimide (PDINO) into the PVK precursor solution. This incorporation optimized the formation of PVK crystals, effectively reduced defects in the film, improved exciton transport and facilitated rapid exciton separation within the PVK layer. As illustrated in the **Figure 2.10(e)**, solar cell devices with and without PDINO were fabricated with the structure $FTO/SnO_2/Cs_{0.05}(FA_{0.85}MA_{0.15})_{0.95}Pb(I_{0.85}Br_{0.15})_3$/Spiro-OMeTAD/$MoO_3$/Ag, and their performance under 1000 lux LED light was evaluated. The PDINO-based device demonstrated a higher iPCE of 37.9%, compared to iPCE of 34.2% for the control device without PDINO. To produce high quality triple cation PVK with the composition of $(FA_{0.45}MA_{0.49}Cs_{0.06}Pb(I_{0.62}Br_{0.32}Cl_{0.06})_3)$ and a bandgap of 1.80 eV, Penpong et al. [136] developed vacuum thermal annealing (VTA) approach for films deposited using a one-step deposition method with chlorobenzene as an antisolvent. The VTA treatment facilitated the formation of compact, dense, and robust morphologies while suppressing trap states at the surfaces and grain boundaries of the resulting films. As a result, in a low-cost carbon-electrode n-i-p architecture, the champion device based on VTA-treated triple-cation PVK achieved a peak iPCE of 32.0%, surpassing the 30.7% iPCE of the control champion device. Moreover, to realize annealing-free PVK films for IPVs compatible with both rigid and flexible substrates, Dong et al. [137] comparatively investigated the suitability of Cs-, MA-, and FA-based single cation, FA/MA-based double cation and Cs/FA/MA-based triple cation PVKs by introducing 3,4-ethoxylene dioxy thiophene (EDOT) into anti-solvent during their synthesis processes. The morphological, structural, optical and electrical

characterizations revealed better suitability of Cs/FA/MA-based triple cation PVKs among others with enlarged crystal grains and reduced defects. By incorporating Cs/FA/MA-based triple-cation PVKs into rigid and flexible n-i-p structured devices, they achieved an iPCE of 22.79% for flexible champion device and 32.61% for rigid champion device under 1000 lux indoor light illumination.

Surface treatment investigations, involving the direct application of various materials on the PVK surface, is considered an effective approach to enhance absorber quality, optimize band alignment, prevent oxygen ingress, and improve charge transfer, which ultimately results in the improvement of performance and stability of devices. In this regard, Lee et al. [138] deposited PEAI on the top of $Cs_{0.05}(FA_{0.6}MA_{0.4})_{0.95}Pb(I_{0.6}Br_{0.4})_3$ PVK films (bandgap >1.74 eV) and investigated its effect on device performance under indoor illumination. The characterizations revealed beneficial influence of 2 mg PEAI deposition on the top of absorber layer which resulted in improved film crystallinity, healing of surface defects, and turning the surface increasingly p-type, which in turn facilitated the transport of holes to the HTL. As a result, under 1000 lux halogen lighting, PEAI-treated devices achieved average iPCEs of 23.09 ± 0.20%, compared to 20.30 ± 0.10% for reference devices. Similarly, under 1000 lux cool white LED lighting, PEAI-treated devices delivered average iPCEs of 33.42 ± 0.15%, significantly higher than the 28.01 ± 0.17% achieved by reference devices. To effectively minimize the residual stress of the triple-cation PVK absorber film, eliminate excess PbI_2 and metallic lead (Pb^0) defects, and suppress their future formation, Li et al. [139] successfully addressed these challenges by passivating the PVK surface with formamidinium triiodide (FAI_3). This treatment improved energy band alignment within the device and enhanced the uniformity of microelectrical properties of the film. As a result, the FAI_3-treated device achieved an impressive iPCE of 35.14% under 300 μW cm^{-2} LED illumination, compared to 32.48% for the control device. Additionally, the FAI_3-treated device exhibited remarkable stability and retained 99.5% of its initial performance after continuous strobe light soaking for 2160 hours. In addition, to enhance both intrinsic and environmental stabilities and prevent moisture and oxygen erosion, Dong et al. [140] introduced a botanical antioxidant, tomato lycopene, as a thin layer (~2.3 nm) in a triple-cation PVK-based n-i-p structure device, applied on top of the absorber layer, as illustrated in the **Figure 2.10(f)**. The molecular structure of tomato lycopene, extracted from tomato peel, is also illustrated in the **Figure 2.10(g)**. They found that the incorporation of lycopene not only shielded the PVK absorber from moisture and oxygen but also interacted with it through carbon-halogen bonds and improved its crystallinity as well as reduced its surface defects. As a result, the device with tomato lycopene achieved a remarkable iPCE of 40.24% under 1000 lux indoor light illumination, compared to 37.26% for the control device. This represents the highest reported iPCE to date for

n-i-p structured IPV devices based on triple-cation PVKs. Furthermore, the addition of tomato lycopene significantly enhanced the stability of a device.

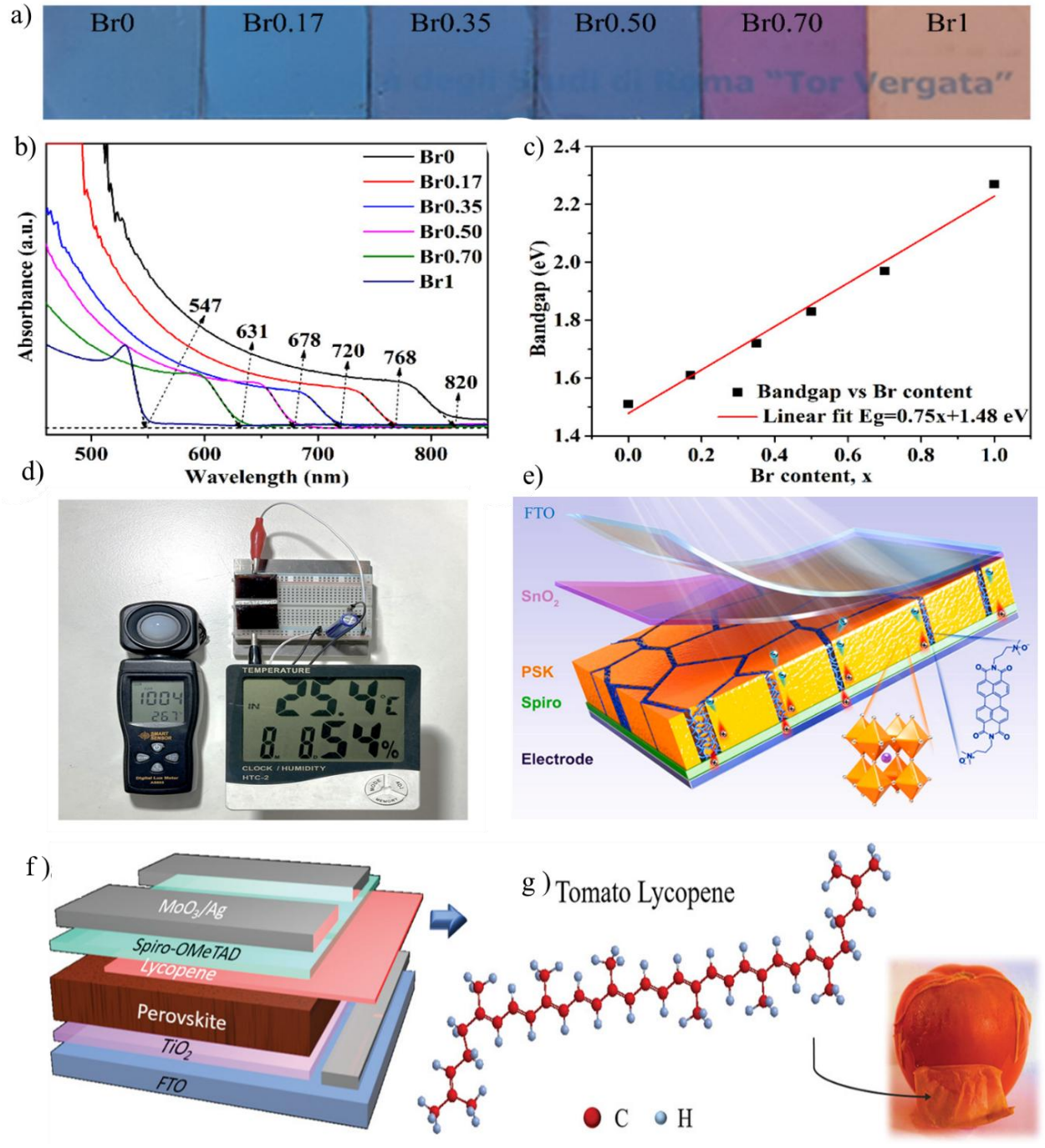

Figure 2.10. a) Photographs, b) absorption spectra, c) linear relationship between bandgap (Eg) and Br– content (x) [131], and d) Photograph of thermo-hygrometer (HTC-2 model) powered by the indoor solar cell under 1004 lux [133], e) schematic illustration of PDINO-based device [135], f) a) Schematic illustration of device structure with inserted tomato lycopene thin film. g) Molecular structure of tomato lycopene extractable from tomato peel [140].

As previously mentioned, TiO_2 and SnO_2 are widely regarded as the ETLs of choice for n-i-p structured PSCs. However, determining the most suitable ETL for n-i-p devices with triple-cation PVK absorbers for IPV applications requires in-depth and comprehensive investigations,

considering various parameters and conditions. To address this, Asada et al. [141] recently studied the influence of ETLs on the performance of PSCs under indoor light illumination. They fabricated TCO/ETL/$FA_{0.81}MA_{0.1}Cs_{0.09}Pb(I_{0.9}Br_{0.1})_3$/PEACl/spiro-OMeTAD/Au structured devices and compared TiO_2 and SnO_2 as ETLs. They found that compared to TiO_2-based devices, SnO_2-based devices exhibited lower charge transfer resistance particularly in low-light environments. This improvement in charge transfer properties led SnO_2-based champion device to achieve a higher iPCE of 27.7%, compared to 22.5% for TiO_2-based champion device under 1000 lux white LED illumination. Additionally, they found that under low light illumination, the defect density of the ETLs significantly influenced device performance.

2.11 Issues to be addressed

While Pb-based triple-cation PSCs have demonstrated exceptional performance in both outdoor and indoor PV applications, several challenges must be addressed to enable their widespread commercial adoption. The following sections outline these challenges and propose potential solutions:

2.11.1 Hysteresis

Hysteresis in PSCs refers to the dependence of J-V characteristics on both the direction and rate of the voltage sweep, resulting in discrepancies between forward and reverse J-V curves. This affects the accuracy, reproducibility, and stability of the device [129,142,143]. Hysteresis can be categorized as normal, where the reverse scan shows better performance, or inverted, where the forward scan performs better [144]. Devices with minimal or no hysteresis are considered more reliable and stable.

The Hysteresis Index (HI) quantifies the degree of hysteresis in J-V characteristics of PSCs, and calculated as:

$$\mathrm{HI}\ (\%) = \left(\frac{\mathrm{PCE_{Rev}} - \mathrm{PCE_{For}}}{\mathrm{PCE_{Rev}}}\right) \times 100$$

Where PCE_{Rev} and PCE_{For} are the PCEs during reverse and forward voltage scans, respectively. Hysteresis in PSCs arises from factors such as ion migration, charge trapping/de-trapping at interfaces, ferroelectric polarization, capacitive effects, interfacial defects, scan rate dependence, material composition and morphology, etc [143,145–149]. Dopants in HTL also contribute to hysteresis [150,151].

In addition to OPVs, hysteresis remains a significant challenge for PSCs operating indoors, often more pronounced than in outdoor conditions [133,152]. While considerable progress has been made in addressing hysteresis under outdoor conditions, focused efforts are still needed for indoor applications. Transitioning from n-i-p to p-i-n architectures is one promising approach, as hysteresis is typically less severe in p-i-n devices [153]. However, strategies to address hysteresis in n-i-p structure devices operating indoors have also shown promise. For instance, Bulloch et al. [154] reported that the p-i-n architecture with organic charge transport layers is preferable to the n-i-p architecture with metal oxides like TiO_2 and SnO_2 for maximizing the steady-state iPCE of $MAPbI_3$-based IPV devices. This is because $MAPbI_3$ exhibits active ion migration, causing significant hysteresis in n-i-p devices. However, they also discovered that using a triple-cation PVK absorber in n-i-p structures effectively reduces hysteresis by minimizing ion migration. Improving PVK quality and minimizing intrinsic defects, as demonstrated by Han et al. [155], also suppresses hysteresis. Device interface optimization plays a critical role as well. Srathongsian et al. [133] achieved significant reductions in hysteresis by optimizing the ETL with a bilayer SnO_2 and replacing Spiro-OMeTAD with CuSCN as HTL, resulting in higher efficiency and stability of PVK-based IPV device. In short, optimizing PVK composition, absorber quality, and interface materials offers viable pathways to address hysteresis in n-i-p structure PSCs operating indoors.

2.11.2 Stability

Despite the remarkable progress of PSCs in both outdoor and indoor environments, they haven't yet transitioned from research labs to practical applications. A valid question can arise why is this the case? The answer to this lies in the "golden triangle" of solar cells, which emphasizes three essential criteria for commercialization: high efficiency, low cost, and high stability (**Figure 2.11**). While PSCs excel in efficiency and affordability, their stability remains a critical hurdle. Therefore, addressing this challenge is essential for PVK-based PV technologies to compete and thrive in the market [156].

The lifetime and stability of PSCs are influenced by both extrinsic and intrinsic factors [157]. Extrinsic factors include environmental conditions such as moisture, oxygen, heat, UV radiation, and light exposure. Advanced encapsulation techniques can mitigate the degradation caused by these environmental factors [157,158]. The impact of environmental conditions also differs between indoor and outdoor settings. Indoor light intensity is typically 2 to 3 orders of magnitude lower than outdoor sunlight, resulting in stable cell temperatures and reduced photoinduced degradation. In contrast, outdoor conditions expose devices to intense sunlight, including heat from infrared radiation and higher light intensity, leading to inevitable photoinduced damage [159–161]. Intrinsic

factors that affect the lifetime and stability of PSCs stem from material properties and device design. These include PVK composition [128], ion migration (e.g., I^-, Br^-, and MA^+) within the PVK layer [162], defect formation such as grain boundaries, voids, and surface traps [77,163], and interface degradation between the absorber and charge transport layers [164–166]. Among them, surface traps, arising from the polycrystalline nature of PVK films, are particularly detrimental. Surface trap densities are reported to be 1–2 orders of magnitude higher than those within the bulk material, significantly compromise device stability and performance [167]. These traps are even more detrimental under low intensity indoor light, where fewer charge carriers are generated, making it easier for surface traps to capture them. Conversely, outdoor sunlight produces a higher carrier density, mitigating the impact of traps as many carriers remain untrapped [168].

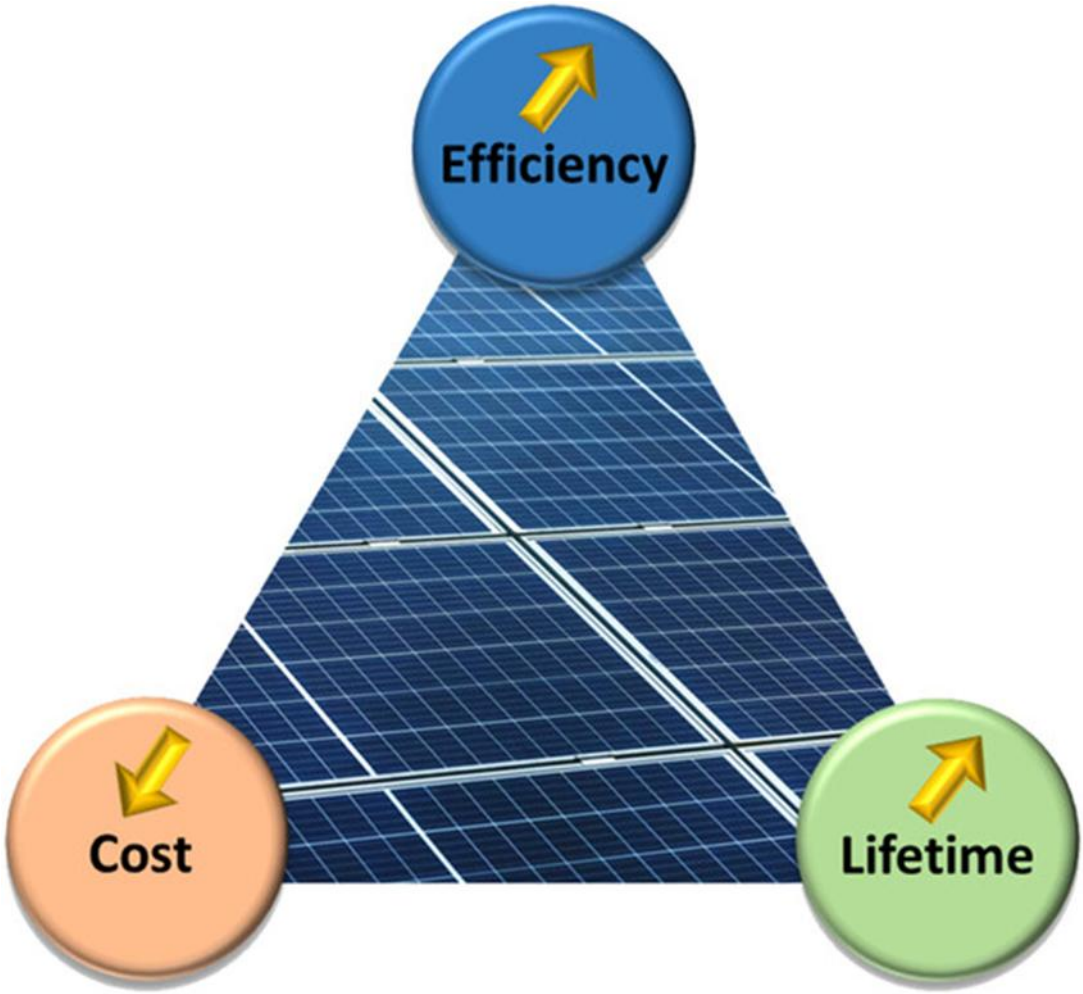

Figure. 2.11. The quintessential or golden triangle for solar cells [156].

Passivation, as defined by the International Union of Pure and Applied Chemistry (IUPAC), refers to making a material less reactive or susceptible to environmental degradation by forming a protective layer, often through chemical interactions. In PSCs, passivation serves a dual purpose:

chemical passivation reduces defect trap states, enhancing charge transfer across interfaces, while physical passivation protects functional layers from environmental factors, thereby preventing degradation [169]. Effective defect passivation has emerged as a pivotal strategy for overcoming the performance and stability challenges of PSCs. In this regard, various approaches have been developed to address these issues, each leveraging different mechanisms. These include incorporating excess lead iodide (PbI_2) [170], utilizing Lewis acid/base interactions [171], and introducing two-dimensional (2D) PVKs with functional groups [172–174]. These methods reduce defect-induced losses and optimize interfacial properties, significantly improving device efficiency and stability. Compared to outdoor conditions, surface defects are especially problematic for PVK devices operating indoors, where lower light intensities magnify their impact. Passivation technology is therefore critical for indoor-operating PVKs devices. Although passivation strategies have been extensively applied to PVKs devices operating in outdoor conditions, their application to devices designed for indoor environments remains comparatively limited [138,175]. Moving forward, it is vital to develop new passivation materials/stratagies and assess the effectiveness of existing ones under varying operating conditions. Comparative studies will be instrumental in advancing the performance and stability of PVKs devices optimized for both indoor and outdoor environments.

While tackling intrinsic and extrinsic factors influencing the PVKs degradation is critical for advancing the technology. However, device stability also depends on other functional layers, not just the PVK absorber. For instance, while $CsPbBr_3$ PVK is highly stable under harsh humidity conditions, incorporating organic HTLs compromises the overall stability of $CsPbBr_3$-based devices [176]. In most efficient n-i-p structure PVK devices, Spiro-OMeTAD is the commonly used HTL [177]. Although it contributes to high efficiencies, Spiro-OMeTAD has notable drawbacks. It is unstable at elevated temperatures (60–120 °C) [178] and exhibits low hole mobility and conductivity due to its bulky molecular structure, leading to high R_s and reduced performance of corresponding devices [179]. To mitigate these issues, doping Spiro-OMeTAD with compounds like lithium bis(trifluoromethanesulfonyl)imide (Li-TFSI), 4-tert-butylpyridine (tBP), and FK 209 Co(III) TFSI has been widely adopted to enhance conductivity, mobility, and energy alignment with the PVK layer [180]. The chemical structures of Spiro-OMeTAD and its dopants, respectively, are shown in **Figure 2.12(a) and Figure 2.12(b)**. However, these dopants come with their own challenges. Li-TFSI and tBP are hygroscopic and corrosive, with tBP reacting with PbI_2 to corrode the PVK layer and Li^+ from Li-TFSI diffusing into and degrading the PVK structure [181–183]. Thus, while doped Spiro-OMeTAD improves device performance, its limitations underscore the need

for alternative HTLs or improved strategies to ensure long-term stability. Factors contributing to Spiro-OMeTAD instability are summarized in **Figure 2.12(c)**.

In addition to the Spiro-OMeTAD HTL, the widely used TiO_2 ETL and Au back electrodes in n-i-p structured PVKs devices also significantly contribute to device degradation. TiO_2 contains oxygen vacancy defects (Ti^{3+} sites), particularly on its surface, which act as deep electron-donating sites. Under UV light, these defects oxidize iodide ions at the TiO_2/PVK interface, leading to PVK decomposition [184]. Additionally, Au electrodes are prone to corrosion by halides migrating from the PVK layer, reducing conductivity. Corroded metal ions can also diffuse into the PVK, further accelerating device degradation [185].

Although Spiro-OMeTAD remains the preferred HTL for PSCS, contributing significantly to their performance in both outdoor and indoor environments. However, addressing the stability issues associated with traditional dopants is crucial. The possible and applied strategies to mitigate these effects are summarized in **Figure 2.12(d)** [186]. Recently, Du et al. [187] achieved a stable PCE of over 20% under standard 1-sun illumination using undoped Spiro-OMeTAD as the HTL in their PVK-based device under standard light illumination. They developed a solvent-annealing-assisted thermal evaporation (SATE) method for Spiro-OMeTAD deposition. Consequently, without dopants, the film morphology and optoelectronic properties improved. As a result, the device achieved excellent performance without the need for traditional dopants. Moreover, under indoor low-light conditions, our group very recently demonstrated that the reduced influence of R_s eliminates the need for traditional dopants in Spiro-OMeTAD to achieve efficient and stable IPV performance [188]. Interestingly, devices using both doped and undoped Spiro-OMeTAD achieved comparable performance under indoor illumination. However, the device structure utilized TiO_2 as the ETL, which requires high-temperature processing and compromises device stability, as previously discussed.

Overall, these findings renew optimism for the potential of undoped Spiro-OMeTAD-based devices. Nevertheless, further research is needed to optimize deposition methods for Spiro-OMeTAD and explore alternative PVK compositions and, especially develop and explore alternative ETL materials in device architectures. These efforts are expected to yield significant benefits, helping to avoid "out of the frying pan into the fire" scenarios while enhancing device performance, improving stability, and mitigating hysteresis-related challenges in PVK devices operating in both outdoor and indoor environments.

2.11.3 Toxicity

The toxicity of Pb-based PVKs is a critical issue that cannot be ignored. Similar to the challenges faced by CdTe due to "Cd" toxicity, the presence of Pb in PVKs raises concerns about environmental sustainability and human health [189]. While Pb toxicity is comparatively lower than Cd due to a higher toxicity threshold [190], its environmental impact remains significant. To address this, extensive efforts have been made to find alternatives to Pb. Substitutes such as Sn, Ge, Bi, Sb, In, Ag, and Te have been explored [191]. Among these, only Sn-based PVKs have shown notable progress in efficiency [192], but they remain highly unstable and prone to self-oxidation. Furthermore, Sn also poses environmental and health concerns similar to Pb [193]. Despite ongoing research, the unique properties of Pb, such as its ionic radius, spin-orbit coupling effects, and electronic configuration, continue to make it integral to the success of PVKs in PVs and optoelectronic applications [194]. While future breakthroughs in Pb-free PVKs may offer environmentally friendly and stable alternatives, it remains uncertain whether they can surpass Pb-based counterparts. Proper encapsulation and recycling methods can mitigate some risks, and it has been argued that with these measures, the benefits of Pb in PV technology can outweigh its drawbacks [195].

While breakthroughs in Pb-free alternatives are vital for addressing Pb toxicity, efforts can also be directed toward reducing the overall toxicity of Pb-based PVK devices. One notable advantage of these devices is their fabrication via low-cost solution processing. However, this often involves toxic organic solvents like N,N-dimethylformamide (DMF), dimethyl sulfoxide (DMSO), and chlorobenzene as antisolvent, which pose significant environmental and health risks. Chlorobenzene is also commonly used as a solvent in preparing HTL solutions such as Spiro-OMeTAD and PTAA [196]. To mitigate these risks, exploring greener solvents and antisolvents or developing efficient vacuum-based deposition techniques can significantly reduce toxicity and eliminate the costs associated with these in the fabrication process. This thesis acknowledges these concerns and contributes to the reduction of toxicity in triple-cation PVK-based IPV devices to some extent. Notably, to date, there are no reported studies on the use of greener antisolvents in the synthesis of triple-cation absorber PVKs for IPV devices. While this claim is specific to triple-cation PVK-based IPV devices, similar efforts have been reported for other PVKs compositions in IPV devices. For instance, Passatorntaschakorn et al. [197] used green anisole as an antisolvent during the synthesis of the double-cation PVK, $Cs_{0.17}FA_{0.83}Pb(I_{0.83}Br_{0.17})_3$ for IPV devices. The resulting device achieved a peak iPCE of just 20.19% under 1000 lux cool daylight LED illumination. Additionally, Naikaew et al. [198] investigated the indoor performance of semi-

transparent devices based on single-cation ($MAPbI_3$), double-cation ($Cs_{0.17}FA_{0.83}PbI_{2.49}Br_{0.51}$), and triple-cation ($Cs_{0.05}FA_{0.81}MA_{0.14}PbI_{2.55}Br_{0.45}$) PVKs. In their work, they employed greener anisole as an antisolvent for single- and double-cation PVKs but used toxic chlorobenzene for triple-cation PVKs. Therefore, this thesis aims to fabricate triple-cation PVKs for IPV devices while using greener anisole as an antisolvent for the first time, thus addressing the gap in greener synthesis practices of these materials for IPV applications.

2.12 Summary

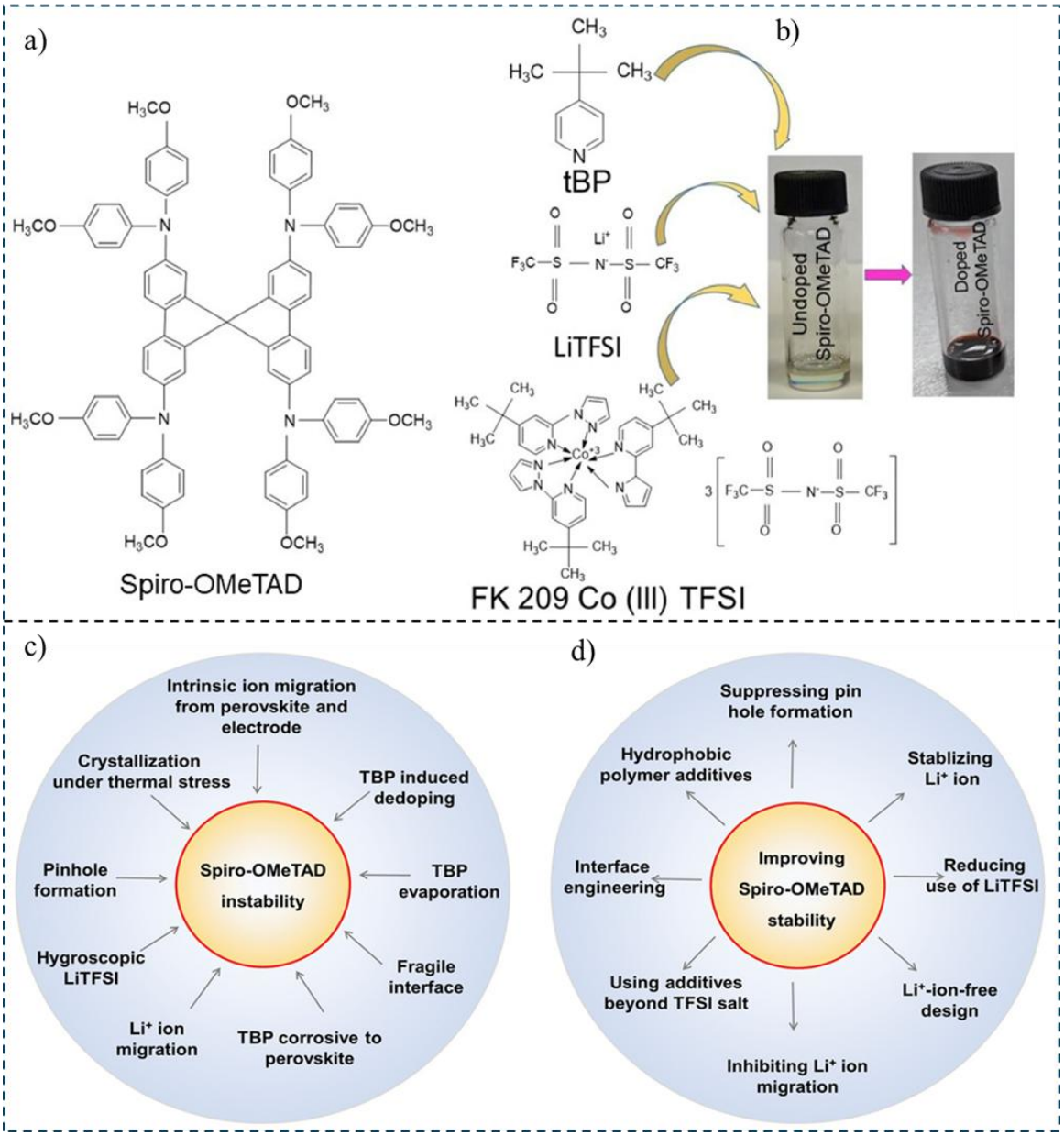

Figure 2.12. a) Chemical structure of Spiro-OMeTAD. (b) Doping Li-TFSI, tBP and FK 209 as common dopants in Spiro-OMeTAD and the colors of pristine (undoped) and doped Spiro-OMeTAD solution [180], b) a brief summary of factors responsible for Spiro-OMeTAD instability, c) a brief summary of available strategies for improving Spiro-OMeTAD stability [186].

In summary, PVKs are outstanding materials for PV applications, with mixed-cation PVKs emerging as exceptional choices due to their enhanced structural and environmental stability. Their low-cost solution processability further distinguishes them from other materials used in PV and optoelectronic applications. However, issues related to the solution processability of these materials, particularly the formation of detrimental defects, remain a significant concern as they compromise both performance and stability. Notably, defect formation in PVKs is even more detrimental for IPVs compared to OPVs. Therefore, strategies aimed at mitigating these defects in PVKs are more crucial than merely optimizing the bandgap for IPVs. Current research on n-i-p structured triple-cation PVKs for IPV applications underscores the importance of defect mitigation and improving absorber layer quality. Implementing novel strategies to enhance the quality of triple-cation PVK absorbers could be a key step toward further improving device performance and stability under indoor illumination. Passivation strategies appear particularly beneficial, as they not only enhance the quality of the PVK absorber but also protect it from environmental degradation. While passivation techniques have been widely applied to PVK-based devices for outdoor applications, they remain largely unexplored in the context of IPV technology. In addition to performance improvement, challenges such as hysteresis, stability, and toxicity must also be addressed to fully harness the potential of PVK-based devices for both indoor and outdoor applications. Since the stability and hysteresis issues of PVK-based devices are not solely linked to the absorber layer but also influenced by other functional layers, there is an urgent need to revisit device design, particularly in the context of IPVs, which is an emerging field. The shift in operating conditions from outdoor to indoor environments, along with necessary design modifications, may yield significant advantages for the successful commercialization of this promising technology.

References

1. Duan, T., Mora-Seró, I. & Zhou, Y. Introduction to Perovskite. in *Halide Perovskite Semiconductors* 1–8 (Wiley, 2024). doi:10.1002/9783527829026.ch1.

2. Bello, S., Urwick, A., Bastianini, F., Nedoma, A. J. & Dunbar, A. An introduction to perovskites for solar cells and their characterisation. *Energy Reports* **8**, 89–106 (2022).

3. Locock, A. J. & Mitchell, R. H. Perovskite classification: An Excel spreadsheet to determine and depict end-member proportions for the perovskite- and vapnikite-subgroups of the perovskite supergroup. *Comput Geosci* **113**, 106–114 (2018).

4. Diouf, B., Muley, A. & Pode, R. Issues, Challenges, and Future Perspectives of Perovskites for Energy Conversion Applications. *Energies (Basel)* **16**, 6498 (2023).

5. Zhang, L. *et al.* Advances in the Application of Perovskite Materials. *Nanomicro Lett* **15**, 177 (2023).

6. Han, B. *et al.* Energy storage research of metal halide perovskites for rechargeable batteries. *Nano Energy* **115**, 108646 (2023).

7. Moghadamzadeh, S. *et al.* Triple-cation low-bandgap perovskite thin-films for high-efficiency four-terminal all-perovskite tandem solar cells. *J Mater Chem A Mater* **8**, 24608–24619 (2020).

8. Paul, S., Ariga, K., Sarma, D. D. & Acharya, S. Dimension-controlled halide perovkites using templates. *Nano Today* **39**, 101181 (2021).

9. Gao, P., Grätzel, M. & Nazeeruddin, M. K. Organohalide lead perovskites for photovoltaic applications. *Energy Environ. Sci.* **7**, 2448–2463 (2014).

10. Kieslich, G., Sun, S. & Cheetham, A. K. An extended Tolerance Factor approach for organic–inorganic perovskites. *Chem Sci* **6**, 3430–3433 (2015).

11. Valipour, F., Yazdi, E., Torabi, N., Mirjalili, B. F. & Behjat, A. Improvement of the stability of perovskite solar cells in terms of humidity/heat via compositional engineering. *J Phys D Appl Phys* **53**, 285501 (2020).

12. Gao, W. *et al.* A-Site Cation Engineering of Metal Halide Perovskites: Version 3.0 of Efficient Tin-Based Lead-Free Perovskite Solar Cells. *Adv Funct Mater* **30**, (2020).

13. Stoumpos, C. C. & Kanatzidis, M. G. The Renaissance of Halide Perovskites and Their Evolution as Emerging Semiconductors. *Acc Chem Res* **48**, 2791–2802 (2015).

14. Xu, S., Yang, L., Zhang, X., Wang, L. & Sun, W. Research Progress of Cs-Based All-Inorganic Perovskite Solar Cells. *Energies (Basel)* **17**, 2671 (2024).

15. Chen, Y., Li, F., Zhang, M. & Yang, Z. Recent Progress on Boosting the Perovskite Film Quality of All-Inorganic Perovskite Solar Cells. *Coatings* **13**, 281 (2023).

16. Jin, H. *et al.* Phase stabilization of cesium lead iodide perovskites for use in efficient optoelectronic devices. *NPG Asia Mater* **16**, 24 (2024).

17. Qiu, Z., Li, N., Huang, Z., Chen, Q. & Zhou, H. Recent Advances in Improving Phase Stability of Perovskite Solar Cells. *Small Methods* **4**, (2020).

18. Mahapatra, A., Kumar, S., Kumar, P. & Pradhan, B. Recent progress in perovskite solar cells: challenges from efficiency to stability. *Mater Today Chem* **23**, 100686 (2022).

19. Ji, D. *et al.* Regulatory tolerance and octahedral factors by using vacancy in APbI3 perovskites. *Vacuum* **164**, 186–193 (2019).

20. Kim, H.-S. *et al.* Lead Iodide Perovskite Sensitized All-Solid-State Submicron Thin Film Mesoscopic Solar Cell with Efficiency Exceeding 9%. *Sci Rep* **2**, 591 (2012).

21. Frost, J. M. *et al.* Atomistic Origins of High-Performance in Hybrid Halide Perovskite Solar Cells. *Nano Lett* **14**, 2584–2590 (2014).

22. Targhi, F. F., Jalili, Y. S. & Kanjouri, F. MAPbI3 and FAPbI3 perovskites as solar cells: Case study on structural, electrical and optical properties. *Results Phys* **10**, 616–627 (2018).

23. Tao, S. *et al.* Absolute energy level positions in tin- and lead-based halide perovskites. *Nat Commun* **10**, 2560 (2019).

24. Mangrulkar, M. & Stevenson, K. J. The Progress of Additive Engineering for CH3NH3PbI3 Photo-Active Layer in the Context of Perovskite Solar Cells. *Crystals (Basel)* **11**, 814 (2021).

25. Chen, Z. *et al.* Single-Crystal MAPbI $_3$ Perovskite Solar Cells Exceeding 21% Power Conversion Efficiency. *ACS Energy Lett* **4**, 1258–1259 (2019).

26. Alsalloum, A. Y. *et al.* Low-Temperature Crystallization Enables 21.9% Efficient Single-Crystal MAPbI $_3$ Inverted Perovskite Solar Cells. *ACS Energy Lett* **5**, 657–662 (2020).

27. He, X. *et al.* 40.1% Record Low-Light Solar-Cell Efficiency by Holistic Trap-Passivation using Micrometer-Thick Perovskite Film. *Advanced Materials* **33**, (2021).

28. Conings, B. *et al.* Intrinsic Thermal Instability of Methylammonium Lead Trihalide Perovskite. *Adv Energy Mater* **5**, (2015).

29. Eperon, G. E. *et al.* Formamidinium lead trihalide: a broadly tunable perovskite for efficient planar heterojunction solar cells. *Energy Environ Sci* **7**, 982 (2014).

30. Min, H. *et al.* Efficient, stable solar cells by using inherent bandgap of α-phase formamidinium lead iodide. *Science (1979)* **366**, 749–753 (2019).

31. Zhumekenov, A. A. *et al.* Formamidinium Lead Halide Perovskite Crystals with Unprecedented Long Carrier Dynamics and Diffusion Length. *ACS Energy Lett* **1**, 32–37 (2016).

32. Niu, T. *et al.* Phase-Pure α-FAPbI $_3$ Perovskite Solar Cells via Activating Lead–Iodine Frameworks. *Advanced Materials* **36**, (2024).

33. Li, Z. *et al.* Stabilizing Perovskite Structures by Tuning Tolerance Factor: Formation of Formamidinium and Cesium Lead Iodide Solid-State Alloys. *Chemistry of Materials* **28**, 284–292 (2016).

34. Lu, H. *et al.* Vapor-assisted deposition of highly efficient, stable black-phase FAPbI $_3$ perovskite solar cells. *Science (1979)* **370**, (2020).

35. Wang, P. *et al.* Solvent-controlled growth of inorganic perovskite films in dry environment for efficient and stable solar cells. *Nat Commun* **9**, 2225 (2018).

36. Hutter, E. M. *et al.* Vapour-Deposited Cesium Lead Iodide Perovskites: Microsecond Charge Carrier Lifetimes and Enhanced Photovoltaic Performance. *ACS Energy Lett* **2**, 1901–1908 (2017).

37. Dastidar, S., Li, S., Smolin, S. Y., Baxter, J. B. & Fafarman, A. T. Slow Electron–Hole Recombination in Lead Iodide Perovskites Does Not Require a Molecular Dipole. *ACS Energy Lett* **2**, 2239–2244 (2017).

38. Xu, D. *et al.* Record-Efficiency Inverted CsPbI $_3$ Perovskite Solar Cells Enabled by Rearrangement and Hydrophilic Modification of SAMs. *Adv Funct Mater* **35**, (2025).

39. Wang, K. *et al.* Ion–Dipole Interaction Enabling Highly Efficient CsPbI $_3$ Perovskite Indoor Photovoltaics. *Advanced Materials* **35**, (2023).

40. Travis, W., Glover, E. N. K., Bronstein, H., Scanlon, D. O. & Palgrave, R. G. On the application of the tolerance factor to inorganic and hybrid halide perovskites: a revised system. *Chem Sci* **7**, 4548–4556 (2016).

41. Song, J. *et al.* Ultralarge All-Inorganic Perovskite Bulk Single Crystal for High-Performance Visible–Infrared Dual-Modal Photodetectors. *Adv Opt Mater* **5**, (2017).

42. Yang, Z. *et al.* Engineering the Exciton Dissociation in Quantum-Confined 2D CsPbBr $_3$ Nanosheet Films. *Adv Funct Mater* **28**, (2018).

43. Becker, P. *et al.* Low Temperature Synthesis of Stable γ-CsPbI $_3$ Perovskite Layers for Solar Cells Obtained by High Throughput Experimentation. *Adv Energy Mater* **9**, (2019).

44. Sanehira, E. M. *et al.* Enhanced mobility CsPbI $_3$ quantum dot arrays for record-efficiency, high-voltage photovoltaic cells. *Sci Adv* **3**, (2017).

45. Sutton, R. J. *et al.* Bandgap-Tunable Cesium Lead Halide Perovskites with High Thermal Stability for Efficient Solar Cells. *Adv Energy Mater* **6**, (2016).

46. Straus, D. B. & Cava, R. J. Tuning the Band Gap in the Halide Perovskite $CsPbBr_3$ through Sr Substitution. *ACS Appl Mater Interfaces* **14**, 34884–34890 (2022).

47. Zhou, Q. *et al.* Tailored Lattice "Tape" to Confine Tensile Interface for 11.08%-Efficiency All-Inorganic $CsPbBr_3$ Perovskite Solar Cell with an Ultrahigh Voltage of 1.702 V. *Advanced Science* **8**, (2021).

48. Guo, Z. *et al.* A Universal Method of Perovskite Surface Passivation for $CsPbX_3$ Solar Cells with V_{OC} over 90% of the S-Q limit. *Adv Funct Mater* **32**, (2022).

49. Noh, J. H., Im, S. H., Heo, J. H., Mandal, T. N. & Seok, S. Il. Chemical Management for Colorful, Efficient, and Stable Inorganic–Organic Hybrid Nanostructured Solar Cells. *Nano Lett* **13**, 1764–1769 (2013).

50. Ono, L. K., Juarez-Perez, E. J. & Qi, Y. Progress on Perovskite Materials and Solar Cells with Mixed Cations and Halide Anions. *ACS Appl Mater Interfaces* **9**, 30197–30246 (2017).

51. Correa-Baena, J.-P. *et al.* The rapid evolution of highly efficient perovskite solar cells. *Energy Environ Sci* **10**, 710–727 (2017).

52. Pellet, N. *et al.* Mixed-Organic-Cation Perovskite Photovoltaics for Enhanced Solar-Light Harvesting. *Angewandte Chemie International Edition* **53**, 3151–3157 (2014).

53. Ünlü, F. *et al.* Understanding the interplay of stability and efficiency in A-site engineered lead halide perovskites. *APL Mater* **8**, (2020).

54. Byranvand, M. M. *et al.* Recent Progress in Mixed A-Site Cation Halide Perovskite Thin-Films and Nanocrystals for Solar Cells and Light-Emitting Diodes. *Adv Opt Mater* **10**, (2022).

55. Elangovan, N. K. *et al.* Recent developments in perovskite materials, fabrication techniques, band gap engineering, and the stability of perovskite solar cells. *Energy Reports* **11**, 1171–1190 (2024).

56. Zhang, C. & Park, N.-G. Materials and methods for cost-effective fabrication of perovskite photovoltaic devices. *Commun Mater* **5**, 194 (2024).

57. Shi, S., Li, Y., Li, X. & Wang, H. Advancements in all-solid-state hybrid solar cells based on organometal halide perovskites. *Mater Horiz* **2**, 378–405 (2015).

58. Djurišić, A. B. *et al.* Perovskite solar cells - An overview of critical issues. *Prog Quantum Electron* **53**, 1–37 (2017).

59. Liu, X. *et al.* A Review of Perovskite Photovoltaic Materials' Synthesis and Applications via Chemical Vapor Deposition Method. *Materials* **12**, 3304 (2019).

60. Singh, H., Dey, P., Chatterjee, S., Sen, P. & Maiti, T. Formamidinium containing tetra cation organic–inorganic hybrid perovskite solar cell. *Solar Energy* **220**, 258–268 (2021).

61. Im, J.-H., Kim, H.-S. & Park, N.-G. Morphology-photovoltaic property correlation in perovskite solar cells: One-step versus two-step deposition of CH3NH3PbI3. *APL Mater* **2**, (2014).

62. Chaudhary, S., Gupta, S. K. & Singh Negi, C. M. Enhanced performance of perovskite photodetectors fabricated by two-step spin coating approach. *Mater Sci Semicond Process* **109**, 104916 (2020).

63. Aharon, S., Cohen, B. El & Etgar, L. Hybrid Lead Halide Iodide and Lead Halide Bromide in Efficient Hole Conductor Free Perovskite Solar Cell. *The Journal of Physical Chemistry C* **118**, 17160–17165 (2014).

64. Xiao, Z. *et al.* Efficient, high yield perovskite photovoltaic devices grown by interdiffusion of solution-processed precursor stacking layers. *Energy Environ. Sci.* **7**, 2619–2623 (2014).

65. Zhou, H., Chen, Q. & Yang, Y. Vapor-assisted solution process for perovskite materials and solar cells. *MRS Bull* **40**, 667–673 (2015).

66. Tafazoli, S., Timasi, N., Nouri, E. & Mohammadi, M. R. The role of a vapor-assisted solution process on tailoring the chemical composition and morphology of mixed-halide perovskite solar cells. *CrystEngComm* **20**, 4428–4435 (2018).

67. Kosasih, F. U., Erdenebileg, E., Mathews, N., Mhaisalkar, S. G. & Bruno, A. Thermal evaporation and hybrid deposition of perovskite solar cells and mini-modules. *Joule* **6**, 2692–2734 (2022).

68. Heidrich, R. *et al.* Impact of dynamic co-evaporation schemes on the growth of methylammonium lead iodide absorbers for inverted solar cells. *Sci Rep* **12**, 19167 (2022).

69. Li, J. *et al.* Highly Efficient Thermally Co-evaporated Perovskite Solar Cells and Mini-modules. *Joule* **4**, 1035–1053 (2020).

70. Li, H. *et al.* Sequential vacuum-evaporated perovskite solar cells with more than 24% efficiency. *Sci Adv* **8**, (2022).

71. Niu, Z. *et al.* A cation-regulation strategy for achieving high-performance perovskite solar cells via a fully-evaporation process. *Org Electron* **82**, 105710 (2020).

72. Du, P. *et al.* Thermal Evaporation for Halide Perovskite Optoelectronics: Fundamentals, Progress, and Outlook. *Adv Opt Mater* **10**, (2022).

73. Ponseca, C. S. *et al.* Organometal Halide Perovskite Solar Cell Materials Rationalized: Ultrafast Charge Generation, High and Microsecond-Long Balanced Mobilities, and Slow Recombination. *J Am Chem Soc* **136**, 5189–5192 (2014).

74. Boix, P. P., Raga, S. R. & Mathews, N. Working Principles of Perovskite Solar Cells. in *Halide Perovskites* 81–99 (Wiley, 2018). doi:10.1002/9783527800766.ch2_01.

75. Mora-Seró, I. How Do Perovskite Solar Cells Work? *Joule* **2**, 585–587 (2018).

76. Gonzalez-Pedro, V. *et al.* General Working Principles of $CH_3NH_3PbX_3$ Perovskite Solar Cells. *Nano Lett* **14**, 888–893 (2014).

77. Kumar, A., Gupta, S. K., Dhamaniya, B. P., Pathak, S. K. & Karak, S. Understanding the origin of defect states, their nature, and effects on metal halide perovskite solar cells. *Mater Today Energy* **37**, 101400 (2023).

78. Jin, H. *et al.* It's a trap! On the nature of localised states and charge trapping in lead halide perovskites. *Mater Horiz* **7**, 397–410 (2020).

79. Laxmi, Singh, S. & Kabra, D. Defects in Solution-Processed Perovskite Semiconductors: Photophysics and Impact on Solar Cell Performance. in *Halide Perovskites for Photonics* 8-1-8–34 (AIP Publishing LLCMelville, New York, 2021). doi:10.1063/9780735423633_008.

80. Wang, S., Li, M.-H., Jiang, Y. & Hu, J.-S. Instability of solution-processed perovskite films: origin and mitigation strategies. *Materials Futures* **2**, 012102 (2023).

81. Zhao, W. *et al.* Synchronous Passivation of Defects with Low Formation Energies via Terdentate Anchoring Enabling High Performance Perovskite Solar Cells with Efficiency over 24%. *Adv Funct Mater* **32**, (2022).

82. Pratheek, M., Abhinav, T., Bhattacharya, S., Chandra, G. K. & Predeep, P. Recent progress on defect passivation in perovskites for solar cell application. *Mater Sci Energy Technol* **4**, 282–289 (2021).

83. Min, J., Choi, Y., Kim, D. & Park, T. Beyond Imperfections: Exploring Defects for Breakthroughs in Perovskite Solar Cell Research. *Adv Energy Mater* **14**, (2024).

84. Seshaiah, K. V. & Kim, J. H. Nature of defects and their passivation engineering for advancements in perovskite solar cells. *Chemical Engineering Journal* **492**, 152370 (2024).

85. Bera, S. *et al.* Review of defect engineering in perovskites for photovoltaic application. *Mater Adv* **3**, 5234–5247 (2022).

86. Lu, H., Krishna, A., Zakeeruddin, S. M., Grätzel, M. & Hagfeldt, A. Compositional and Interface Engineering of Organic-Inorganic Lead Halide Perovskite Solar Cells. *iScience* **23**, 101359 (2020).

87. Guo, X. *et al.* Mitigating Surface Deficiencies of Perovskite Single Crystals Enables Efficient Solar Cells with Enhanced Moisture and Reverse-Bias Stability. *Adv Funct Mater* **33**, (2023).

88. Wang, F., Bai, S., Tress, W., Hagfeldt, A. & Gao, F. Defects engineering for high-performance perovskite solar cells. *npj Flexible Electronics* **2**, 22 (2018).

89. Niu, T. *et al.* Stable High-Performance Perovskite Solar Cells via Grain Boundary Passivation. *Advanced Materials* **30**, (2018).

90. Choi, H. *et al.* A Review on Reducing Grain Boundaries and Morphological Improvement of Perovskite Solar Cells from Methodology and Material-Based Perspectives. *Small Methods* **4**, (2020).

91. Yu, H. *et al.* The Role of Chlorine in the Formation Process of "$CH_3NH_3PbI_{3-x}Cl_x$" Perovskite. *Adv Funct Mater* **24**, 7102–7108 (2014).

92. Ran, C., Xu, J., Gao, W., Huang, C. & Dou, S. Defects in metal triiodide perovskite materials towards high-performance solar cells: origin, impact, characterization, and engineering. *Chem Soc Rev* **47**, 4581–4610 (2018).

93. Wu, X., Li, B., Zhu, Z., Chueh, C.-C. & Jen, Alex. K.-Y. Designs from single junctions, heterojunctions to multijunctions for high-performance perovskite solar cells. *Chem Soc Rev* **50**, 13090–13128 (2021).

94. Yang, S., Fu, W., Zhang, Z., Chen, H. & Li, C.-Z. Recent advances in perovskite solar cells: efficiency, stability and lead-free perovskite. *J Mater Chem A Mater* **5**, 11462–11482 (2017).

95. https://resources.system-analysis.cadence.com/blog/msa2021-an-overview-of-the-types-of-perovskite-solar-cells.

96. Meng, L., You, J., Guo, T.-F. & Yang, Y. Recent Advances in the Inverted Planar Structure of Perovskite Solar Cells. *Acc Chem Res* **49**, 155–165 (2016).

97. Duan, H. *et al.* A two-fold interfacial electric-field strategy: boosting the performance of electron transport layer-free perovskite solar cells with low-cost and versatile inorganic acid treatment. *J Mater Chem C Mater* **9**, 12920–12927 (2021).

98. Hui, W. *et al.* Stable Electron-Transport-Layer-Free Perovskite Solar Cells with over 22% Power Conversion Efficiency. *Nano Lett* **23**, 2195–2202 (2023).

99. Zhou, Z. & Pang, S. Highly efficient inverted hole-transport-layer-free perovskite solar cells. *J Mater Chem A Mater* **8**, 503–512 (2020).

100. Sum, T. C. & Mathews, N. Advancements in perovskite solar cells: photophysics behind the photovoltaics. *Energy Environ. Sci.* **7**, 2518–2534 (2014).

101. Xing, G. *et al.* Long-Range Balanced Electron- and Hole-Transport Lengths in Organic-Inorganic $CH_3NH_3PbI_3$. *Science (1979)* **342**, 344–347 (2013).

102. Kalaiselvi, C. R., Muthukumarasamy, N., Velauthapillai, D., Kang, M. & Senthil, T. S. Importance of halide perovskites for next generation solar cells – A review. *Mater Lett* **219**, 198–200 (2018).

103. Chavan, G. T. *et al.* A Brief Review of Transparent Conducting Oxides (TCO): The Influence of Different Deposition Techniques on the Efficiency of Solar Cells. *Nanomaterials* **13**, 1226 (2023).

104. Gong, J., Liang, J. & Sumathy, K. Review on dye-sensitized solar cells (DSSCs): Fundamental concepts and novel materials. *Renewable and Sustainable Energy Reviews* **16**, 5848–5860 (2012).

105. Khelifi, C., Attaf, A., saidi, H., Yahia, A. & Dahnoun, M. Investigation of F doped SnO2 thin films properties deposited via ultrasonic spray technique for several applications. *Surfaces and Interfaces* **15**, 244–249 (2019).

106. Wang, J. *et al.* Application of Indium Tin Oxide/Aluminum-Doped Zinc Oxide Transparent Conductive Oxide Stack Films in Silicon Heterojunction Solar Cells. *ACS Appl Energy Mater* **4**, 13586–13592 (2021).

107. Wang, W. *et al.* Wet-chemical surface texturing of AZO substrate for improved perovskite solar cells. *J Alloys Compd* **963**, 171105 (2023).

108. Hussain, I. *et al.* Functional materials, device architecture, and flexibility of perovskite solar cell. *Emergent Mater* **1**, 133–154 (2018).

109. Liao, Y.-H., Chang, Y.-H., Lin, T.-H., Lee, K.-M. & Wu, M.-C. Recent Advances in Metal Oxide Electron Transport Layers for Enhancing the Performance of Perovskite Solar Cells. *Materials* **17**, 2722 (2024).

110. Du, B., He, K., Tian, G., Che, X. & Song, L. Robust electron transport layers of SnO_2 for efficient perovskite solar cells: recent advances and perspectives. *J Mater Chem C Mater* **11**, 13625–13646 (2023).

111. Wang, K. *et al.* Novel inorganic electron transport layers for planar perovskite solar cells: Progress and prospective. *Nano Energy* **68**, 104289 (2020).

112. Li, S., Cao, Y.-L., Li, W.-H. & Bo, Z.-S. A brief review of hole transporting materials commonly used in perovskite solar cells. *Rare Metals* **40**, 2712–2729 (2021).

113. Huang, D. *et al.* Recent Advances in Nanostructured Inorganic Hole-Transporting Materials for Perovskite Solar Cells. *Nanomaterials* **12**, 2592 (2022).

114. Sajid, S., Alzahmi, S., Salem, I. Ben, Park, J. & Obaidat, I. M. Inorganic hole transport materials in perovskite solar cells are catching up. *Mater Today Energy* **37**, 101378 (2023).

115. Rombach, F. M., Haque, S. A. & Macdonald, T. J. Lessons learned from spiro-OMeTAD and PTAA in perovskite solar cells. *Energy Environ Sci* **14**, 5161–5190 (2021).

116. Wang, Y. *et al.* PTAA as Efficient Hole Transport Materials in Perovskite Solar Cells: A Review. *Solar RRL* **6**, (2022).

117. Nakka, L., Cheng, Y., Aberle, A. G. & Lin, F. Analytical Review of Spiro-OMeTAD Hole Transport Materials: Paths Toward Stable and Efficient Perovskite Solar Cells. *Advanced Energy and Sustainability Research* **3**, (2022).

118. Cheng, M. *et al.* Progress and Application of Halide Perovskite Materials for Solar Cells and Light Emitting Devices. *Nanomaterials* **14**, 391 (2024).

119. Wang, L., Li, G.-R., Zhao, Q. & Gao, X.-P. Non-precious transition metals as counter electrode of perovskite solar cells. *Energy Storage Mater* **7**, 40–47 (2017).

120. Chen, D. *et al.* Ultrahigh fill-factor all-inorganic CsPbBr3 perovskite solar cells processed from two-step solution method and solvent additive strategy. *Journal of Materiomics* **9**, 717–724 (2023).

121. Chang, X. *et al.* Carbon-Based CsPbBr $_3$ Perovskite Solar Cells: All-Ambient Processes and High Thermal Stability. *ACS Appl Mater Interfaces* **8**, 33649–33655 (2016).

122. Jiang, F. *et al.* Metal electrode–free perovskite solar cells with transfer-laminated conducting polymer electrode. *Opt Express* **23**, A83 (2015).

123. Jeon, N. J. *et al.* Compositional engineering of perovskite materials for high-performance solar cells. *Nature* **517**, 476–480 (2015).

124. Zhao, B. *et al.* High Open-Circuit Voltages in Tin-Rich Low-Bandgap Perovskite-Based Planar Heterojunction Photovoltaics. *Advanced Materials* **29**, (2017).

125. Liu, D., Yang, C. & Lunt, R. R. Halide Perovskites for Selective Ultraviolet-Harvesting Transparent Photovoltaics. *Joule* **2**, 1827–1837 (2018).

126. Lei, Y., Chen, Y. & Xu, S. Single-crystal halide perovskites: Opportunities and challenges. *Matter* **4**, 2266–2308 (2021).

127. Juang, S. S.-Y. *et al.* Energy Harvesting Under Dim-Light Condition With Dye-Sensitized and Perovskite Solar Cells. *Front Chem* **7**, (2019).

128. Saliba, M. *et al.* Cesium-containing triple cation perovskite solar cells: improved stability, reproducibility and high efficiency. *Energy Environ Sci* **9**, 1989–1997 (2016).

129. Raifuku, I. *et al.* Segregation-free bromine-doped perovskite solar cells for IoT applications. *RSC Adv* **9**, 32833–32838 (2019).

130. Yaghoobi Nia, N., Saranin, D., Palma, A. L. & Di Carlo, A. Perovskite solar cells. in *Solar Cells and Light Management* 163–228 (Elsevier, 2020). doi:10.1016/B978-0-08-102762-2.00005-7.

131. Xu, J. *et al.* Key Parameters and Thresholds Values for Obtaining High Performance Perovskite Solar Cells Indoors from Full Br Compositional and Bandgap Engineering. *ACS Appl Energy Mater* **6**, 10215–10224 (2023).

132. Skafi, Z. *et al.* Highly Efficient Flexible Perovskite Solar Cells on Polyethylene Terephthalate Films via Dual Halide and Low-Dimensional Interface Engineering for Indoor Photovoltaics. *Solar RRL* **7**, (2023).

133. Srathongsian, L. *et al.* Cs and Br tuning to achieve ultralow-hysteresis and high-performance indoor triple cation perovskite solar cell with low-cost carbon-based electrode. *iScience* **27**, 109306 (2024).

134. Mica, N. A. *et al.* Triple-cation perovskite solar cells for visible light communications. *Photonics Res* **8**, A16 (2020).

135. Yang, F. *et al.* Enhancement of exciton separation in indoor perovskite photovoltaics by employing conjugated organic chromophores. *J Power Sources* **520**, 230785 (2022).

136. Penpong, K. *et al.* Robust perovskite formation via vacuum thermal annealing for indoor perovskite solar cells. *Sci Rep* **13**, 10933 (2023).

137. Dong, C. *et al.* Annealing-free perovskite films by EDOT-assisted anti-solvent strategy for flexible indoor and outdoor photovoltaics. *Nano Energy* **94**, 106866 (2022).

138. Lee, M. *et al.* Enhanced Hole-Carrier Selectivity in Wide Bandgap Halide Perovskite Photovoltaic Devices for Indoor Internet of Things Applications. *Adv Funct Mater* **31**, (2021).

139. Li, C. *et al.* High-performance pulse light stable perovskite indoor photovoltaics. *Sci Bull (Beijing)* **69**, 334–344 (2024).

140. Dong, C. *et al.* Lycopene-Based Bionic Membrane for Stable Perovskite Photovoltaics. *Adv Funct Mater* **31**, (2021).

141. Asada, T. *et al.* Influence of the Electron Transport Layer on the Performance of Perovskite Solar Cells under Low Illuminance Conditions. *ACS Omega* (2024) doi:10.1021/acsomega.4c03643.

142. Wali, Q. *et al.* Fundamentals of Hysteresis in Perovskite Solar Cells: From Structure-Property Relationship to Neoteric Breakthroughs. *The Chemical Record* **22**, (2022).

143. Wu, F., Pathak, R. & Qiao, Q. Origin and alleviation of J-V hysteresis in perovskite solar cells: A short review. *Catal Today* **374**, 86–101 (2021).

144. Wu, F. *et al.* Inverted Current–Voltage Hysteresis in Perovskite Solar Cells. *ACS Energy Lett* **3**, 2457–2460 (2018).

145. Pavu, K. S., Jacob, J. & Arun, A. V. Modeling of Hysteresis in Perovskite Solar Cells: An Overview. in *Handbook of Emerging Materials for Semiconductor Industry* 391–407 (Springer Nature Singapore, Singapore, 2024). doi:10.1007/978-981-99-6649-3_28.

146. Chen, B., Yang, M., Priya, S. & Zhu, K. Origin of J – V Hysteresis in Perovskite Solar Cells. *J Phys Chem Lett* **7**, 905–917 (2016).

147. Singh, R. & Parashar, M. Origin of Hysteresis in Perovskite Solar Cells. in *Soft-Matter Thin Film Solar Cells* 1-1-1–42 (AIP Publishing LLCMelville, New York, 2020). doi:10.1063/9780735422414_001.

148. Tress, W. *et al.* Understanding the rate-dependent J–V hysteresis, slow time component, and aging in $CH_3NH_3PbI_3$ perovskite solar cells: the role of a compensated electric field. *Energy Environ Sci* **8**, 995–1004 (2015).

149. Kang, D. & Park, N. On the Current–Voltage Hysteresis in Perovskite Solar Cells: Dependence on Perovskite Composition and Methods to Remove Hysteresis. *Advanced Materials* **31**, (2019).

150. Luo, J. *et al.* The novel dopant for hole-transporting material opens a new processing route to efficiently reduce hysteresis and improve stability of planar perovskite solar cells. *J Power Sources* **342**, 886–895 (2017).

151. Luo, J. *et al.* Toward high-efficiency, hysteresis-less, stable perovskite solar cells: unusual doping of a hole-transporting material using a fluorine-containing hydrophobic Lewis acid. *Energy Environ Sci* **11**, 2035–2045 (2018).

152. Dagar, J., Castro-Hermosa, S., Lucarelli, G., Cacialli, F. & Brown, T. M. Highly efficient perovskite solar cells for light harvesting under indoor illumination via solution processed SnO2/MgO composite electron transport layers. *Nano Energy* **49**, 290–299 (2018).

153. Saranin, D. *et al.* Hysteresis-free perovskite solar cells with compact and nanoparticle NiO for indoor application. *Solar Energy Materials and Solar Cells* **227**, 111095 (2021).

154. Bulloch, A., Wang, S., Ghosh, P. & Jagadamma, L. K. Hysteresis in hybrid perovskite indoor photovoltaics. *Philosophical Transactions of the Royal Society A: Mathematical, Physical and Engineering Sciences* **380**, (2022).

155. Han, E. *et al.* High-Performance Indoor Perovskite Solar Cells by Self-Suppression of Intrinsic Defects via a Facile Solvent-Engineering Strategy. *Small* **20**, (2024).

156. Sen, S., Gopalan, S., Sellappan, R., Grace, A. N. & Sonar, P. Tin-Based Eco-Friendly Perovskites for Sustainable Future. *Advanced Energy and Sustainability Research* **4**, (2023).

157. Meng, L., You, J. & Yang, Y. Addressing the stability issue of perovskite solar cells for commercial applications. *Nat Commun* **9**, 5265 (2018).

158. Li, J. *et al.* Encapsulation of perovskite solar cells for enhanced stability: Structures, materials and characterization. *J Power Sources* **485**, 229313 (2021).

159. Belisle, R. A. *et al.* Impact of Surfaces on Photoinduced Halide Segregation in Mixed-Halide Perovskites. *ACS Energy Lett* **3**, 2694–2700 (2018).

160. Brennan, M. C., Draguta, S., Kamat, P. V. & Kuno, M. Light-Induced Anion Phase Segregation in Mixed Halide Perovskites. *ACS Energy Lett* **3**, 204–213 (2018).

161. Muhammad, B. T., Kar, S., Stephen, M. & Leong, W. L. Halide perovskite-based indoor photovoltaics: recent development and challenges. *Mater Today Energy* **23**, 100907 (2022).

162. Zai, H., Ma, Y., Chen, Q. & Zhou, H. Ion migration in halide perovskite solar cells: Mechanism, characterization, impact and suppression. *Journal of Energy Chemistry* **63**, 528–549 (2021).

163. Guo, Z. *et al.* Understanding Defects in Perovskite Solar Cells through Computation: Current Knowledge and Future Challenge. *Advanced Science* **11**, (2024).

164. Njema, G. G., Kibet, J. K. & Ngari, S. M. A review of interface engineering characteristics for high performance perovskite solar cells. *Measurement: Energy* **2**, 100005 (2024).

165. Zhao, C., Zhang, H., Krishna, A., Xu, J. & Yao, J. Interface Engineering for Highly Efficient and Stable Perovskite Solar Cells. *Adv Opt Mater* **12**, (2024).

166. Wu, Y., Wang, D., Liu, J. & Cai, H. Review of Interface Passivation of Perovskite Layer. *Nanomaterials* **11**, 775 (2021).

167. Garai, R., Gupta, R. K. & Iyer, P. K. Trap State Passivation for Stabilizing Perovskite Solar Cells via Multifunctional Molecules. *Acc Mater Res* **4**, 560–565 (2023).

168. Ann, M. H. *et al.* Device design rules and operation principles of high-power perovskite solar cells for indoor applications. *Nano Energy* **68**, 104321 (2020).

169. Zhao, P., Kim, B. J. & Jung, H. S. Passivation in perovskite solar cells: A review. *Mater Today Energy* **7**, 267–286 (2018).

170. Lim, K., Ji, S. G., Kim, J. Y. & Lee, T. Effect of Interfacial Layers on the Device Lifetime of Perovskite Solar Cells. *Small Methods* **4**, (2020).

171. Ali, J. *et al.* Interfacial and structural modifications in perovskite solar cells. *Nanoscale* **12**, 5719–5745 (2020).

172. Yang, S. *et al.* Tailoring Passivation Molecular Structures for Extremely Small Open-Circuit Voltage Loss in Perovskite Solar Cells. *J Am Chem Soc* **141**, 5781–5787 (2019).

173. Wang, R. *et al.* Constructive molecular configurations for surface-defect passivation of perovskite photovoltaics. *Science (1979)* **366**, 1509–1513 (2019).

174. Xia, J. *et al.* Deep surface passivation for efficient and hydrophobic perovskite solar cells. *J Mater Chem A Mater* **9**, 2919–2927 (2021).

175. Li, Z. *et al.* Minimized surface deficiency on wide-bandgap perovskite for efficient indoor photovoltaics. *Nano Energy* **78**, 105377 (2020).

176. Ullah, S. *et al.* All-inorganic CsPbBr $_3$ perovskite: a promising choice for photovoltaics. *Mater Adv* **2**, 646–683 (2021).

177. Kim, S.-G. *et al.* Photo-doping of spiro-OMeTAD for highly stable and efficient perovskite solar cells. *Joule* **8**, 1707–1722 (2024).

178. Jena, A. K., Numata, Y., Ikegami, M. & Miyasaka, T. Role of spiro-OMeTAD in performance deterioration of perovskite solar cells at high temperature and reuse of the perovskite films to avoid Pb-waste. *J Mater Chem A Mater* **6**, 2219–2230 (2018).

179. Caliò, L., Salado, M., Kazim, S. & Ahmad, S. A Generic Route of Hydrophobic Doping in Hole Transporting Material to Increase Longevity of Perovskite Solar Cells. *Joule* **2**, 1800–1815 (2018).

180. Hatamvand, M. *et al.* The role of different dopants of Spiro-OMeTAD hole transport material on the stability of perovskite solar cells: A mini review. *Vacuum* **214**, 112076 (2023).

181. Fu, Q. *et al.* Ionic Dopant-Free Polymer Alloy Hole Transport Materials for High-Performance Perovskite Solar Cells. *J Am Chem Soc* **144**, 9500–9509 (2022).

182. Habisreutinger, S. N., Wenger, B., Snaith, H. J. & Nicholas, R. J. Dopant-Free Planar n–i–p Perovskite Solar Cells with Steady-State Efficiencies Exceeding 18%. *ACS Energy Lett* **2**, 622–628 (2017).

183. Li, W. *et al.* Montmorillonite as bifunctional buffer layer material for hybrid perovskite solar cells with protection from corrosion and retarding recombination. *J. Mater. Chem. A* **2**, 13587–13592 (2014).

184. Ito, S., Tanaka, S., Manabe, K. & Nishino, H. Effects of Surface Blocking Layer of Sb $_2$ S $_3$ on Nanocrystalline TiO $_2$ for CH $_3$ NH $_3$ PbI $_3$ Perovskite Solar Cells. *The Journal of Physical Chemistry C* **118**, 16995–17000 (2014).

185. Lin, C. *et al.* Electrode Engineering in Halide Perovskite Electronics: Plenty of Room at the Interfaces. *Advanced Materials* **34**, (2022).

186. Shen, Y., Deng, K. & Li, L. Spiro-OMeTAD-Based Hole Transport Layer Engineering toward Stable Perovskite Solar Cells. *Small Methods* **6**, (2022).

187. Du, G. *et al.* Evaporated Undoped Spiro-OMeTAD Enables Stable Perovskite Solar Cells Exceeding 20% Efficiency. *Adv Energy Mater* **12**, (2022).

188. Toikkonen, S. *et al.* Is Doping of Spiro-OMeTAD a Requirement for Efficient and Stable Perovskite Indoor Photovoltaics? *Advanced Devices & Instrumentation* **5**, (2024).

189. Su, P. *et al.* Pb-Based Perovskite Solar Cells and the Underlying Pollution behind Clean Energy: Dynamic Leaching of Toxic Substances from Discarded Perovskite Solar Cells. *J Phys Chem Lett* **11**, 2812–2817 (2020).

190. Rahman, S. U. *et al.* Toxic effects of lead (Pb), cadmium (Cd) and tetracycline (TC) on the growth and development of Triticum aestivum: A meta-analysis. *Science of The Total Environment* **904**, 166677 (2023).

191. Farooq, U. *et al.* Bandgap engineering of lead-free ternary halide perovskites for photovoltaics and beyond: Recent progress and future prospects. *Nano Energy* **92**, 106710 (2022).

192. Aktas, E. *et al.* Challenges and strategies toward long-term stability of lead-free tin-based perovskite solar cells. *Commun Mater* **3**, 104 (2022).

193. Babayigit, A. *et al.* Assessing the toxicity of Pb- and Sn-based perovskite solar cells in model organism Danio rerio. *Sci Rep* **6**, 18721 (2016).

194. Zhang, Z. *et al.* The importance of elemental lead to perovskites photovoltaics. *Chemistry of Inorganic Materials* **1**, 100017 (2023).

195. Schileo, G. & Grancini, G. Lead or no lead? Availability, toxicity, sustainability and environmental impact of lead-free perovskite solar cells. *J Mater Chem C Mater* **9**, 67–76 (2021).

196. Podapangi, S. K. *et al.* Green solvents, materials, and lead-free semiconductors for sustainable fabrication of perovskite solar cells. *RSC Adv* **13**, 18165–18206 (2023).

197. Passatorntaschakorn, W. *et al.* Sustainable Planar Hole-Transporting Material-Free Carbon Electrode-Based Perovskite Solar Cells: Stability Beyond Two Years. *ACS Appl Energy Mater* **7**, 6972–6985 (2024).

198. Naikaew, A. *et al.* Photoexcitation of perovskite precursor solution to induce high-valent iodoplumbate species for wide bandgap perovskite solar cells with enhanced photocurrent. *Sci Rep* **13**, 6125 (2023).

Chapter 3

Materials and Methods

This chapter provides a comprehensive overview of the materials and methods used for solar cells fabrication and characterizations, which are summarized in the subsequent studies. Since most of the functional layers used across the studies are the same, it is important to note that these studies were conducted in two different research groups. While some of the materials are sourced from different companies in each group, the product types remain similar. To avoid confusion for the readers, the materials and their corresponding details will not be presented in a single table; instead, they will be outlined within the context of each study's fabrication approach.

3.1 A Brief Overview of Synthesis and Characterization Approaches

In this thesis, total of two studies are conducted, involving the fabrication of conventional planar n-i-p structure devices based on SnO_2 ETL. In both studies, the device architectures are almost identical, with only minor differences. The first study incorporates different passivation layers between the absorber triple cation PVK and a higher concentration of Spiro-OMeTAD, which is doped with LiTFSI and tBP. In contrast, the second study utilizes a similar device architecture but omits the passivation layer and employs a lower concentration of Spiro-OMeTAD doped with FK209 in addition to LiTFSI and tBP. Additionally, the apparatuses and equipment models used for the characterization of films and devices in the first study differ from those used in the second study.

3.2 Study 1st : Passivation Layers Incorporation in Device Structure

3.2.1 Materials

SnO_2 colloid precursor (tin (IV) oxide, 15% in H_2O colloidal dispersion) was purchased from Alfa Aesar. DMF (99.8%), DMSO (99.5%), Toluene and Anisole were purchased from Sigma Aldrich. Formamidinium iodide (FAI) (99.99%), and methylammonium bromide (MABr) (99.9%) were purchased from Greatcell solar. Cesium iodide (CsI) (99.99%) was purchased from Sigma Aldrich. PbI_2 and lead bromide ($PbBr_2$) were purchased from TCI. PEAI), OAI, GUI and the Spiro-OMeTAD (≥99.8%) were purchased from Borun NewMaterial Technology Ltd. DPPP was synthesized and provided from the University of Toledo (OH). tBP and LiTFSI were purchased from Sigma-Aldrich. All the purchased materials were used without further purification. Glass/ITO substrates (10 Ω sq^{-1}) were purchased from Kintec.

3.2.2 Perovskite Solution

A triple-cation narrow bandgap PVK with the composition $Cs_{0.08}FA_{0.80}MA_{0.12}Pb(I_{0.88}Br_{0.12})_3$, and with a concentration of 1.38M, was prepared as follows: 25.98 mg of CsI, 17.90 mg of MABr, 58.70 mg of $PbBr_2$, 178.85 mg of FAI, and 548.6 mg of PbI_2 were mixed in a vial containing 1 mL of a 4:1 DMF:DMSO volume ratio, and stirred overnight in the glovebox environment at room temperature.

3.2.3 Passivation Solutions

The solutions of different passivation layers deposited on top of absorber triple cation PVK in this study were prepared as follows: PEAI solution was prepared by dissolving 5 mg of PEAI in 1 mL of isopropanol, GUI solution was prepared by dissolving 3 mg of GUI in 1 mL of isopropanol, OAI solution was prepared by dissolving 3 mg of OAI in 1 mL of isopropanol, and DPPP solution was prepared by dissolving 2 mg of DPPP in 1 mL of isopropanol. All the solutions were stirred overnight in a glovebox before use.

3.2.4 Spiro-OMeTAD Solution

The Spiro-OMeTAD solution was prepared by dissolving 70 mg of spiro precursor in 1 mL of toluene. The solution, which had been stirred overnight, was further doped 2 hours before use by adding 17.5 µl of LiTFSI and 28.5 µl of tBP.

3.2.5 Devices Fabrication

Initially, glass/ ITO substrates underwent patterning using a UV ns laser (Spectra Physics - Andover, MA, USA) and were diced with a glass cutter (Dyenamo – Stockholm, Sweden). Subsequently, the patterned glass/ITO substrates (25 mm × 25 mm) underwent a systematic cleaning process by scrubbing with a water and soap solution (Hellmanex 2% in deionized water) and were cleaned through three stages of an ultrasonic bath: first in water and soap, then in deionized water, and finally in isopropanol (IPA), each for a duration of 15 minutes. The cleaned substrates were then dried with a nitrogen purge and subjected to UV–ozone treatment for 30 minutes.

For the fabrication of ITO/SnO_2/$Cs_{0.08}FA_{0.80}MA_{0.12}Pb(I_{0.88}Br_{0.12})_3$/Passivation/Spiro-OMeTAD/Au devices, SnO_2 precursor solution was prepared by combining SnO_2 (15% in H_2O colloidal dispersion) with deionized water (1:3, v:v), followed by sonicating for 10 minutes. Subsequently, the SnO_2 solution was spin-coated onto the glass/ITO substrate at 3000 rpm for 30

seconds in an ambient air environment and annealed at 100 °C for 30 minutes. Prior to the PVK deposition, the SnO_2 coated glass/ITO substrates underwent UV treatment in UV/O_3 tool (Novasonic) for 30 mins to improve their wettability. After the UV treatment, the SnO_2 coated glass/ITO substrates were transferred to the nitrogen filled glovebox. Before using for deposition, the prepared PVK solution was filtered through 0.45µm PVDF filter to remove any undissolved particles or impurities that may be present in the solution. After filtering the solution, 100 µL of the PVK precursor solution was spin-coated onto glass/ITO/SnO_2 substrates using a two-step program (1000 rpm for 10 s, followed by 5000 rpm for 21 s). Additionally, 150 µL of green anisole, serving as an antisolvent, was applied 6 s before the completion of the second step of the spin-coating program, , as schematically illustrated in the **Figure 3.1(a)**.

In the case of devices where DPPP is first incorporated into the absorber's triple-cation PVK bulk and then post-deposited as a passivation layer, the fabrication process was slightly modified as follows: To incorporate DPPP into the bulk of PVK, the DPPP solution was first mixed with the antisolvent anisole. This mixed solution was then dripped onto the perovskite during spinning, at the antisolvent dripping stage. Afterward, the prepared films, with and without DPPP were annealed at 100°C for 30 mins.

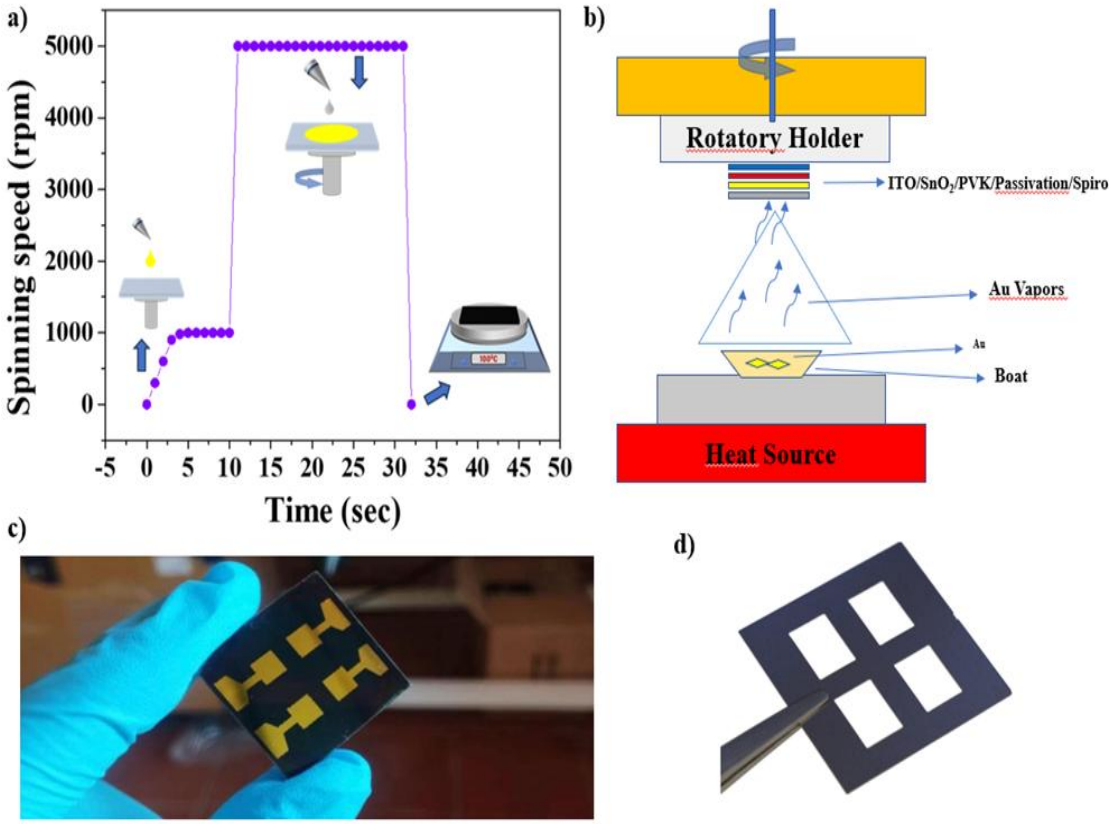

Figure 3.1. a) Schematic illustration of two step spin coating program for absorber triple cation PVK deposition, b) schematic illustration of Au deposition, c) picture of a final device, d) the schematic of a metallic mask.

Subsequently, all the passivation layers (OAI, GUI, PEAI, DPPP) were dynamically deposited on top of the PVK films (without DPPP) via a spin-coating (2500 rpm for 30 s) process. While for the PVK films (with DPPP), only DPPP passivation layer was applied via a spin-coating (2500 rpm for 30 s) process.

After the deposition of passivation layers, the substrates underwent annealing on hotplate at 100°C for 10 minutes. Thereafter, Spiro-OMeTAD doped with tBP and LiTFSI was deposited dynamically with spin-coating method (3000 rpm for 30 s), followed by oxidation in the dryer for 12 h. Finally, 80 nm-thick Au back contacts were deposited by thermal evaporation in a high vacuum chamber (10^{-6} mbar), using a shadow mask to separate the four cells that were fabricated on each substrate. Schematic illustration of Au evaporation is provided in **Figure 3.1(b)** while the picture of final device is provided in **Figure 3.1(c)**. In addition, **Figure 3.2** schematically illustrate the entire fabrication process of devices prepared for the 1st study related to the incorporation of passivation layers into the device structure.

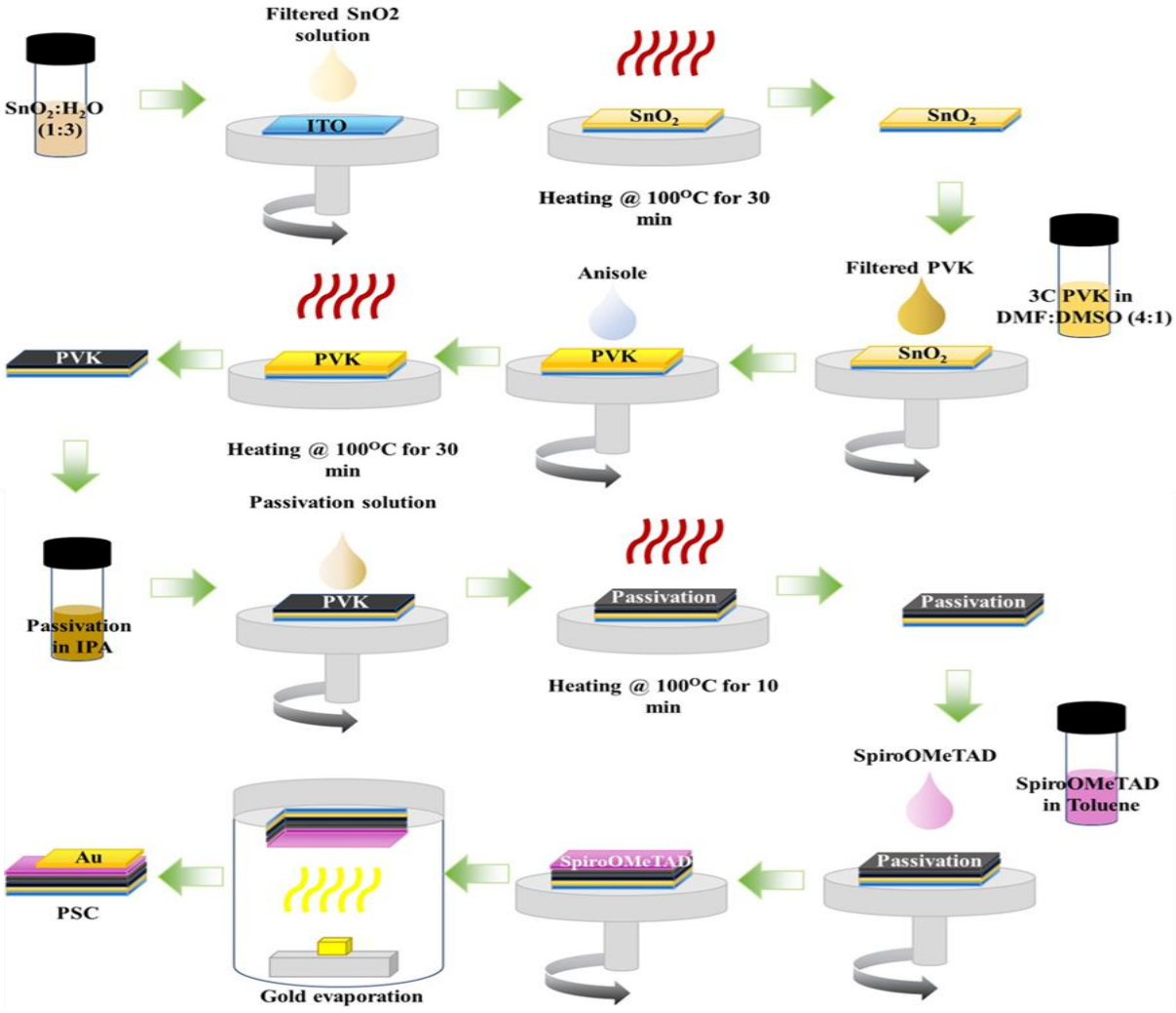

Figure 3.2. Schematic illustration of entire device fabrication for the evaluation of passivation layers study.

3.3 Study 2nd : Fabrication of Devices with Doped- and Undoped-Spiro-OMeTAD

3.3.1 Materials

SnO_2 colloid precursor (tin (IV) oxide, 15% in H_2O colloidal dispersion) was purchased from Alfa Aesar. FAI, MABr were acquired from Greatcell Solar Materials. ($PbBr_2$, >98%) and (PbI_2, >98%) were sourced from TCl, while CsI was acquired from abcr. (DMSO, anhydrous, ≥99.9%), (DMF, anhydrous, 99.8%), chlorobenzene (anhydrous, 99.8%), acetonitrile (99.9%), tBP (98%), Li-TFSI (99.95%) and Anisole (anhydrous, 99.7%) were purchased from Sigma-Aldrich. Spiro-OMeTAD (>99.5%) was obtained from Lumtec, and FK209 Co(III) (>95%) from Dyenamo. All reagents and solvents were used as received, without further purification.

3.3.2 Absorber Triple Cation PVK Solution

The absorber triple cation PVK solution used in this study was prepared inside a glovebox, as shown in the **Figure 3.3**. For the preparation of absorber triple cation PVK, the exact protocol is followed previously described for the preparation of triple cation PVK solution in the study of incorporating passivation layers into the device structure.

Figure 3.3. The glovebox used for the fabrication of PSCs at the University of Tampere, Finland.

3.3.3 Preparation of Dopants Solutions for Spiro-OMeTAD

In this study, three dopants were used: tBP, Li-TFSI, and FK209 Co(III). A pre-prepared tBP solution was sourced from a supplier, while the solutions for the other two dopants were prepared in the lab and inside the glovebox as follows: The Li-TFSI solution was prepared by dissolving 520 mg of Li-TFSI in 1 mL of acetonitrile in a clean vial containing a magnetic stir bar. The solution was stirred overnight at room temperature. Similarly, the FK209 Co(III) solution was prepared by dissolving 300 mg of FK209 Co(III) precursor in 1 mL of acetonitrile in a clean vial with a magnetic stir bar, and it was also stirred overnight at room temperature.

3.3.4 Doped and Undoped Spiro-OMeTAD Solutions Preparation

The Spiro-OMeTAD solutions were prepared by dissolving 36.2 mg of spiro precursor in 1 mL of chlorobenzene in two separate, clean vials, each with a magnetic stir bar. The solutions were stirred for one hour at 70°C to fully dissolve the Spiro-OMeTAD precursor. Once dissolved, both vials were removed from the heating stirrer and placed in a vial holder to cool to glovebox temperature (approximately 23°C). When cooled, 14.4 µL of tBP, 8.8 µL of Li-TFSI, and 14.5 µL of FK209 Co(III) were added to 1 mL of the spiro solution in one of the vials, and the mixture was stirred for an additional 10 to 20 minutes at room temperature, without heating. The solution in the other vial was used undoped, after cooling to room temperature.

3.3.5 Device Fabrication

In this study, the device fabrication protocol was nearly identical to that previously described for investigating the incorporation of passivation layers into the device architecture. However, there were some minor differences, which are outlined below.

Firstly, devices were fabricated on pre-etched ITO-coated glass substrates (OPV Tech) with dimensions of 2.54 cm × 2.54 cm × 0.22 cm. The substrates were cleaned by brushing with a 2% (v/v) Mucasol solution in deionized water, followed by sonication in deionized water, acetone, and 2-propanol for 15 minutes each. After sonication, the substrates were dried using a nitrogen (N_2) flow and subsequently underwent UV ozone treatment for 30 minutes.

Following UV treatment, a SnO_2 solution was deposited onto the glass/ITO substrates, following the same deposition protocol as described earlier in the device fabrication section for the passivation layer study. After annealing and post-UV treatment, the glass/ITO/SnO_2-coated substrates were transferred to a glovebox (as shown in **Figure 3.3**) for the deposition of the triple-

cation PVK absorber layer. The protocol for depositing the triple-cation PVK absorber layer was identical to that previously described for the study of passivation layer incorporation.

Once the glass/ITO/SnO_2/PVK-coated substrates were annealed at 100°C for 30 minutes and cooled to room temperature, 80 μL of either doped or undoped Spiro-OMeTAD solution was dynamically spin-coated onto the substrates at 1,800 rpm for 30 seconds.

To complete the device fabrication, Au layer, 80–100 nm thick, was thermally evaporated onto the samples using an OPTIvap Vacuum Deposition Tool (MBraun) under vacuum (pressure < 10^{-6} mbar) with a metal shadow mask defining an active area of 12 mm^2. The final device pictures from both glass/ITO and Au side, are illustrated in **Figure 3.4(a)** and **Figure 3.4(b)**, respectively.

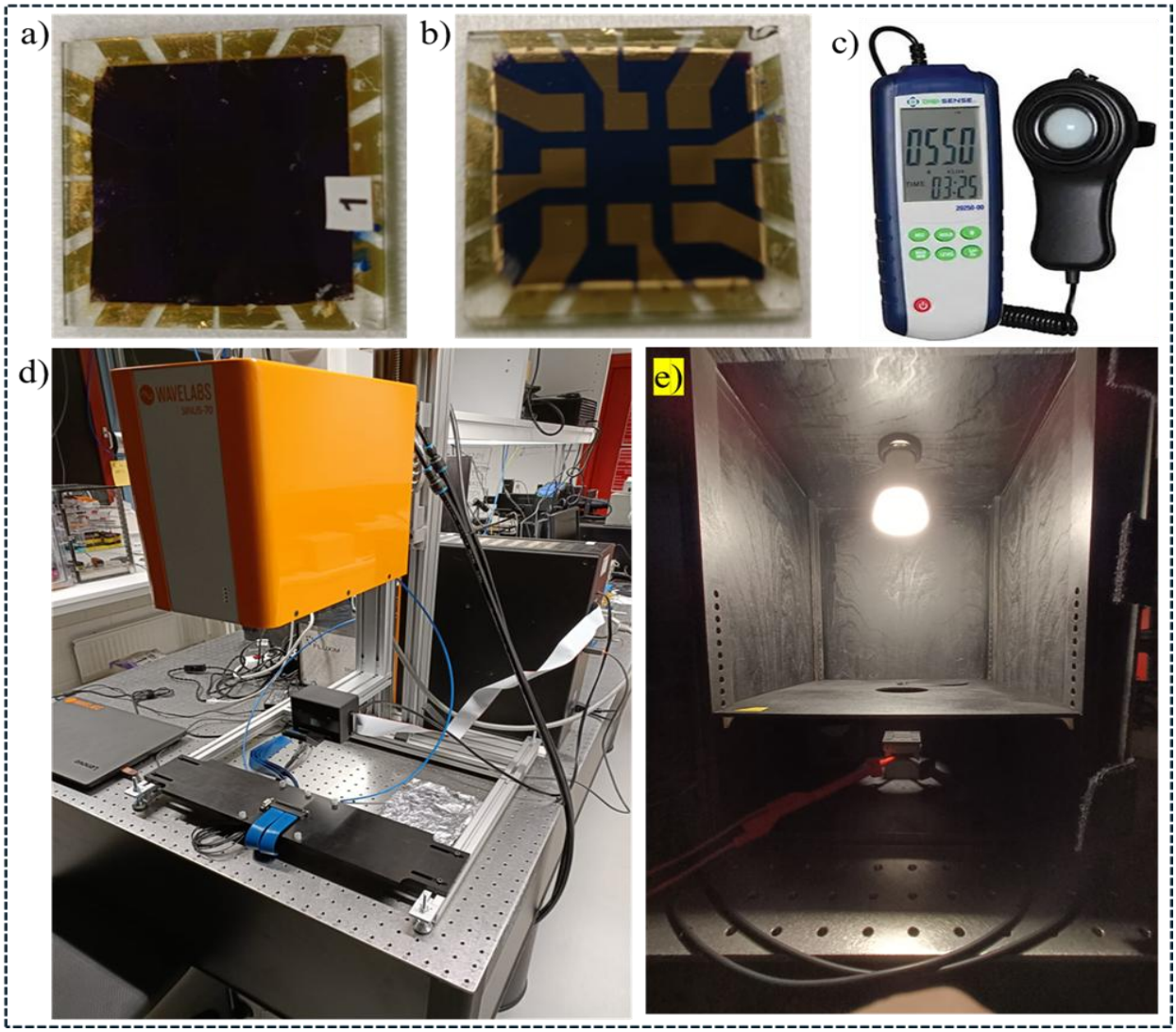

Figure 3.4. a) Image of a triple-cation PVK-based device from the glass/ITO side. b) Image of a triple-cation PVK-based device from the Au side. c) Digi-Sense lux meter. d) Litos Lite system (FLUXiM AG, Switzerland) used for device measurements under 1-sun illumination, and e) black box setup for J-V measurements under indoor illumination at the University of Tampere, Finland.

Moreover, **Figure 3.5** schematically illustrates the complete fabrication process used for the study to evaluate the influence of Spiro-OMeTAD dopants on device performance under low-light indoor illumination.

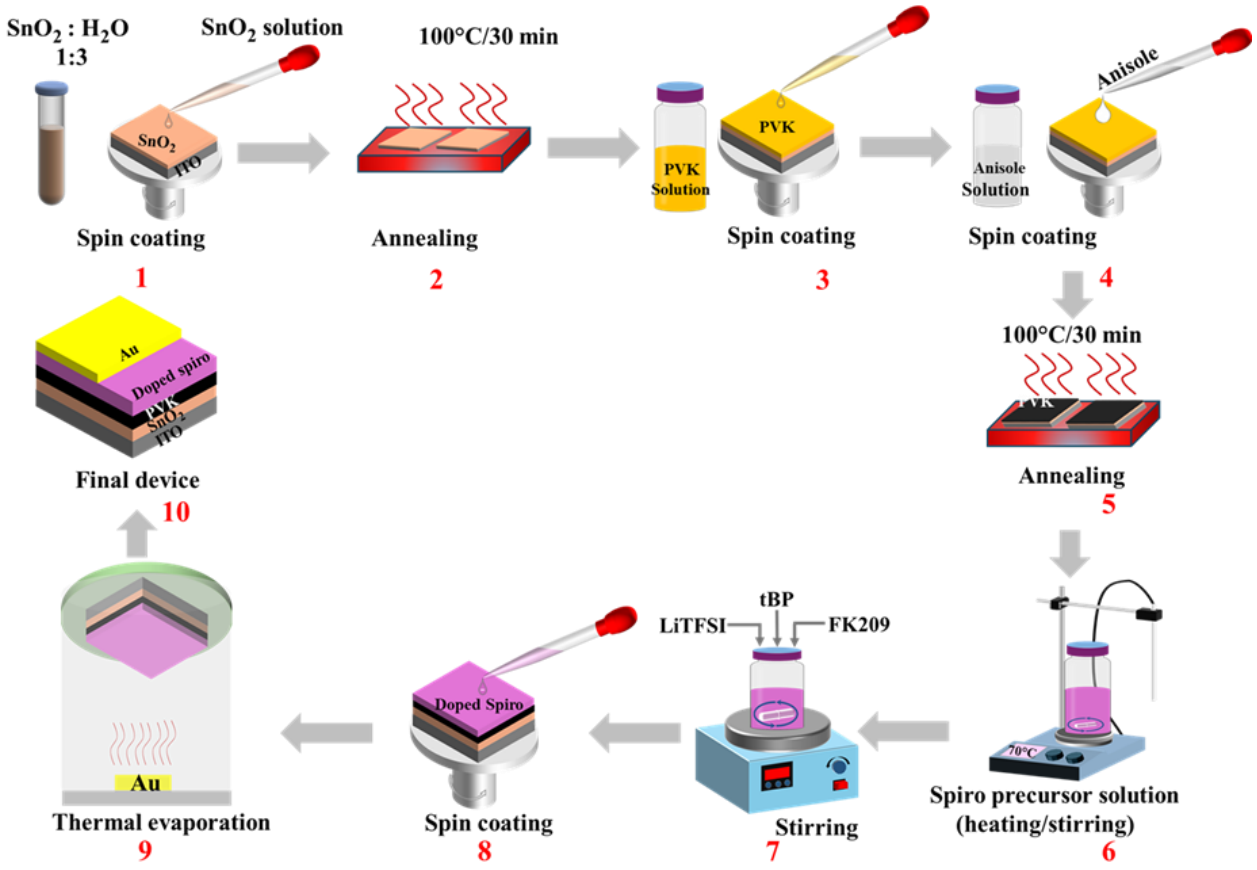

Figure 3.5. Schematic illustration of device fabrication in the study of evaluating the influence of spiro-OMeTAD dopants on device performance under low-light indoor illumination.

3.4 Structural Investigation

3.4.1 X-ray Diffraction (XRD)

XRD measurements were conducted using a Rigaku SmartLab diffractometer operating in (θ–2θ) Bragg–Brentano geometry. The instrument was equipped with a Cu X-ray source, providing Kα radiation at 1.54056 Å, along with a D/teX Ultra 250 silicon strip detector. XRD spectra were collected over a 5° to 60° 2θ range in a single scan, with a step size of 0.01° and a scan speed of 20 °/min.

3.4.2 Scanning Electron Microscopy (SEM)

In study of investigating passivation layers influence on device performance under indoor illumination, a Field-Emission Gun SEM (FEG-SEM LEO 35, Zeiss) was used for morphological characterization of the films. Both the planar view and cross-sectional SEM images were collected

using an In-Lens type-I secondary electron (SE1) detector, with an electron beam energy of 5 (or 3) keV and a working distance of 4 (or 3) mm for planar view (or cross sectional) analysis. The film cross-sections were prepared for SEM analysis by scribing the backside of the substrate with a diamond tip and fracturing the sample, ensuring that the film cross-section intended for observation remained undamaged. These samples were then directly mounted on the stubs for the SEM analysis without any additional polishing or coating deposition. For each sample, several regions (with area varying between 200 and 2000 μm^2) were analyzed changing the magnification settings and two representative images (in cross-sectional and planar view) were chosen and reported in this work.

3.5 Optical measurements

3.5.1 Optical properties

The absorption spectra of doped and undoped Spiro-OMeTAD films deposited on glass substrates, were measured using a dual-beam grating Shimadzu UV-1800 absorption spectrometer (Shimadzu Corporation, Kyoto, Japan).

3.5.2 Photoluminescence (PL) Spectroscopy

The micro-PL spectra are detected with a custom-made microscope setup in a backscattering configuration. The samples are placed on an x-y translation stage (Physik Instruments) to scan the sample surface with fine control on the position of about 250 nm. The excitation sources are a CW diode-pumped solid-state laser emitting at 532 nm (CNI MLL-III-532) and a mode-locked Ti:Sapphire tunable laser (Spectra Physics Tsunami, 700-900 nm spectral range, 200 fs pulse duration, 12.2 ns repetition period). The photoluminescence from the samples is collected by an infinity corrected Mitutoyo 100× objective lens (NIR, NA = 0.7), separated from the excitation by a dichroic mirror, spectrally dispersed by a spectrograph (Acton SP2300i) mounting a 600 gr/mm grating blazed at 1000 nm. The luminescence is detected using a Si CCD Acton Pixis 100F. The spatial resolution of the system was about 700 nm, while the spectral resolution was about 400 μeV. Time-resolved PL (TR-PL) measurements were performed using the time-correlated single photon counting (TCSPC) technique. The excitation source was provided by the pulsed Ti:Sapphire described above. The spectrally dispersed luminescence was selected using the exit slit of the spectrograph and sent to a PerkinElmer SPCM-AQR-16 single photon counting APD. The signal of the APD was analyzed by a time correlator (ID Quantique ID900) interfaced with the PC. The time resolution of the system is about 400 ps.

3.6 Electrical measurements

3.6.1 Current-voltage characteristics

In the study of evaluating passivation layers influence on the performance of PSCs, J–V curves under standard one sun illumination for Reference and passivated devices were acquired using an ABET Sun 2000 class A simulator, calibrated with an Eko MS-602 pyranometer for AM 1.5G sun illumination. The calibration accuracy was verified by measuring the EQE (Arkeo system from Cicci Research, Grosseto, Italy), ensuring that the mismatch between the integrated and measured J_{sc} was less than 2%. Indoor J–V measurements of devices were achieved using a customized home-built installation, as can be seen in **Figure 3.6**, with a detailed description available in reference [1].

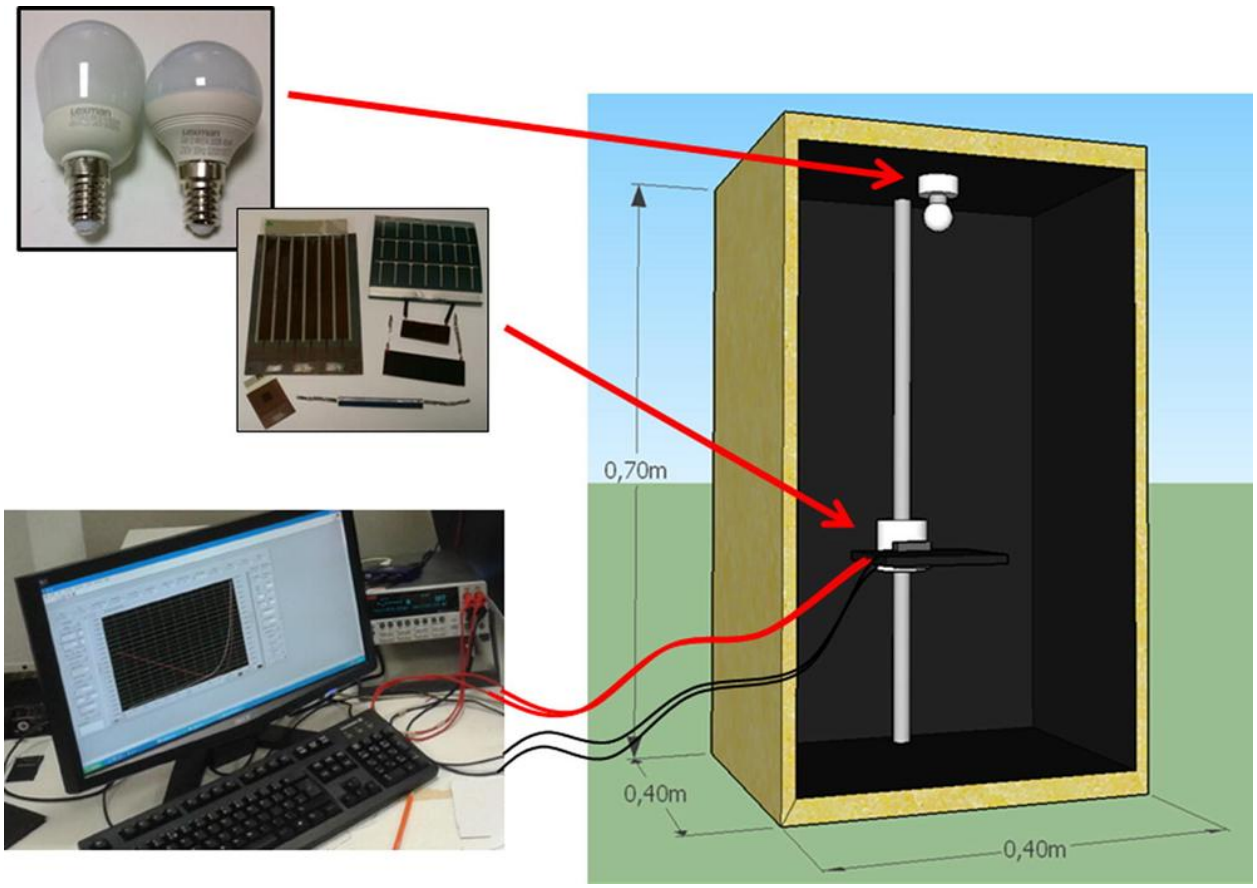

Figure 3.6. Schematics of the setup for *I–V* measurements under indoor illumination in Cenetr for Hybrid and Organic Solar Energy (CHOSE), at the University of Rome Tor Vergata, Rome, Italy [1].

This setup featured a white cold LED (Osram Parathom Classic P25) as the light source. Adjusting the distance between the devices and the LED light source allow specific illuminance levels (e.g., 200, 400, 500, and 1000 lx). Prior to each indoor J-V measurement, the illuminance was calibrated using a luxmeter (NIST-traceable calibrated Digisense 20250-00) to measure at 1000 lx. The spectral irradiance was measured by using AvaSpec-ULS2048CL-EVO spectrometer, calibrated

with a NIST (National Institute of Standards and Technology)-traceable halogen light source (AvaLight-HAL-CALISP50-MINI). The spectral irradiance of a white cold LED lamp at an intensity of 1000 lux with colour temperature of 5000K, is plotted in **Figure 3.7**. This enabled us to calculate the optical power density, ensuring accurate estimation of the iPCE during the study of the influence of passivation layers on device performance under indoor illumination. For all indoor and 1 Sun J–V characterizations, an active area of the devices (0.09 cm²) was defined using a metallic mask, as schematically shown in **Figure 3.1(d)**.

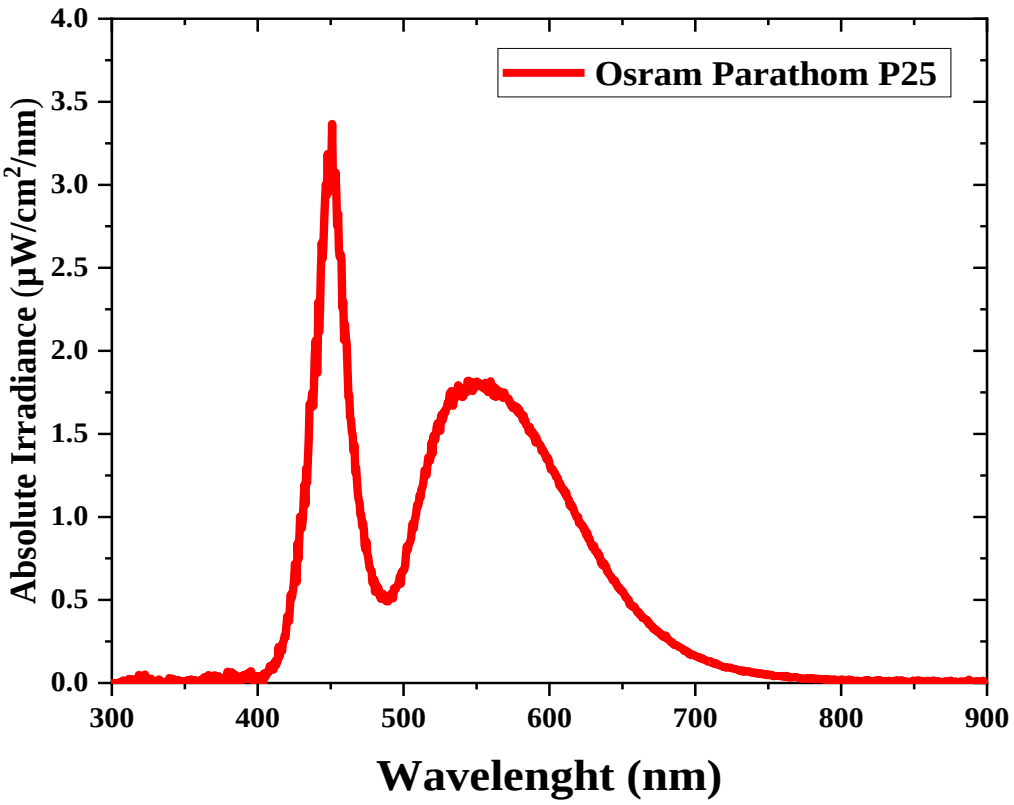

Figure 3.7. Spectrum of the commercial cold LED based lamp for indoor measurements.

In the study evaluating the impact of Spiro-OMeTAD dopants on the performance of devices under indoor conditions, the Litos Lite system (FLUXiM AG, Switzerland), as shown in **Figure 3.4(d)**, was used to record the J–V sweeps in open air in both reverse and forward directions (scan rate 50 mV s^{-1}) under simulated sunlight. The AM1.5G simulated sunlight (1-Sun, 100 mW cm^{-2}) was obtained with an A++A+A solar simulator (Sinus-70 LED simulator from Wavelabs). While for the indoor measurements in this study, a Philips HUE WLED bulb with an adjustable colour temperature was used as the light source for indoor PV characterization, set to a colour temperature of 4,000 K. The illuminance of lamp level was monitored using a calibrated lux meter (Digi-

Sense), as can be seen in **Figure 3.4(c)**. The power density of the WLED bulb at different illuminance levels was measured with a Konica Minolta CL-500A Illuminance Spectrophotometer. For instance, at 1,000 lux WLED intensity, a power density of approximately 0.32 mW cm^{-2} was recorded on the photovoltaic cell surface. J–V measurements, including reverse and forward sweeps (scan rate: 50 mV s^{-1}), as well as steady-state power output (SPO), were conducted using a Keithley 4250 source-measure unit in a 4-wire configuration. All measurements were performed inside a black box as illustrated in **Figure 3.4(e)**, and 7-mm^2 aperture masks were used to ensure accurate testing.

3.6.2 EQE Measurements

In study of evaluating the passivation layers influence on PSCs under indoor illumination, the Incident-Photon-to-Current Efficiency (IPCE) spectra as a function of wavelength was acquired using an optical power density-based measurement system (Arkeo-Cicci research s.r.l.), image of which is provided in **Figure 3.8(a)**. While in study of investigating Spiro-OMeTOD doping influence indoor for PSCs, EQE spectra were measured using a quantum efficiency measurement system (QuantX-300, Newport), image of which is provided in **Figure 3.8(b)**.

Figure 3.8. a) Optical power density-based measurement system (Arkeo-Cicci research s.r.l.) in CHOSE, Italy, b) EQE measurement system (QuantX-300, Newport) in the University of Tampere, Finland.

Reference/s

1. De Rossi, F., Pontecorvo, T. & Brown, T. M. Characterization of photovoltaic devices for indoor light harvesting and customization of flexible dye solar cells to deliver superior efficiency under artificial lighting. *Appl Energy* **156**, 413–422 (2015).

Chapter 4

Comparative Study of Different Passivation Layers for n-i-p Perovskite Solar Cell for Indoor Applications

4.1 Motivation

The synthesis of PVK semiconductors via solution-based approaches makes them highly appealing from an industrial perspective. However, the unavoidable formation of defects in solution-processed PVKs adversely affects the performance of their corresponding devices in PVs and optoelectronic applications. Improving the absorber perovskite quality is therefore regarded as a critical strategy for improving device performance. This issue is particularly critical in the case of IPVs, where the realization of high-quality PVK absorber is a prerequisite to achieve optimal performance. Since under low-light intensity illumination, fewer photogenerated carriers are produced, and any imperfections in the absorber can trap and recombine these carriers, preventing them from contributing to output power generation. Moreover, the environmental and thermal stability issues associated with organic-inorganic hybrid lead halide PVKs remain significant challenges and major barriers to the commercialization of PVK-based PV technologies. To address these challenges, the application of passivation layers on the surface of PVK absorbers has become a common strategy in PSCs designed for outdoor applications. These passivation layers not only improve the surface quality of the PVK absorber but also serve as protective shields, safeguarding the material from moisture and oxygen ingress while enhancing its thermal stability. Consequently, promising outcomes have been reported in the literature. Nevertheless, such approaches for PVK-based IPVs devices have been largely unexplored. Therefore, this study comparatively investigates the influence of several passivation layers on the performance of triple-cation PVK-based solar cells under both low-light indoor and standard 1-sun illumination. Additionally, it examines the impact of these passivation layers on the stability of absorber PVK and their corresponding devices.

4.2 Introduction

IPVs is emerging as a sustainable and reliable energy source for low-power electronics, such as those used in the rapidly growing IoTs [1]. As IoT devices are projected to increase to 75 billion by 2025, the demand for efficient, low-power solutions is skyrocketing [2]. Devices like sensors, wireless nodes, and small displays, which require only nanowatts to milliwatts of power particularly in sleep mode operation, can be effectively powered by IPV systems that harvest light from indoor environments. These technologies are crucial for developing smart buildings, advanced factories, and retail markets [3]. For instance, electronic price tags with embedded PV can update prices wirelessly, demonstrating how IPV can support smart buildings and modern manufacturing lines [1,4].

Among the existent PV technologies, PSCs have demonstrated rapid advancements over the past decades, with PCEs under standard 1-sun light illumination exceeding 26% [5]. PSCs stand out for their tunable bandgaps, excellent EQEs, flexibility, simple, and cost-effective manufacturing processes, and low-temperature fabrication potential, makes them promising for indoor light harvesting [6–9]. Unlike other emerging technologies, such as organic and dye-sensitized solar cells, which struggle with longevity and efficiency, PSCs offer a favourable blend of high performance and practical advantages for IPV applications [4,10,11]. Although standardized methods for evaluating indoor efficiency are still under development and subject to debate, PSCs in both n-i-p and p-i-n architectures have already surpassed the 40% iPCE benchmark (under 1000 lux) at the lab scale [12–15], with the highest certified performance reported to date reaching 44.72% [16]. These remarkable iPCEs, achieved through the use of high-quality PVK active layers with reduced defect densities and minimized non-radiative recombination, significantly outperform other types of solar cells used in IPVs [17–19]. Nevertheless, in solution-processed PVKs, a variety of defects readily form, often related to ionic defects such as iodine vacancies, which are predominantly located at the film surface and at the grain boundaries [20–22]. These surface defects, on the one hand, contribute to the reduced thermal stability of organic-inorganic hybrid PVKs, as degradation typically initiates at film surfaces or grain boundaries upon heating [23]. On the other hand, surface defects significantly impact device performance under low-intensity indoor lighting conditions, causing greater power loss through non-radiative recombination, like Shockley–Read–Hall trap-assisted recombination compared to outdoor conditions [24]. Therefore, passivating these surface defects is essential for improving the performance and stability of solution-processed PSCs, particularly under indoor lighting conditions.

To address the challenges of PVK defects for IPVs, several strategies have been investigated, including the addition of specific additives, halide composition optimization, doping, solvent and antisolvent treatments, an air-knife assisted recrystallization method, and surface passivation [12,24–32]. Among these, surface passivation using halide and non-halide passivators is commonly adopted to enhance PSCs performance under indoor illumination. Non-halide passivators like trifluoroacetamidine (TFA), 2, 5-thiophenedicarboxylic acid (TDCA), and benzyl acrylate form strong bonds with Pb^{2+} and create hydrogen bonds on the PVK surface, suppressing halide vacancies and improving IPV performance [33–35]. In contrast, halide passivators offer notable advantages over other passivators, because they not only passivate surface defects but also address the underlying issues of non-radiative energy loss associated with Shockley–Read–Hall trap-assisted recombination [12,36]. For instance, in an inverted structure device, Li et al. [36] passivated the top surface of a wide-bandgap PVK [$(FA_{0.6}MA_{0.4})_{0.9}Cs_{0.1}Pb(I_{0.6}Br_{0.4})_3$, bandgap ~1.75 eV] using phenethylammonium halides (PEAH: H = I, Br, Cl). While the PEAH layer did not alter the bandgap, PL analysis revealed reduced non-radiative recombination in the treated films. TRPL measurements further revealed that PEACl-treated samples exhibited the highest carrier lifetime compared to PEABr- and PEAI-treated ones. Consequently, PEACl treatment effectively suppressed phase segregation, and improved the resulting device iPCE to 35.6%, compared to 31% of device based on untreated absorber PVK under 1000 lx of 3000 K LED light. In contrast, Lee et al. [31] deposited PEAI onto the top surface of a wide-bandgap PVK (>1.74 eV) in n-i-p structure device. The strong interaction between PEAI and the PVK surface enhanced electrical properties and passivated surface defects. Ultraviolet photoelectron spectroscopy (UPS) indicated a more p-type surface, which facilitated more efficient hole transport to the HTL. As a result, the PEAI-treated device reached an iPCE of 33.42%, compared to 28.01% for the control, under 1000 lux of cool white LED light. Moreover, He et al. [12] treated the 2D $FAGAPbI_4$ PVK film with CH_3O-PEABr passivation, which effectively suppressed charge carrier recombination at the PVK/Spiro-OMeTAD interface. Consequently, under 824.5 lux (301.6 μW cm^{-2}) of 2700 K LED light illumination, their champion device delivered a record iPCE of 40.1%, compared to 37.57% for the control device. In the context of IPV, these breakthroughs highlight the critical importance of surface passivation, particularly through halide passivators, in tackling traps and defects in PVK absorbers. However, despite advancements and understanding in their effects under standard lighting, their effectiveness in IPV applications remains largely unexplored.

In this study, inspired by literature reporting the impressive surface passivation effects of halide passivators on PSCs performance and stability under standard and low lighting conditions, we selected three promising iodide-based passivators for investigation: PEAI, OAI, and GUI.

Moreover, for comparison, we introduced a Lewis base molecule, DPPP, as a passivator into a n-i-p structure device for the first time. This molecule had previously been developed and employed in inverted p-i-n structure devices, demonstrating impressive PCE and excellent stability under standard light illumination [37]. The passivation layers including OAI, GUI, PEAI, and DPPP, were applied as a thin layer, sandwiched between the absorber PVK and the HTL in the devices, and on top of the absorber PVK in the samples. Following deposition, the devices and samples were evaluated to record iPCE and stability performances. The reference (Ref) device and those incorporating GUI, PEAI, OAI, and DPPP achieved iPCEs of 31.35%, 32.32%, 34.47%, 33.71%, and 33.14%, respectively, under 1000 lux LED illumination. Subsequently, the morphological and structural stability of all the samples, including the non-passivated Ref and those with various passivation layers, were evaluated. Among them, the DPPP-passivated sample exhibited exceptional stability compared to the others after one year of storage in air environment. To examine thermal stability, the Ref and passivated devices were subjected to thermal stress tests at 85°C, following the ISOS-T1 protocol under indoor conditions. Under these conditions, the device incorporating DPPP achieved the highest T80 lifetime (time taken for a solar cell to degrade to 80% of its initial efficiency) of 753 h under indoor illumination, highlighting DPPP's strong potential as a passivation layer for PVK-based IPV applications. Overall, this study provides valuable insights into the functioning and stability of passivation layers for PSCs under indoor lighting conditions, opening new pathways for optimizing performance and stability.

4.3 Results and Discussions

To investigate the influence of various passivation layers on the optical and morphological properties of films as well as performance of PSC devices, based on our prior work, we selected a PVK composition featuring mixed cations and halides, $Cs_{0.08}FA_{0.80}MA_{0.12}Pb(I_{0.88}Br_{0.12})_3$ that revealed high efficiency and high stability [32]. The samples were fabricated on bare glass and ITO substrates coated with SnO_2 ETL, via a two-step spin-coating process, as schematically shown in **Figure 3.1(a)**. employing green anisole as an anti-solvent and annealed at 100 °C for 30 minutes. However, to evaluate the PV characteristics, standard n-i-p structured devices with and without passivation layers were fabricated. The entire schematic illustration of absorber PVK deposition on top of the ITO/SnO_2 substrates is illustrated in **Figure 3.2**. After PVK annealing, the solutions of passivating molecules including GUI, PEAI, OAI and DPPP were dynamically dropped onto the PVK films during spinning. Subsequently, another annealing at 100°C for 10 minutes was sustained to ensure complete removal of residual solvents and formation of passivated PVK layer. Hereinafter, the film, sample, and device without a passivation layer are referred to as the Ref. The

other films, samples, and devices, treated with passivation layers of OAI, PEAI, GUI, and DPPP (shown in **Figure 4.1a** along with their corresponding chemical structures in **Figure 4.1b**), are referred to as the OAI-, PEAI-, GUI-, and DPPP- respectively.

4.3.1 Surface Morphology of the PVK Films

SEM was used to examine the morphology of the prepared PVK films. **Figure 4.2(a–e)** presents the SEM top-view of the analysed samples, allowing for a direct comparison of each with the Ref (non-passivated sample).

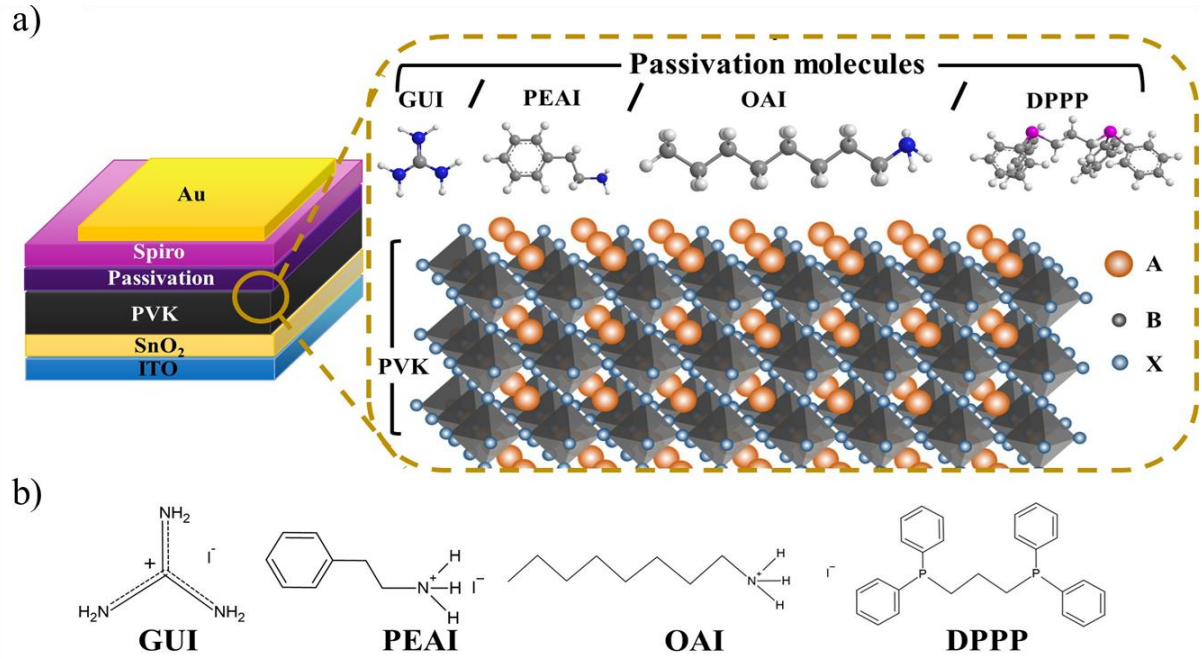

Figure 4.1. a) Schematic of PSC structure (n-i-p) with the passivation molecules. b) Molecular structures of molecules used in the study.

The Ref sample exhibits a compact morphology with uniformly distributed grains. Small white particles are visible on the top surface, located at grain boundaries, and could likely correspond to PbI_2 segregations, as confirmed by XRD analysis and frequently reported in the literature [38]. These segregations were either absent or only occasionally detected by SEM in the other samples with passivation layer on the top surface, in accordance with XRD results discussed below. PVK films with OAI and PEAI revealed similar surface morphologies, both featuring compact and elongated grains. In contrast, the sample passivated with GUI exhibited an uneven surface with more rounded structures. SEM analysis of the DPPP sample was challenging in planar-view due to a top-surface degradation effect caused by the electron beam, which hindered the acquisition of clear images of this sample. However, a distinct morphology was found from those of the previous samples, revealing small (≤ 100 nm) and triangle-shaped features that cover the typical PVK grains.

Analysis of the cross-sections, as shown in **Figure 4.2(f-j)**, revealed that no evident continuous overlayer was formed on top of the PVK film. The images indicate that the morphology of the Ref film and the iodide-based passivated films is comparable, displaying compact and large grains, ranging in size from hundreds of nanometres up to the entire thickness of the PVK film. In contrast, the DPPP passivated sample demonstrated a slight reduction in both film thickness (decreasing from 650-630 nm to 600 nm) and grains size.

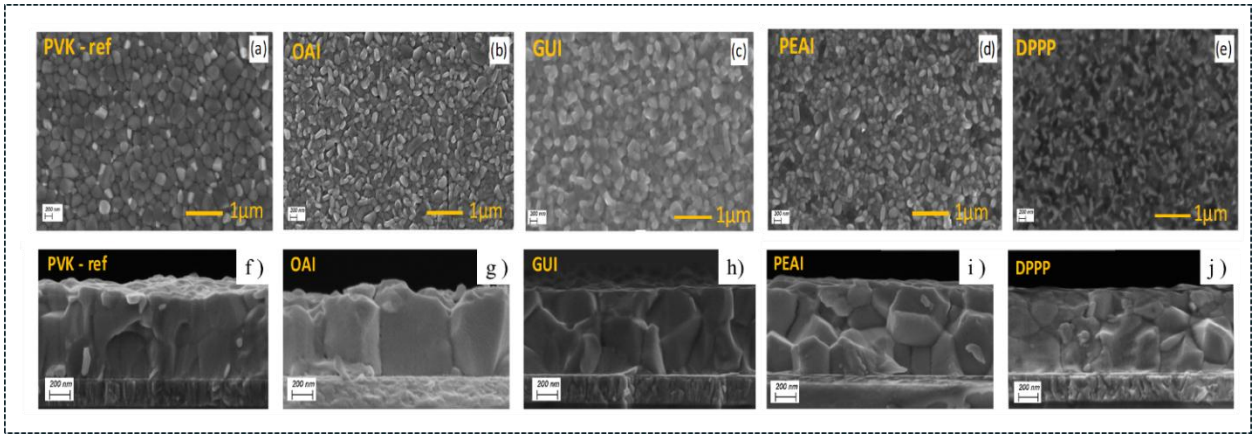

Figure 4.2. a-f) top-view SEM images and f-j) cross-sectional images of perovskite (PVK) samples with different passivation layers (PVK Ref, OAI, GUI, PEAI, and DPPP, respectively) deposited on glass/ITO/SnO_2 substrates.

4.3.2 XRD Analysis

To assess the impact of the different passivation layers on the bulk PVK crystallization, we conducted XRD analysis on ITO/SnO_2/PVK with and without surface modification (**Figure 4.3a**). All the samples display the characteristic features of a triple cation PVK film with high crystallinity in the 3D bulk structure. Notably, the intensity of the (100) peak at 14.1° is increased, corresponding to the α-cubic phase of the PVK structure (**Figure 4.3b**). The reduction in the intensity of the peaks related to the cubic structure of triple cation PVK in the DPPP sample is primarily due to the reduced thickness of the active layer, as shown by SEM cross-section images in **Figure 4.2f-j**. A slight but noticeable narrowing of the full width at half maximum (FWHM) of the (100) peak is observed, particularly with GUI, PEAI, and DPPP passivation layers. Another beneficial effect of applying passivation is the decrease in crystalline PbI_2 compound, evidenced by the significant reduction in the intensity of the (001) peak at 12.7° (**Figure 4.3c**). Moreover, the application of these passivation films introduces distinct patterns, indicating the potential formation of 2D perovskite layers on top of 3D bulk structure. Specifically, in the case of PEAI passivation, a prominent peak at 5.4° is observed, corresponding to the (002) crystallographic plane of the PEA_2PbI_4 2D perovskite. Additional peaks at 10.9°, 16.2°, and 27.3° are attributed the 004, 006, and 001 planes, respectively [39]. Similarly, for OAI passivation, the presence of a peak

at 10.5° suggest the possible formation of $OA_2(MA, Fa)_2Pb_3I_{10}$ 2D perovskite [40,41]. In contrast, no characteristic peak below 11° are detected for GUI and DPPP passivation, indicating an absence of 2D phase. These observations suggest that passivation effect primarily occurs at the grain boundaries, as confirmed by SEM images, which reveal a reduction in whitish crystallites upon applying passivation layers. Additionally, a secondary effect of the passivation is evident in slight morphological modifications, which vary depending on the passivation layer used. Thus, the elongated grain morphology observed in the top-view SEM images for PEAI and OAI is likely attributed to the formation of a 2D thin film.

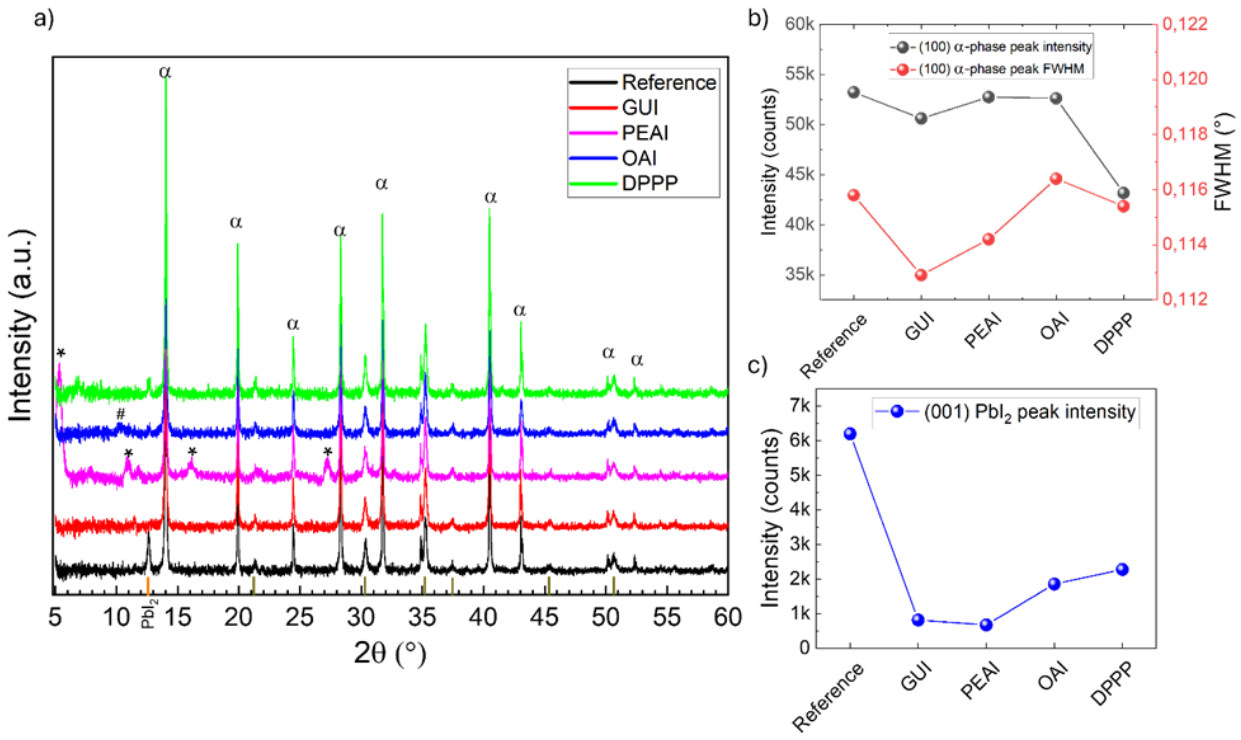

Figure 4.3. a) XRD plot comparing the Ref sample without passivation to samples with various passivation layers (GUI, PEAI, OAI, and DPPP), all deposited on ITO/SnO_2. Peaks associated with the α-cubic structure are highlighted by α, PEA_2PbI_4 by * and $OA_2(MA, FA)_2Pb_3I_{10}$ by #. The orange bar on the x-axis marks the (001) PbI_2 peak, while the grey bars indicate the positions of ITO substrate peaks. b) The (100) α-peak intensity and FWHM, and c) the (001) PbI_2 peak intensity are shown for all samples.

4.3.3 PL Measurements

In **Figure 4.4(a)**, the normalized average steady-state PL spectra for each solar cell, excited from the glass side, are presented. The pulsed excitation laser is set at 710 nm with a photon flux of 4×10^{20} cm^{-2} s^{-1}. All samples show a single PL peak. The absolute intensity is not presented due to its inhomogeneity; however, all samples exhibit similar intensities within a factor of 3. It is worth noting that an appreciable variation in the width of the peak (75-90 meV) is observed among the samples, which correlates with a redshift of the peak energy (from 1.61 eV to 1.60 eV). These

variations can be attributed to a faster or slower degradation during the acquisition time, as explained below:

In **Figure 4.4(b),** representative TR-PL decays at room temperature for each solar cell, excited from the glass side, are presented. Since the signal duration exceeds the laser repetition period ($T \approx 12$ ns) and because of the periodic nature of the time-correlated single photon counting (TCSPC) technique, only the initial portion of the decay is observed, superimposed to a non-constant pedestal due to the periodic folding of the decay exceeding the laser repetition period. This has been taken into account in our fitting function, a sum of two exponentials to describe both the rise and the decay (pulse function), which becomes:

$$I_{\mathrm{PL}} = I_0 \left[\frac{e^{-T/\tau}}{1 - e^{-T/\tau}} + \left(1 - e^{-(t-t_0)/\tau_{\mathrm{rise}}}\right)\theta(t - t_0) \right] e^{-(t-t_0)/\tau} \tag{5.1}$$

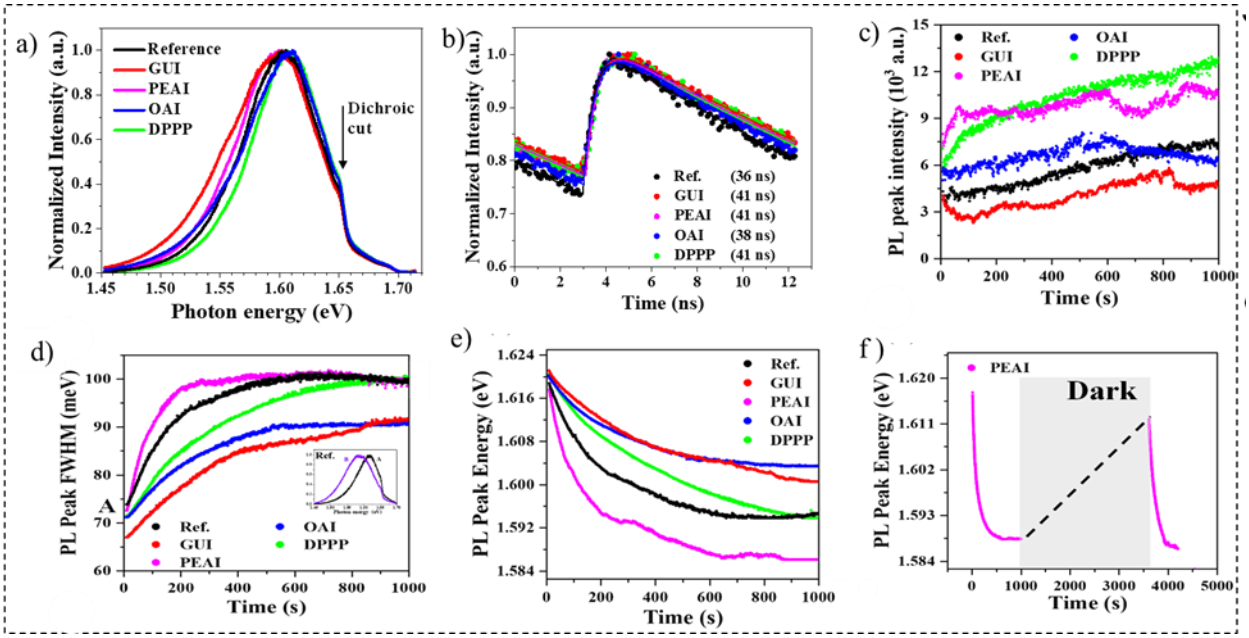

Figure 4.4. PL characterization of the solar cells from the glass side. a) Normalized average PL spectra. The intensity drops at 1.66 eV, as indicated in the figure, is attributed to the dichroic mirror. b) Time-resolved PL. The numbers in parentheses represent the decay time constants obtained through the fitting procedure described in the main text. c) PL intensity, d) full width at half maximum (FWHM), and e) PL peak energy under continuous laser excitation. The inset in (d) shows the spectrum of the reference (Ref) sample at the beginning and end of the acquisition. f) PL peak energy of the PEAI sample as a function of time under continuous excitation, including a 1-hour break midway through the measurement.

where θ is the Heaviside step function, τ_{rise} (assumed $\ll T$) is the rise time constant, and τ is the decay time constant. The decay profiles are well described by our fitting function, at least within the time interval we can explore. The obtained rise times are nearly identical (≈ 100 ps) and are entirely attributed to the system response. Moreover, deconvolution procedures are not necessary for the decay time constants, as they are much longer than the system response. The decay time

constants cover a range from 36 ns to 41 ns, with a relative uncertainty of approximately 10%. Even though all the passivated samples seem to exhibit a longer decay time constant with respect to the Ref sample, pointing to a positive effect of the passivation layers, the uncertainties limit our possibility to draw certain conclusions [42–44]. Indeed, no clear correlation is observed between the average values of the decay time constants and the PV parameters.

To gain insight into the different time scales of the processes governing the degradation of the samples, we performed continuous PL acquisition. **Figure 4.4(c), 4.4(d), and 4.4(e)** show the effect of a Continuous Wave (CW) 532 nm laser illumination with a flux density of 4×10^{20} cm^{-2} s^{-1}. Both the intensity and the FWHM increase, while the energy of the maximum of the peak redshifts. Although the intensity change is not entirely monotonic, the FWHM and the energy of the peak clearly approach a saturation value. The effect becomes more pronounced with increasing excitation power. This degradation under laser light has been explained in the literature by the formation of iodine-rich PVK clusters due to light-induced migration of iodine ions of the PVK layer [45–50]. These clusters are more radiatively efficient, which explains the increase in the PL intensity with time (**Figure 4.4c**) and they emit at lower energies (**Figure 4.4e**). The increase of the FWHM (**Figure 4.4d** and the inset) is an inhomogeneous effect due to the coexistence of clusters/regions of different iodine composition. This demixing of the alloy, as reported in the cited papers, is reversible: after reaching the plateau of the emission energy, keeping the sample 1 h in the dark at room temperature, restores the emission energy and the FWHM to values close to their original ones (**Figure 4.4f**). In contrast, the intensity value is not reversible and tends to remain higher compared to its initial value. This can be explained by a non-reversible trapping of some iodines by non-radiative defects, allowing their passivation.

Regarding the speed of light-induced iodine-migration in our devices, the order from slowest to fastest is as follows: GUI, OAI, DPPP, Ref, PEAI. It is evident that PEAI-based device exhibits the worst stability, as observed also below for thermal aging tests. However, due to the different time scales of these processes, and the inhomogeneities of the samples at the scale of our spatial resolution, caution must be taken when drawing such correlations. A final remark regards the illumination from the back side of the solar cells (close to the gold contact). Since the passivation layers are deposited on the rear side of the cells, and since the penetration depth of the excitation light affects roughly half thickness of the PVK layer, it is expected that the passivation effects would be more prominent when exciting the sample from the gold side. On average, the results from the back show a 100-fold higher signal, a PL peak shifted 25 meV lower in energy, and TR-PL decay times that are three times faster, as shown in **Figure 4.5(a-c)**. However, these features

are general and are observed in the Ref sample also. Regarding the stability, during CW illumination, the intensity decreases rather than increases (a trend common to all the samples); the energy decrease has the same speed but larger delta (for all samples except Ref and DPPP which show the same delta as in front illumination); the FWHM increase is faster but with a smaller delta (for all samples except for Ref which shows a similar characteristic time). Finally, the FWHM with back illumination shows a maximum and a subsequent decrease. This is expected considering the transformation of all the clusters towards a specific iodine concentration, however, the maximum is reached in the following order: PEAI (100 s), OAI (200 s), GUI (250 s), Ref (600 s), DPPP (1000 s). (**See Figure 4.5d-g**).

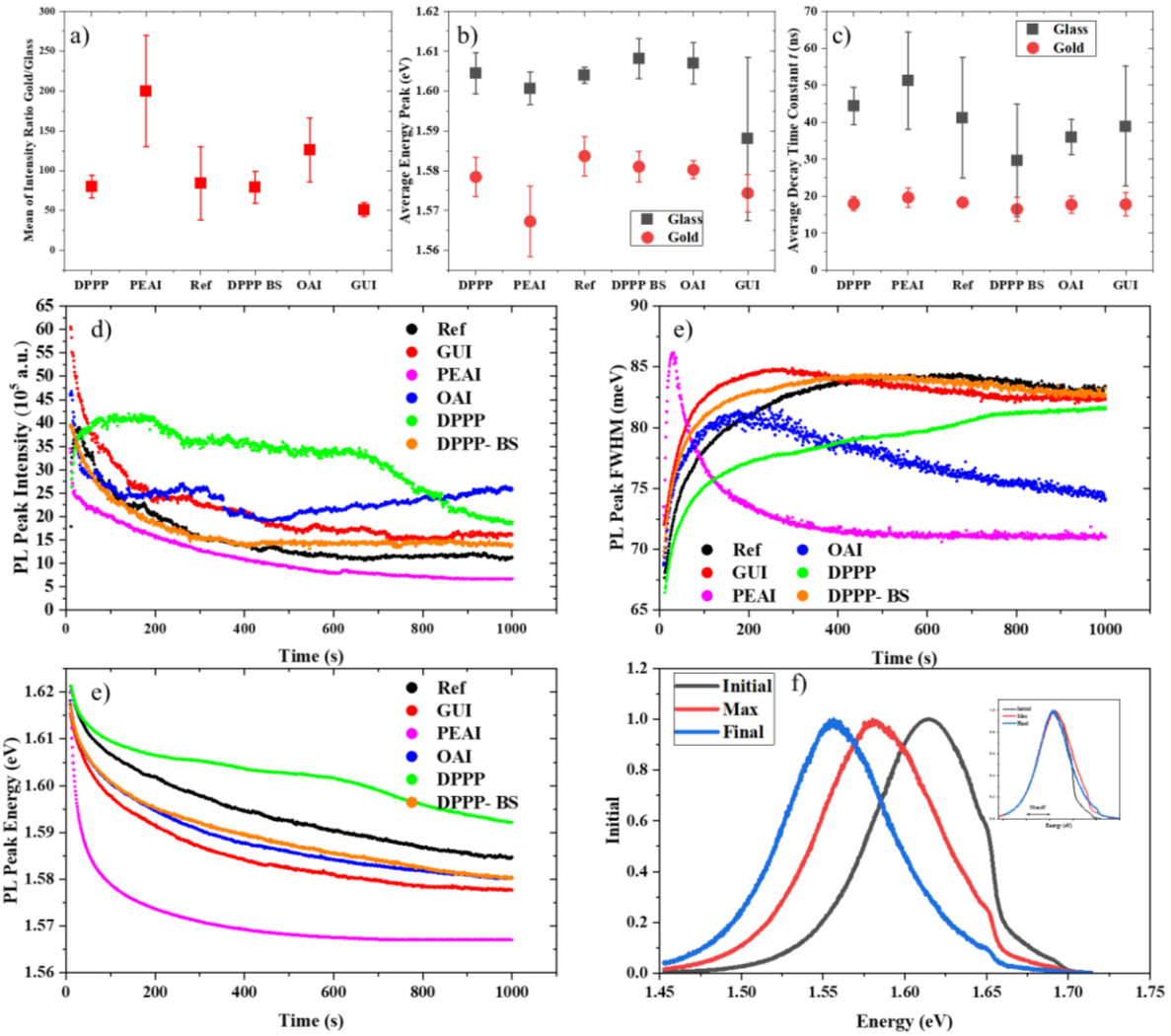

Figure 4.5. Comparison of PL characteristics for devices labelled 04, 05, 16, 21, 28, and 47, corresponding to DPPP, PEAI, Ref, DPPP-BS (introduced below), OAI, and GUI, respectively, under front (glass side) and back (gold side) excitation: a) Intensity ratio of the integrated PL spectra, b) PL peak energy, c) TR-PL decay constants. PL characteristics under continuous laser excitation from the back side (gold side) of the cells: d) PL intensity, e) FWHM, f) PL peak energy, g) Normalized PL spectra of the PEAI sample at three time points: the beginning, the maximum FWHM value, and the end of the acquisition (refer to the top-right panel). The inset shows a comparison of the shapes of these three spectra.

4.3.4 PV performances of the PSCs under indoor light illumination

To investigate the influence of passivation layers on device performance compared to the Ref device without passivation, indoor J-V measurements were conducted. These measurements were distinct from standard testing conditions (STC, AM1.5G, 1000 W/m²) and were instead carried out under low-light illumination condition from a white cold LED lamp at an intensity of 1000 lux with color temperature of 5000K (irradiance plotted in **Figure 3.7**). Even though the power density from traditional indoor light sources is approximately 300 times lower than that of sunlight, it is still sufficient to power IoT sensors [28,51]. Moreover, it is imperative to mention that the decision to examine indoor performance was motivated by the remarkable light response exhibited by PVK absorbers in the 300–850 nm range, encompassing the emission spectrum of typical indoor light sources [52,53]. **Table 4.1** below presents the detailed PV parameters of all devices under indoor illumination.

Table 4.1. Average of the Indoor PV parameters (and of the champion devices in the brackets) for different passivation layers measured under 1000 lux LED Light.

Type	Scan	V_{oc} (V)	J_{sc} (mA/cm²)	FF (%)	Eff (%)
Ref	FW	0.86 ± 0.01 (0.87)	0.18 ± 0.00 (0.19)	65.09 ± 3.08 (66.12)	26.74 ± 1.15 (27.87)
	RV	0.87 ± 0.02 (0.88)	0.18 ± 0.00 (0.19)	74.51 ± 2 (73.78)	30.62 ± 0.59 (31.35)
GUI	FW	0.86 ± 0.01 (0.88)	0.17 ± 0.01 (0.19)	64.23 ± 1.96 (68.52)	24.69 ± 2.5 (29.38)
	RV	0.88 ± 0.01 (0.89)	0.17 ± 0.01 (0.19)	72.25 ± 3.36 (75.18)	28.08 ± 2.92 (32.31)
PEAI	FW	0.93 ± 0.02 (0.96)	0.17 ± 0.01 (0.19)	66.48± 3.14 (69.46)	27.41 ± 2.78 (32.26)
	RV	0.93 ± 0.02 (0.96)	0.17 ± 0.01 (0.19)	73.58 ± 4.40 (74.44)	29.55 ± 2.53 (34.47)
OAI	FW	0.92 ± 0.01 (0.91)	0.18 ± 0.01 (0.19)	69.15 ± 3.71 (71.44)	29.87 ± 1.55 (31.64)
	RV	0.92 ± 0.01 (0.92)	0.18 ± 0.01 (0.19)	76.40 ± 0.36 (76.33)	32.19 ± 1.08 (33.71)
DPPP	FW	0.88 ± 0.02 (0.88)	0.18 ± 0.01 (0.19)	71.76 ± 3.51 (74.77)	29.44 ± 1.39 (31.92)
	RV	0.88 ± 0.02 (0.89)	0.18 ± 0.01 (0.19)	76.65 ± 1.64 (77.60)	31.00 ± 1.04 (33.14)

Interestingly, as provided in **Table 4.1**, the performance of champion devices with the same PVK absorber but passivated with different molecules showed comparative improvement due to significant increase in FF values over the Ref champion device, which achieved an iPCE of 31.35% in a reverse scan. Notably, primarily due to a significant increase in V_{oc} coupled with an optimal increase in FF, the PEAI-based champion device delivered an impressive iPCE of 34.47% in a reverse scan, which is the highest achieved value in this study. Moreover, the OAI-based champion device also performed exceptionally well in a reverse scan due to a notable increase in V_{oc} and FF, achieving the second highest iPCE of 33.71%. Similarly, the DPPP-based champion device also delivered an iPCE of 33.14% in a reverse scan, proving the potential of this novel passivation layer in improving the performance of a device under low light illumination. The box plot diagrams illustrating the PV statistics for each variable of the devices under indoor conditions, measured in both forward and reverse scans, are presented in **Figure 4.6(a-d)**.

From **Figure 4.6(d)**, it is evident that OAI-based devices achieved the highest average iPCEs in reverse scan measurements. Furthermore, **Figure 4.6(a-d)** indicates that the PV parameters of all devices, including the unpassivated Ref, are relatively consistent across both forward and reverse scans. Additionally, the calculated average PV statistics and the PV parameters of the champion devices are given in **Table 4.1**. The J-V curves of the champion indoor devices of each variable in both forward and reverse scans are provided in **Figure 4.6(e)**.

As illustrated in the box plot (**Figure 4.6f**), the HI, where ($HI = \frac{PCE_{RV} - PCE_{FW}}{PCE_{RV}}$) of devices with various passivation layers shows distinct variations when compared to the Ref device. The Ref device exhibits noticeable hysteresis, as seen by higher HI value. Hysteresis is often observed as a mismatch in the PCE depending on the scan direction and is linked to various factors like ion migration, charge trapping, and interface quality within the cell [54]. Hysteresis can be problematic because it affects the reliability of the efficiency measurement and may indicate stability issues in the device. Passivated devices show reduced hysteresis, suggesting that passivation layers effectively suppress charge recombination and improve stability. However, among the passivated devices, notably, DPPP devices demonstrate the lowest HI, highlighting the potential effectiveness of DPPP as a passivation strategy in minimizing hysteresis and enhancing the stability of PSCs.

Overall, under indoor light illumination, the addition of passivation layers led to a modest improvement in performances compared to the Ref device and highlighted the beneficial impact of passivation in reducing non-radiative losses and enhancing charge transport in low-light conditions, though the improvements in iPCEs were not particularly striking.

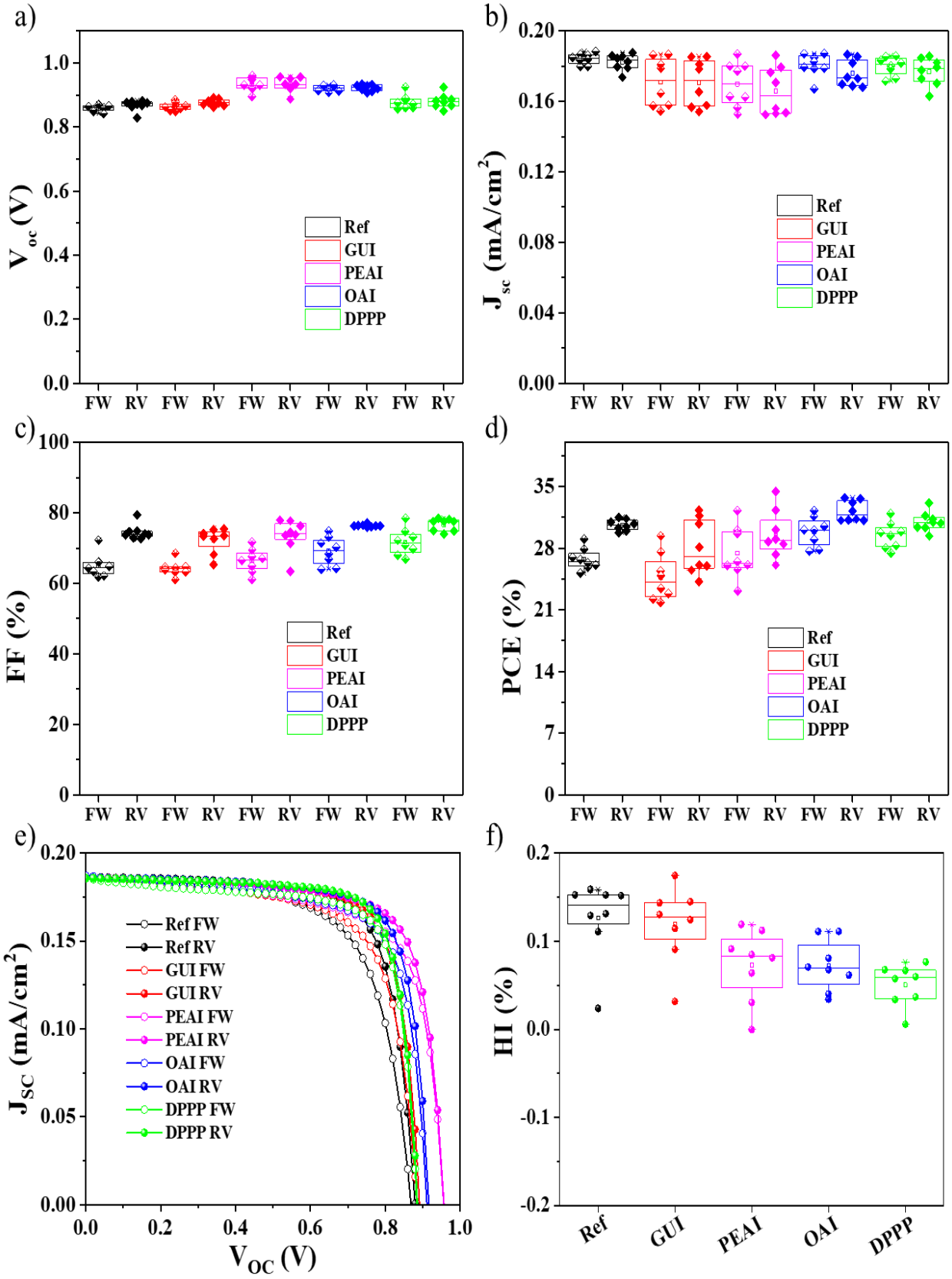

Figure 4.6. The statistical distribution of a) V_{oc}, b) J_{sc}, c) FF, d) PCE, f) HI, respectively, of the best 8 Ref and passivated devices in both forward and reverse scans, and e) J-V curves in both forward and reverse scans of champion devices under 1000 lux, LED illumination.

4.3.5 PV performances of the PSCs under STC

In contrast, when these devices were evaluated under 1 sun, STC, interestingly, the influence of passivation became even more striking, . **Table 4.2** presents the detailed performance data under STC of best 8 devices average data (in brackets) and the performance data of the champion devices (outside the brackets). As clear from the **Table 4.2**, under STC, devices with OAI, PEAI, and DPPP treatments showed substantial efficiency gains, with OAI achieving the highest efficiency of 20.20%, significantly outperforming the highest 16.05% efficiency of the Ref device.

Table 4.2. Average PV parameters of the best 8 devices for different passivation layers and the photovoltaic parameters of their champion devices (in brackets) measured under standard test conditions (STC), AM1.5G, 1000 W/m².

Type	Scan	Voc (V)	Jsc (mA/cm²)	FF (%)	Eff (%)
Ref	FW	0.99 ± 0.02	19.80 ± 0.88	69.81 ± 5.97	13.75 ± 1.46
		(1.02)	(21.69)	(72.53)	(16.05)
	RV	1.00 ± 0.02	19.74 ± 0.65	70.20 ± 2.07	13.85 ± 0.61
		(1.02)	(20.92)	(70.84)	(15.18)
GUI	FW	1.05 ± 0.04	20.62 ± 0.76	66.63 ± 6.03	14.37 ± 1.26
		(1.00)	(20.51)	(71.25)	(14.56)
	RV	1.05 ± 0.3	20.40 ± 1.04	69.55 ± 6.18	14.84 ± 0.91
		(1.00)	(20.75)	(79.24)	(16.44)
PEAI	FW	1.12 ± 0.02	21.29 ± 0.47	73.89 ± 1.95	17.63 ± 0.64
		(1.09)	(22.26)	(73.82)	(17.95)
	RV	1.12 ± 0.03	21.02 ± 0.46	73.21 ± 2.39	17.24 ± 0.66
		(1.10)	(22.09)	(78.07)	(18.92)
OAI	FW	1.13 ± 0.01	20.99 ± 0.78	76.31 ± 1.30	18.36 ± 1.04
		(1.12)	(22.93)	(75.48)	(19.37)
	RV	1.13 ± 0.01	21.29 ± 0.88	77.62 ± 2.24	18.73 ± 0.82
		(1.12)	(22.59)	(79.85)	(20.20)
DPPP	FW	1.07 ± 0.02	21.04 ± 0.55	74.30 ± 4.71	16.74 ± 1.28
		(1.08)	(21.92)	(77.93)	(18.39)
	RV	1.07 ± 0.01	20.86 ± 0.64	76.34 ± 1.11	17.02 ± 0.44
		(1.07)	(21.85)	(75.94)	(17.80)

The major boost in in the performance of passivated devices stemmed from notable increase in V_{OC} and FF values compared to Ref device, which can be attributed to the reduced non-radiative recombination and enhance carriers injection [55,56].

The box plot diagrams illustrating the PV statistics for each variable of the devices under STC, measured in both forward and reverse scans, are presented in **Figure 4.7(a-d)**. While the J-V curves of the champion devices of each variable in both forward and reverse scans under STC are provided in **Figure 4.7(e)**.

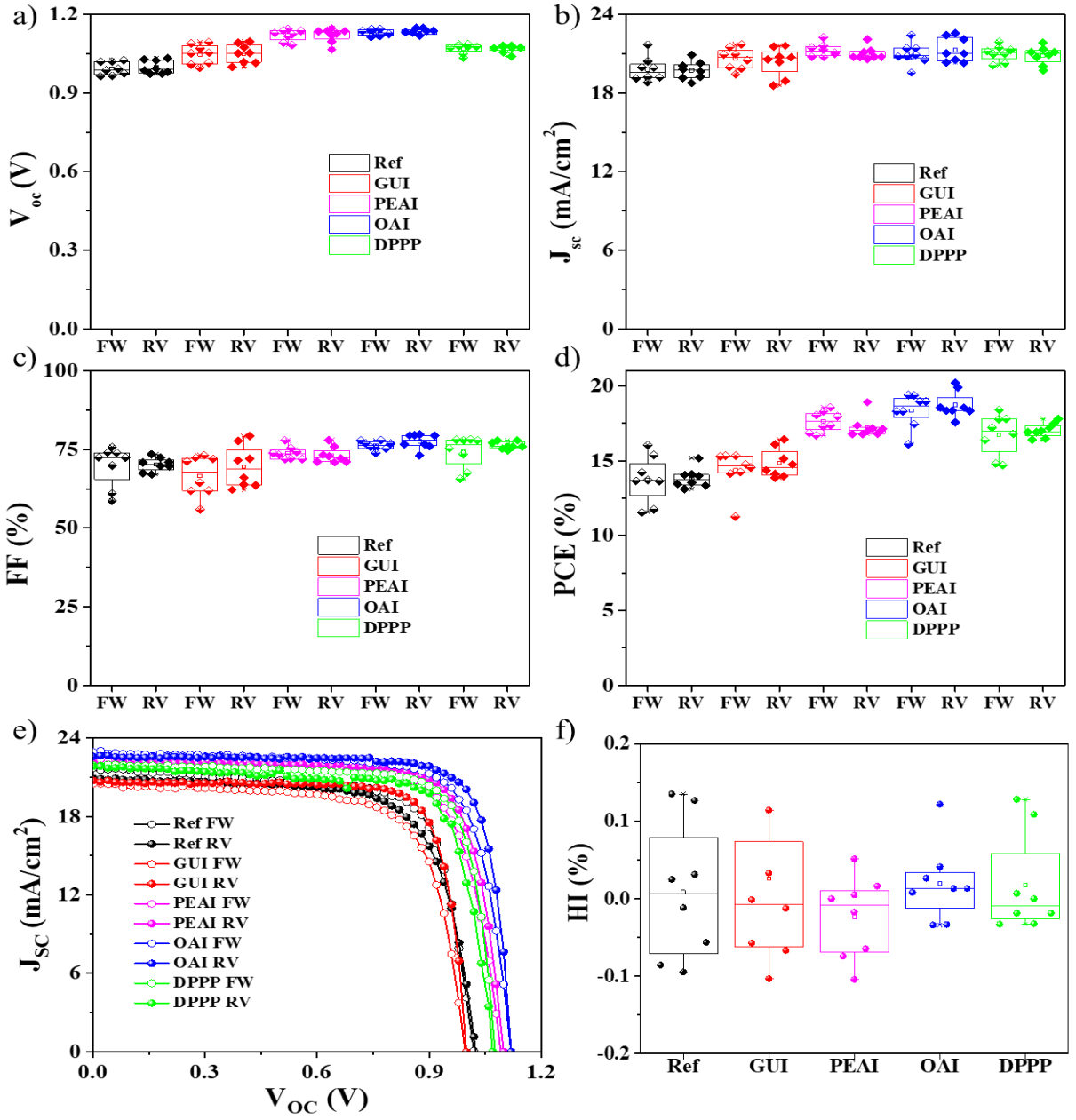

Figure 5.7. The statistical distribution of a) V_{oc}, b) J_{sc}, c) FF, d) PCE, f) HI, respectively, of the best 8 Ref and passivated devices in both forward and reverse scans, and e) *J-V* curves in both forward and reverse scans of champion devices under STC.

Moreover, as can be seen in **Figure 4.7f**, the reduction in HI for passivated devices is more substantial under STC than under indoor illumination (**Figure 4.6f**). This observation aligns with literature, as PSCs often exhibit higher hysteresis operating under indoor illumination compared to outdoor illumination. This phenomenon can be attributed to several factors. At lower light intensities, fewer charge carriers are generated, limiting the filling of defect states (traps) that act as recombination centres and hinder charge accumulation. Additionally, the distinct spectral characteristics and lower intensity of indoor lighting result in a weaker electric field near the front interface, where most of the indoor light is absorbed. In contrast, 1 Sun illumination provides a more uniform charge generation rate across the thickness of the perovskite layer, mitigating these effects [57–59]. To further elucidate our obtained results, further characterizations are performed, which are discussed in the subsequent lines.

The IPCE and the corresponding integrated J_{sc} as a function of wavelength for Ref and passivated devices are presented in **Figure 4.8**.

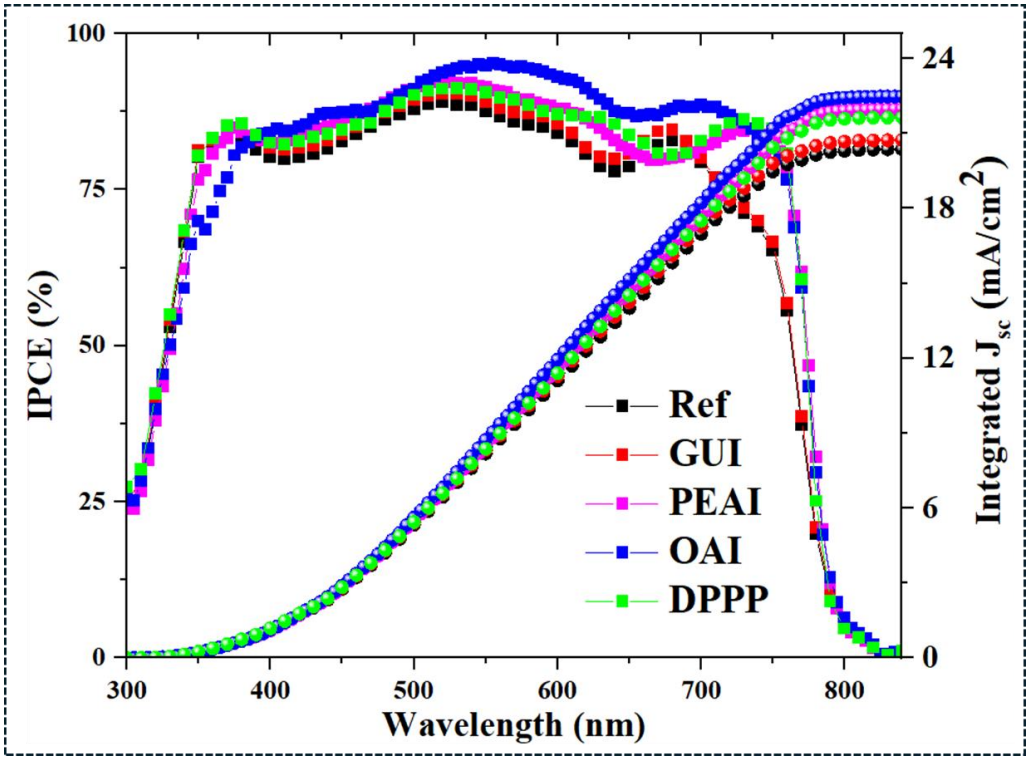

Figure 4.8. IPCE spectra of the Ref and passivated champion devices.

The IPCE curves show that both the Ref and passivated devices exhibit a broad light response ranging from 300 to 785 nm, with no shift observed in the onset of the IPCE spectra for the passivated devices, confirming an absorber bandgap of ~1.59 eV. Furthermore, the passivated devices demonstrate enhanced IPCE values across the entire visible spectrum, indicating improved

material quality and crystallinity (as confirmed by XRD analysis). This enhancement enables more efficient light absorption and increases the number of photogenerated carriers in longer wavelengths which confirms reduced non-radiative recombination due to the passivation of surface defects at the PVK/HTL interface, as detailed in the subsequent lines. Moreover, the integrated J_{sc} values of Ref and passivated devices, as determined from their IPCE results, align well with the J_{sc} values obtained from their J-V measurements, confirming the accuracy of the device parameters.

In **Figure 4.9(a)** and **Figure 4.9(b)**, the dependence of J_{sc} and V_{oc} on the light intensity, respectively is presented, respectively.

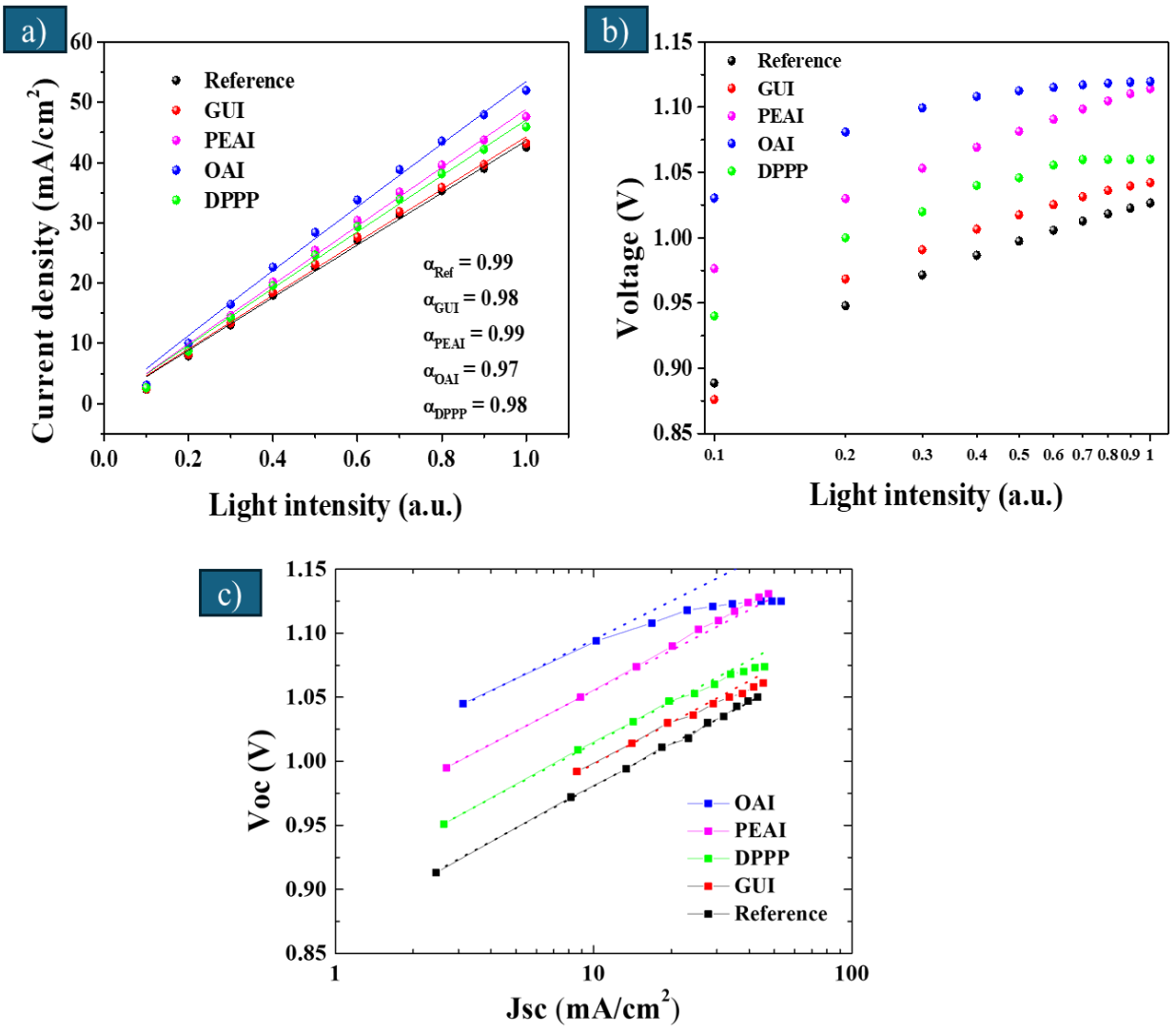

Figure 4.9. a) J_{sc} and b) V_{oc} as a function of light intensity for devices with different passivation, and c) V_{oc} versus log(J_{sc}) based on measurements at various light intensities. The dotted lines represent fits obtained using the expression described in the main text.

These data can be used to obtain an estimate of the diode ideality factor (n) and the reverse saturation current (J_0) using the standard approximate expression for the V_{oc} as a function of the J_{sc}:

$$V_{oc} = \frac{nkT}{q} ln\left(\frac{J_{sc}}{J_0}\right) \quad (5.2)$$

In this approximation, a plot of V_{oc} vs log(J_{sc}) should yield a straight line, with a slope proportional to "n" and an intercept at $V = 0$ for a current density equal to J_0. The results of these linear fits for the data presented in **Figure 4.9(c)** are summarized in **Table 4.3,** which show a clear reduction in J_0 for the passivated devices, indicating reduced recombination at the PVK/HTL interface. Thus, the efficiency gains observed in devices with passivation layers, compared to the Ref device, under both indoor and STC conditions, can partly be attributed to the reduction in J_0 for the passivated devices.

Table 4.3. Values of the diode ideality factor n and of the reverse saturation current J_0 for devices using different passivation obtained from the fits in Figure 4.9.

Sample	n	Jo (mA/cm^2)
Reference	1.82	1.0 10^{-8}
GUI	1.8	5.5 10^{-9}
DPPP	1.8	3.9 10^{-9}
PEAI	1.75	8.5 10^{-10}
OAI	1.68	1.3 10^{-10}

4.3.6 Aging and stability

To investigate the impact of passivation layers on the stability of absorber PVK films after one year of storage, morphological and crystalline characterizations (SEM and XRD) were conducted on the same samples that were initially characterized as fresh, as described before.

In this regard, following the initial characterizations, the samples were stored in a dark condition, air-exposed environment and relative humidity (RH) = 40% ± 10% without any encapsulation. All the samples exhibited visible colour changes after storage. **Figures 4.10(a-d)** show the top-view SEM images of the passivated films, where surface modifications are evident, including the formation of several elongated crystals on top of the inner PVK grains, except for the DPPP sample.

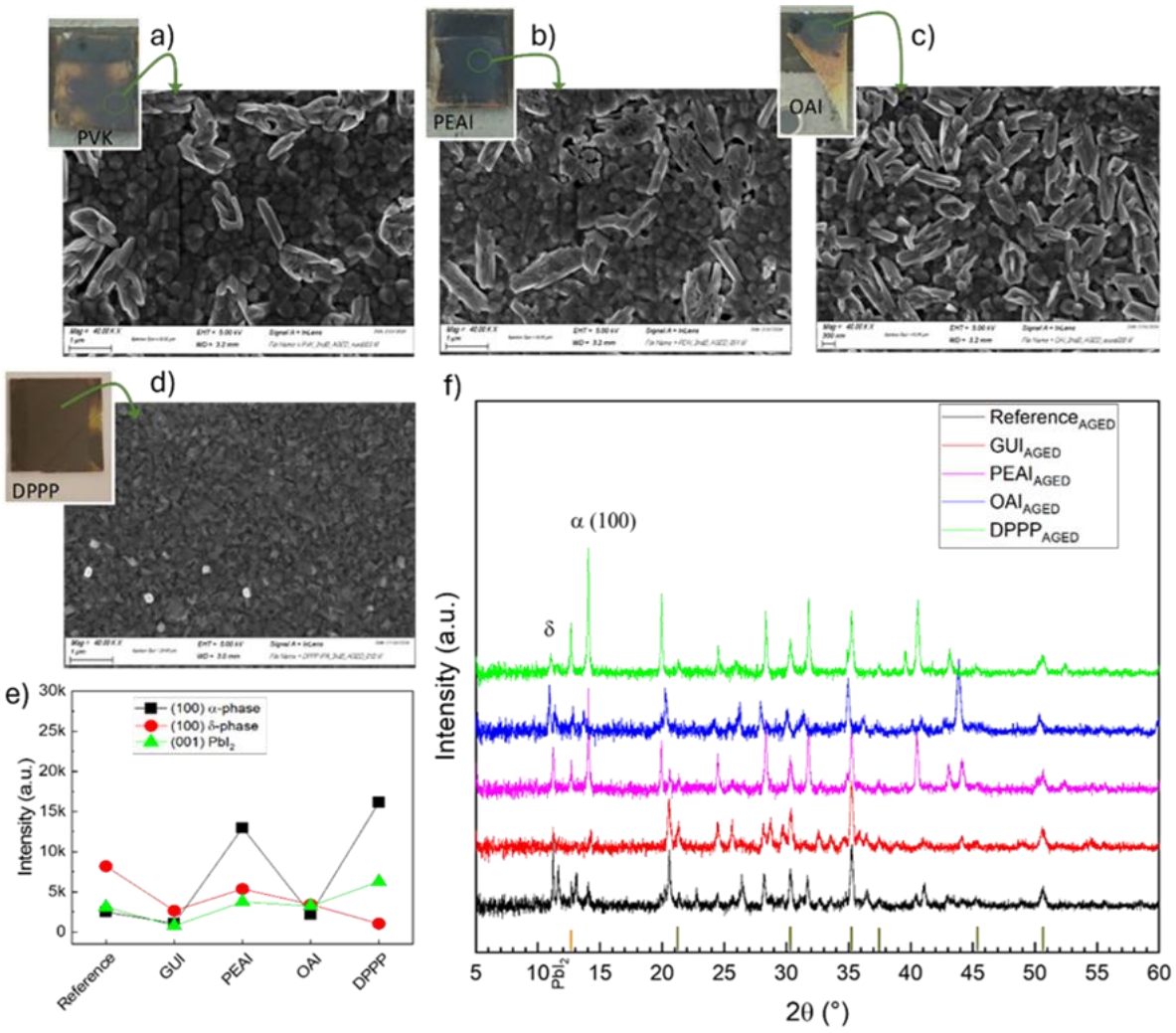

Figure 4.10. a-d) SEM images of aged samples stored in air environment for Ref, PEAI, OAI, DPPP respectively; e-f) XRD analysis on the aged samples.

In the case of the DPPP sample, the surface remains almost unchanged, with triangle-shaped features. These formations may be attributed to PbX_2 sub-products, or to a DMSO intermediate complex, or to a dihydrate phase, leading to an increase in the PbI_2 phase, which eventually evolves into a non-photoactive δ-phase. The hydration reaction has been reported as a two-step process: first, the formation of a monohydrate product, which is a reversible process occurring on a timescale of a few h, followed by the formation of a dihydrate complex. This second step is an irreversible process, characterized by a distorted pseudo-cubic lattice consisting of $[PbI_6]^{4-}$ octahedra and dimers such as $(CH_3NH_3\cdots H_2O\cdots CH_3NH_3)_2^{4+}$ or $(CH_3N_2H_5\cdots H_2O\cdots CH_3N_2H_5)_4^{+}$ [60–63]. This is reflected in a diffraction peak at approximately 11.1°-11.3° in the XRD patterns of the aged samples (**Figure 4.10f**), which is distinct from the peak at 11.6° associated with the δ-phase. The slight variations in these peak positions can be attributed to differences in the interactions between the PVK layer and the molecular charge distributions, as well as the dipole interactions introduced by the nature of the passivation layers. It is also important to note that XRD

measurements provide averaged information from the sample's stack. Consequently, the XRD beam probes both degraded and non-degraded regions of the aged samples, reflecting the surface inhomogeneity that develops through the one year of aging process. Indeed, the XRD results provide clear evidence of degradation in all tested samples, with a significant decrease in the intensity of the α-phase peaks. For the Ref, GUI, and OAI-treated films, the α-phase intensity decreased by more than 95% compared to the initial value, while for the PEAI and DPPP samples, the decreases were 75% and 62%, respectively. A fine analysis of the degradation mechanism associated with these passivation layers over the presented timescale lies beyond the primary scope of this study.

4.3.7 Fabrication and Characterization of DPPP-BS devices and Samples

Given the initial attempt to use DPPP material in the n-i-p structured device and observing its positive effect in protecting the PVK film from environmental degradation, as discussed earlier in the "Aging and Stability" section, distinct from surface passivation of PVK as top layer, we further explored both bulk and surface DPPP passivation (denoted as DPPP-BS). To achieve this, we first added the DPPP solution to the antisolvent anisole and applied the resulting mixture onto the PVK during the antisolvent step. Following this, DPPP was applied as a passivation layer. The PV performance statistics of the DPPP-BS-based devices are given in **Figure 4.11(a-d)** and **Table 4.4**. While the DPPP-BS passivation had no significant impact on the performance under 1-sun STC as compared to Ref device, a more pronounced improvement in PV performance was observed under 1000 lux LED illumination.

Table 4.4. Average PV parameters of the best 8 devices for DPPP - BS and the photovoltaic parameters of the champion device.

Type	Illumination	Scan	V_{oc} (V)	J_{sc} (mA/cm²)	FF (%)	Eff (%)
DPPP - BS	1 sun	FW	1.03 ± 0.03 (1.06)	18.00 ± 0.45 (18.66)	48.42 ± 10.77 (66.65)	9.00 ± 2.30 (13.12)
		RV	1.03 ± 0.03 (1.06)	18.19 ± 0.33 (18.70)	53.06 ± 11.29 (71.32)	9.97 ± 2.39 (14.09)
	1000 lux	FW	0.85 ± 0.01 (0.87)	0.18 ± 0.01 (0.19)	72.15 ± 4.97 (74.64)	28.35 ± 2.33 (31.19)
		RV	0.86 ± 0.01 (0.87)	0.18 ± 0.01 (0.19)	74.71 ± 4.37 (77.28)	29.69 ± 2.3 (32.36)

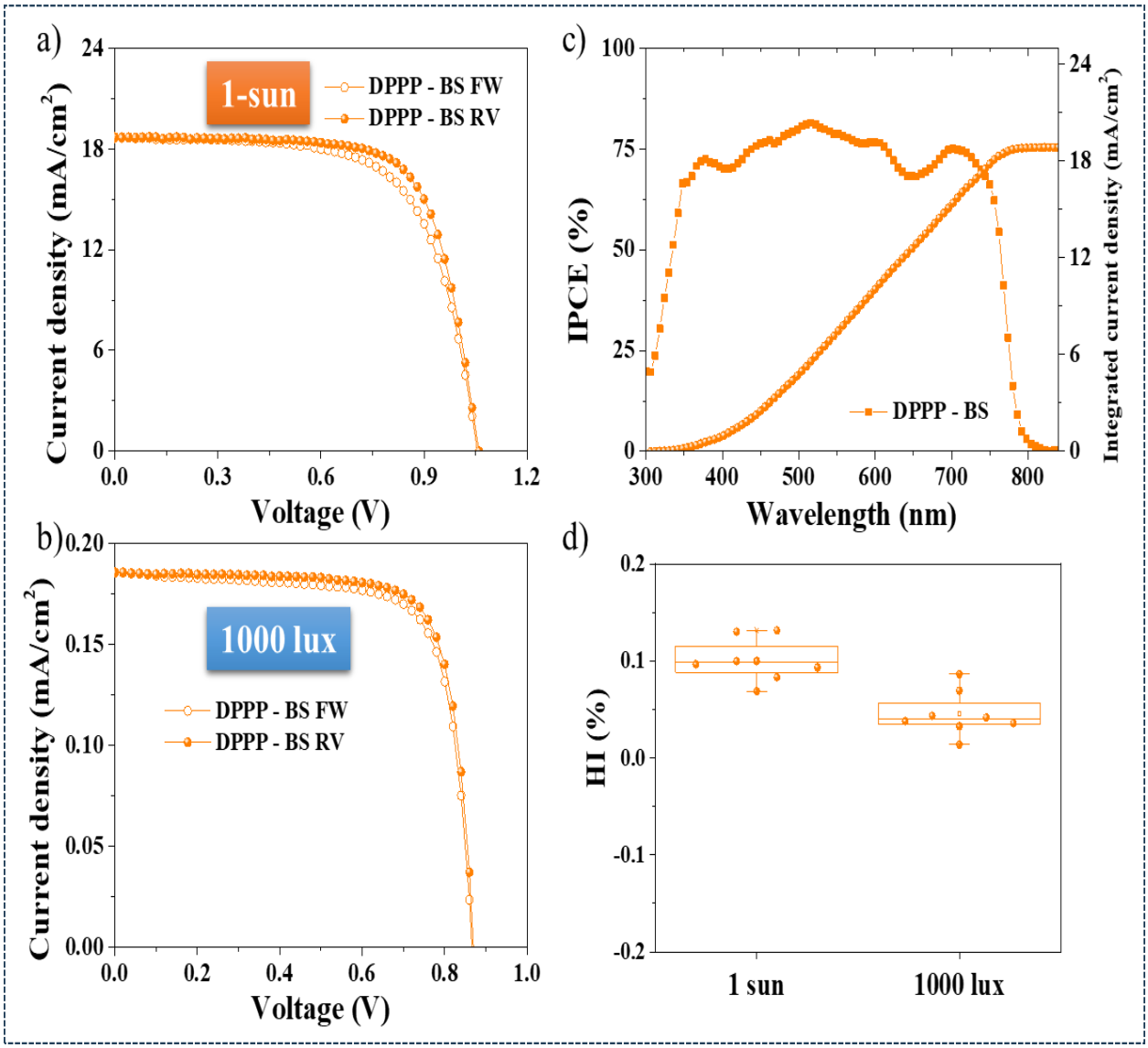

Figure 4.11. a) JV curve of champion device with DPPP – BS under 1 sun, STC, b) IPCE spectra of device with DPPP – BS, c) JV curve of champion device with DPPP – BS under 1000 lux, LED illumination, d) HI of device with DPPP – BS under 1 sun and indoor conditions.

Figure 4.12(a) and **Figure 4.12(b)** presents the SEM and XRD characterizations of as-deposited (fresh) and aged DPPP-BS samples. The morphology of the fresh DPPP-BS sample closely resembles that of the fresh DPPP sample, with some triangular shaped features. The XRD plot of the fresh DPPP-BS sample shows a diffraction peak at 11.1°. The morphology of the aged DPPP-BS sample remains like the fresh sample, with no observable whitish or elongated crystals. After analyzing the XRD plot of the aged DPPP-BS sample, we observed that the (100) α-peak at 14.1°

decreased by only 49%, and there is no evidence of the delta-phase peak at 11.6°, indicating improved resistance to extrinsic degradation factors (**Figure 4.12b**).

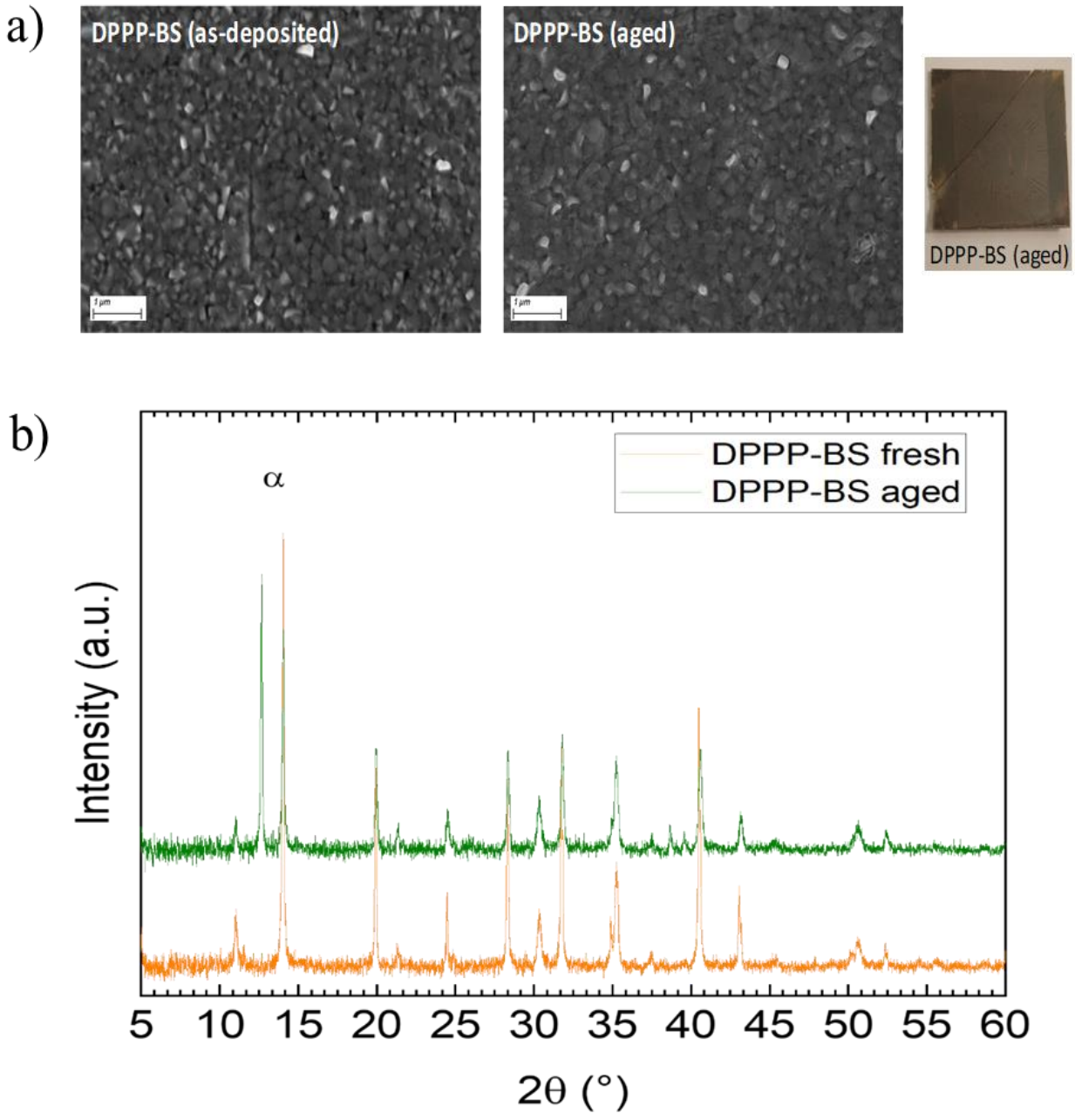

Figure 4.12. a) SEM planar views of the DPPP-BS sample analysed as-deposited (fresh) and after 1 year of aging in air. On the right is a photo of the aged sample, b) XRD spectra of samples with DPPP-BS as deposited (fresh) and after one year of storage in ambient environment.

4.3.8 Thermal Stability Testing

The stability of both the Ref and passivated devices was investigated by subjecting them to thermal stress at 85°C in dark (according to ISOS T-1 protocol). The devices were then measured at different aging times, not only under 1 sun, STC, but also under indoor conditions (1000 lux) [64]. The devices were only encapsulated with Kapton tape to minimize the harmful impact of extrinsic

degradation factors. While this type of encapsulation provides only partial protection against moisture and oxygen permeation, it helps slow down environmental-induced degradation. Among all devices, the DPPP-BS passivated device exhibited the highest thermal stability, with a T80 of 822 h, followed by the DPPP-based device (T80 = 814 h) under thermal stress measured under 1-sun STC conditions, as given in **Figure 4.13(a)**.

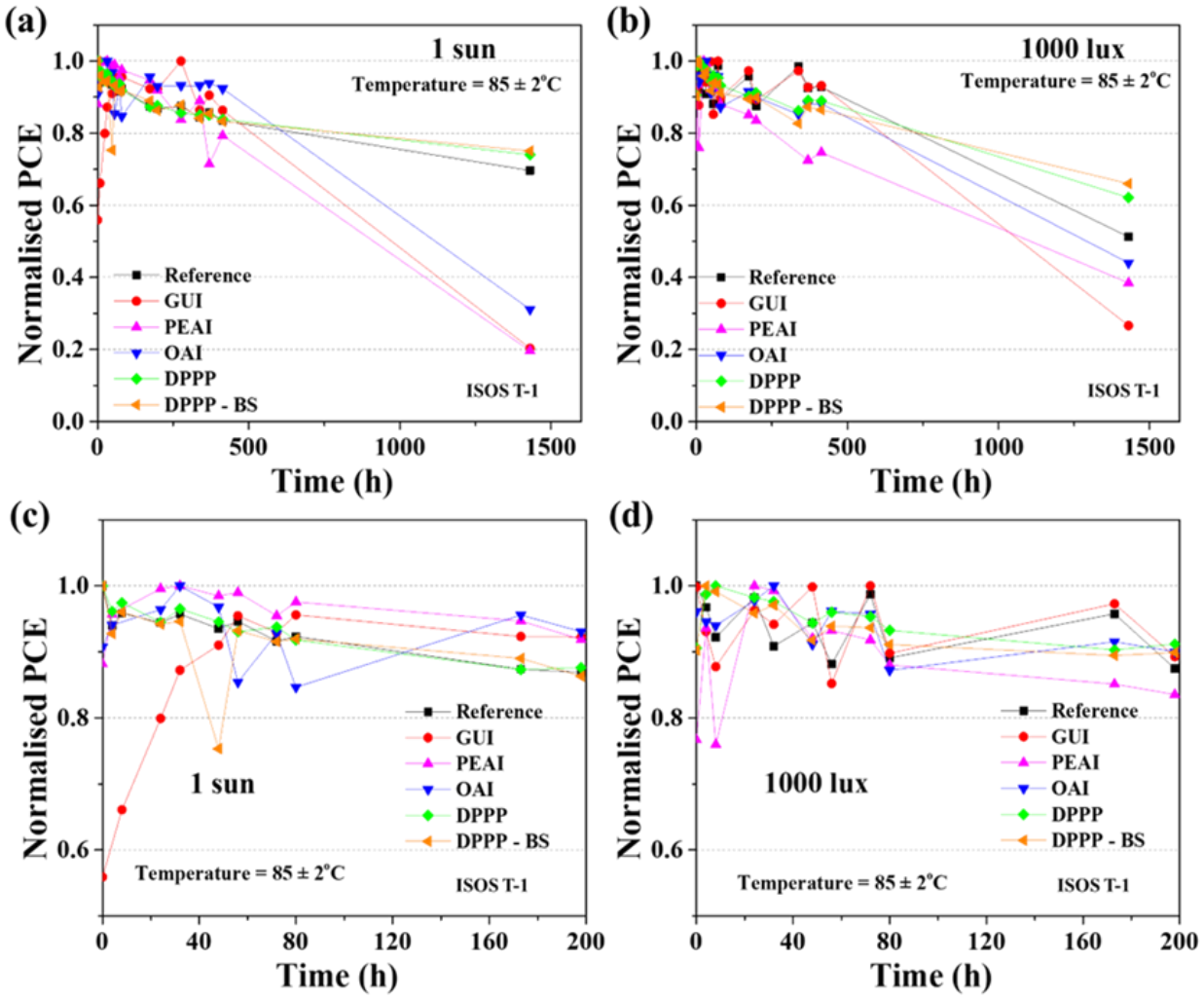

Figure 4.13. Thermal stability of devices with different passivation layers under a) 1 sun (STC, AM 1.5 1000 W/m^2) and b) 1000 lux (indoor conditions) according to ISOS T-1 (thermal stress at 85°C). Thermal stability of devices with different passivation layers in the first 200 h under c) 1 sun (STC, AM 1.5 1000 W/m^2) and d) 1000 lux (indoor conditions) according to ISOS T-1 (thermal stress at 85°C).

Even under indoor conditions, the DPPP-based device exhibited the highest thermal stability, reaching a T80 of 753 h, followed by DPPP-BS device at 734 h, as given in **Figure 4.13(b)**. In **Figure 4.13(c-d)**, the thermal stability plot focuses only on the starting 200 h of the test, during which the Iodine based passivators (GUI, PEAI and OAI) had slightly higher stability than the Ref and DPPP-based passivations. However, after 200 h the Iodine based passivations showed lower stability compared to DPPP, DPPP–BS and even respect to the Ref cell under both 1-sun and

indoor conditions. This could be attributed to I^- migration, I_2 vapor formation, or I^- vacancies creation, which induce the degradation of the device after some initial thermal stress [65–67]. In contrast, the DPPP-based passivation appears to improve stability probably because of the strong bonding between the P atoms and the uncoordinated Pb^+ atoms [37]. However, a more in-depth analysis is needed to better understand the degradation mechanisms, which is beyond the scope of the current study.

4.4 Conclusion

In summary, in this study, the effects of various iodine-based passivation layers (GUI, PEAI, and OAI) and a novel DPPP passivation layer on top surface of triple-cation PVK in n-i-p PSCs for IPVs. Structural, morphological, and optoelectrical analyses confirmed the benefits of these passivation layers. Under indoor illumination, all devices, including non-passivated Refs, achieved impressive iPCEs exceeding 30%. However, the difference in iPCE between the Ref and optimized passivated devices was minimal, with the highest improvement of less than 10% for PEAI-based device achieving an iPCE = 34.47%. In contrast, under standard 1-sun conditions, the passivated devices showed a more substantial performance boost, with the highest of over 20% enhancement in PCE of OAI-based device compared to the Ref device, with the best cell showing a PCE of 20.20%. XRD and SEM analysis of year-old samples stored in air environment (dark, RT and a RH = 40% ± 10%) revealed the exceptional stability of DPPP treated films. Under indoor conditions, devices with DPPP and DPPP - BS achieved the highest thermal stability, with T80 values of 753 and 734 h respectively, while iodine-based passivators maintained stability for only around 200 h. This study offers key insights into enhancing PSC performance and stability with passivation layers under indoor conditions, highlighting the potential of innovative Lewis base passivation materials in n-i-p structures. Future work will explore DPPP passivation on wide-bandgap PVKs, focusing on optimizing concentration and thickness for enhanced device performance and stability.

References

1. Lee, H. K. H. *et al.* Outstanding Indoor Performance of Perovskite Photovoltaic Cells – Effect of Device Architectures and Interlayers. *Solar RRL* **3**, (2019).

2. Michaels, H. *et al.* Emerging indoor photovoltaics for self-powered and self-aware IoT towards sustainable energy management. *Chem Sci* **14**, 5350–5360 (2023).

3. Matiko, J. W., Grabham, N. J., Beeby, S. P. & Tudor, M. J. Review of the application of energy harvesting in buildings. *Meas Sci Technol* **25**, 012002 (2014).

4. Chakraborty, A. *et al.* Photovoltaics for indoor energy harvesting. *Nano Energy* **128**, 109932 (2024).

5. https://www.nrel.gov/pv/cell-efficiency.html.

6. Kumar, P., Shankar, G. & Pradhan, B. Recent progress in bifacial perovskite solar cells. *Applied Physics A* **129**, 63 (2023).

7. Kim, J. Y., Lee, J.-W., Jung, H. S., Shin, H. & Park, N.-G. High-Efficiency Perovskite Solar Cells. *Chem Rev* **120**, 7867–7918 (2020).

8. Sharma, S. K. *et al.* HaHc (Hydroxylamine Hydrochloride) Assisted Dual Surface Passivation via Charge Neutralization and Coordination Bond Formation of $Cs_2AgBiBr_6$ Double Perovskite for Solar Cell Application. *The Journal of Physical Chemistry C* **128**, 1024–1033 (2024).

9. Kumar, P., Mahapatra, A. & Pradhan, B. Perovskite Solar Cells: Fundamental to Commercialization. in 149–214 (2024). doi:10.1007/978-3-031-57663-8_6.

10. Shankar, G., Kumar, P. & Pradhan, B. Synergetically Optimized Perovskite Subcells with a V_{OC} beyond 2 V in Tandem Architecture. *Energy & Fuels* **37**, 12291–12300 (2023).

11. Tiwari, S. K., Shankar, G., Kumar, P., Laref, A. & Pradhan, B. Efficiency Approaching 26% in Triple Cation Mixed Halide Perovskite Solar Cells by Numerical Simulation. *IEEE J Photovolt* **13**, 242–249 (2023).

12. He, X. *et al.* 40.1% Record Low-Light Solar-Cell Efficiency by Holistic Trap-Passivation using Micrometer-Thick Perovskite Film. *Advanced Materials* **33**, (2021).

13. Shi, Z. *et al.* Enhanced Indoor Perovskite Solar Cells: Mitigating Interface Defects and Charge Transport Losses with Polyarene-Based Hole-Selective Layers. *Adv Energy Mater* (2024) doi:10.1002/aenm.202404234.

14. Liu, C. *et al.* Flexible Indoor Perovskite Solar Cells by In Situ Bottom-Up Crystallization Modulation and Interfacial Passivation. *Advanced Materials* **36**, (2024).

15. Shi, Z.-E. *et al.* Achieving over 42 % indoor efficiency in wide-bandgap perovskite solar cells through optimized interfacial passivation and carrier transport. *Chemical Engineering Journal* **498**, 155512 (2024).

16. Ma, Q. *et al.* One-step dual-additive passivated wide-bandgap perovskites to realize 44.72%-efficient indoor photovoltaics. *Energy Environ Sci* **17**, 1637–1644 (2024).

17. Kumar, P., Shankar, G. & Pradhan, B. Improved performance study of monolithic all perovskite tandem solar cell in nip and pin structure. *Mater Today Proc* **66**, 3392–3396 (2022).

18. Chen, R. *et al.* Reduction of bulk and surface defects in inverted methylammonium- and bromide-free formamidinium perovskite solar cells. *Nat Energy* **8**, 839–849 (2023).

19. Shankar, G., Kumar, P. & Pradhan, B. All-perovskite two-terminal tandem solar cell with 32.3% efficiency by numerical simulation. *Materials Today Sustainability* **20**, 100241 (2022).

20. Laxmi, Singh, S. & Kabra, D. Defects in Solution-Processed Perovskite Semiconductors: Photophysics and Impact on Solar Cell Performance. in *Halide Perovskites for Photonics* 8-1-8–34 (AIP Publishing LLCMelville, New York, 2021). doi:10.1063/9780735423633_008.

21. Stranks, S. D. Nonradiative Losses in Metal Halide Perovskites. *ACS Energy Lett* **2**, 1515–1525 (2017).

22. Sherkar, T. S. *et al.* Recombination in Perovskite Solar Cells: Significance of Grain Boundaries, Interface Traps, and Defect Ions. *ACS Energy Lett* **2**, 1214–1222 (2017).

23. Zhuang, J. *et al.* Interfacial Passivation for Perovskite Solar Cells: The Effects of the Functional Group in Phenethylammonium Iodide. *ACS Energy Lett* **4**, 2913–2921 (2019).

24. Han, E. *et al.* High-Performance Indoor Perovskite Solar Cells by Self-Suppression of Intrinsic Defects via a Facile Solvent-Engineering Strategy. *Small* **20**, (2024).

25. Han, E. *et al.* High-Performance Indoor Perovskite Solar Cells by Self-Suppression of Intrinsic Defects via a Facile Solvent-Engineering Strategy. *Small* **20**, (2024).

26. Dong, C. *et al.* Lead Oxalate-Induced Nucleation Retardation for High-Performance Indoor and Outdoor Perovskite Photovoltaics. *ACS Appl Mater Interfaces* **12**, 836–843 (2020).

27. Cheng, R. *et al.* Tailoring Triple-Anion Perovskite Material for Indoor Light Harvesting with Restrained Halide Segregation and Record High Efficiency Beyond 36%. *Adv Energy Mater* **9**, (2019).

28. Mathews, I. *et al.* Self-Powered Sensors Enabled by Wide-Bandgap Perovskite Indoor Photovoltaic Cells. *Adv Funct Mater* **29**, (2019).

29. Xu, J. *et al.* 30% efficient triple-cation perovskite solar cells under indoor illumination enabled by rare earth $EuCl_3$ doping. *Sustain Energy Fuels* **7**, 3404–3411 (2023).

30. Cheng, R. *et al.* An Air Knife–Assisted Recrystallization Method for Ambient-Process Planar Perovskite Solar Cells and Its Dim-Light Harvesting. *Small* **15**, (2019).

31. Lee, M. *et al.* Enhanced Hole-Carrier Selectivity in Wide Bandgap Halide Perovskite Photovoltaic Devices for Indoor Internet of Things Applications. *Adv Funct Mater* **31**, (2021).

32. Castriotta, L. A. *et al.* A universal multi-additive strategy to enhance efficiency and stability in inverted perovskite solar cells. *Nano Energy* **109**, 108268 (2023).

33. Zhang, H. *et al.* Fluorine-Containing Passivation Layer via Surface Chelation for Inorganic Perovskite Solar Cells. *Angewandte Chemie* **135**, (2023).

34. Guo, Z. *et al.* A Universal Method of Perovskite Surface Passivation for $CsPbX_3$ Solar Cells with V_{OC} over 90% of the S-Q limit. *Adv Funct Mater* **32**, (2022).

35. Zhu, X. *et al.* Photoinduced Cross Linkable Polymerization of Flexible Perovskite Solar Cells and Modules by Incorporating Benzyl Acrylate. *Adv Funct Mater* **32**, (2022).

36. Li, Z. *et al.* Minimized surface deficiency on wide-bandgap perovskite for efficient indoor photovoltaics. *Nano Energy* **78**, 105377 (2020).

37. Li, C. *et al.* Rational design of Lewis base molecules for stable and efficient inverted perovskite solar cells. *Science (1979)* **379**, 690–694 (2023).

38. Chen, Q. *et al.* Controllable Self-Induced Passivation of Hybrid Lead Iodide Perovskites toward High Performance Solar Cells. *Nano Lett* **14**, 4158–4163 (2014).

39. Chen, P. *et al.* In Situ Growth of 2D Perovskite Capping Layer for Stable and Efficient Perovskite Solar Cells. *Adv Funct Mater* **28**, (2018).

40. Wang, H. *et al.* Interfacial Residual Stress Relaxation in Perovskite Solar Cells with Improved Stability. *Advanced Materials* **31**, (2019).

41. Aharon, S. & Etgar, L. Two Dimensional Organometal Halide Perovskite Nanorods with Tunable Optical Properties. *Nano Lett* **16**, 3230–3235 (2016).

42. Wu, Y. *et al.* Realizing High-Efficiency Perovskite Solar Cells by Passivating Triple-Cation Perovskite Films. *Solar RRL* **6**, (2022).

43. Kirchartz, T., Márquez, J. A., Stolterfoht, M. & Unold, T. Photoluminescence-Based Characterization of Halide Perovskites for Photovoltaics. *Adv Energy Mater* **10**, (2020).

44. Ramanujam, R. *et al.* Interfacial Layer Materials with a Truxene Core for Dopant-Free NiO_x -Based Inverted Perovskite Solar Cells. *Small* **20**, (2024).

45. Hoke, E. T. *et al.* Reversible photo-induced trap formation in mixed-halide hybrid perovskites for photovoltaics. *Chem Sci* **6**, 613–617 (2015).

46. Bischak, C. G. *et al.* Origin of Reversible Photoinduced Phase Separation in Hybrid Perovskites. *Nano Lett* **17**, 1028–1033 (2017).

47. Cacovich, S. *et al.* Light-Induced Passivation in Triple Cation Mixed Halide Perovskites: Interplay between Transport Properties and Surface Chemistry. *ACS Appl Mater Interfaces* **12**, 34784–34794 (2020).

48. Pydzińska-Białek, K. *et al.* Understanding the Interfaces between Triple-Cation Perovskite and Electron or Hole Transporting Material. *ACS Appl Mater Interfaces* **12**, 30399–30410 (2020).

49. Gautam, S. K. *et al.* Reversible Photoinduced Phase Segregation and Origin of Long Carrier Lifetime in Mixed-Halide Perovskite Films. *Adv Funct Mater* **30**, (2020).

50. Staub, F. *et al.* Beyond Bulk Lifetimes: Insights into Lead Halide Perovskite Films from Time-Resolved Photoluminescence. *Phys Rev Appl* **6**, 044017 (2016).

51. Barichello, J., Shankar, G., Mariani, P., Di Carlo, A. & Matteocci, F. Unveiling the potential of Cs2AgBiBr6 perovskites for next-generation see-through photovoltaics. *Mater Today Energy* **46**, 101725 (2024).

52. Min, H. *et al.* Efficient, stable solar cells by using inherent bandgap of α-phase formamidinium lead iodide. *Science (1979)* **366**, 749–753 (2019).

53. Kim, M. *et al.* Methylammonium Chloride Induces Intermediate Phase Stabilization for Efficient Perovskite Solar Cells. *Joule* **3**, 2179–2192 (2019).

54. Parashar, M., Shukla, V. K. & Singh, R. Metal oxides nanoparticles via sol–gel method: a review on synthesis, characterization and applications. *Journal of Materials Science: Materials in Electronics* **31**, 3729–3749 (2020).

55. Yang, B. *et al.* Interfacial Passivation Engineering of Perovskite Solar Cells with Fill Factor over 82% and Outstanding Operational Stability on n-i-p Architecture. *ACS Energy Lett* **6**, 3916–3923 (2021).

56. Du, B., He, K., Zhao, X. & Li, B. Defect Passivation Scheme toward High-Performance Halide Perovskite Solar Cells. *Polymers (Basel)* **15**, 2010 (2023).

57. Dagar, J., Castro-Hermosa, S., Lucarelli, G., Cacialli, F. & Brown, T. M. Highly efficient perovskite solar cells for light harvesting under indoor illumination via solution processed SnO2/MgO composite electron transport layers. *Nano Energy* **49**, 290–299 (2018).

58. Srathongsian, L. *et al.* Cs and Br tuning to achieve ultralow-hysteresis and high-performance indoor triple cation perovskite solar cell with low-cost carbon-based electrode. *iScience* **27**, 109306 (2024).

59. Bulloch, A., Wang, S., Ghosh, P. & Jagadamma, L. K. Hysteresis in hybrid perovskite indoor photovoltaics. *Philosophical Transactions of the Royal Society A: Mathematical, Physical and Engineering Sciences* **380**, (2022).

60. Kakavelakis, G. *et al.* Extending the Continuous Operating Lifetime of Perovskite Solar Cells with a Molybdenum Disulfide Hole Extraction Interlayer. *Adv Energy Mater* **8**, (2018).

61. Leguy, A. M. A. *et al.* Reversible Hydration of $CH_3NH_3PbI_3$ in Films, Single Crystals, and Solar Cells. *Chemistry of Materials* **27**, 3397–3407 (2015).

62. Calabrò, E. *et al.* Easy Strategy to Enhance Thermal Stability of Planar PSCs by Perovskite Defect Passivation and Low-Temperature Carbon-Based Electrode. *ACS Appl Mater Interfaces* **12**, 32536–32547 (2020).

63. Vincent, B. R., Robertson, K. N., Cameron, T. S. & Knop, O. Alkylammonium lead halides. Part 1. Isolated PbI_6^{4-} ions in $(CH_3NH_3)_4PbI_6 \cdot 2H_2O$. *Can J Chem* **65**, 1042–1046 (1987).

64. Khenkin, M. V. *et al.* Consensus statement for stability assessment and reporting for perovskite photovoltaics based on ISOS procedures. *Nat Energy* **5**, 35–49 (2020).

65. Zhang, D., Li, D., Hu, Y., Mei, A. & Han, H. Degradation pathways in perovskite solar cells and how to meet international standards. *Commun Mater* **3**, 58 (2022).

66. Fu, F. *et al.* I_2 vapor-induced degradation of formamidinium lead iodide based perovskite solar cells under heat–light soaking conditions. *Energy Environ Sci* **12**, 3074–3088 (2019).

67. Li, N. *et al.* Microscopic Degradation in Formamidinium-Cesium Lead Iodide Perovskite Solar Cells under Operational Stressors. *Joule* **4**, 1743–1758 (2020).

Chapter 5
To Dope or Not to Dope: Investigating the Necessity of Spiro-OMeTAD Doping in Perovskite Solar Cells for IPVs

The study presented in this chapter is still in progress and has not yet reached its final objectives. A complete version of the study will be published later, likely after my PhD defence. However, as I conceptualized and initiated this project, I have been granted special permission to present the results obtained thus far, as my thesis submission deadline precedes the planned manuscript submission deadline. I have received special permission from the Hybrid Solar Cells (HSC) group at Tampere University, Finland, where I initiated the project. The group is now working on completing the project to achieve the desired outcomes. Given that my stay in Finland was for a limited duration, I was unable to finish the entire project independently. Nevertheless, the results I obtained during my time there were encouraging, leading the group and me to decide to continue working on the project rather than publishing the initial findings. Therefore, the final conclusions and results will be published later, and I have been granted permission to include part of these results in my thesis.

5.1 Motivation

To improve the performance and stability of PSCs under standard 1-sun illumination, numerous strategies have been reported in the literature, yielding promising results. However, in some cases, these strategies enhance one aspect (performance or stability) at the expense of the other. Consequently, efforts have been refocused on finding solutions to maintain a delicate balance between performance and stability for PSCs operating in outdoor conditions. In contrast to outdoor conditions, indoor environments present several orders of magnitude lower light intensities. Consequently, it is yet largely unexplored if the applied strategies for improving the performance of PSCs operating outdoor, are equally important for PSCs operating indoor. Since IPV is an emerging field and a lot is yet to be explored and unlocked, this study aims to address this gap to some extent. Specifically, this study attempts to find an answer to a question if the traditional dopants of Spiro-OMeTAD HTL in n-i-p structure PSCs operating outdoor, are equally important for the performance of PSCs operating indoor, or the case is otherwise.

5.2 Introduction

To date, various types of HTLs have been extensively investigated in n-i-p structure PSCs, leading to significant advancements in cost-effectiveness, performance, and stability. Despite these developments, state-of-the-art PSCs with PCEs exceeding 25% still rely on the benchmark HTL, spiro-OMeTAD [1], due to its large band gap, deep HOMO energy level, solution processability, and good thermal stability [2]. Achieving high performance with spiro-OMeTAD, however, requires doping with molecular additives to enhance hole mobility, electrical conductivity, and energy band alignment with the absorber PVK layer. Without doping, its low intrinsic hole mobility leads to high R_S, low FF, and low V_{OC} [3,4], limiting PCEs to around 10% due to inefficient charge transport and increased recombination [5].

The most common molecular additives for doping spiro-OMeTAD include tBP, Li-TFSI, and FK209 Co(III) [6–9]. Snaith and Grätzel [10] reported that doping spiro-OMeTAD with Li-TFSI increases hole mobility from 1.6×10^{-4} to 1.6×10^{-3} cm² V^{-1} s^{-1}, while Juarez-Perez et al. [11] found that Li-TFSI enhances conductivity but can cause film inhomogeneity. In contrast, tBP smooths the film surface and promotes uniform Li-TFSI distribution, improving the spiro-OMeTAD-perovskite interface. Additionally, Noh et al. [12] reported that FK209 oxidizes spiro-OMeTAD even in the dark, generating additional carriers and increasing conductivity. Together, these dopants enhance the spiro-OMeTAD conductivity, surface smoothness, and dopant distribution, ultimately optimizing its performance and boosting PSCs efficiency.

Apart from the beneficial impacts of the spiro-OMeTAD dopants outlined above, tBP and Li-TFSI present challenges [2,13] that significantly impact device stability. Both are hygroscopic and chemically sensitive, leading to ion accumulation [14,15], PVK corrosion [16–18], and accelerated degradation under light or applied bias due to Li^+ ion migration. Additionally, the slow oxidation of spiro-OMeTAD by Li-TFSI under ambient conditions compromises device stability and reproducibility [14]. The low boiling point of tBP exacerbates these issues, as its evaporation forms pinholes and aggregates Li-TFSI residues [19], while its corrosive nature dissolves PbI_2, further degrading the perovskite layer [20].

Unlike traditional solar cells that convert sunlight into electricity, IPVs have emerged as a sustainable solution to power billions of wireless IoT sensors by converting low intensity indoor lighting into electricity [21]. Among IPV technologies, PVK-based IPVs are particularly promising due to their superior material and optoelectronic properties [22]. Most reported perovskite-based IPV devices use doped spiro-OMeTAD as the HTL, as its dopants reduce resistive losses and enhance

iPCE [23,24]. However, performance under standard 1-sun illumination does not always correlate with indoor performance, as observed in technologies like CIGS and Si [25]. Inspired by this, our group recently demonstrated that under indoor lighting, the reduced impact of R_s enables PVK-based devices without doped spiro-OMeTAD to achieve comparable iPCEs to their doped counterparts, while offering improved stability due to the absence of dopant-induced degradation [26]. However, these findings were based on mesoporous devices requiring high-temperature TiO_2 sintering, incompatible with flexible substrates. As IoT adoption grows, flexible, low-temperature, and stable MHP-based IPV devices will be essential to meet future demands.

In this study, we fabricated low-temperature, planar n-i-p structure devices using a SnO_2 ETL that requires annealing at just 100°C, making it compatible with flexible substrates. While ITO substrates were used for this research, the protocol can easily be adapted for flexible substrates in the future. The champion doped-spiro-based device achieved an iPCE of 29.36% in reverse bias, while the champion undoped-spiro-based device delivered 28.37% in forward bias under 1000 lux WLED illumination, which is the highest reported iPCE for a PVK device based on undoped spiro-OMeTAD HTL under similar conditions to date. Under extremely low-light conditions (50 lux), undoped spiro-based devices outperformed their doped counterparts. At 50 lux, the highest iPCE of 13.65% was achieved under reverse bias with reduced hysteresis for the undoped spiro-based device. In contrast, doped spiro-based devices demonstrated poor performance, achieving a maximum iPCE of only ~4% and exhibiting significant hysteresis. These initial results confirm and strengthen our group's previous findings and highlights the critical role of the ETL material in optimizing device performance under low light illumination.

5.3 Results and Discussions

As described earlier, we employed the conventional n-i-p configuration of glass/ITO/SnO_2/PVK/Spiro-OMeTAD/Au to fabricate planar triple-cation mixed halide PVK PV cells. For comparative analysis, devices were fabricated using both doped and undoped Spiro-OMeTAD as the HTL. Hereafter, devices incorporating doped Spiro-OMeTAD are referred to as "Doped-Spiro" while those with undoped Spiro-OMeTAD are referred to as "Undoped-Spiro." Detailed fabrication protocols for all devices are provided in **Chapter 3**. It is important to note that the absorber perovskite composition used in this study is identical with our previous study detailed in **Chapter 4**, with the exception of a few precursors that were sourced from different suppliers during its synthesis in the current study. These differences are outlined in **Chapter 3**. While SnO_2 nano-particles solution were sourced from the same company and its deposition parameters were exactly the same. Therefore, before assessing the performance of fabricated

devices, we measured the absorption spectra of Spiro-OMeTAD (doped and undoped), as it was the only functional layer in the device with a concentration different from that used in the previous study.

UV–visible absorption spectra for the doped- and undoped-spiro-OMeTAD films deposited on bare glass substrates were measured in the wavelength range of 300–850 nm. As shown in **Figure 5.1**, both undoped and doped spiro-OMeTAD (doped with LiTFSI, tBP, and FK209) exhibit a strong absorption peak around 390 nm, which corresponds to the neutral spiro-OMeTAD absorption [27]. However, in the spectra of doped spiro-OMeTAD, a significant increase in absorbance is observed in the wavelength range of 425–560 nm compared to the undoped counterpart, along with the appearance of a distinct new absorption peak near 520 nm. This broad peak is attributed to the oxidation of spiro-OMeTAD [28]. In contrast, no such peak is observed in the absorption spectrum of undoped spiro-OMeTAD, indicating the absence of oxidation. Previous studies have reported that the formation of oxidized-state spiro-OMeTAD enhances hole mobility [29,30], which plays a crucial role in improving device performance.

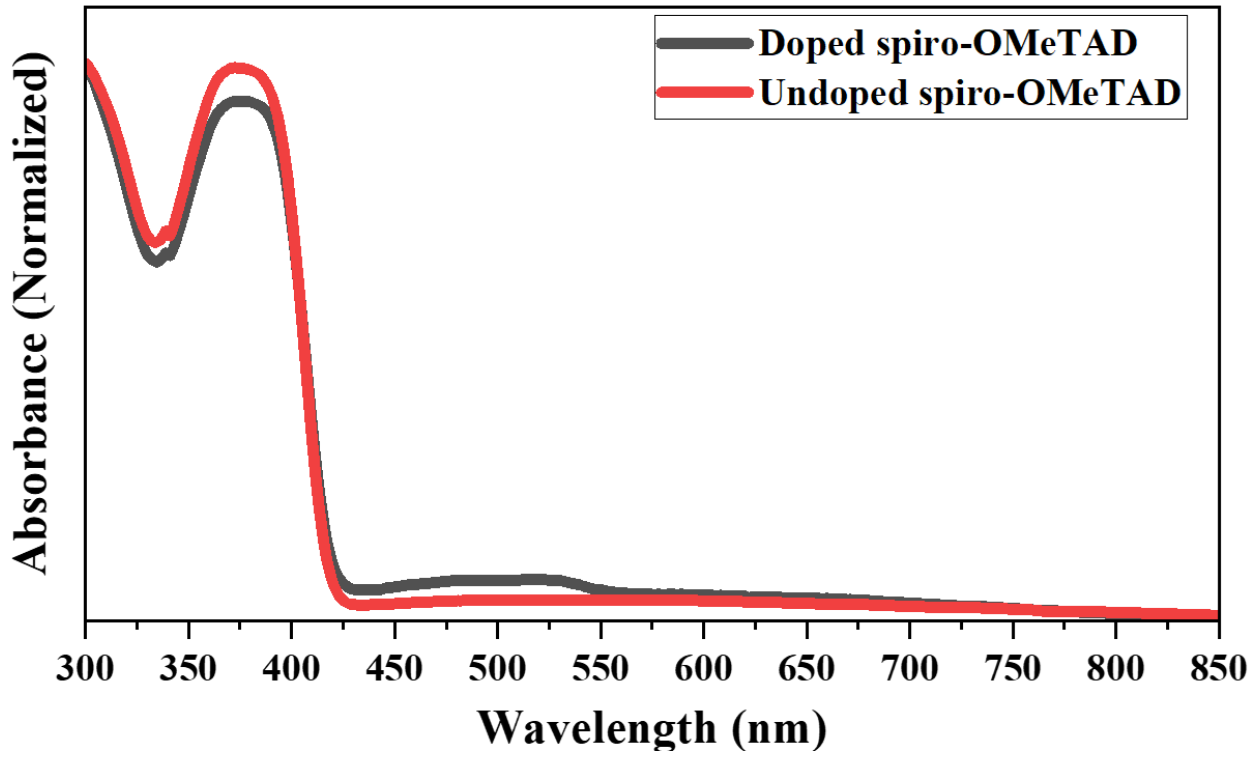

Figure 5.1. UV-vis absorption of doped- and undoped- Spiro-OMeTAD.

5.3.1 Measurements Under Standard 1-Sun Illumination

Firstly, we characterized both types of devices under standard 1-Sun illumination by measuring J–V curves for 57 devices in both forward and reverse scans at a scan rate of 50 mV/s. **Figure 5.2(a-d)** show the statistical distribution of PV parameters for both device types. Doped-Spiro devices exhibited significantly higher PCEs due to higher FFs and J_{SC}s in both scan directions. However, the Undoped-Spiro devices achieved higher V_{OC}s. Interestingly, Doped-Spiro devices showed higher average PCEs in reverse scans but lower in forward scans, while Undoped-Spiro devices exhibited the opposite trend.

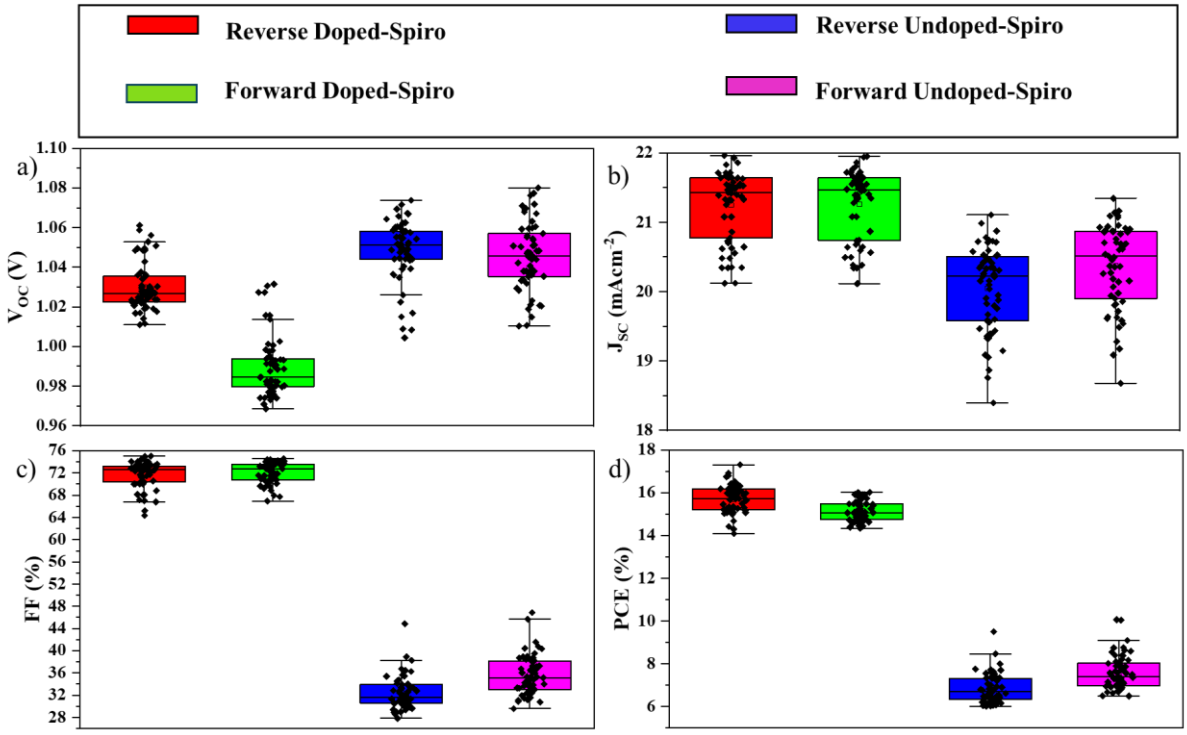

Figure 5.2. Box chart diagrams of PV parameters, a) V_{oc}, b) J_{sc}, c) FF, and d) PCE of Doped- and Undoped-Spiro devices under standard 1-sun illumination.

A critical challenge affecting both the performance and stability of PSCs is the presence of J–V hysteresis. The HI, as detailed in **Chapter 2**, quantifies the extent of hysteresis in these devices. The **Figure 5.3** illustrates the HI of 57 devices of both types of devices under standard 1-sun illumination. As can be seen, the HI values differ significantly between the two device types. The Doped-Spiro devices predominantly exhibit positive hysteresis, with only a few devices showing negative hysteresis, resulting in an average HI of 3.92%. In contrast, the Undoped-Spiro devices consistently display negative hysteresis, with an average HI of -10.93%. The predominant negative hysteresis, also referred to as inverted hysteresis, observed in Undoped-Spiro devices aligns with findings in the literature. Studies have highlighted that the interface between the perovskite and

charge transport layers, such as the ETL and HTL, plays a crucial role in the occurrence of the inverted hysteresis effect due to unfavourable band offset [31,32]. Additionally, as the undoped Spiro-OMeTAD could lead to weaker separation of charges in devices compared to doped-Spiro-OMeTAD, this also causes negative hysteresis in PSCs [33].

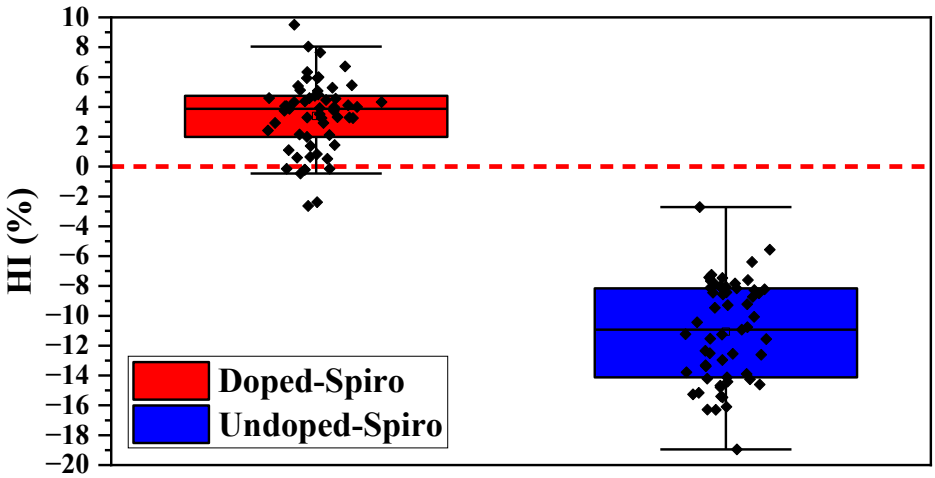

Figure 5.3. HI of doped- and undoped- Spiro-OMeTAD devices evaluated under 1-sun illumination.

Our champion Doped-Spiro device achieved a PCE of 17.3% in the reverse scan, with a V_{oc} of 1.06 V, J_{sc} of 21.86 mA/cm², and FF of 75.00%, as shown in **Figure 5.4(a)**. In comparison, the champion Undoped-Spiro device delivered a PCE of 10.03% in the forward scan, with a V_{oc} of 1.00 V, J_{sc} of 21.10 mA/cm², and FF of 44.84%. The PV parameters of both champion devices are also provided in the inset of **Figure 5.4(a)**.

A key difference between the two devices is the FF, which is significantly higher in the Doped-Spiro device. According to the literature, the higher FF of the Doped-Spiro devices can be attributed to its lower R_S, efficient hole collection by the doped Spiro-OMeTAD HTL, and well-matched energy level alignment between the PVK absorber and the doped Spiro-OMeTAD HTL [34]. However, to validate these observations, characterizations are necessary to be performed to confirm and will be carried out in the later stages of manuscript preparation.

To validate our results, EQE measurements are performed for both champion devices and presented in **Figure 5.4(b)**. Both devices exhibit high photon-to-electron conversion efficiencies, exceeding 80% in the wavelength range of 400 to 680 nm. Beyond this range, the EQE of the Undoped-Spiro device begins to decrease, while the EQE of the Doped-Spiro device shows a rise, continuing to increase up to 750 nm. The integrated J_{SC} values derived from the EQE

measurements closely align with the J_{SC} values obtained from the J–V characteristics of both champion devices and ensure the accuracy of the obtained results.

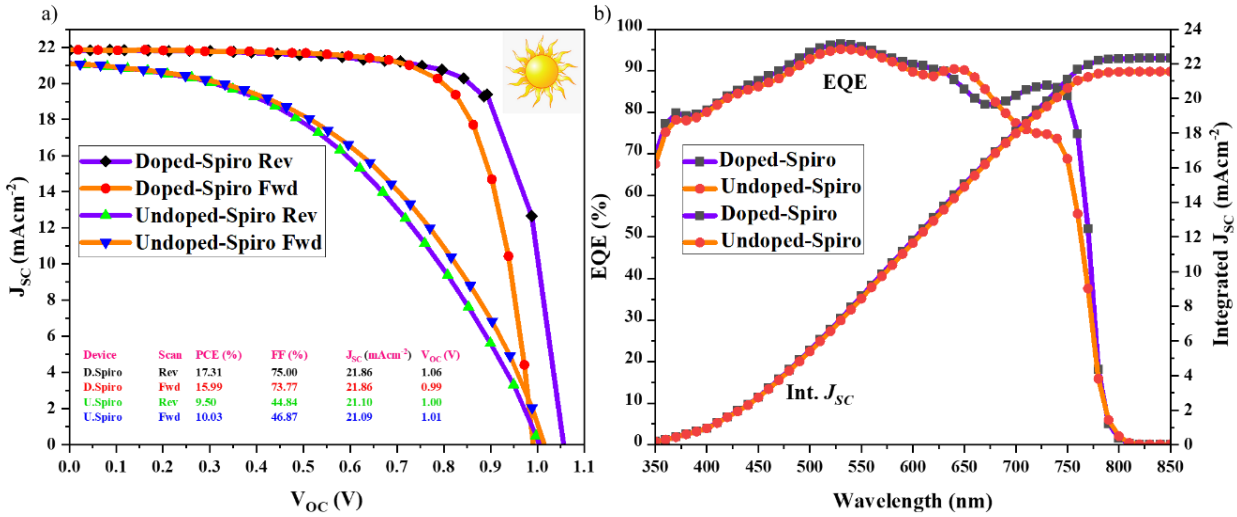

Figure 5.4. a) J-V curves and b) EQE and integrated J_{SC}s of champion devices based on doped- and undoped- Spiro-OMeTAD HTL obtained under 1-sun illumination.

5.3.2 Measurements Under Indoor Illumination

We then evaluated the performance of both types of devices under WLED indoor lighting at various light intensities, ranging from 1000 lux to the extremely dim 50 lux. The box plot diagrams shown in **Figure 5.5(a-d)** present the PV parameters of both types of devices measured under 1000 lux WLED illumination, with a power density of approximately 0.32 mW cm^{-2}. As can be seen in **Figure 5.5(b)**, the FF is a distinguishing parameter, consistent with the 1-sun data discussed earlier. The Doped-Spiro devices exhibit significantly higher FF values in the reverse scan compared to the Undoped-Spiro devices. However, compared to the 1-sun data, the FF values of the Undoped Spiro devices are notably higher under low-light conditions. As previously mentioned, the lower FF values of the Undoped-Spiro devices under standard 1-sun illumination are attributed to the significant negative impact of R_s on device performance due to the absence of dopants in the HTL of device. Nevertheless, the higher FF values of these devices under low light illumination indicate a reduction in the effect of R_s at lower light intensities [35].

The increased FF under 1000 lux LED illumination significantly enhanced the performance of Undoped-Spiro devices, bringing them closer to their doped counterparts, as shown in **Figure 5.5(b)**. This improvement was accompanied by increases in V_{oc} and J_{sc}. It is important to note that the summarized data represents only the higher-performing Undoped-Spiro devices, with an average J_{sc} of 0.132 mA/cm². However, the overall average J_{sc} for all fabricated devices of this

type was slightly lower, around 0.129 mA/cm². To ensure accuracy, a new batch of devices will be fabricated before manuscript submission to confirm whether the reported average J_{sc} of 0.132 mA/cm² in this thesis is accurate or slightly overestimated.

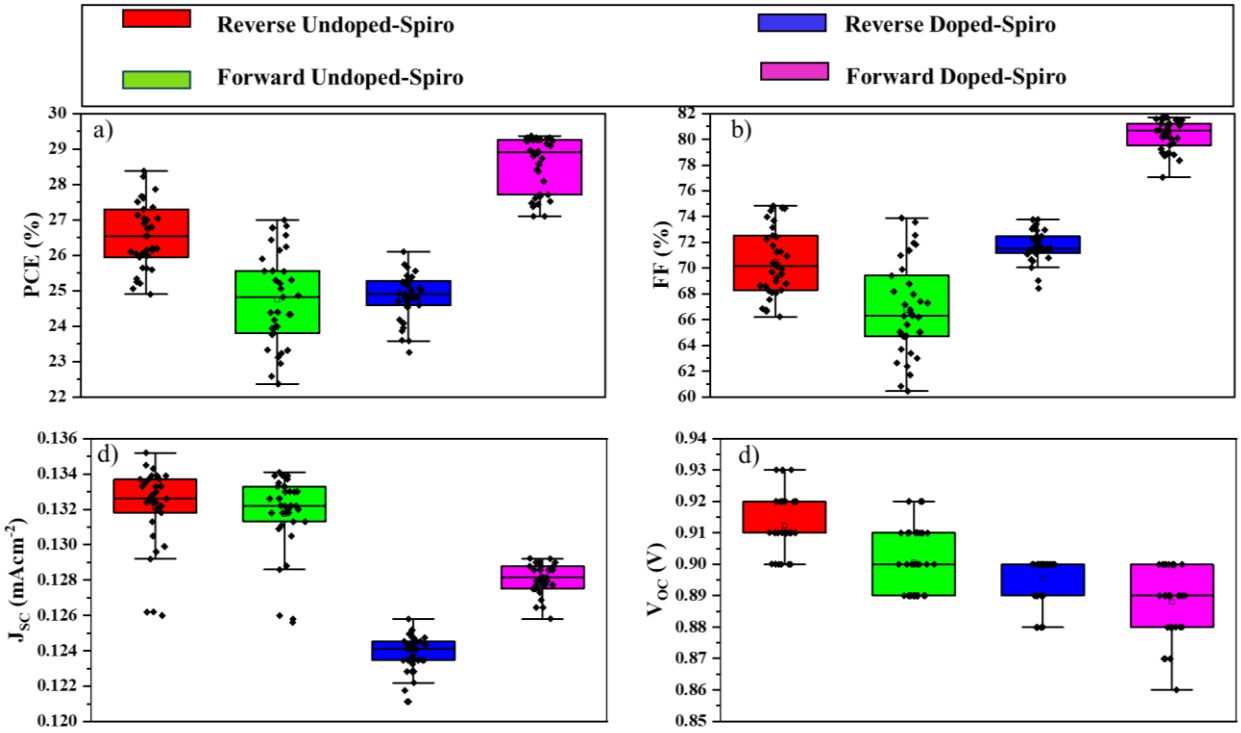

Figure 5.5. Box chart diagrams of a) PCE, b) FF, c) J_{SC}, d) V_{OC} of devices based on Doped- and Undoped-Spiro HTL obtained under 1000 lux WLED illumination.

The HI of devices measured under 1000 lux WLED illumination is shown in Figure **5.6**. Interestingly, the HI trend under indoor illumination is opposite to that observed under standard 1-sun illumination.

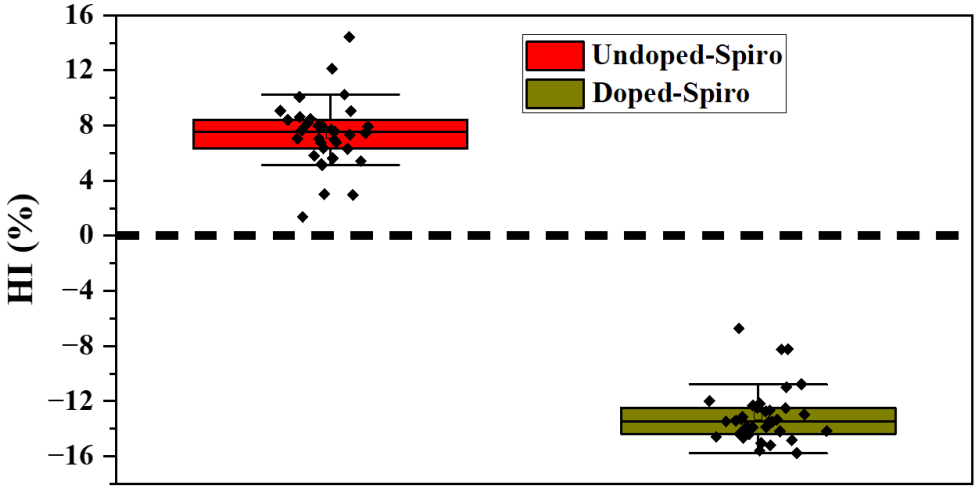

Figure 5.6. HI of doped- and undoped- Spiro-OMeTAD devices evaluated under 1-sun illumination.

As can be seen in **Figure 5.6**, Doped-Spiro devices exhibit negative hysteresis under indoor illumination, in contrast to their positive hysteresis observed under 1-sun conditions (**Figure 5.3**). Conversely, as shown in **Figure 5.6**, Undoped-Spiro devices display positive hysteresis under indoor illumination, whereas they exhibit negative hysteresis under 1-sun conditions (**Figure 5.3**). These observations highlight how device performance parameters vary significantly with changes in light intensity.

The champion Doped-Spiro device achieved highest iPCE of 29.36% in reverse scan, with a J_{sc} of 0.128 mA/cm², V_{oc} of 0.89 V, and FF of 81.21%. In contrast, the champion Undoped-Spiro device achieved highest iPCE of 28.37% in forward scan, with a J_{sc} of 0.130 mA/cm², V_{oc} of 0.90 V, and FF of 74.83%. The J-V curves and corresponding PV parameters for both champion devices are presented in **Figure 5.7(a)**.

The integrated current density values for both champion indoor devices were calculated using a combination of their EQE spectra and the incident photon flux density spectrum. As plotted in **Figure 5.7(b)**, the integrated J_{sc} value obtained for champion Undoped-Spiro device is 131.25 $mAcm^{-2}$, a bit higher than its J-V J_{sc} value but still in acceptable limit. In contrast, the integrated J_{sc} value obtained for champion Undoped-Spiro device is 129.79 $mAcm^{-2}$, a slightly lower than its J-V J_{sc} value but in acceptable limit. These calculations confirm the accuracy of our obtained results.

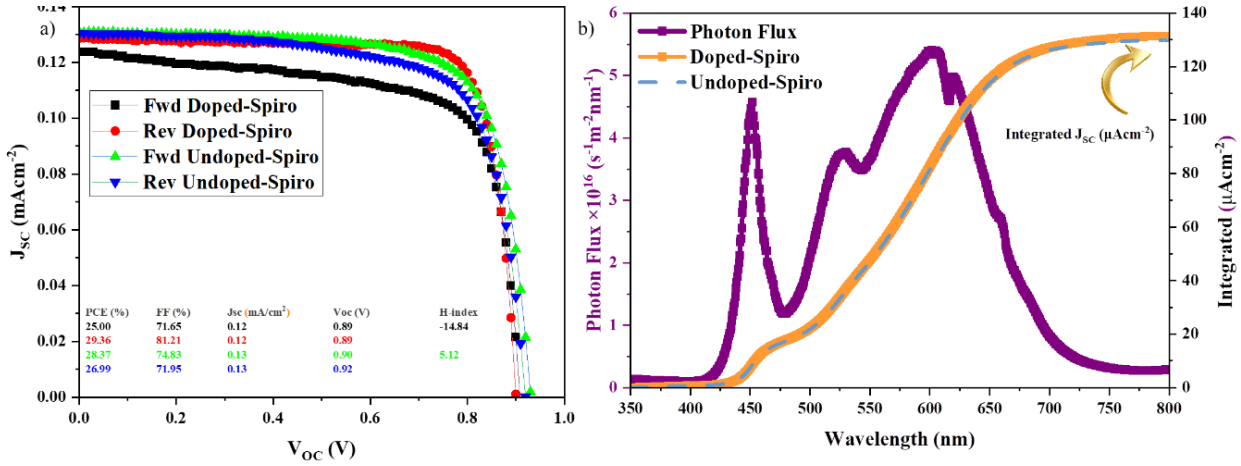

Figure 5.7. a) J-V curves of champion devices based on doped- and undoped- Spiro-OMeTAD HTL obtained under 1000 lux WLED illumination, b) the integrated J_{SC}s of champion devices based on doped- and undoped- Spiro-OMeTAD HTL obtained under 1000 lux WLED illumination.

To evaluate the steady-state indoor efficiency of both device types and address variations in J-V measurements due to scan direction, stabilized power output (SPO) measurements were

performed. Under operational conditions, SPO provides a reliable measure of the actual performance of device [36]. During SPO measurements, the device is maintained at its MPP under continuous illumination, and the output power is tracked until it stabilizes. The stabilized value is then recorded as the true efficiency of a device.

Unfortunately, due to technical issues, we could not perform SPO measurements for the champion Undoped-Spiro device on the day its high performance of 28.37% in forward scan was achieved. Instead, an average-performing Undoped-Spiro device, with performance parameters detailed in the inset of **Figure 5.8(b)**, was selected for comparison with the champion Doped-Spiro device, and SPO measurements were conducted for both. As shown in the insets of **Figure 5.8(a)** and **Figure 6.8(b)**, the peak J-V iPCEs for the champion Doped-Spiro and average-performing Undoped-Spiro devices were 29.36% and 26.39%, respectively. However, the SPO values were lower, approximately 26% for the Doped-Spiro device and 25% for the Undoped-Spiro device, respectively. Notably, the champion Doped-Spiro device exhibited a larger drop in SPO compared to its peak J-V efficiency, likely due to increased hysteresis attributed to the negative effects of Spiro-OMeTAD dopants [37].

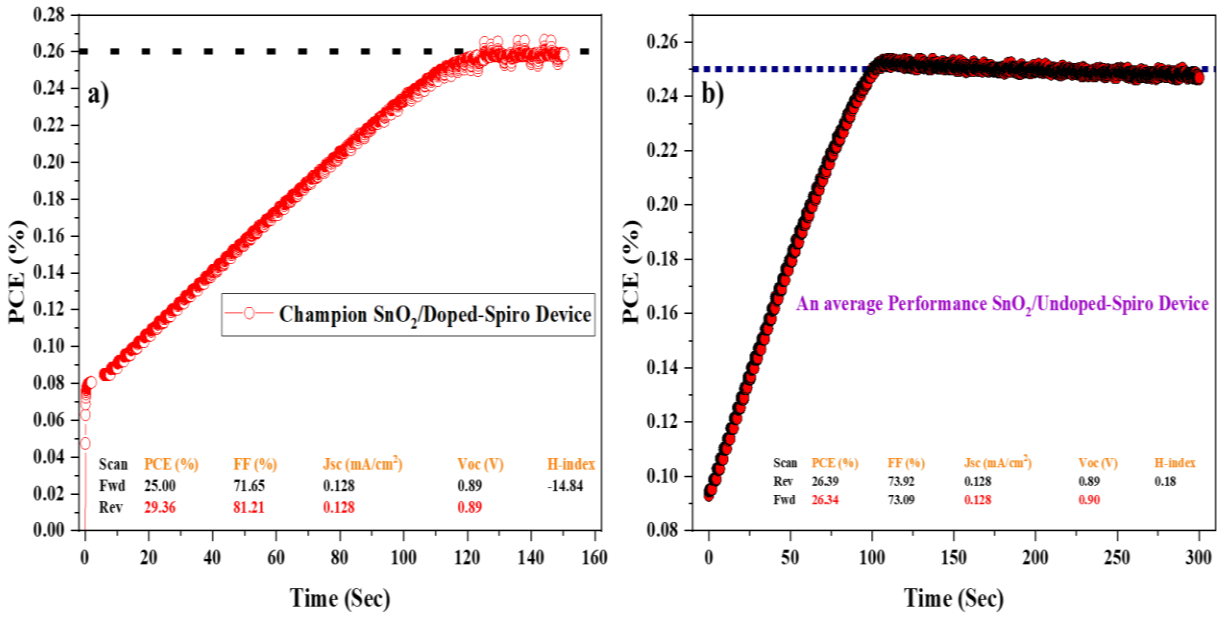

Figure 5.8. SPO of a) champion SnO_2/Doped-Spiro and b) an average performing SnO_2/Undoped-Spiro device obtained under 1000 lux WLED illumination.

5.3.3 Measurements at Varying Light WLED Illumination

To measure the performance of the devices under illumination levels lower than 1000 lux, we reduced both the light intensity and lamp power accordingly, and then measured the device

performance at 900, 800, 700, 600, 500, 400, 300, 200, 100 and 50 lux. **Figure 5.9(a-d)** presents the PV parameters of the champion Doped-Spiro device at different light intensities.

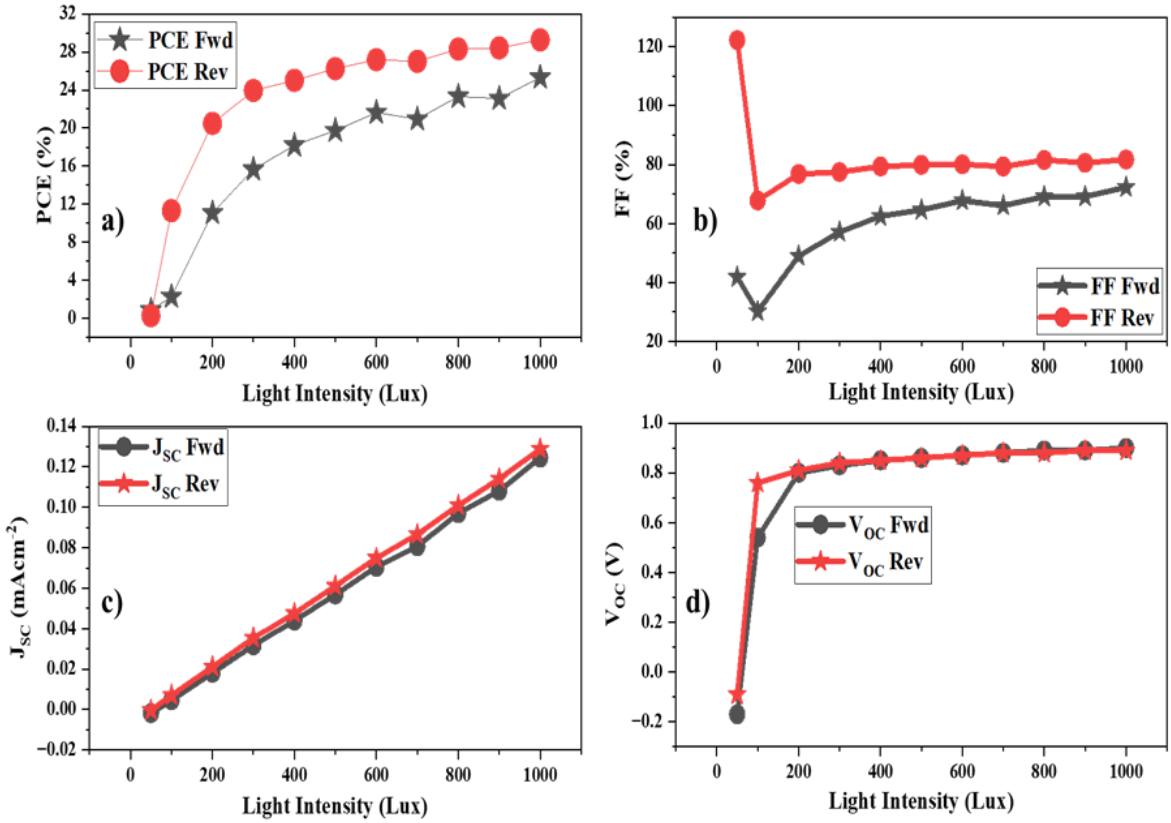

Figure 5.9. a) PCE, b) FF, c) J_{SC}, and d) V_{OC} of the champion SnO_2/Doped-Spiro device under WLED light illumination at varying light intensities ranging from 1000 lux to 50 lux.

As shown in **Figure 5.9(c)**, the J_{sc} of the device decreases linearly with decreasing light intensity in both forward and reverse scan directions. However, the V_{oc} and FF decrease much more gradually as the light intensity decreases. As a result, the device maintains encouraging performance even at lower light intensities down to 100 lux. At 50 lux, however, the device performance approaches zero, as it fails to generate any measurable J_{sc}. This causes the V_{oc} to drop sharply and resulting in an unrealistic FF value. In addition to the champion Doped-Spiro device, we measured several other SnO_2/Doped-Spiro devices to confirm whether these devices truly fail to yield performance at 50 lux. Interestingly, a similar trend was observed across all devices, with the majority showing performance approaching zero in one of the scan directions. Further details will be provided in the manuscript of this work.

The hysteresis index of the champion Doped-Spiro device at different light intensities is shown in **Figure 5.10(a)**. As can be seen in the **Figure 5.10(a)**, the device consistently exhibits negative hysteresis across all measured light intensities. Furthermore, the hysteresis increases significantly

at lower light intensities compared to higher light intensities. We are particularly interested in gaining a deeper understanding of the influence of light intensity on the hysteresis behaviour of the PVK-based devices. In this regard, we plan to conduct theoretical studies along with additional experimental investigations before drawing any logical conclusion.

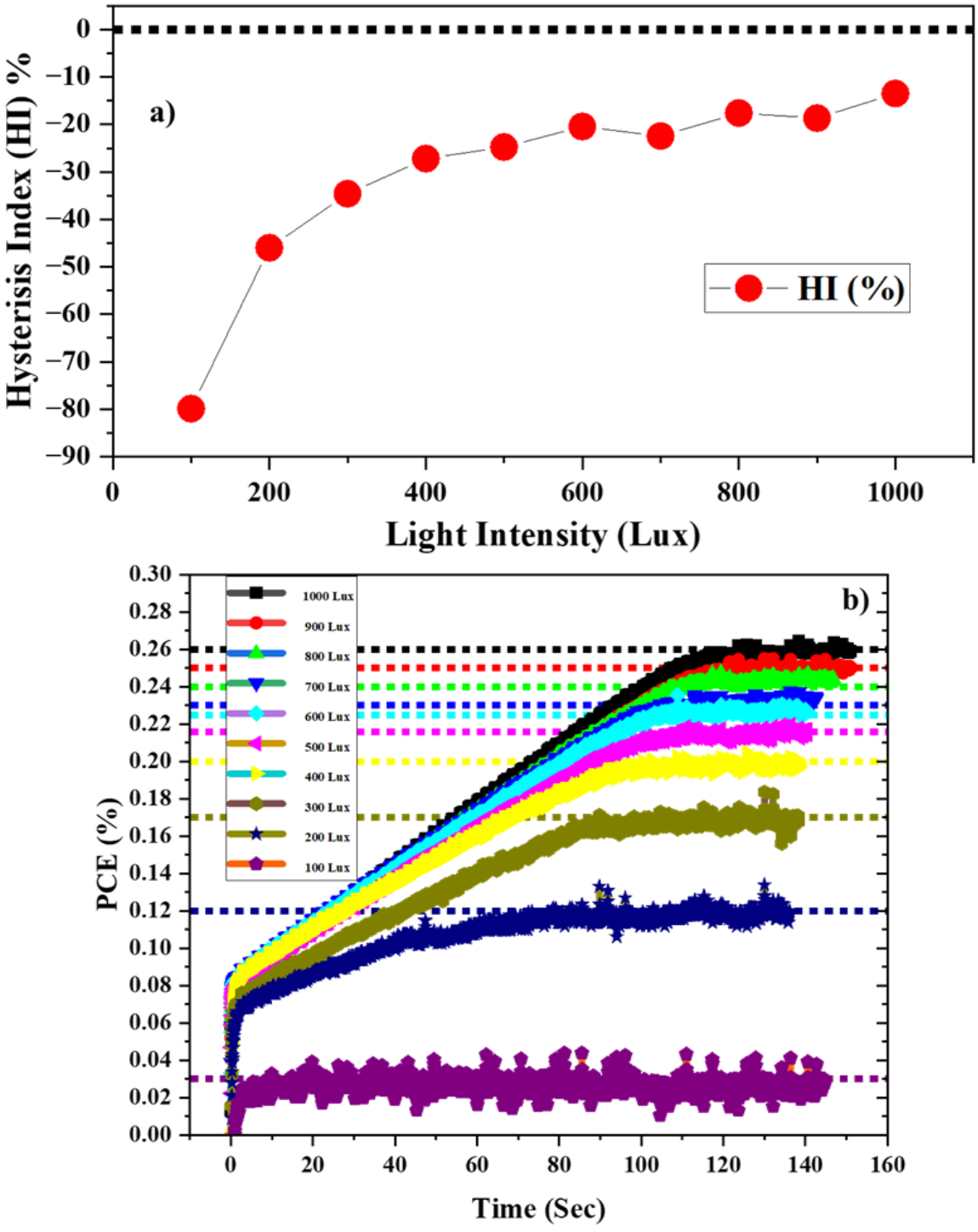

Figure 5.10. a) HI and b) SPO data for the Doped-Spiro device under varying light intensities of WLED illumination.

In order to evaluate the steady-state efficiency at different light intensities of Doped-Spiro device, SPO measurements are performed for over two minutes following the completion of J-V measurements at each light intensity. The **Figure 5.10(b)** presents the SPO data of a device at different light intensities. As can be seen, the device maintains steady state efficiency of over 20% down to 400 lux, with a slight decrease in SPO observed as the light intensity decreases from 1000 lux to 400 lux in increments of 100 lux. This can be attributed to comparatively lower hysteresis in the device performance at higher lux intensities. However, as can be seen in the **Figure 5.10(a)**, as the hysteresis increases at lower light intensities from 300 to 100 lux, the SPO drops sharply, with only 3% efficiency achieved at 100 lux (**Figure 5.10b)**.

In addition to the champion Doped-Spiro-OMeTAD device, we measured the performance of several Undoped-Spiro devices at varying light intensities. The PV parameters of one such device at different light intensities is summarized in the **Table 5.1**.

Table 5.1. Indoor PV parameters in forward and reverse scan directions for an average Undoped-Spiro device under varying light intensities of WLED illumination.

Light Intensity (Lux)	Scan	PCE (%)	FF (%)	J_{SC} (μAcm^{-2})	V_{OC} (V)	HI (%)
1000	Reverse	25.30	71.34	127.5	0.89	-2.8408
	Forward	26.04	74.14	127.7	0.88	
900	Reverse	24.99	70.49	114.7	0.89	-2.0615
	Forward	25.52	73.63	114.7	0.87	
800	Reverse	24.48	70.46	101.1	0.88	-2.5500
	Forward	25.13	74.45	100.5	0.86	
700	Reverse	24.30	69.69	88.8	0.88	-1.6008
	Forward	24.70	72.82	88.3	0.86	
600	Reverse	23.93	69.88	75.6	0.87	-2.3505
	Forward	24.50	73.25	75.6	0.85	
500	Reverse	23.23	68.61	63	0.86	-2.5750
	Forward	23.85	72.10	63	0.84	
400	Reverse	22.75	67.33	50.9	0.85	-3.2876
	Forward	23.52	71.30	50.9	0.83	
300	Reverse	21.56	66.53	37	0.84	-2.8573
	Forward	22.19	69.75	37.3	0.82	
200	Reverse	19.53	61.75	24.7	0.82	-7.2917
	Forward	21.07	67.69	24.9	0.80	
100	Reverse	16.23	54.87	12.1	0.78	-11.5961
	Forward	18.36	62.61	12.3	0.76	
50	Reverse	11.06	44.65	5.7	0.69	-16.7991
	Forward	13.30	54.17	5.5	0.71	

Interestingly, two notable trends were observed from these measurements. Firstly, compared to the Doped-Spiro devices, which exhibited significant fluctuations in hysteresis at different light intensities, the hysteresis fluctuation in the Undoped-Spiro devices was much less pronounced. Secondly, the Undoped-Spiro devices consistently maintained performances close to or above 10% even at very low 50 lux intensities, which was not the case for the Doped-Spiro devices.

Since J-V J_{SC} of a device is the only metric when it correlates with the integrated J_{SC} from EQE, it serves as a reliable indicator of device performance. To validate our results at very low light intensities for Undoped-Spiro device, we compared the J-V J_{SC} of a one such Undoped-Spiro device at various light intensities with the integrated J_{SC}, calculated using the EQE spectra, incident photon flux density, and light intensity. The PV parameters of a corresponding device at different lux and the calculated integrated J_{SC} values are summarized in **Table 5.2**. Interestingly, the calculated J_{SC} validated the experimental data and enabled performance measurements of a device down to 30 lux. As shown in **Table 5.2**, from 1000 lux to 100 lux, the lamp power corresponds exactly to the light intensity at which the device is measured. Interestingly, within this range, the J_{SC} values obtained from the J-V curves at different light intensities closely match the calculated integrated J_{SC} values, with only slight variations within acceptable ranges. However, at 50 lux, the J_{SC} of 4.3 μA/cm² from J-V curves was significantly lower than the calculated 6.58 μA/cm². At such low light intensity, the loss in J_{SC} critically affects the performance of device. This led us to consider that, since the 50-lux light intensity is very low, it might not be precisely stabilized at the device surface. Therefore, we kept the lamp power at 0.016 mW/cm² but increased the light intensity from 50 to 60 lux and subsequently remeasured the performance of device. Interestingly, as a result of this adjustment, the J_{SC} in the reverse scan increased from 4.3 μA/cm² to 6 μA/cm², which was closer to the calculated integrated J_{SC} of 6.58 μA/cm². As a result, the performance of device significantly improved. Similarly, we continued measuring the performance of device performance at 40 and 30 lux, following the same approach by setting the lamp power correspond to 40 and 30 lux, but measuring these devices at 50 and 40 lux, respectively. Interestingly, the integrated J_{SC} values closely matched the measurements at 40 and 30 lux when the lamp power was set to 40 and 30 lux, respectively. Additionally, we attempted to measure the performance of device at 20 lux. However, the device did not generate any measurable performance. Nevertheless, when the lamp power for 20 lux was unchanged and the light intensity was increased to 30 lux, the device generated performance with a J_{SC} close to the integrated J_{SC} calculated for the device at 20 lux.

Table 5.2. Indoor PV parameters in forward and reverse scan directions for an average Undoped-Spiro device under varying light intensities of WLED illumination.

Light Intensity (Lux)	Lamp Power (mW cm^{-2})	Scan	PCE (%)	FF (%)	J_{SC} (μAcm^{-2})	Integrated J_{SC} (μAcm^{-2})	V_{OC} (V)	HI (%)
1000	0.32	Rev	26.54	73.28	128.8	131.97	0.90	-0.3321
		Fwd	26.63	73.98	129.4		0.89	
900	0.288	Rev	25.99	71.58	116.2	118.61	0.90	-1.47
		Fwd	26.38	73.46	116.2		0.89	
800	0.256	Rev	25.91	71.74	103.9	105.43	0.89	-1.19
		Fwd	26.22	73.43	103.9		0.88	
700	0.224	Rev	25.71	71.36	90.7	92.25	0.89	-0.91
		Fwd	25.94	73.67	90.7		0.87	
600	0.192	Rev	25.51	70.87	78.6	79.07	0.88	-0.63
		Fwd	25.67	72.34	78.3		0.87	
500	0.16	Rev	24.93	69.72	65.8	65.95	0.87	-1.49
		Fwd	25.31	72.30	65.1		0.86	
400	0.128	Rev	24.44	69.20	52.6	52.71	0.86	-0.31
		Fwd	24.52	70.23	52.6		0.85	
300	0.096	Rev	23.95	67.97	39.8	39.53	0.8500	-1.33
		Fwd	24.28	70.08	39.6		0.84	
200	0.064	Rev	22.26	64.50	26.6	26.35	0.83	-3.42
		Fwd	23.04	67.60	26.6		0.82	
100	0.032	Rev	20.75	58.21	14.3	13.17	0.80	-8.69
		Fwd	22.73	66.37	14		0.78	
60	0.016	Rev	12.89	46.76	6	6.58	0.74	-16.10
		Fwd	15.36	57.80	5.7		0.74	
50	0.016	Rev	7.95	43.33	4.3	6.58	0.69	-21.83
		Fwd	10.17	54.64	4.3		0.70	
50	0.0128	Rev	11.24	41.98	4.9	5.27	0.70	-18.06
		Fwd	13.72	54.56	4.5		0.7200	
40	0.0128	Rev	4.39	36.26	2.8	5.27	0.56	-10.80
		Fwd	4.92	33.55	3		0.63	
40	0.0096	Rev	9.40	33.55	4	3.95	0.67	-8.22
		Fwd	10.24	33.30	3.4		0.6800	
30	0.0096	Rev	2.52	42.46	1.5	3.95	0.28	-20.82
		Fwd	3.19	58.16	1.3		0.58	
30	0.0064	Rev	5.18	41.37	1.9	2.63	0.43	-13.33
		Fwd	5.98	40.30	1.9		0.62	
20	0.0064	No Results						

To investigate the SPO of Undoped-Spiro devices at lower light intensities, we selected a lower-performing device instead of a higher-performing one. This choice was based on the observation that Undoped-Spiro devices exhibit reduced hysteresis compared to their doped counterparts at lower light intensities, ensuring more reliable SPO performance, as witnessed in **Figure 5.8(b)**. Therefore, rather than measuring SPO for higher-performing devices, we conducted measurements at varying light intensities for the lower-performing Undoped-Spiro device at 1000 lux to determine whether it could still maintain appreciable performance at 50 lux, and to determine the extent of the SPO it could generate. The performance parameters at varying light intensities of one such device with lower performance at 1000 lux are summarized in **Table 5.3**. As shown in the table, the device achieves a maximum performance of 23.5% in the reverse scan at 1000 lux and, interestingly, maintains a performance of 9.79% in the reverse scan even at 50 lux.

Table 5.3. Indoor PV parameters in forward and reverse scan directions for a low performing SnO_2/Undoped-Spiro device under varying light intensities of WLED illumination.

Light Intensity (Lux)	**Scan**	**PCE (%)**	**FF (%)**	**J_{SC} ($mAcm^{-2}$)**	**V_{OC} (V)**	**HI (%)**
1000	Rev	22.91	67.23	0.1299	0.84	-1.43
	Fwd	23.25	68.21	0.1299	0.84	
900	Rev	22.19	65.83	0.1156	0.84	-0.31
	Fwd	22.26	66.96	0.1154	0.83	
800	Rev	21.76	65.05	0.102	0.84	-0.32
	Fwd	21.83	66.05	0.102	0.83	
700	Rev	21.19	64.76	0.0883	0.83	-0.31
	Fwd	21.26	65.76	0,0883	0.82	
600	Rev	21.02	64.17	0.0758	0.83	0.25
	Fwd	20.97	65.41	0.076	0.81	
500	Rev	20.40	63.20	0.063	0.82	1.56
	Fwd	20.09	64.00	0.0628	0.80	
400	Rev	19.79	61.77	0.05	0.82	1.04
	Fwd	19.59	62.66	0.05	0.80	
300	Rev	18.99	61.20	0.0373	0.80	1.05
	Fwd	18.80	62.47	0.037	0.78	
200	Rev	17.76	59.53	0.0245	0.78	-1.63
	Fwd	18.05	61.57	0.0247	0.76	
100	Rev	15.16	57.05	0.0115	0.74	-1.72
	Fwd	15.43	59.67	0.0115	0.72	
50	Rev	9.15	46.02	0.0049	0.65	-6.52
	Fwd	9.79	48.48	0.0049	0.66	

The **Figures 5.11(a)** and **5.11(b)** present the SPO measurements of the lower-performing Undoped Spiro device at varying light intensities as summarized above in **Table 5.3**.

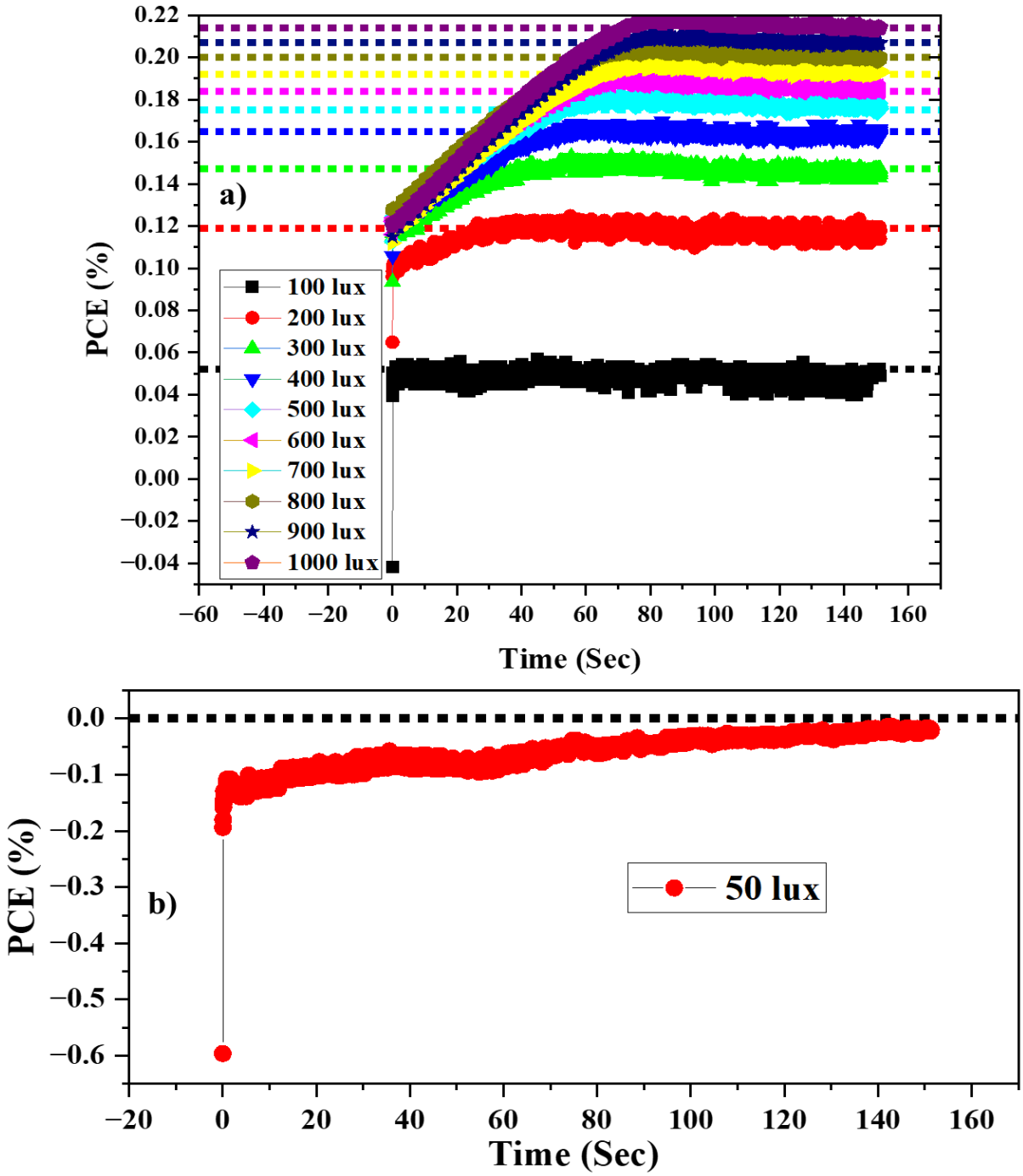

Figure 5.11. SPO data for a low performing SnO_2/Undoped-Spiro device under (a) varying light intensities ranging from 1000 lux to 100 lux, and (b) 50 lux WLED illumination.

As expected, owing to reduced hysteresis behaviour of the device performance at varying light intensities and especially at reduced light intensities, the decline in SPO was gradual and not as dramatic as was observed in the case of champion Doped Spiro-OMeTAD device, as given in

Figure 5.10. Interestingly, at 200 lux intensity, the lower performing Undoped-Spiro device SPO was comparable to champion Doped-Spiro device at the same lux (**Figure 5.10**). Even more interestingly, at 100 lux, lower-performing Undoped-Spiro device outperformed (**Figure 5.11**) the SPO of champion Doped-Spiro device (**Figure 5.10**). However, as shown in **Figure 5.11(b)**, the SPO of device at 50 lux struggled to approach zero from the negative SPO range. Nevertheless, the trend displayed a gradual increase over time. Since the SPO measurements were conducted over a duration of two minutes at varying light intensities, the SPO of device did not reach zero within this time frame.

After observing a gradual increase in the SPO of the lower-performing Undoped-Spiro device (Herein after labelled as "Device 1") over time at 50 lux, we hypothesized that a longer measurement duration might be required to obtain accurate SPO results at such low light intensity.

To investigate, we remeasured the performance of the device labelled as "Device 2" at the same intensity and extended the SPO duration from 2.5 minutes to 10 minutes. As shown in the inset of **Figure 5.12**, the PV performance parameters of Device 2, particularly J_{SC}, improved significantly compared to the initial measurement (Device 1), as summarized in **Table 5.3** and in the inset of **Figure 5.12**.

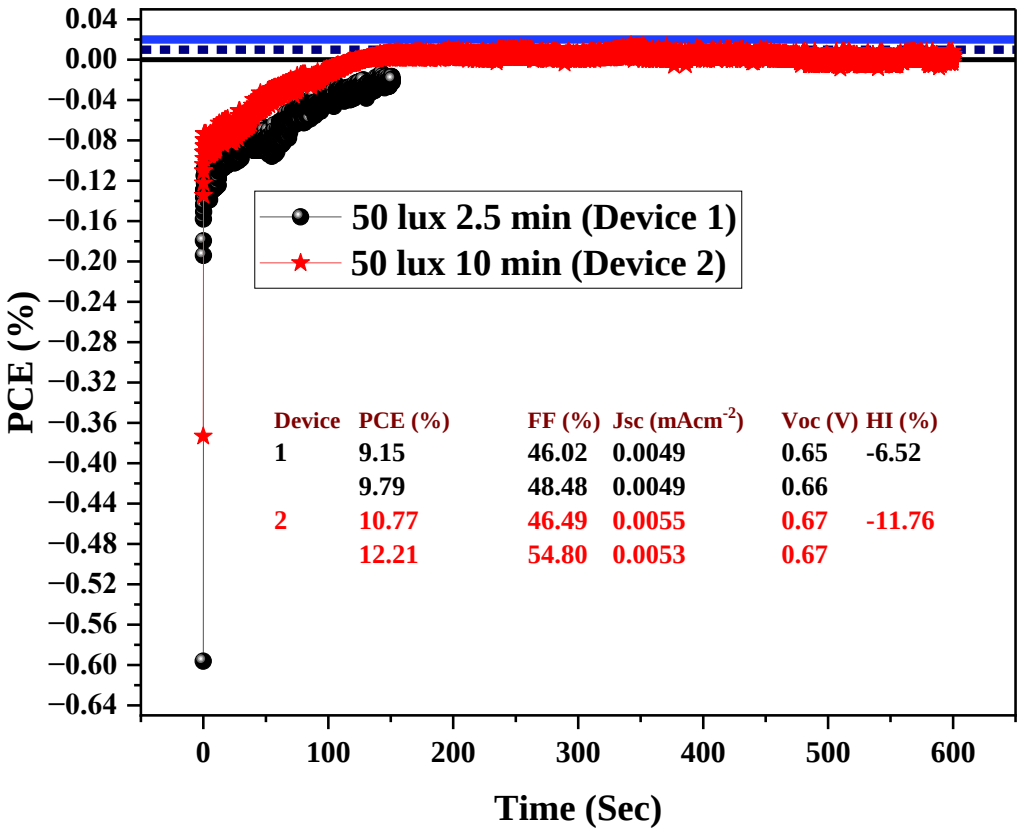

Figure 5.12. SPO data for "Device 1" and "Device 2" under 50 lux WLED illumination.

This improvement is surprising, as improving J_{SC} at such low light intensity is challenging. What could be the reason behind it, is not yet very clear to us. However, we hypothesize that some unfilled traps may have been filled during the initial measurement and subsequent SPO process. Another possibility is that light on the device surface might be more stabilized in a later measurement owing to the prolong exposure of the device to light at 50 lux. Since the device initially measured at 50 lux, then underwent post SPO measurement for another more than 2.5 minutes. Later we changed the conditions in the measurement program instead of disturbing device and changing light intensity and then remeasured it. Although at this stage, we can't provide more meaningful explanation, however, we expect to provide some useful comments on it in the manuscript of this work.

The SPO of the device labelled "Device 2", compared to "Device 1", is plotted in the **Figure 5.12**. As can be seen, "Device 2" transitions from the negative SPO region to zero in a shorter duration and surpasses zero, reaching the positive SPO region. It touches even the 2% PCE range at certain points before stabilizing at 1% PCE region rather than increasing further. This indicates that, rather than depending on the measurement duration, the performance parameters of the device play a critical role in determining the reasonable SPO of the corresponding device.

5.4 Conclusion

In conclusion, this study validated previous findings of our group [26] that dopants in spiro-OMeTAD are not essential for achieving reliable and high performance in PSCs under indoor light illumination. Furthermore, this work, for the first time, demonstrated the potential of PSCs incorporating undoped spiro-OMeTAD and a low-temperature SnO_2 ETL. As expected, the Doped-Spiro devices delivered superior performance under standard lighting conditions due to higher FFs. However, under low-light conditions, the Undoped-Spiro devices exhibited higher FFs, enabling their performance to approach that of the Doped-Spiro devices. Additionally, the Undoped-Spiro devices demonstrated significantly lower hysteresis under indoor illumination compared to their counterparts. Notably, under extremely low-light intensities, the SPO of Undoped-Spiro devices outperformed that of Doped-Spiro devices. The highest recorded iPCE of 28.37% for the champion Undoped-Spiro device represents the highest reported efficiency to date for PVK-based devices with undoped spiro-OMeTAD. Furthermore, achieving average efficiencies exceeding 10% under extremely low light (50 lux) is an additional key distinguishing outcome of this study. Overall, these findings highlight the potential of undoped spiro-OMeTAD and the critical role of ETL materials in optimizing device performance, particularly under challenging low-light conditions. The adaptability of the fabrication process to flexible substrates

provides new opportunities for further research and development in high-performance, flexible IPV devices.

5.5 Future Work

As mentioned before, this study is still in progress and has not yet reached its final conclusions. A parallel comparative investigation of similar devices utilizing TiO_2 ETL is underway to further explore the role of ETLs in the hysteresis behaviour of PSCs under indoor illumination. Additionally, a theoretical study is planned to gain deeper insights into the mechanisms driving hysteresis in these devices under such conditions. To support and validate the findings, a comprehensive range of optical and electrical characterizations will be conducted. Stability measurements will also be performed on both SnO_2 and TiO_2-based devices under various lighting and environmental conditions. These measurements aim to assess the influence of spiro-OMeTAD dopants and ETL materials on overall device stability. The final outcomes of this research, incorporating both experimental and theoretical insights, will be consolidated and submitted as a manuscript for journal publication. This will provide a detailed understanding of the performance and stability of PSCs incorporating SnO_2, TiO_2, and spiro-OMeTAD under indoor illumination.

References

1. Ye, L. *et al.* Superoxide radical derived metal-free spiro-OMeTAD for highly stable perovskite solar cells. *Nat Commun* **15**, 7889 (2024).
2. Zhu, G. *et al.* Unveiling the Critical Role of Oxidants and Additives in Doped Spiro-OMeTAD toward Stable and Efficient Perovskite Solar Cells. *ACS Appl Energy Mater* **5**, 3595–3604 (2022).
3. Zhou, S. *et al.* Low-Cost Dopant-Free Carbazole Enamine Hole-Transporting Materials for Thermally Stable Perovskite Solar Cells. *Solar RRL* **6**, (2022).
4. Shen, Y., Deng, K. & Li, L. Spiro-OMeTAD-Based Hole Transport Layer Engineering toward Stable Perovskite Solar Cells. *Small Methods* **6**, (2022).
5. Fuentes Pineda, R. *et al.* Star-shaped triarylamine-based hole-transport materials in perovskite solar cells. *Sustain Energy Fuels* **4**, 779–787 (2020).
6. Rombach, F. M., Haque, S. A. & Macdonald, T. J. Lessons learned from spiro-OMeTAD and PTAA in perovskite solar cells. *Energy Environ Sci* **14**, 5161–5190 (2021).
7. Nakka, L., Cheng, Y., Aberle, A. G. & Lin, F. Analytical Review of Spiro-OMeTAD Hole Transport Materials: Paths Toward Stable and Efficient Perovskite Solar Cells. *Advanced Energy and Sustainability Research* **3**, (2022).
8. Tumen-Ulzii, G., Matsushima, T. & Adachi, C. Mini-Review on Efficiency and Stability of Perovskite Solar Cells with Spiro-OMeTAD Hole Transport Layer: Recent Progress and Perspectives. *Energy & Fuels* **35**, 18915–18927 (2021).
9. Ouedraogo, N. A. N. *et al.* Oxidation of Spiro-OMeTAD in High-Efficiency Perovskite Solar Cells. *ACS Appl Mater Interfaces* **14**, 34303–34327 (2022).
10. Snaith, H. J. & Grätzel, M. Enhanced charge mobility in a molecular hole transporter via addition of redox inactive ionic dopant: Implication to dye-sensitized solar cells. *Appl Phys Lett* **89**, (2006).
11. Juarez-Perez, E. J. *et al.* Role of the Dopants on the Morphological and Transport Properties of Spiro-MeOTAD Hole Transport Layer. *Chemistry of Materials* **28**, 5702–5709 (2016).
12. Noh, J. H. *et al.* Nanostructured TiO2/CH3NH3PbI3 heterojunction solar cells employing spiro-OMeTAD/Co-complex as hole-transporting material. *J Mater Chem A Mater* **1**, 11842 (2013).
13. Ding, C. *et al.* Synergetic effects of electrochemical oxidation of Spiro-OMeTAD and Li^+ ion migration for improving the performance of n–i–p type perovskite solar cells. *J Mater Chem A Mater* **9**, 7575–7585 (2021).
14. Wang, S., Yuan, W. & Meng, Y. S. Spectrum-Dependent Spiro-OMeTAD Oxidization Mechanism in Perovskite Solar Cells. *ACS Appl Mater Interfaces* **7**, 24791–24798 (2015).
15. Sanchez, R. S. & Mas-Marza, E. Light-induced effects on Spiro-OMeTAD films and hybrid lead halide perovskite solar cells. *Solar Energy Materials and Solar Cells* **158**, 189–194 (2016).

16. Kasparavicius, E., Magomedov, A., Malinauskas, T. & Getautis, V. Long-Term Stability of the Oxidized Hole-Transporting Materials used in Perovskite Solar Cells. *Chemistry – A European Journal* **24**, 9910–9918 (2018).

17. Domanski, K. *et al.* Not All That Glitters Is Gold: Metal-Migration-Induced Degradation in Perovskite Solar Cells. *ACS Nano* **10**, 6306–6314 (2016).

18. Guarnera, S. *et al.* Improving the Long-Term Stability of Perovskite Solar Cells with a Porous Al $_2$ O $_3$ Buffer Layer. *J Phys Chem Lett* **6**, 432–437 (2015).

19. Schulz, A. D. *et al.* Doping Strategies for Tetrasubstituted Paracyclophane Hole Transport Layers in Perovskite Solar Cells. *Adv Funct Mater* **34**, (2024).

20. Ren, G. *et al.* Overcoming Perovskite Corrosion and De-Doping Through Chemical Binding of Halogen Bonds Toward Efficient and Stable Perovskite Solar Cells. *Nanomicro Lett* **14**, 175 (2022).

21. Pecunia, V., Occhipinti, L. G. & Hoye, R. L. Z. Emerging Indoor Photovoltaic Technologies for Sustainable Internet of Things. *Adv Energy Mater* **11**, (2021).

22. Wang, K.-L., Zhou, Y.-H., Lou, Y.-H. & Wang, Z.-K. Perovskite indoor photovoltaics: opportunity and challenges. *Chem Sci* **12**, 11936–11954 (2021).

23. Wang, K. *et al.* Ion–Dipole Interaction Enabling Highly Efficient CsPbI $_3$ Perovskite Indoor Photovoltaics. *Advanced Materials* **35**, (2023).

24. Skafi, Z. *et al.* Highly Efficient Flexible Perovskite Solar Cells on Polyethylene Terephthalate Films via Dual Halide and Low-Dimensional Interface Engineering for Indoor Photovoltaics. *Solar RRL* **7**, (2023).

25. Kim, S., Jahandar, M., Jeong, J. H. & Lim, D. C. Recent Progress in Solar Cell Technology for Low-Light Indoor Applications. *Current Alternative Energy* **3**, 3–17 (2019).

26. Toikkonen, S. *et al.* Is Doping of Spiro-OMeTAD a Requirement for Efficient and Stable Perovskite Indoor Photovoltaics? *Advanced Devices & Instrumentation* **5**, (2024).

27. Pellaroque, A. *et al.* Efficient and Stable Perovskite Solar Cells Using Molybdenum Tris(dithiolene)s as p-Dopants for Spiro-OMeTAD. *ACS Energy Lett* **2**, 2044–2050 (2017).

28. Yuan, P. *et al.* High-Performance Perovskite Solar Cells Using Iodine as Effective Dopant for Spiro-OMeTAD. *Energy Technology* **8**, (2020).

29. Ashassi-Sorkhabi, H. & Salehi-Abar, P. How the change of OMe substituent position affects the performance of spiro-OMeTAD in neutral and oxidized forms: theoretical approaches. *RSC Adv* **8**, 18234–18242 (2018).

30. Scully, S. R., Armstrong, P. B., Edder, C., Fréchet, J. M. J. & McGehee, M. D. Long-Range Resonant Energy Transfer for Enhanced Exciton Harvesting for Organic Solar Cells. *Advanced Materials* **19**, 2961–2966 (2007).

31. Tress, W., Correa Baena, J. P., Saliba, M., Abate, A. & Graetzel, M. Inverted Current–Voltage Hysteresis in Mixed Perovskite Solar Cells: Polarization, Energy Barriers, and Defect Recombination. *Adv Energy Mater* **6**, (2016).

32. Wu, F. *et al.* Inverted Current–Voltage Hysteresis in Perovskite Solar Cells. *ACS Energy Lett* **3**, 2457–2460 (2018).

33. Sepalage, G. A. *et al.* Copper(I) Iodide as Hole-Conductor in Planar Perovskite Solar Cells: Probing the Origin of *J – V* Hysteresis. *Adv Funct Mater* **25**, 5650–5661 (2015).

34. Hatamvand, M. *et al.* The role of different dopants of Spiro-OMeTAD hole transport material on the stability of perovskite solar cells: A mini review. *Vacuum* **214**, 112076 (2023).

35. Glowienka, D. & Galagan, Y. Light Intensity Analysis of Photovoltaic Parameters for Perovskite Solar Cells. *Advanced Materials* **34**, (2022).

36. Kim, H.-S. *et al.* Power output stabilizing feature in perovskite solar cells at operating condition: Selective contact-dependent charge recombination dynamics. *Nano Energy* **61**, 126–131 (2019).

37. Yekani, R. *et al.* Impact of Photo-Induced Doping of Spiro-OMeTAD as HTL on Perovskite Solar Cell Hysteresis Dynamics. *The Journal of Physical Chemistry C* **128**, 710–722 (2024).

Chapter 6

Conclusions and Future Work

This chapter would review on the general findings of this thesis and provide some possible directions for future research.

6.1 Conclusions

This thesis has focused on addressing key challenges associated with PVK-based IPV technology to facilitate their future development. Firstly, considering the unique operational conditions and challenges of IPVs, significant emphasis has been placed on improving the surface quality of triple-cation PVK absorber to enhance device performance and stability. A range of passivation layers, including GUI, PEAI, OAI, and DPPP, were explored to mitigate surface defects and minimize carrier recombination. These improvements are particularly crucial under dim indoor lighting, where photogenerated carrier production is inherently lower compared to standard 1-sun illumination. A key scientific contribution of this thesis is the novel use of DPPP as a passivation layer in n-i-p structured PSCs. As demonstrated, DPPP effectively enhances the stability of triple-cation PVK and the performance of their corresponding devices under operational conditions. This breakthrough could drive significant progress in the field of PVK-based IPVs. The findings of the thesis reveal that while passivation layers significantly improve performance under standard light conditions, their impact under low-light indoor illumination is less pronounced. However, their combined benefits in performance enhancement and stability improvement make them invaluable for the advancement of PVK-based IPVs. Additionally, the thesis highlights that performance improvements achieved under standard illumination cannot always be directly extrapolated to indoor conditions; in some cases, passivation layers may exhibit contrasting effects under low-light environments.

Secondly, this thesis investigates, in detail, the role of dopants in the traditional Spiro-OMeTAD HTL on the performance of SnO_2-based n-i-p structure PSCs under indoor illumination for the first time. The initial findings are both intriguing and promising, validating our group's previous results for TiO_2-based devices, which demonstrated that Spiro-OMeTAD dopants are unnecessary for PVK-based devices operating under indoor illumination. Furthermore, the findings underscore the critical influence of the ETL selection on device performance and hysteresis behaviour. While ongoing research in this project aims to uncover the underlying mechanisms driving performance improvements under indoor illumination without Spiro-OMeTAD dopants, as well as the

variations in performance and hysteresis behaviour with different ETLs, the current findings mark a significant step forward. Notably, this work opens a promising pathway for the development of flexible IPV devices incorporating SnO_2 ETL and eliminating the need for dopants in Spiro-OMeTAD, paving the way for more efficient, stable, and cost-effective designs.

6.2 Outlook and Future Prospects

The need of the hour is to explore new directions for improving the performance and stability of PVK-based IPV technology. While extensive efforts and rapid advancements have been reported in recent years, much remains to be done to fully harness the potential and benefits of this technology.

One major challenge is the lack of standardized protocols for evaluating device performance under indoor illumination, making it difficult to distinguish accurate results from misleading ones. Current lab-specific protocols, developed by esteemed research groups worldwide, cannot be universally adopted as standards unless the broader scientific community working in this field reaches a consensus on standard guidelines. Establishing such protocols would ensure uniformity in device evaluation, guiding the field toward consistent and meaningful advancements. At present, many research groups are investing significant resources and efforts into the development of IPV technology. However, the absence of standardized evaluation protocols could compel them in the future to revisit and revise their device designs and research objectives. Addressing this issue promptly is essential to streamline efforts and drive progress effectively in this promising field.

In addition to establishing standard protocols, attention should be directed toward wide-bandgap PVKs for IPVs, which are theoretically more suitable for these applications compared to lower-bandgap PVKs. This thesis primarily investigated devices for IPVs using low-bandgap triple-cation PVKs. Therefore, exploring the role of passivation layers, as done in this study, for enhancing the performance and stability of wide-bandgap PSCs could yield significant advantages in the future. In this context, similar comparative studies could be conducted by either employing other wide-bandgap PVK materials or by tuning the bandgap of triple-cation PVKs through modifications in elemental composition. For instance, increasing the concentration of cesium at the A-site and bromine at the X-site in triple-cation PVKs presents a promising approach to achieve bandgap tuning and optimize performance for IPV applications.

In n-i-p structure perovskite solar cells, passivation layers are typically sandwiched between the absorber PVK and the HTL. Therefore, conducting comparative investigations with HTLs other than Spiro-OMeTAD, as utilized in this thesis, could yield exciting discoveries. A more compatible HTL with the adjacent passivation layer could facilitate improved hole transport to the counter electrode, resulting in enhanced device performance. Thus, exploring alternative HTLs in such devices represents an intriguing avenue for future research.

In this thesis, the DPPP passivation layer is used for the first time in n-i-p structure PSCs, and its potential is evaluated under both standard 1-sun and indoor illumination. Previously, DPPP has been employed as a passivation layer in p-i-n structure devices, but its performance was assessed exclusively under standard 1-sun illumination. Therefore, future investigations into the potential of the DPPP passivation layer in p-i-n structure PVK-based devices under indoor illumination could represent a promising research direction and lead to exciting discoveries in the field.

In this thesis, comparative studies are conducted to investigate the role of different passivation layers under various illumination conditions for devices based on SnO_2 ETL. SnO_2 is particularly advantageous due to its low-temperature processing requirements, with annealing achievable at just 100°C, making it compatible with several flexible substrates. Consequently, in future research, these passivation layers could be explored to enhance the performance and stability of flexible PSCs under indoor illumination.

As demonstrated in this thesis, Spiro-OMeTAD dopants are not essential for IPVs. Based on these findings, it is important to similarly investigate the role of dopants in other HTLs for IPVs. In this context, poly[bis(4-phenyl)(2,4,6-trimethylphenyl)amine] (PTAA), which traditionally uses the same dopants as Spiro-OMeTAD, could be a promising candidate for future studies.

As established in this thesis, the use of passivation layers plays a significant role in addressing the hysteresis issue in PSCs. An intriguing avenue for future research would be to explore devices incorporating passivation layers but without Spiro-OMeTAD dopants. Such investigations could potentially yield promising results in terms of both performance and stability.

The demonstrated potential of SnO_2-based devices with dopant-free Spiro-OMeTAD HTL for IPVs in this thesis could also be extended to flexible device designs. This represents an excellent avenue for future research with significant potential for commercialization.

Last but not least, the hysteresis behaviour of IPVs needs to be thoroughly understood, both experimentally and theoretically. A deeper investigation into the underlying mechanisms causing and governing hysteresis under indoor illumination is crucial for future advancements. As demonstrated in this thesis, the performance of devices exhibiting significant hysteresis cannot be considered reliable. Therefore, understanding the factors responsible for hysteresis under indoor illumination and implementing strategies to mitigate it should be given meticulous attention. In this context, a combination of theoretical and experimental studies could yield valuable insights and promising results.

La borsa di dottorato è stata cofinanziata con risorse del
Programma Operativo Nazionale Ricerca e Innovazione 2014-2020, risorse FSE REACT-EU
Azione IV.4 “Dottorati e contratti di ricerca su tematiche dell’innovazione”
e Azione IV.5 “Dottorati su tematiche Green”